



## The interplay between domains, defects and electric field induced phase transformations in bulk ferroelectrics

Ormstrup, Jeppe

*Publication date:*  
2020

*Document Version*  
Publisher's PDF, also known as Version of record

[Link back to DTU Orbit](#)

*Citation (APA):*  
Ormstrup, J. (2020). *The interplay between domains, defects and electric field induced phase transformations in bulk ferroelectrics*. Department of Physics, Technical University of Denmark.

---

### General rights

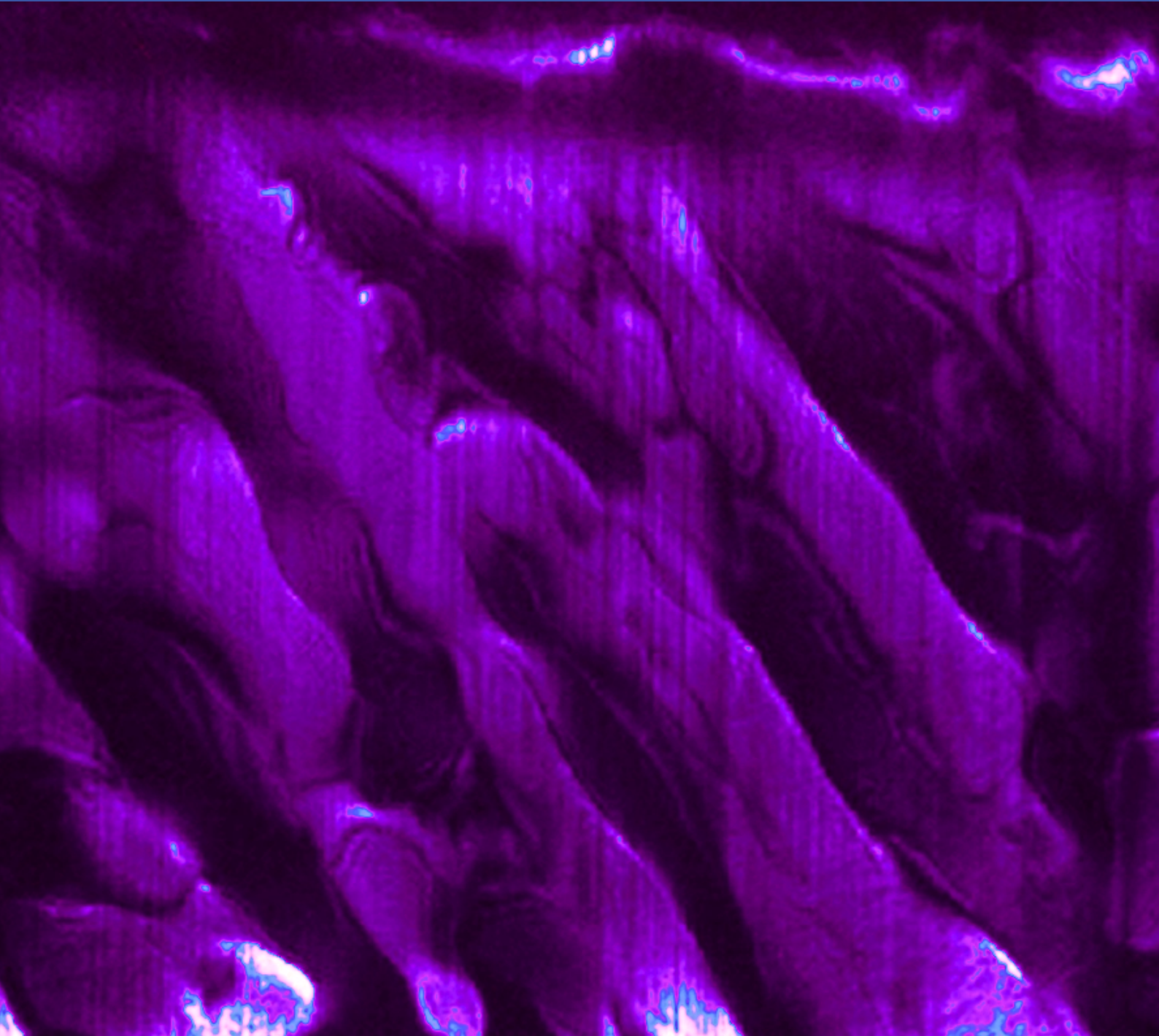
Copyright and moral rights for the publications made accessible in the public portal are retained by the authors and/or other copyright owners and it is a condition of accessing publications that users recognise and abide by the legal requirements associated with these rights.

- Users may download and print one copy of any publication from the public portal for the purpose of private study or research.
- You may not further distribute the material or use it for any profit-making activity or commercial gain
- You may freely distribute the URL identifying the publication in the public portal

If you believe that this document breaches copyright please contact us providing details, and we will remove access to the work immediately and investigate your claim.

# The interplay between domains, defects and electric field induced phase transformations in bulk ferroelectrics

Ph.D. Thesis, Jeppe Ormstrup





**The interplay between domains, defects and electric field induced phase transformations in bulk ferroelectrics**

Ph.D. Thesis  
June, 2020

By  
Jeppe Ormstrup, MSc Materials and Manufacturing Engineering

Copyright:

Reproduction of this publication in whole or in part must include the customary bibliographic citation, including author attribution, report title, etc.

Cover photo: Jeppe Ormstrup, 2017

Published by:

DTU, Department of Physics, Fysikvej, Building 307, 2800 Kgs. Lyngby Denmark

[www.fysik.dtu.dk](http://www.fysik.dtu.dk)

## Approval

This thesis is the culmination of three years work on the Ph.D. project *Multi-Scale 3D Imaging of Heterogeneous Nucleation in Ferroelectrics* with the NEXMAP section under the department of Physics at the Technical University of Denmark, DTU, in fulfilment of the Ph.D. degree.

Jeppe Ormstrup



.....  
*Signature*

June 14, 2020

.....  
*Date*

## Abstract

The manipulation of local morphological features, such as domains, domain walls and defects, is reported to have a dramatic influence on the local and global properties of electro-active materials. The majority of local techniques for characterizing and quantifying have been limited to two dimensions (2D), such as surface and thin films, leaving no methods sufficient for investigating the bulk. The role of morphological features in structural dynamics is not fully understood and thus validation and guidance for bulk and 3D models does not yet exist. This work has produced an experimental approach to overcome these limitations based on imaging of the structural dynamics *in situ* with dark field x-ray microscopy, accompanied by relevant analytical methods for the data analysis. As a first step, we have designed and manufactured the Stable Temperature and Electric Field (STEF) holder system capable of applying an electric field and keeping a stable temperature in the range 26-200 °C with stability of 0.01 K. This facilitates spatial resolution of the electric field induced phase transformation morphology in deeply embedded material. We observe domain-like structures well above the Curie temperature, indicating bulk domain imprinting previously only observed near surfaces. Combined with density functional theory (DFT) calculations, our results suggests that point defects, such as oxygen vacancies, plays an important role in determining morphology both above and below the Curie temperature. In an effort to quantify this role of oxygen vacancies, I then developed a method for detecting defect clusters in bulk material based on their volume expansion. The combined observations throughout this thesis consistently points towards a complex model of the interactions between the various morphological features, which is necessary to understand and predict phase transformation dynamics and related phenomena, such as the heterogeneous nucleation of ferroelectric domains. Here, I present the hypothesis for such a complex interaction behaviour, and our findings and framework to further deepen the knowledge of such claims.

## Populærvidenskabeligt resumé

Manipulationen af lokale morfologiske former, så som domæner, domænevægge og defekter, rapporteres at have en dramatisk indflydelse på de lokale og globale egenskaber af elektroaktive materialer. Størstedelen af lokale karakteriserings- og kvantificeringsmetoder er begrænset til undersøgelser i to dimensioner, såsom overflade- og tynde film. Dette har efterladt os uden en metode til at undersøge lokal variation dybt inde i en prøve. Den rolle som morfologiske former spiller for strukturdynamikkerne er ikke fuldt ud forstået, og der findes derfor ikke validering og retningslinjer til modeller der simulere dybt inde i prøven eller i 3D. Dette arbejde har produceret en eksperimentel tilgang til billeddannelse af den strukturelle dynamik *in situ* og analysemetoder til data fra røntgenbaseret mørkfeltmikroskopi, for at overvinde 2D af overflade begrænsningerne. Specifikt har vi designet og fremstillet STEF-holderen (Stabil Temperatur og Elektrisk Felt), der er i stand til at anvende et elektrisk felt og holde en stabil temperatur i området 26-200 °C med en stabilitet på 0,01 K. Dette giver en rumlig opløsning af morfologien og den spændings tilstand der sker dybt inde i prøven under en elektriske feltinduceret faseovergang. Vi har observeret domænelignende strukturer langt over Curie-temperaturen, hvilket indikerer domæne indtryk fra dybt inde i materialet, der ellers tidligere kun er blevet observeret nær overflader. Beregninger af densitets funktions teori (DFT) antyder, at punktdefekter, så som ilt-ledige positioner, spiller en meget vigtig rolle i morfologiske strukturer over Curie-temperaturen. I et forsøg på at kvantificere deres rolle har jeg udviklet en metode til at detektere defektklynger dybt inde i et materiale, baseret på deres volumen udvidelse kvantificeret af DFT. De kombinerede observationer i hele denne afhandling peger på en mere kompleks interaktionsmodel mellem de forskellige morfologiske former for at forstå og forudsige dynamikken i en faseovergang, såsom heterogen kimdannelse af ferro-elektriske domæner. Her præsenterer jeg hypotesen for en sådanne kompleks interaktionsadfærd med vores opdagelser og rammer for i fremtiden at kunne yderligere uddybe den viden.

## Acknowledgements

**Jeppe Ormstrup**, MSc Materials and Manufacturing Engineering, DTU  
Creator of this thesis template.

By submitting my thesis as the culmination of my Ph.D. project, I would like to express my sincerest gratitude to DTU and NTNU for the funding of the joint project and DANSCATT for its support with essential travel funding, for the many trips to ESRF in France. The project could not have been realised without any of your support.

I would like to express my deep gratitude to Assc. Prof. Hugh Simons, who has been an excellent supervisor and mentor for initiating me into the academic world, who has masterfully guided me through the complex topics and critical thinking needed to navigate and understand the projects complexity fully.

I am particularly grateful for my senior supervisor Prof. Henning F. Poulsen, who's expert insight and knowledge have always given a deep understanding of fundamental x-ray methods. Furthermore, I thank Henning for creating a good group environment and supporting our efforts to create social events and Friday breakfasts.

A special thank goes to my Norwegian senior supervisor during my external stay in Trondheim Prof. Ragnvald. H. Mathiesen. Ragnvald has been a grate mentor and friend, both with inspiring academic insights and introduction into the Norwegian culture.

I would particularly like to thank the Beam-line Scientist Carsten Detlefs for help in the design process of our holder system for the DFXM at ID06. Similarly, I would like to thank Carsten and the team of Post. Doc.'s Can Yilidirim, Philip Cook and my fellow Ph.D. student Mustafacan Kutsal for excellent assistance at ESRF when conducting the experiment and the insightful scientific discussions and feedback when formulating articles and at conferences.

I would especially like to thank Søren Nimb, Dan Shacham, Peder Heise and Finn B. Saxild in their effort and support with creating our experimental holder system. Likewise, a great thanks goes to Yves Watier and Carlos Coscolluela from ESRF sample environment team for helping with the final steps in creation of the holder system.

I would like to express my appreciation to Julia Glaum and Antonius T. J. van Helvoort for their help and the often ad hoc scientific discussion in the hall of NTNU, which were always an inspiration and insightful. Furthermore, without your help our samples for experimentation would not have been of such a high quality. Thank you.

I am grateful to have been a part of NEXMAP and all my colleagues whom have facilitated in the creation of a pleasant and cooperative scientific environment. It has been a pleasure sharing the past 3 years with a staff that have supported each other through the constant "noisy" environment. In particular thanks to Kristoffer Haldrup, Carsten Gundlach, Mads Almind and Nikolaj Langemark, for always having an open door when times have been rough.

I can only be humbled and grateful for our skilled and patient administration staff Hanne Sørensen and Helle L. Grunnet-Jepsen, helping in all regards. The importance of their tireless effort in helping with the hurdles of accounting and navigation of the bureaucracy, CAN NOT, be understated. Thank you.

A very unique and whole hearted thanks goes out to fellow scientist and friend Dr. Julian Walker. He has ever been willing to share his knowledge and engage in deep scientific

and technical discussion. I owe you much of my development as a scientist and as a person over the last 3 years, you have my deepest gratitude.

# Contents

Preface . . . . .	ii
Abstract . . . . .	iii
Populævidenskabelig resumé . . . . .	iv
Acknowledgements . . . . .	v
<b>1 Introduction</b>	<b>1</b>
1.1 Ferroelectric materials . . . . .	1
1.2 Domains, defects and phase transformations in ferroelectric materials . . . . .	1
1.3 Challenges and limitations . . . . .	3
1.4 Aim of this work . . . . .	6
1.5 Dissemination . . . . .	6
<b>2 Background</b>	<b>9</b>
2.1 Structural dynamics in ferroelectrics . . . . .	9
2.2 Prevalent approaches to understanding structural dynamics in ferroelectrics . . . . .	14
2.3 <b>Paper 1:</b> Dynamics and grain orientation dependence of the electric field induced phase transformation in Sm modified BiFeO <sub>3</sub> ceramics . . . . .	19
2.4 Limitations of our current approach . . . . .	27
<b>3 Hypothesis</b>	<b>28</b>
<b>4 Methodologies</b>	<b>29</b>
4.1 Hard- and Dark-Field X-Ray Microscopy (HXRM and DFXM) . . . . .	29
4.2 <b>Paper 2:</b> Imaging microstructural dynamics and strain fields in electro-active materials <i>in situ</i> with dark field x-ray microscopy . . . . .	33
4.3 Discussion and implications of the STEF-holder . . . . .	42
<b>5 The interaction between defects and domain walls</b>	<b>44</b>
5.1 Domain wall imprinting . . . . .	44
5.2 <b>Paper 3:</b> Bulk heterogeneity in barium titanate above the Curie temperature . . . . .	48
5.3 Further discussion . . . . .	63
<b>6 Electric field induced defect migration</b>	<b>64</b>
6.1 <b>Paper 4:</b> Non-destructive imaging of mesoscopic oxygen vacancy diffusion in barium titanate . . . . .	65
6.2 Discussion of the fitting of strains from vacancy clusters . . . . .	72
6.3 Discussion of the diffusion/migration of charged defects in oxide perovskites . . . . .	73
<b>7 Discussion and Conclusion</b>	<b>75</b>
7.1 General Discussion . . . . .	75
7.2 Conclusions . . . . .	77
7.3 Outlook . . . . .	78
<b>A Appendix</b>	<b>87</b>
A.1 <b>Co-authorship 1:</b> The thermal and electric field stability of square-net domain patterns in barium titanate . . . . .	87
A.2 <b>Co-authorship 2:</b> The ESRF dark-field x-ray microscope at ID06 . . . . .	93

A.3 **Co-authorship 3:** Reciprocal space mapping and strain scanning using X-ray diffraction microscopy . . . . . 116

# 1 Introduction

## 1.1 Ferroelectric materials

The technological and societal importance of ferroelectric and related electro-active materials should not be underestimated. In an increasingly digitized society we are surrounded by electronic devices that rely on ferroelectric materials (mostly bulk), be it sensors, actuators for fuel injection, medical devices, memory components, energy conversion, energy storage and devices for energy harvesting [1][2]. Crucial components such as capacitors rely on ferroelectrics for their continued optimization and miniaturization. As the global demand for energy increases, so to will the demand for such ferroelectric devices, where e.g. ferroelectric capacitors plays a crucial role for affordable and effective power inversion and energy harvesting [1][3]. Despite these demands, we face a huge bottleneck in advancing the development of these materials. Mainly, we lack the capability to properly understand how to design new materials with new or optimized properties. Often, these properties are related to the local structural and morphological features emerging in the atomic- to nano-scale range [1]. However, techniques capable of visualizing micro- and mesoscopic features in bulk materials during realistic operations conditions remain absent. This inability to characterize local structural effects over several length scales has limited our knowledge of important fundamental mechanisms. by lacking the understanding of the microscale fundamentals, we will consequently lack the ability to reliably design, manufacture and drive materials under their optimal conditions.

The benefits to society and environment would seem clear, so are we simply lacking the economic motivation to push development forward? In 2019 the market for ceramics capacitors (bulk ferroelectrics) is estimated to around 19 billion USD [4], while the sensor and actuator market is around 17 billion USD [5]. The market for electro-active and structured materials is huge, and needless to say that market calls for development with the funding and drive to back it up. It would seem that my earlier statement regarding the bottleneck in development is the main culprit, and in other fields as well.

## 1.2 Domains, defects and phase transformations in ferroelectric materials

So far, I have spoken of ferroelectrics in broad terms. In this thesis, I also focus on the subclasses of piezoelectric, pyroelectric, ferroelectric and ferroelastic materials. Hence, I will shortly introduce them and their characteristics.

- The **piezoelectric** effect is exhibited in crystals with no inversion symmetry and internal polarization, consequently generating a current when an external stress is applied. While the inverse effect is achieved by applying an electric field, which generates an internal strain.
- The **Pyroelectric** effect is the change in polarization with respect to a change in temperature, as an effect of the thermal energy shifting the atomic positions. This is measured as an inversions point in current after a critical temperature for a phase transformation is reached.

- The **Ferroelectric** effect is exhibited by crystal structures where the spontaneous polarization can be reversed by an external field, manifested as a hysteresis loop when measuring the polarization as an effect of an alternating electric field. Importantly, ferroelectricity is a subgroup of pyroelectricity and a subgroup of piezoelectricity, where each subgroup possesses all the characteristics of the previous group.
- The **ferroelastic** effect is a change in the direction of a spontaneous strain in response to an external stress, which can manifest as twin planes with differing spontaneous strain orientations.

Many bulk ferroelectric materials possess all of these characteristics and, as a result, can have a complex response to external driving forces since they will inherently exhibit one or another of the effects outlined above.

The fundamental mechanisms governing the structural dynamics in ferroelectric and piezoelectric materials underpin the functional properties that make them technologically useful [6]. Usually, these dynamics are only used to predict a macroscopic response, such as the change in dielectric coefficient with temperature or expansion induced by an electric field. More recently, manipulating the local morphology (domain walls, defects etc.) and the local strain has become part of the core functionality; e.g. domain walls are now being used as either parts in a circuit or as memory bits [7]. This has been proclaimed as a paradigm shift towards functionalizing a material's inherent structure, proclaimed with the statement "the interface is *still* the device" [8].

Relevant to the use of interfaces in ferroic materials, especially in *pervoskite* materials and other metal oxides, is their affinity for forming networks of lattice defects and heterogeneous features [9]. These networks of grain boundaries, vacancies, domain walls, with their specific distributions and compositions are difficult to control in production, and hence also the local and global properties related to them. Often, these interface structures are designed to achieve coupling effects, e.g. piezoelectricity, electrostriction, magnetoelectricity etc., which are highly sensitive to any defects that break spatial symmetry and hence affect local electric structure. Difficulty in manufacturing is then compounded with the need for specific control and understanding of the fundamental mechanisms for reliable production [10].

For many years, it has been believed that defects, either naturally occurring or introduced in production, can be detrimental to material or device properties (especially within the semiconductor industry). But with increased understanding of the role defects play, this paradigm is shifting and now defects play an essential role in creating and enhancing desired properties, i.e. they are "the new good guys" [11]. Oxygen vacancies, the most common type of defects in complex metal oxides, can pin domain walls creating an undesired frequency response, act as charge traps, influence sensitive coupling or interface effects through their induced strain [10][12][13]. But at the same time, this might affect important properties, depending on the system and its specific use. Numerous studies have shown that defects can be overwhelmingly beneficial to material properties, for example vacancies can stabilize a specific domain pattern and enhance the recoverable strain or stabilize a conducting domain wall, effectively creating circuits on demand [14][15][16]. Even with the extensive computational and experimental research into the role of defects, many fundamental mechanisms on the local structural scale still elude us. Furthermore, the majority of these studies have been limited to 2D systems, where the vast majority of applications are 3D. Thus, there is a huge deficit in our knowledge regarding buried defects

and how they affect the local system, their distribution and migration.

Studies of the electrical characteristics of phase transformations, might be one of the most researched topics for electro-active materials such as ferroelectrics, and much progress has been gained in this area [17]. Notably, the different categories of electro-active materials, i.e. piezo-, pyro and ferroelectrics, each have characteristic responses with which they can be identified. These characteristic responses are well studied both for the average electrical response, and the average change to their crystallographic structure [18]. However, many questions still remain regarding the dynamics of these processes, from the point of view of both from average and local structure. Previous work shows complex dynamic interaction with several structural phases, which have been further illustrated with TEM images of the multiple morphological phases existing as interwoven patterns simultaneously [19]. From this study, we can conclude that to understand the local structural effects of phase boundaries in the bulk, or in reality any lattice inhomogeneities, spatial resolution on the relevant length scale with an equal temporal resolution is a requirement.

Understanding the interaction of the different morphological features and external drivers is essential to the development of ferroelectric devices and is, in essence, the overarching goal of this thesis [1]. Domains, domain walls and defects can all be affected by temperature, electric field and stress fields applied to a given system. Theoretical and simulation work has given insight to the interaction between defects (vacancies) and heterogeneities (domain structures), while others have investigated the dynamic process of migration in such environments [20][21]. Crucially, all lack the proper experiments to conclusively validate their findings. Some effects of the interaction between defects and electric field induced nucleation have been experimentally studied [22]. These experiments have been carried out with surface sensitive techniques that do not access the full 3D structure of the defect's effect on material responses. Currently, it is only dark field x-ray microscopy (DFXM) which can obtain the multiscale 3D data needed to fully capture and quantify the complexity of interactions of the local morphological features. Hence, this work has created the methods with which to gather such data sets, to guide and validate the material simulations and models of the future.

### 1.3 Challenges and limitations

At this point, it is important to consider our current capabilities regarding the characterization of structural dynamics in ferroelectrics. This should also serve to highlight the relevance of the work carried out for this thesis and the developments of the experimental techniques and analysis methods. When characterizing ferroelectric materials, three types of methods are typically used: Macroscopic characterization, scattering and microscopy. However, there is an emerging technique dark field x-ray microscopy (DFXM). Dark field x-ray microscopy enables "3D multiscale microscopy" providing for experimental guidance and validation based on local structural information over many length scales.

**Macroscopic electromechanical measurements**, reveal the electromechanical responses and electric characteristics of the average macroscopic sample. Most ferroelectric laboratories have such capabilities, and they have been used to great effect in determining material properties and their use in a multitude of devices. It is based on electronic measurements from an electrode with a known area attached to the sample, and as such cannot provide any local structural information or local electric characteristics. Nonetheless, this makes the technique able to ascertain the average response of the material, such as the coercive field, dielectric coefficient and piezoelectric coefficient, without the ability to

quantify the local variations that may impact the measured response. This method has been a key factor in pushing the knowledge of ferroelectric materials forward, allowing us to gain an understanding of the macroscopic properties and their usability in electronic devices.

**Powder diffraction** experiments have regularly been used to determine the average crystallographic structure or structural dynamics of a crystalline material. It has been particularly useful for determining the phase composition by analysing the relative intensity of the diffracted x-ray signal. With time resolution down to the millisecond range, different phase dynamics can be ascertained. Such measurements will be demonstrated later in section 2.3. In ferroelectrics and other multiferroics, phase transformation can often be driven by a multitude of parameters such as temperature, strain, electric- and magnetic-fields [17][18]. Importantly, the strain and electrostatic driver can originate from local lattice distortions, such as defects and other heterogeneities. The observation of phase transformations dynamics with classical powder diffraction, will not be able to quantify the full extent of local effects from the distortions. My work on *in situ* powder diffraction on Sm doped BiFeO<sub>3</sub> in section 2.3, illustrates this point, and provides insight into the average texture and dynamics of the electric field induced phase transformations. The usefulness of powder diffraction in exploring mechanisms in the bulk and surface layers can not be overstated, however the local information is not obtained with this technique. While the lack of local information prohibits the characterization of morphological features in the bulk, the average dynamics and phase compositions are easily accessible.

**Reciprocal Space Mapping**(RSM), like powder diffraction is used to characterize the average structure of the materials through x-ray diffraction and the subsequent visualization of the reflection peaks in 2D q-space. Different from powder diffraction, this technique requires large grains or single crystal samples. RSMs are often used to derive additional information in terms of peak broadening and displacement, since the direction of broadening and displacement in 2D q-space can be related to grain sizes, and the type and direction of strains present in a crystalline material [23]. Furthermore, it can give clarity to peak overlaps from various phases, and reveal the nature the average phase transformation in bulk materials. This will be shown in a case study of *in situ* electric field induced phase transformation in BaTiO<sub>3</sub> in section 4.2.

**Optical microscopy**, mainly polarized light microscopy, has been used to visualize morphological features, such as domain walls and phase fronts. Already in 1954, Merz showed domains structure in BTO via optical microscopy and formulated rules for the dynamics of domains and phase fronts [24]. Using polarized light microscopy, domains and their dynamics can be measured, giving the basic information for which to formulate a model for the specific polarization configuration in the sample [25][26]. Since it is based on visual light transmission, it requires the samples to be equally transparent, with the observed morphological features being superimposed throughout the thickness of the sample. Even with this limitation, however, it has been used to discover many properties of ferroelectric materials, but lacks the spatial resolution to understand the local microscopic changes and specific changes to the crystallographic structure [27].

**Transmission Electron Microscopy**(TEM) offers local information of single atomic displacements due to its spacial resolution, which can be less than 0.5 Angstroms [28]. How-

ever, in the case of this specific work, the method relied on ptychography and does not support the acquisition of time resolved data, which can be gained with HR-TEM at a resolution of less than one nanometer [29]. The main drawback of TEM methods is the sample preparation and nature of the thin samples [30]. The approximately 100 nm thick samples are hard to manufacture and are influenced by the process, as well as surface effects that may arise [31][20]. When studying membranes, this rarely poses any major concern, however, studying the nature of fundamental mechanisms in the bulk of materials where out of plane constraint is important, will be obscured by induced artifacts, potentially biasing the results and conclusion [30][32]. TEM and its many associated measurement types are restricted to thin samples with surface effects impacting the measurements and material properties. Hence, it lacks access to the bulk information needed to validate and confirm models dealing with dynamics and structures in bulk materials.

**Piezo Force Microscopy**(PFM) is another popular microscopy technique often used in characterizing ferroelectrics surfaces, with a spatial resolution of few nanometers. The PFM obviously can't measure bulk properties, since it is a surface device based technique. However, PFM is uniquely capable of directly measuring the local electric fields from domains and morphological changes in the near-surface region [7]. The ability to make local macroscopic measurements effectively combines microscopy with electric property measurements, expanding the scope of knowledge which can be gained from such local surface techniques [22][33]. The nanosized surface features on ferroelectrics will influence the domain configuration and act as nucleation sites [12][31]. Furthermore, the surface interface creates a dead layer or space charge region, shielding the underlying structure from such measurements and obscuring the results [31]. Furthermore, it is not really established how large the interaction volume is from a PFM tip. This leads to the conclusion that PFM should not be solely used to obtain information representative of the bulk environment.

**Dark field X-ray Microscopy**(DFXM) is an emerging techniques that overcome many of the limitations for bulk microscopic characterization, present in the techniques described above. DFXM can be seen as an analogy to TEM, where the interaction mechanisms is now based of x-ray photons and their diffraction from crystalline materials. Usually, the instrument is operated in a "line-beam" configuration, where a slice of a sample is illuminated in a transmission geometry. By the use of compound refractive lenses (CRL), the diffraction beam at an oblique angle can be formed into a real space image of the microstructures whose lattice spacing relates to the specific diffraction angle. The penetration of x-ray photons allows for characterization of the bulk, giving us intensity images with a spatial resolution of  $\approx 70$  nm. Since the microscope is placed at the ESRF synchrotron, the high brilliance allows for movies of the morphological changes in the intensity images. Furthermore, by scanning the the CRL and/or sample through the oblique angle, spatially resolved strain and orientation maps can be generated from the bulk, which give further insight into the influence local morphological features have on the local environment. Essentially, the strain maps possess the local RSM from which we obtain the axial strain. By translation of the line beam, 3D mapping of the strain is possible.

With the advent of DFXM, which will be described in in chapter 4, local information in the bulk can be gained from crystalline materials. With the careful design of *in situ* experiments, we can gather local structural information of morphological dynamics, electric characteristics and strain maps within bulk materials. A prime example of the knowledge

able to gain from this is reported by H. Simons [32], which showed changes to the domain topology, orientation and distribution, during a typical P-E hysteresis loop. Specifically, this study was able to show long-ranging strain field from heterogeneities, which was previously expected to be orders of magnitude shorter in their extension. This study effectively instigated this thesis work, since we now possess the capabilities to not only find, but also characterise the nature of local heterogeneities. With DXFM, we can tackle many unsolved problems regarding the dynamics and local effects in ferroelectrics, potentially progressing the field significantly.

## 1.4 Aim of this work

The technical aim of the thesis has been to develop a framework and pipeline for utilizing DXFM as a means to record and quantify the complex interplay of defects, domain structures and the electric field induced phase transformation in bulk ferroelectrics. This forms the basis for addressing my scientific core question; How do defects and heterogeneities interact with an electric field induced phase transformation in the bulk? While this work may not answer the question exhaustively, it does lay the foundation for studies that do.

To guide the reader towards my answer of these question and explain the novelty of our methods, the following chapter will focus on the scientific concepts related to ferroelectric materials and their structure-property relationships. These concepts will be important throughout the thesis as they all build on these concepts. The first paper will be presented in the following chapter, which serves to give the reader an insight into the complexity of *in situ* experiments and analysis, while also illustrating the limitations of powder diffraction and macroscopic measurements towards answering the core question in the hypothesis. Furthermore, we introduce the concept Landau-Ginsburg-Devonshire (LGD) based simulations of material behaviour, since it is the goal to supply experimental guidance and validation to thermodynamic (and other) simulations. With this basic knowledge in place, I then state my hypothesis in 3, the core scientific questions, and explain why they haven't been answered and what novel approach is needed in order to do so.

The following chapters will then be used to describe and demonstrate the novel capabilities developed as part of this thesis work (chapter 4), the effects of local heterogeneities and strain in bulk crystals of barium titanate, (chapter 5) and the migration of oxygen vacancies under the application of an electric field (chapter 6). Each chapter contains a peice of the larger puzzle of the core scientific question. All together the chapters and papers from a background and experimental evidence for the novelty of our methods and scientific proof of the complexity of defects, domains and their interplay with a field induced phase transformation in ferroelectric materials.

## 1.5 Dissemination

Scientific articles in published and manuscript form are contained within the various chapters of this thesis . For convencience, I here provided a list of reference for each of these articles, along with their current state with respect to publication:

- Paper 1: Ormstrup, J., Makarovic, M., Majkut, M., Rojac, T., Walker, J. and Simons, H. (2018). Dynamics and grain orientation dependence of the electric field induced phase transformation in Sm modified BiFeO<sub>3</sub> ceramics. *Journal of Materials Chemistry C*, 6(28), 7635–7641. <https://doi.org/10.1039/c8tc01951g>.

- Paper 2: Ormstrup, J., Østergaard, E. V., Detlefs, C., Mathiesen, R., Yildirim, C., Kutsal, M., Cook, P. K., Watier, Y., Cosculluela, C. and Simons, H. (2020). Imaging microstructural dynamics and strain fields in electro-active materials in-situ with dark field x-ray microscopy, 065103(December 2019), 1–9. <https://doi.org/10.1063/1.5142319>.
- Paper 3: Ormstrup, J., Østergaard, E. V., Christensen, M. S., Yildirim, C., Cook, P. K., Kutsal, M., Olsen, T. and Simons, H. (2020). Bulk heterogeneity in barium titanate above the Curie temperature. (preprint)
- Paper 4: Ormstrup, J., Olsen, T. and Simons, H. (2020). Non-destructive imaging of mesoscopic oxygen vacancy diffusion in barium titanate. (preprint)

In addition, the appendix contains further articles of which I am a co-author. The first article in the list I have supervised and directed. The latter two, I have given input in form of figures and experimental assistance during beamtimes.

- Co-authorship 1: Østergaard, E. V., Ormstrup, J. and Simons, H. (2020). The thermal and electric field stability of square-net domain patterns in barium titanate. (preprint)
- Co-authorship 2: M. Kutsal, P. Bernard, G. Berruyer, P. K. Cook, R. Hino, A. C. Jakobsen, W. Ludwig, J. Ormstrup, T. Roth, H. Simons, K. Smets, J. X. Sierra, J. Wade, P. Wattecamps, C. Yildirim, H. F. Poulsen and C. Detlefs, (2020). The ESRF dark-field x-ray microscope at ID06, IOP Conf. Ser.: Mater. Sci. Eng. 580 012007. [doi.org/10.1088/1757-899X/580/1/012007](https://doi.org/10.1088/1757-899X/580/1/012007).
- Co-authorship 3: H. F. Poulsen, P. K. Cook, H. Leemreize, A. F. Pedersen, C. Yildirim, M. Kutsal, A. C. Jakobsen, J. X. Trujillo, J. Ormstrup, C. Detlefs. (2018). Reciprocal space mapping and strain scanning using X-ray diffraction microscopy, Journal of Applied Crystallography, vol: 51, issue: 5. <https://doi.org/10.1107/S1600576718011378>.

In addition, this work has resulted in oral and poster presentations, presented at various national and international venues throughout the project duration. Oral presentations I have given and prepared throughout my Ph.D, at named conferences:

- EMA 2018, Conference on Electronic and Advanced Materials, “The kinetics and grain orientation dependence of the electric field induced phase transition in Sm modified BiFeO<sub>3</sub> ceramics”.
- ISAF 2018, IEEE International Symposium on Applications of Ferroelectrics, “The kinetics and grain orientation dependence of the electric field induced phase transition in Sm modified BiFeO<sub>3</sub> ceramics”.
- ISAF 2019, IEEE International Symposium on Applications of Ferroelectrics, “Real-time imaging of electric-field-induced phase transformations in bulk ferroelectrics”.

Posters I have presented at conferences:

- 3DMS 2018, the 4th International Congress on 3D Materials Science 2018, “Real Time Imaging of Microstructural Transformations in Bulk Ferroelectrics”
- SCANDEM 2018, The 69th Annual Conference of the Nordic Microscopy Society, “Real Time Imaging of Microstructural Transformations in Bulk Ferroelectrics”

Awards received at conferences:

- 3DMS 2018, poster winner
- Scandem 2018, poster winner

Two grants were also successfully applied for to support the travels undertaken for this thesis work:

- Reinholdt W. Jorck og Hustrus Fond, 25000 dkk ( $\approx$  3800 usd), Received for my stay at Norwegian University of Science and Technology (NTNU).
- Augustinus Fonden, 6000 dkk ( $\approx$  900 usd), Received to be used for the UNSW summerschool in Ferroelectric 2018.

And finally, album covers:

- Bend the Future - Pendellösung; A progressive rock album featuring a DFXM intensity image of a barium titanate single crystal as their album cover. See the [album cover](#), or video, courtesy of the [BTO Wizard](#).

## 2 Background

Given that we should understand how material heterogeneities interact with electric-field induced phase transitions in bulk ferroelectrics, this chapter will focus on the key underlying concepts: the structural dynamics in ferroelectric materials, and how they manifest themselves in the most prevalent characterization techniques. I begin by describing the nature of phase transformations, domains structures and defects in ferroelectrics. Here, the discussion on phase transformations introduces the overarching concept of 2.1, from which domains form from and defects influence. I then describe how the manifestation of these phenomena in ferroelectric materials can be investigated using both experimental and computational methods, and demonstrate their use in our study of domain and phase dynamics and texture in a ferroelectric ceramic. Specifically, in section 2.3, I present our study of phase dynamics and texture which illustrate the concepts in this chapter. Collectively, however I illustrate their inability to conclusively determine how defects and heterogeneities interact with an electric field induced phase transformation in the bulk (the primary scientific aim of this thesis).

### 2.1 Structural dynamics in ferroelectrics

#### 2.1.1 The ferroelectric phase transformation

Tagantsev, Cross and Fousek provide a concise definition of of the ferroelectric phase transition: *"A phase transition is called ferroelectric if it results in a lower symmetry phase in which the vector of pyroelectric coefficients acquires new components which were zero, by symmetry, in the high-symmetry phase."* - [6]. Arguably the most important feature of a ferroelectric material is its ability to change the direction of spontaneous polarization,  $\mathbf{P}_S$ , when in the low-symmetry phase. "Switching" the polarization can in theory, be achieved under either applied electric field (purely ferroelectric) or under elastic fields (ferroelastic and ferroelectric). Depending on whether the mechanism for the switching procedure relies on displacement, order-disorder or rotation,  $\mathbf{P}_S$  will change continuously, in discrete steps, or it may maintain its magnitude. The concept of switching is extremely important and is the primary mechanism used in memory devices [34] and many sensors.

Crystalline materials can have different types of structural phase transformation, of which many are not ferroelectric. Classifying materials into these types of phase transformation is useful in predicting properties. A overview of these classifications is given in figure 2.1, along with the requirements for the different steps in the classification process. The first step is the distortive requirement, e.g. the exhibiting of a small ionic displacement in the material's crystal structure that does not break bonds, and is important to all ferroelectrics. With the definition of a ferroelectric phase transformation from above and the neatly marked requirements in figure 2.1, every step in classification can be easily followed.

Given that ferroelectric materials and their properties are strongly related to their crystallographic structure, it is important to understand what we can ascertain from these structures, i.e. their structure-property relation. The symmetry of different crystal families defined by their point groups are particularly useful, since they can define the crystallographic directions of the spontaneous polarization. To illustrate this concept, consider a cubic-to-tetragonal or -orthorhombic phase transformation, with the structures annotated in in H-M notation  $m\bar{3}m$ ,  $m_xm_y2_z$  and  $m_xym_x2_z$ , for the structures respectively. The cubic

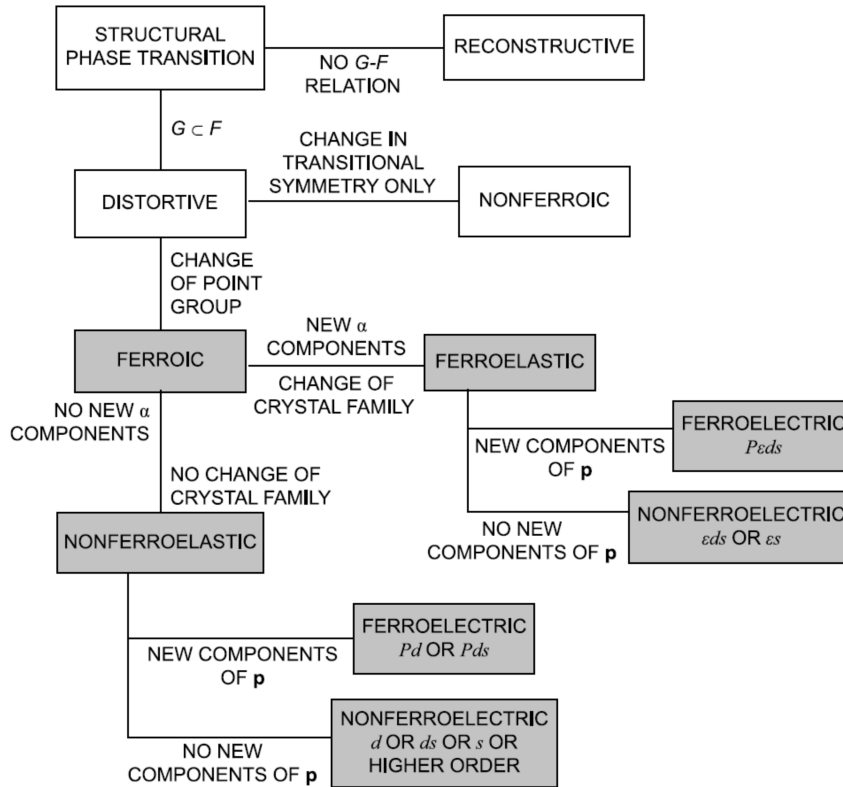


Figure 2.1: Classifications of structural phase transformations. Shaded items indicates a ferroic transformation.[6]

phase has its orientation and mirror planes shown in figure 2.2a and marked as the parent phase with a dashed line in figure 2.2 b and c. For the latter two depictions in 2.2 it should be apparent they do not all have the same mirror planes as their parent phase. The tetragonal structure is lacking the diagonal mirror plane and the orthorhombic is lacking the primary axis planes, both exhibiting a lower symmetry than the parent phase [6].

This is a primitive picture of how the ions are moved into a configuration where the charge density is unequally distributed within the unit cell, as indicated by the lowering of the symmetry. This allows for the probability of charge distribution shifting to cause a dipole moment of the simple unit cell, i.e. via the central ion in a perovskite structure being displaced along the  $x$ -axis, the  $xy$ - or  $x\bar{y}$ -axis. Figure 2.2d) and e) show the perovskite structure of  $\text{BaTiO}_3$  in the cubic (paraelectric) phase and tetragonal (ferroelectric) phase, respectively. In the tetragonal phase, the  $\mathbf{P}_S$  is indicated along the elongated  $c$ -axis. Depending on the crystal symmetry, the direction of  $\mathbf{P}_S$  can be along a different direction, and in the case of an orthorhombic structure, it can be along any of the body diagonals, albeit with preference along the longest of the body diagonals, crystallographic given by the  $[1,1,1]$  direction.

Indicated in figure 2.2, lattice parameters will change during a transformation, as the system settles into an energy minimum depending on the external parameters [17][35]. The ferroelectric phase transformation is often discussed from a thermodynamical view, with the temperature as the driving force. Figure 2.3 depicts the change in lattice parameters with respect to temperature in the range of the phase transformation for the cubic to tetrag-

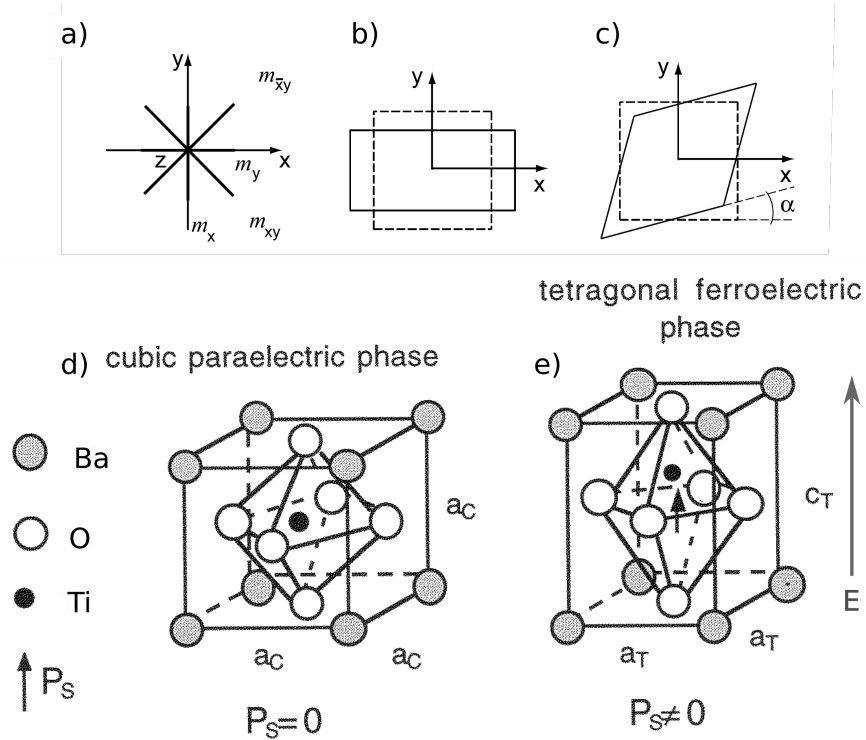


Figure 2.2: a) orientation of mirror planes passing through the z-axis in the point group  $m\bar{3}m$ ; b) and c) schematic representations of changes of the cubic unit cell (dashed) into the tetragonal and orthorhombic unit cell at transitions  $m\bar{3}m - m_x m_y 2_z$  and  $m\bar{3}m - m_{xy} m_x 2_z$ , respectively [6]. d) show the perovskite ABO<sub>3</sub> structure of BaTiO<sub>3</sub> in its paraelectric cubic phase and e) in its ferroelectric tetragonal phase. Indicating the lattice parameter in the cubic phase is  $a_c$ , while for the tetragonal phase  $a_T$  and  $c_T$  indicates two different lattice parameters [17].

onal or orthorhombic structure from figure 2.2 a and b, respectively. This is a classical view of a thermally-driven first order phase transformation, which is ideally instantaneous at its critical temperature [6]. The oft referred to Curie temperature is the critical temperature where the structure changes phase from a paraelectric to a ferroelectric state when cooled (or vice versa). Upon further cooling, several other lower symmetry ferroelectric phases can be accessed, where the points groups and phase transformations temperature is specific to the individual material system. Usually, these transformations are more complex and may exhibit intermediate phases, in contrast to the classical picture of a sharp transformation between two phases [35]. The intermediate phase is often explained as a "slow" rotation of  $\mathbf{P}_S$  between two states.

Thermal hysteresis also adds a further complication to notion of a "sharp" phase transformation at a given temperature. Upon cooling or heating, the critical temperature for a given phase transformation will change, i.e. higher or lower, respectively. This is often attributed to latent heat, and can be thought of as analogous to the remanent field from a P-E loop. Unlike an applied electric field with bias aligning  $\mathbf{P}_S$  in a specific direction, a thermally-driven phase transformation has a random orientation of  $\mathbf{P}_S$ . This is due to the fact that the temperature field doesn't affect the ordering of the polar ion displacement along a specific macroscopic orientation[18]. The nature of these fluctuating and sharp

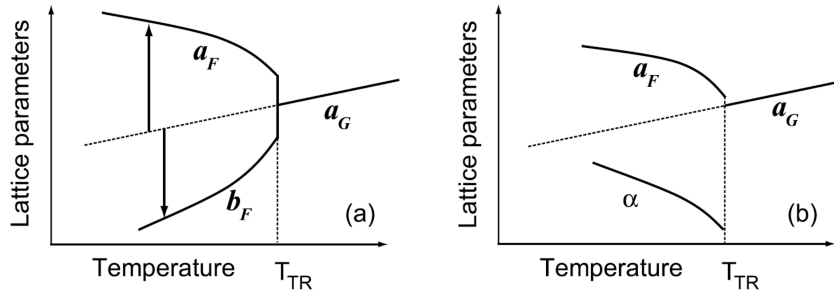


Figure 2.3: Temperature dependence of unit cell lattice parameters in the XY plane, for the tetragonal and orthorhombic transformation given in figure 2.2, shown in a) and b) respectively. Dotted lines show the cubic lattice constant linearly extrapolated to the low-symmetry phases. Angle  $\alpha$  measures small rotation of the cubic axis, also seen in figure 2.2 [6].

temperature transformations have motivated the creation of a stable *in-situ* temperature holder, which will be presented in 4.2.

The nature of the phase transformation is different when it is induced by an electric field. In a paraelectric to ferroelectric transformations in  $\text{BaTiO}_3$ , the emerging  $\mathbf{P}_S$  in the tetragonal phase will be induced in the direction of the field, illustrated in figure 2.2e. The  $\mathbf{P}_S$  can subsequently be switched or poled with an electric field. Poling is illustrated in figure 2.4, by the random  $\mathbf{P}_S$  in a polycrystalline material being polled to align direction of an applied electric field. In the figure, it can be seen that not all  $\mathbf{P}_S$  align perfectly to the electric field. This is a consequence of the distortive requirement, where the crystal structure can only distort into specific point groups. Each of these point groups can only possess  $\mathbf{P}_S$  along specific direction and will distort into the one where  $\mathbf{P}_S$  is most closely aligned with the field. Furthermore, the internal residual stress field from e.g. grain boundaries, dislocations and other defects can affect switching or polarization so that one specific direction is more favorable [17]. The polarization of a material will create regions that possess  $\mathbf{P}_S$  with the same orientation called domains. The following section will introduce this important concept in more detail.

### 2.1.2 Ferroelectric and ferroelastic domains and domain structures

Domains are regions within in a ferroelectric crystalline material exhibiting a (nominally) uniform  $\mathbf{P}_S$ . The boundaries between two domains are domain walls, and are often only a few unit cells thick [36]. Domain walls can be generated in several configurations, and are named depending on the polarization orientations on either side of the wall. For example, we name walls with polarization on either side parallel but in opposite direction  $180^\circ$  domain walls, while walls with perpendicular angled polarization orientations on either side are called  $90^\circ$  domain walls. It is noteworthy that, in the case of a  $90^\circ$  domain wall in a tetragonal system, the angle will be slightly less than  $90^\circ$  due to the compatibility requirement between the two anisometric unit cell lattice parameters. As a consequence, the twinning operation also distorts the lattice around the domain wall. The actual angle between domain orientations on either side of a  $90^\circ$  domain wall will be,  $90^\circ - 2\phi$ , where  $\phi = 40^\circ - \arctan(a/c)$ . Here,  $c$  is the elongated lattice parameter and  $a$  the two equal length lattice parameters in the tetragonal phase.  $2\phi$  is often referred to as the *clapping angle*; the rotation criteria required for two domains to stay in physical contact [6]. If con-

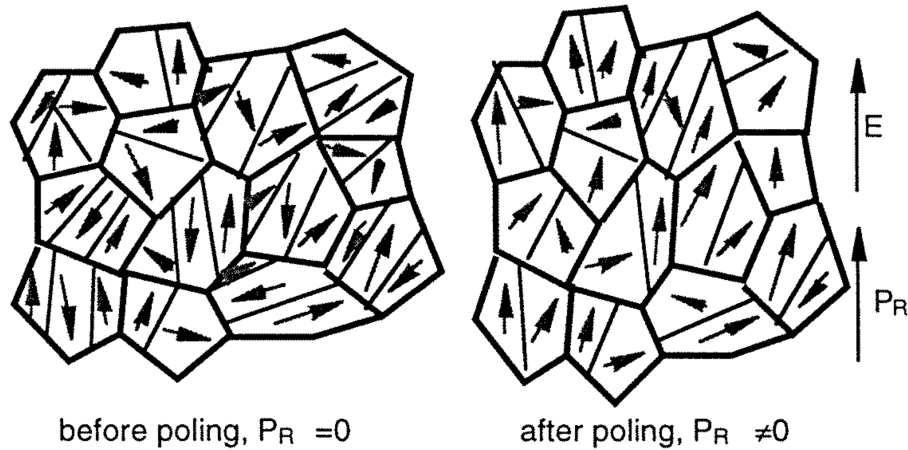


Figure 2.4: The figure illustrate what happens to the random orientated  $\mathbf{P}_S$  in a polycrystalline ferroelectric during an the application of a electric field, aka poling. [17]

sidering a tetragonal phase, depending on the twinning operation in a single crystal of  $\text{BaTiO}_3$  it will create 6 possible domain variants (i.e. unique values of  $P_S$ ). This is important when characterizing samples with single crystal x-ray diffraction, since it will possess the same number of reflections peaks in  $q$ -space (seen in chapter 4).

Ferroelectric domains form in order to minimize the energy built up from the depolarization field,  $E_d$ . This field is produced when a material is polarised and in turn produce surface charges, which create the depolarization field  $E_d$  oriented opposite to  $\mathbf{P}_S$  [17]. For example, if we have a single domain in large piece of material, a large surface charge would accumulate on either side of the material and create a similarly large depolarization field. The large electrostatic potential energy of this field is unfavourable, and the natural principle of finding the minimum energy state will force the material to reconfigure to a state with a lower total potential energy. The material will thus compensate the depolarization field by either (i) creating domains of opposite directions or (ii) creating conduction pathway through the material [20][17].

Conducting domain walls are known to occur when the polarization in neighboring domains  $\mathbf{P}_S$  has a component directly towards or away from each other [16][37], effectively driving charge carriers to accumulate at the domain wall. Conductive domain walls can be functionalized as nanoscale circuit components and used in logical or memory devices [16], usually written with a PFM in current experiments. If a ferroelectric material is inserted into a heterostructure with conducting layers (e.g. electrodes), charge can be compensated since the conductor can act as a sink for the build up of charges carriers on the surface.

Creating such heterostructures can also induce stress due to the lattice mismatch between layers, influencing the domain formation. Hence, it is no longer the spontaneous polarization alone that drive the domain formation, but also the stress. Indeed, when stress drives the reconfiguration of domains (in all manner of ferroelectrics beyond just heterostructures), the material is classified as ferroelastic. The domain formation in the ferroelastic materials occurs due to mechanically stressed, either externally or by internal variations. As an example, applying a uniaxial compressive stress on a 001-oriented

single crystal of  $\text{BaTiO}_3$  would cause the formation of domains whose spontaneous strain (and hence polarization) is perpendicular to the stress in order to minimize the elastic energy.

Overall, the types of domains and domain walls that occur in a ferroelectric and ferroelastic materials depends on the specific material crystallographic symmetry rules for both the ferroelectric and nonferroelectric phases. The configuration of these domains and the resulting polarization and strain generated in the material will, unsurprisingly, affect the macroscopic properties.

### 2.1.3 Structural defects

While our discussion of phase transformations and domains may be sufficient to describe ferroelectric materials in a perfect and static world, it does not suffice for the *real* world, where dynamics and defects must be considered. Structural lattice defects come in a number of varieties and can have a number of different effects on the local crystallographic environment. Most notable (and common) are oxygen vacancies, which are known to pin domain walls and locally suppress the polarization. This is due the vacancies being a charge carrier, hence the discontinues polarization from the domain wall will attract it, effectively creating a charge trap[17].

In this light, defects can be seen as a bad influence. However correctly distributing them. i.e. during an aging process, can enhance important properties of the material. For example, it has been shown that aging  $\text{BaTiO}_3$  can enhance the recoverable strain [15], and that oxygen vacancies can enhance both static and switchable polarization [12][21]. Usually, defects such as oxygen vacancies distort the lattice, since they have a different effective atomic radius than the previous occupant of their specific site in the lattice. Naturally, this means that defects induce a strain field. However, this strain field can help stabilise a specific structure [21] or domain configuration [14]. Theory, such as DFT and molecular dynamics suggests the strain field induced by point-defects extends typically tens of angstroms [38] from the defect, however experimental validation of this spatial range in bulk materials remains exceedingly rare. Nonetheless, it should be made clear that a defect will affect the local environment, the impacts of which I will present evidence for in chapters 5 and 6.

## 2.2 Prevalent approaches to understanding structural dynamics in ferroelectrics

The complex natures - and critical importance - of phase transformations, domains and defects present a major challenge in understanding the relationship between structure and properties in ferroelectrics. Crucially, this understanding of the structure-property relationship is indisputably essential for the intelligent design of new ferroelectrics with tailored/optimized properties and functionalities. There is, however, an arsenal of tools at the disposal of ferroelectricians to aid in this regard. In the following, I describe the advantages and limitations of some of the most prevalent such tools.

### 2.2.1 Macroscopic electromechanical property measurements

The defining feature of a ferroelectric is its ability to switch the polarization via an externally-applied electric field. However, this ability can be significantly affected by the phase transformations, domains and defects. The most common means of measuring phenomena

associated with ferroelectric switching is the polarization-electric field loop, often referred to as the P-E loop. These loops enable a number of property assessments to be made, given sufficient knowledge of the material system and the fundamental concept of switching.

Figure 2.5i illustrates the development of a P-E hysteresis loop from an unpoled sample and the corresponding domain configurations as a consequence of an external electrical field [18]. Here,  $\mathbf{P}_{\max}$  is the maximum polarization achieved during the poling, usually measured in  $C/cm^2$ . The saturation polarization  $\mathbf{P}_{\text{sat}}$  is estimated by extrapolating the linear region at  $\mathbf{P}=\mathbf{P}_{\max}$  back to vertical axis (i.e. where  $E=0$ ). Characteristically, when reaching  $\mathbf{P}_{\text{sat}}$  the domain configuration is significantly changed from the state at the  $\mathbf{E}_c$  and even the  $\mathbf{E}_r$ .  $\mathbf{P}_r$  is the remanent polarization; the retained magnitude of the polarization in the material once the field is removed.  $\mathbf{E}_c$  is the coercive field; the field needed to reduce the polarization back to zero.

Since ferroelectrics are also piezoelectric, a strain-electric-field loop, or S-E loop, will inevitably evolve alongside the P-E loop. The development of the S-E loops is marked by the dashed purple line in figure 2.5i. From the S-E curve, the piezoelectric coefficient can be derived by  $d_{ij}^* = \frac{x_{ij}}{E_j}$  [17], assuming we are far away from a phase transformation, where several other mechanism related to strain may influence the signal. Most often, the piezoelectric coefficient  $d_{33}$  is the main parameter relevant to the electromechanical response, since it describe the lattice expansion along the applied electric field direction. The ability to measure and optimize the  $d_{33}$  is important for all types of actuator devices, and for understanding the strain development and its effect on the fundamental ferroelectric response [17][18][6]

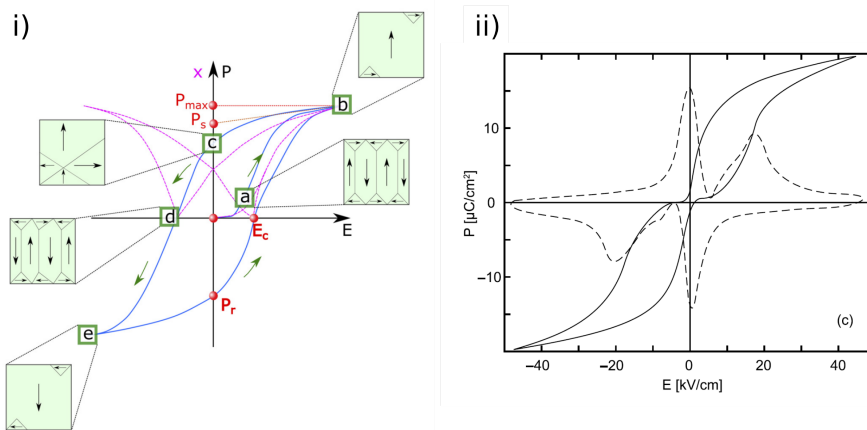


Figure 2.5: Figure i) shows the polarization–electric field hysteresis loop of ferroelectric crystal with remanent polarization  $P_r$  and coercive field  $E_c$  where the polarization is set back to zero. (a), (b), (c), (d), and (e) represent different polarization configurations under an applied electric field. The strain-electric field butterfly loop is also shown [18]. ii) show a double hysteresis loop (solid line) and its derivative (dashed line), which is representative of the current generated from such a P-E loop [6].

Because  $\mathbf{P}_S$  is equivalent to the integrated current, the derivative of the polarization loop must in return give us the electric-field-dependent current, as shown in figure 2.5ii. Here, the solid line is a double hysteresis loop of the polarization and the dashed line is the

derivative of that polarization. The current is often measured directly, and is an important parameter for detecting switching of the polarization. The generated current arises from the change in polarization, creating a build up of charges on the surface of the ferroelectric materials. This can be particularly useful when analysing samples with a weak P-E signature, or a more complicated form of the P-E loop, such as in very leaky samples.

The double loop can be the consequence of several different factors. One important such factor can be an aging process where oxygen vacancies result in the pinning and eventual de-pinning of domain walls [14][15]. It can be difficult to detect these kind of processes from the P-E loops, so the current is often, used since the variation in magnitude of the current is easier to detect. Even so, the shape of the P-E loops can be a good indication of switching and aging characteristics at a first glance. If the P-E loop has an almost vertical line through  $\mathbf{E}_c$ , it can be said to have a sharper switching and likely have a very uniform crystalline structure (i.e. free of defects that cause domain wall pinning). Some materials develop a sharper P-E loop after several cycles, indicating the successive de-pinning of domain walls and reduction of bulk conductivity, normally referred to as a wake up period [12].

The different hysteresis loops and their characteristics are clearly affected by multiple factors, both external and internal, such as number of field cycles, sample preparation, external stress, charges defects etc. These effects can be hard (if not impossible) to separate out from the measurements, preventing the analysis of their specific impact on the measured response. Nonetheless, this has not stopped researchers from developing creative ways to use macroscopic measurements extensively to ascertain crucial information about these individual factors. However, there doesn't seem to be a common fundamental rule governing all types of ferroelectric switching behaviors dynamically. Ferroelectric material systems can exhibit different behaviours, such as domain wall motion, the growth of antiparallel domains, the nucleation and growth of new domains and phase transformations pathways with similar starting and end points. With such a complex interaction between all the effects described in this chapter, pipelines and frameworks for handling such a task do not exist and need to be developed.

### 2.2.2 Landau-Ginzburg-Devonshire theory

Landau-Ginzburg-Devonshire (LGD) theory is based on the thermodynamics of phase transformations described by Landau, which was further expanded upon by Devonshire in the case of ferroelectricity, and finally by Ginzburg, who applied the theoretical framework to materials of a finite size. LGD theory is essentially a Taylor series of the order parameter  $\mathbf{P}_S$ . The order parameter, in this case the polarization, can be calculated or compared from microscopic data as derived by Devonshire [21][39][6]. It is important to note that the precision of this theory depends on the validity of the coefficients, since both these and the order parameter are influenced by temperature, and small deviations from the correct values will quickly lead the results astray. Since it is still difficult to measure the local behaviour of domains and phases in bulk ferroelectrics, LGD approaches have been used extensively to predict properties and behaviors in the bulk with a high degree of success.

The Landau free energy for a phase transformation with an external field applied can in

general be written as,

$$G(T, E) = \frac{A(T - T_C)}{2} \mathbf{P}^2 + \frac{B}{4} \mathbf{P}^4 + \frac{C}{6} \mathbf{P}^6 - \mathbf{P}\mathbf{E}. \quad (2.1)$$

Here, A, B and C are coefficients and  $T_C$  is the Curie temperature. Depending on the sophistication of the model, several of the coefficients can be expressed as temperature dependent. From this model, we can intuitively see what is meant by first and second order transformations: The definition is that the free energy  $G$  is discontinuous at the  $n^{\text{th}}$  order derivative at the Curie temperature, and continuous at the  $(n - 1)^{\text{th}}$  order [39]. By solving equation 1 under the assumption that the electric field is parallel to the polarization and with the boundary condition of  $\frac{\partial G(T, E)}{\partial P} = 0$  and  $E = 0$  we get

$$\mathbf{P} = 0 \quad \mathbf{P}^2 = \frac{-B \pm \sqrt{B^2 - 4AC}}{2C}. \quad (2.2)$$

Modern approaches to investigating phase transformations in ferroelectrics usually have a vastly more complex energy description taking into account the energy density from domain patterns, the elastic energy density and the electrostatic energy for long range interaction of spontaneous polarization [21]. Specifically, the last term has proven to be useful in predicting domain and defect behavior in the bulk, since it can be expanded to take the density of defects into account. The work referent to here is by L. Hong [21], which simulated the interaction between domain and defect in a bulk sample. But, as the work also state, it provides ideas for further experimental and computational guidance and validation.

### 2.2.3 Average structure measurements (diffraction)

So far, the information used to guide and validate models of bulk behavior in functional materials has been of the averaged variety, where the measurements represent the cumulative response of the entire sample. Addressing the shortcoming of this type of data is a key motivator for this thesis work, and to that end I provide some more specific examples of the type of information relevant to understanding phase transformations and defects in ferroelectric materials that can be obtained with these techniques.

Information of the average crystal structure can be gained with via two main techniques: powder diffraction and single crystal diffraction (i.e. reciprocal space mapping). These two methods require samples in a powdered (or agglomerated powder, i.e. a ceramic) state, or very large - preferably single - crystals, respectively. Examples of data generated by these two techniques are shown in figure 2.6. The diffractogram from a powder diffraction measurement of a phase-transforming ferroelectric ceramic, as shown in figure 2.6a, can reveal the volumetric phase fraction by using Reitveld refinement and assuming known structures (e.g. from similar materials), whose unique Bragg reflections are indicated with blue marks in the bottom of the figure. With an *in situ* experiments, such as that as shown in figure 2.6a of a unpoled and poled sample, one can understand the influence of the driving force (in this case electric field) on the phase fraction. Moreover, changes to the diffracted intensity intensity, marked by the gray profile in the figure, indicates that some of the peaks are “splitting”. Peak splitting occur due to the difference in spontaneous strain directions induced by the polarization and subsequent formation of the 90° domain walls [17]. The emerging peak due to the orientation of domains or the emergence of a new phase can help us quantify both the degree of domain switching and phase transformation.

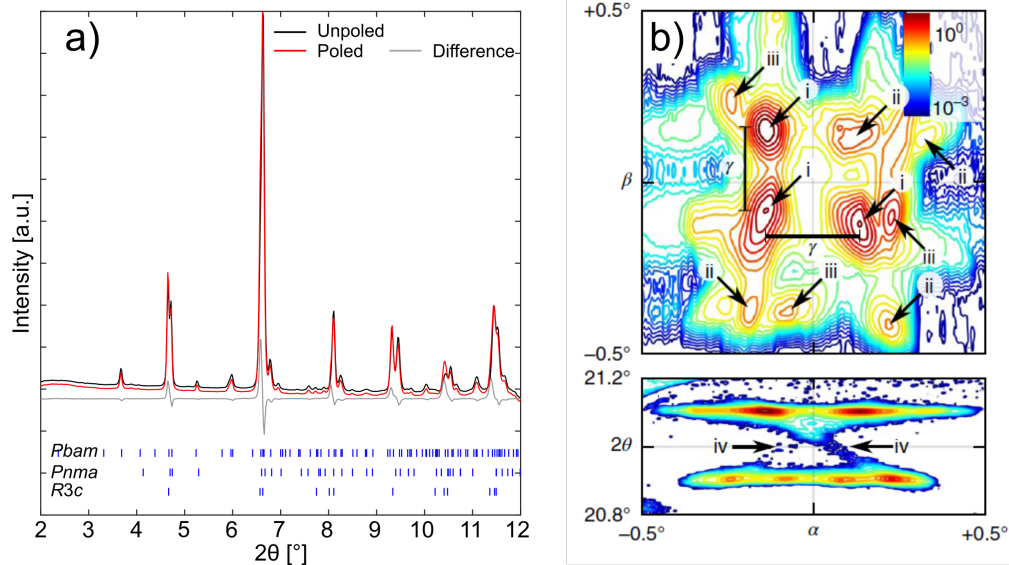


Figure 2.6: a) shows a powder diffraction pattern from a  $\text{Sm-BiFeO}_3$  sampled in the unpoled and poled state along with the difference in intensity. The blue marks in the bottom correspond to the reflection angle for the three different phases, *Pbam*, *Pnma* and *R3c*[40]. b) shows a RSM from a grain embedded in a ceramic  $\text{BaTiO}_3$  sample. The sample is in the tetragonal phase and nominally it should have very distinct Bragg peaks. However, the diffuse and additional peaks marked by iii and iv, are inexplicable by only accounting for the tetragonal symmetry [32].

Similarly, reciprocal space maps (RSMs) can provide us with information about the strain from heterogeneities, such as domains and grain boundaries. Exemplified in Figure 2.6b, the tetragonal phase expected here would produce *only* the nominal peak indicated by i). Here, the additional peaks by ii) indicate multiple twinning from domain walls, while the additional peaks iii) and the diffuse intensity between iv) are attributed to further, symmetry-breaking distortion to the nominal tetragonal structure, such as from grain boundaries. Crucially, this type of local information tends to be completely lost in average structure measurements, as the additional peaks and streaks disappear into the tails of the Gaussian diffraction peaks.

It is important to stress that the depth to which the distortions near grain boundaries extend cannot be quantified by pure diffraction techniques such as those described above. Though useful and convenient in many cases, the averaging nature of these techniques makes it impossible to obtain local information from any morphological features in the bulk, both from ceramics and single crystal samples alike. Section 1.3 and 1.4, have stated the need for this capability in the realization of the goals for the project. Nonetheless, it is still important to understand the average dynamics and morphological characteristics to get the full multi-scale picture. To this end, I include my work with *in situ* powder diffraction on ferroelectric dynamics in the following.

### **2.3 Paper 1: Dynamics and grain orientation dependence of the electric field induced phase transformation in Sm modified BiFeO<sub>3</sub> ceramics**

*The experimental approaches described above have served the needs of ferroelectricians for many years. In particular, they enable the quantitative measurement of structural changes during electric-field induced phase transformations, which may then be correlated to the macroscopic electrical properties. As a demonstration of this well-used approach, I here present our article from a beamtime in July 2017 at ESRF's beamline ID11. In it, we investigated Sm-modified BiFeO<sub>3</sub> with in situ powder diffraction, and analysed the phase composition and its dynamics during the application of an electric field. From the same dataset we could extract the preferential direction of the domains, which show to be aligned with the electric field. The comparison of the powder diffraction data with macroscopic measurements of the sample, caused us to suggest that the slow dynamics of some phase could also be the explanation for the slow wake up and remanent strain behavior observed in the material.*

Cite this: *J. Mater. Chem. C*, 2018,  
6, 7635

## Dynamics and grain orientation dependence of the electric field induced phase transformation in Sm modified BiFeO<sub>3</sub> ceramics

Jeppe Ormstrup,<sup>a</sup> Maja Makarovic,<sup>b</sup> Marta Majkut,<sup>c</sup> Tadej Rojac,<sup>b</sup>  
Julian Walker<sup>id</sup>\*<sup>d</sup> and Hugh Simons<sup>id</sup>\*<sup>a</sup>

Samarium-modified bismuth ferrite ((Bi,Sm)FeO<sub>3</sub> or BSFO) is a room-temperature multiferroic with a morphotropic phase boundary near 15.5 mol% Sm, where ferroelectric, antiferroelectric and paraelectric phases coexist and the electromechanical response ( $S_{\max}/E_{\max}$  and  $d_{33}$ ) is maximized. Recently, an electric field induced phase transformation was discovered, which is believed to play a significant role in the macroscopic electromechanical response. Here, we used *in situ* synchrotron X-ray powder diffraction to directly measure this transformation in real time within bulk ceramics to determine the dynamics, structural pathway and crystallographic orientation dependence of the transformation. Our results show that there are two transformation pathways; an antiferroelectric-to-ferroelectric transformation, which is reversible, and a paraelectric-to-ferroelectric transformation, which is irreversible. Furthermore, these transformations occur with a strong orientation dependence with respect to the applied electric field direction, and with extremely slow dynamics – just 2 to 10 minutes – orders of magnitude longer than in other ferroelectrics (e.g. Bi<sub>1/2</sub>Na<sub>1/2</sub>TiO<sub>3</sub>–BaTiO<sub>3</sub> or BNT–BT). These findings point to texturing and the elimination of the paraelectric phase to enhance the electromechanical response. Moreover, they provide a detailed picture of the transformation dynamics and a greater understanding of electric field induced transformations in ferroelectric ceramics.

Received 24th April 2018,  
Accepted 25th June 2018

DOI: 10.1039/c8tc01951g

rsc.li/materials-c

### Introduction

Bismuth ferrite (BiFeO<sub>3</sub>, or BFO) is a room temperature multiferroic with promising magnetic, dielectric and electromechanical properties.<sup>1</sup> Chemical modification of BFO with rare earth elements (e.g. Sm, Nd, Gd, Dy) induces a polar-to-nonpolar phase boundary (often referred to as a morphotropic phase boundary, or MPB) where these functional properties are enhanced.<sup>2,3</sup> Depending on the rare earth species and their concentrations, chemical modification may result in the coexistence of antiferroelectric orthorhombic *Pbam*, ferroelectric rhombohedral *R3c* and paraelectric orthorhombic *Pnma* phases at the MPB.<sup>4,5</sup>

The complex coexistence of polar, anti-polar and non-polar phases is believed to have a significant effect on the electromechanical response of rare earth modified BFO. In Sm-modified BFO compositions near the MPB, *i.e.* (Bi<sub>(1-x)</sub>Sm<sub>(x)</sub>FeO<sub>3</sub>) ( $x = 0.12$ – $0.16$ ), electric field induced phase transformations

from anti-polar *Pbam* and non-polar *Pnma* to polar *R3c* are correlated with enhanced electromechanical strains in excess of ~0.3%.<sup>6,7</sup> Our understanding of this transformation is currently based on macroscopic hysteresis behavior, *ex situ* X-ray diffraction (XRD) measurements<sup>6</sup> and local *in situ* electron microscopy.<sup>7</sup> While these studies provide an invaluable first insight into the transformation and its effect, many details of this transformation remain unknown. Here, we describe an *in situ* structural analysis of the electric field induced phase transformations in polycrystalline Bi<sub>0.845</sub>Sm<sub>0.155</sub>FeO<sub>3</sub> (BSFO), including its dynamics, transformation pathway, and grain orientation dependence.

Measuring the structural transformation in bulk BSFO requires a quantitative and time-resolved means to differentiate between crystallographically similar (*i.e.* pseudo-cubic) lattice symmetries to capture the transformation dynamics (in the time-frame of seconds-to-minutes<sup>8</sup>). In this study we use *in situ* high-energy synchrotron X-ray powder diffraction to measure the volume fractions and crystallographic textures of the *Pbam*, *Pnma* and *R3c* phases in BSFO, in real time during electrical poling. The data provide statistically significant measurements of these dynamics in the bulk, which we argue is paramount to understanding the physical origin of the electromechanical behavior and properties of rare-earth modified BFO materials.

<sup>a</sup> Department of Physics, Technical University of Denmark, 2800 Kgs. Lyngby, Denmark. E-mail: husimo@fysik.dtu.dk

<sup>b</sup> Electronic Ceramics Department, Jozef Stefan Institute, Ljubljana 1000, Slovenia

<sup>c</sup> ESRF – The European Synchrotron, Avenue des Martyrs, 38000 Grenoble, France

<sup>d</sup> Materials Research Institute, The Pennsylvania State University, University Park, Pennsylvania 16802, USA. E-mail: jxw512@psu.edu

## Methods

$\text{Bi}_{0.845}\text{Sm}_{0.155}\text{FeO}_3$  ceramics were prepared by mechanochemical activation assisted synthesis, as detailed by Walker *et al.*<sup>9</sup> Starting powders of  $\text{Bi}_2\text{O}_3$  (99.998%, Alfa Aesar),  $\text{Fe}_2\text{O}_3$  (99.999%, Alfa Aesar) and  $\text{Sm}_2\text{O}_3$  (99.99%, Metall) were separately ball-milled to a mean particle size of  $<1\ \mu\text{m}$ , mixed into stoichiometric ratios, and mechanochemically activated for 40 hours. Based on an XRD analysis (not shown), the mechanochemical activation process resulted in powders with a fine crystallite size and in a semi-amorphous state, increasing their reactivity and sinterability. Powders were dried, ball-milled again, then uniaxially pressed into pellets at 150 MPa and sintered at 800 °C for 3 hours with cooling and heating rates of 10 °C  $\text{min}^{-1}$ . The low sintering temperature with practically complete chemical reaction is most likely achievable due to the mechanochemical activation.<sup>9</sup> Unlike unmodified BFO ceramics, the polarization and strain responses of the BSFO ceramics prepared by the described method show no sign of pinching of  $P$ - $E$  loops.<sup>9,10</sup> The sintered pellets had an average grain size of 1–3  $\mu\text{m}$  and a relative density of 95% (or absolute density of 8150  $\text{kg m}^{-3}$ ). These pellets were then cut into bars of dimensions 5 mm (length), 0.3 mm (height) by 0.5 mm (thickness) using a wire saw. Gold electrodes were sputtered onto the 0.5 × 5 mm faces. No electric field was applied to the samples prior to the experiment (*i.e.* the samples were unpoled).

Synchrotron experiments were carried out at ID11 of the European Synchrotron Radiation Facility (ESRF). The X-ray beam was rectangular, with dimensions 0.6 mm (horizontal) by 0.3 mm (vertical), and a wavelength of 0.31 Å (40 keV energy). Two-dimensional powder diffraction patterns were measured on a FReLoN CCD detector located 245 mm from the sample. The detector sampled a  $q$ -range of 4.24 Å<sup>-1</sup>, spanning the first 6 diffraction rings (*i.e.* up to the 211<sub>PC</sub>, where PC denotes pseudo-cubic Miller indices). The samples were immersed in silicone oil within a custom-made sample holder, and a DC electric field was applied *in situ* in the following scheme: a continuous ramp from 0  $\text{kV mm}^{-1}$  to 10  $\text{kV mm}^{-1}$  over 1200 s (20 minutes), poling at 10  $\text{kV mm}^{-1}$  for 900 s (15 minutes), followed by the immediate removal of the field and a relaxation period at 0  $\text{kV mm}^{-1}$  for 300 s (5 minutes). Images were acquired every two seconds. This voltage ramping scheme was required to minimize the likelihood of dielectric breakdown during the application of the electric field. The raw 2D images were corrected for detector distortions and background intensity, and azimuthally segmented into 36, 10°-wide bins (see *e.g.* ref. 11). Ferroelectric hysteresis measurements were made using an aixACCT TF 2000 Analyzer, SIOS meßtechnik Laser Interferometer and TREK model 609E-6 (4 kV) high-voltage amplifier using a sinusoidal wave form with frequencies of 100 Hz.

## Results and discussion

The measured XRD patterns enabled identification of both the crystallographic symmetry of the coexisting phases, as well as their changes due to the applied electric field (Fig. 1). Rietveld refinement was used to identify three coexisting phases and their

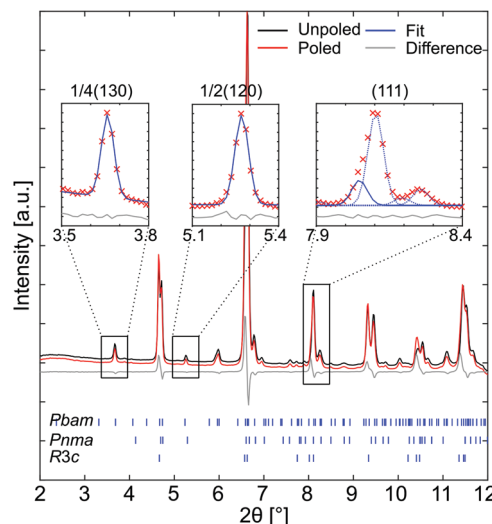


Fig. 1 Synchrotron X-ray diffraction patterns from a BSFO sample in both the unpoled (*i.e.* zero electric field with no electrical history), and poled (*i.e.* immediately after the 900 s, 10  $\text{kV mm}^{-1}$  poling process; see methods) states. The structural changes during poling are evident in the intensity difference line (grey) showing the difference of the pattern of poled and unpoled sample. Peak locations for each symmetry are indexed by blue ticks. Insets: Close-ups of three peaks of the poled sample uniquely associated with the three observed crystal symmetries. Here, experimental data points are marked by red crosses, while a Gaussian fit of each peak is given by the continuous blue line. The grey line in the inset is the difference between the data and the fit.

respective weight fractions prior to electric field application: anti-ferroelectric *Pbam* (73 wt%), paraelectric *Pnma* (10 wt%), and ferroelectric *R3c* (17 wt%). These phases are consistent with reports of Sm-modified BFO thin films<sup>3,12</sup> and ceramics.<sup>6</sup> The XRD patterns for each phase overlap significantly, however, each phase has at least one unique peak within the measured  $2\theta$  range. The intensities of these peaks were used to track changes in their respective volume fractions as a function of electric field and crystal lattice orientation. Specifically: *Pbam* with the 1/4(130), *Pnma* with the 1/2(120), and *R3c* with the characteristically split (111)/(11 $\bar{1}$ ) (shown in the Fig. 1 insets). Applying an external electric field with magnitude greater than the coercive field ( $E_c$ ) causes domain switching in the rhombohedral *R3c* phase (*i.e.* poling). This is identifiable by an increase in the (111) peak intensity, which is unique to the *R3c* phase, when measured parallel to the direction of the applied electric field and a proportional decrease in the (11 $\bar{1}$ ) peak intensity. Thus, the (111)/(11 $\bar{1}$ ) peak intensity ratio can be utilized to quantify the rhombohedral *R3c* domain texture.<sup>11</sup> The (11 $\bar{1}$ ) peak intensity distribution includes contributions from all phases in the material, as illustrated by the multiple peak profiles in Fig. 1. Therefore, changes to the (11 $\bar{1}$ ) peak intensity represent changes to the relative volume fractions of *Pnma* and *Pbam* phases, as well as to the fraction of *R3c* domains whose non-polar axes are perpendicular to the X-ray scattering vector (therefore, this peak will be further referred to as “(11 $\bar{1}$ ) all phases”). On the other hand, since the (111) peak corresponds to domains that are *R3c* with their polar axis oriented parallel to

the X-ray scattering vector, changes to its intensity represent changes to both the volume fraction of the  $R3c$  phase and the volume fraction of the poled domains within it (henceforth this peak will be further referred to as “(111)  $R3c$ ”).

The  $1/4(130)$ ,  $1/2(120)$  and (111) peaks can be accurately modelled by Gaussian profiles, enabling their  $2\theta$  position,  $2\theta$  full-width-at-half-maximum (FWHM) and intensity to be quantitatively determined as a function of time and electric field magnitude. Furthermore, our use of a 2D diffraction detector enables determination of the orientation dependence (texture) of the response since diffraction patterns can be extracted from different azimuthal angles (and hence X-ray scattering vector orientations) with respect to the electric field. Changes to the peak position ( $2\theta$ ) are indicative of lattice strain, while changes in the integrated peak intensity are proportional to changes in the volume fraction of the corresponding phase and/or its concomitant domains.<sup>13</sup>

Fig. 2 shows the relative integrated intensity of the three peaks unique to the  $Pbam$ ,  $Pnma$  and  $R3c$  phases respectively during electric field application. Changes to the peak intensities and current draw during the poling process occurred in four distinct stages. As indicated in Fig. 2a, these stages approximately correspond to: the first and second halves of the electric field ramp (Stages I and II), constant electric field (Stage III), and immediate removal of the field and ensuing zero-field rest period (Stage IV). These stages are characterized as follows:

Stage I: during the first half of the electric field ramp ( $0\text{--}5\text{ kV mm}^{-1}$ ) (Fig. 2a), there was a steady increase in the measured current (Fig. 2b), however little structural change was observable from the relative peak intensities (Fig. 2c–f).

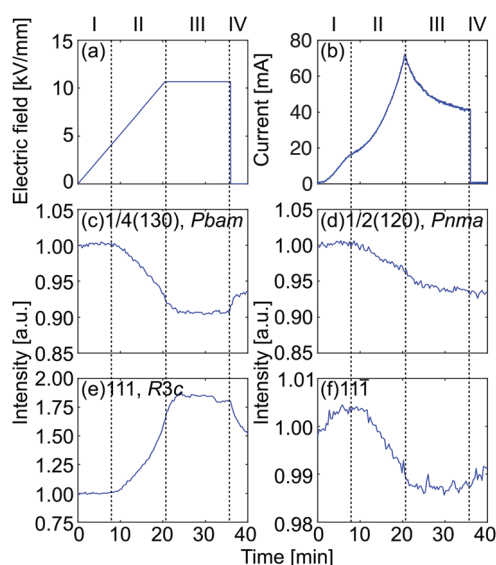


Fig. 2 Time and field-dependent changes in integrated peak intensities (determined by fitting) during the application of the DC electric field. Shown: (a) the electric field–time profile, and (b) corresponding electric current–time profile. The relative integrated peak intensities of (c) the  $1/4(130)$  peak unique to  $Pbam$ , (d) the  $1/2(120)$  peak unique to  $Pnma$ , (e) the (111)  $R3c$  peak, and (f) the (111) peak related to all phases present ( $Pnma$ ,  $Pbam$  and  $R3c$ ). The dashed lines denote the four distinct stages of the poling process. Note that the peak intensities are averaged over all azimuthal angles to the electric fields and are normalized independently.

Stage II: the second half of the electric field ramp ( $5\text{--}10\text{ kV mm}^{-1}$ ) began with a clear inflection in the current, followed by a continued exponential increase (Fig. 2a). Simultaneously, significant changes were observed in the relative peak intensities: the  $1/4(130)$  peak associated with the  $Pbam$  phase decreased by  $\sim 10\%$  (Fig. 2c) and the  $1/2(120)$  peak associated with the  $Pnma$  phase decreased by  $\sim 5\%$  (Fig. 2d). At the same time, the (111) peak associated with  $R3c$  increased exponentially by  $\sim 75\%$  (Fig. 2e), while the (111) peak associated with all phases decreases by only  $\sim 1.5\%$  (Fig. 2f). Stage II thus indicates that the coercive field onset for the electric field induced phase transition in BSFO is at  $\sim 5\text{ kV mm}^{-1}$ .

Stage III: as the field was held at  $10\text{ kV mm}^{-1}$ , the current decayed from its maximum value of  $70\text{ mA}$  to  $40\text{ mA}$  within 15 minutes, a behavior related to a slow capacitor charging (Fig. 2b). At the same time, the intensity of the  $1/4(130)$  peak did not change (Fig. 2c), while the intensity of the  $1/2(120)$  peak continued to decrease, but at a slower rate (Fig. 2d). The intensity of the (111)  $R3c$  peak also continued to increase at a slowing rate for  $\sim 4$  minutes, before a minor linear decrease ensued for the remainder of Stage III (Fig. 2e). The intensity of the (111) peak associated with all phases present (*i.e.*  $Pbam$ ,  $Pnma$  and  $R3c$ ) plateaued during Stage III (Fig. 2f).

Stage IV: structural relaxation occurs once the electric field is removed. The relative intensity of the  $1/4(130)$  peak appeared to increase while the intensity of the  $1/2(120)$  continued to decrease slowly, and the intensity of the (111)  $R3c$  peak fell by  $\sim 30\%$  over 5 minutes (Fig. 2c–e). This could be associated with  $R3c$  domain back-switching or a reversible phase transformation. The (111) peak associated with all phases exhibited a minor increase.

The overall 80% increase in the (111)  $R3c$  peak intensity (Fig. 2e) cannot be attributed purely to domain reorientation because the intensity change begins in Stage II at an electric field of  $\sim 5\text{ kV mm}^{-1}$  (Fig. 2) – less than half of the known mean coercive field for these ceramics (*i.e.* the electric field where the switching rate is greatest).<sup>6</sup> Thus, the peak intensity change likely includes a significant contribution from an electric field induced transformation to the  $R3c$  phase, which is consistent with a clear decrease of  $Pbam$  (Fig. 2c) and  $Pnma$  (Fig. 2d) peaks, and thus a decrease in the volume fraction of the two phases, in the same time frame. The (111)  $R3c$  peak intensity change is strongly correlated with the sharp inflection in the current–time profile (see Fig. 2b), and the ensuing change in the macroscopic polarity of the sample. The current increase associated with ferroelectric domain switching is a known phenomenon of macroscopic current–electric field hysteresis measurements under AC electric fields. Such correlation between structural phase changes and the inflections in the macroscopic current and polarization response is a classical hallmark of electric-field induced phase and order–disorder transformations in Sm-modified BFO and other ferroelectric perovskites such as  $\text{Bi}_{1/2}\text{Na}_{1/2}\text{TiO}_3\text{--}6\%\text{BaTiO}_3$ .<sup>13,14</sup>

The observation of an electric-field induced  $R3c$  phase in a material with both  $Pbam$  and  $Pnma$  phases raises the question as to their role in electric field induced phenomena. Previous studies of the electric field induced  $R3c$  phase in BSFO films

suggest that both the antiferroelectric *Pbam* and paraelectric *Pnma* phases act as parent phases for the induced *R3c* phase.<sup>7</sup> Here, the results suggest that *Pbam* and *Pnma* phases are both involved but are not equal participants in the transformation. This conclusion is derived from the fact that during electric field application the intensity of the 1/2(120) peak (representative of the *Pnma* phase fraction) decreases at approximately half the rate of the 1/4(130) peak (*i.e.* the *Pbam* phase fraction) (compare Fig. 2c with Fig. 2d). In addition, we note that the 1/4(130) *Pbam* peak increases intensity by 3% after the field is removed, while the 1/2(120) does not. This suggests that the *Pbam*-to-*R3c* phase transformation is partially reversible, while the *Pnma*-to-*R3c* phase transformation is likely irreversible under these experimental conditions (*i.e.* electric field magnitude and time scale). This appears to contradict the results of a recent thin film transmission electron microscopy (TEM) investigation,<sup>7</sup> which suggests that the *Pbam*-to-*R3c* and *Pnma*-to-*R3c* transformations are both reversible. This discrepancy could be attributed to the different boundary conditions between the bulk and thin film samples, different electric field conditions and electrical history, the local nature of TEM as a structural probe used in ref. 7 or, in the case of bulk X-ray measurements, insufficient measuring time to detect a slow reversible transformation.

Understanding the different time scales of the transformations and their dependence on crystal lattice orientation requires a comparative analysis of the structural responses measured at each azimuthal scattering angle.<sup>11</sup> Diffraction profiles extracted at different angles around the incident beam correspond to different angles between the applied electric field and the diffraction scattering vector for each peak (and hence the tilt angle of the lattice). Analysis of the structural response (*i.e.* lattice strain, domain reorientation) as a function of this lattice tilt angle to the electric field axis therefore reveals how these responses depend on the orientation of a given crystallite (*e.g.* a grain or domain). In initially untextured ferroelastic polycrystals (as is the case here), the application of an electric field induces an axisymmetric texture, which can be fully characterized in a single 2D diffraction pattern. The change in the texture as a function of the applied electric field (Fig. 3) can then be used to identify if there are crystallite orientations in which electric field induced phase transformations and ferroelectric domain reorientation are preferred. The time-dependent changes to this texture during the application and removal of the electric field can be correlated with the macroscopic electromechanical properties<sup>15</sup> and yields quantitative insight into the orientation-dependent dynamics of the phase transformations.

Fig. 3 shows the azimuthal dependence of the integrated intensity of the 1/4(130), 1/2(120), (111) and (11 $\bar{1}$ ) peaks during the electrical poling process. The ceramic sample was untextured prior to poling (not shown), possessing a random distribution of grain orientations and a random distribution of the eight allowable ferroelectric-ferroelastic domain variants of the *R3c* phase (*i.e.* equal volume fractions of each variant).<sup>16</sup> Electrical poling then induces two superimposed textures: (1) a phase texture, where the phase transformation preferentially occurs in crystallites whose {111} directions are parallel to the electric field, and

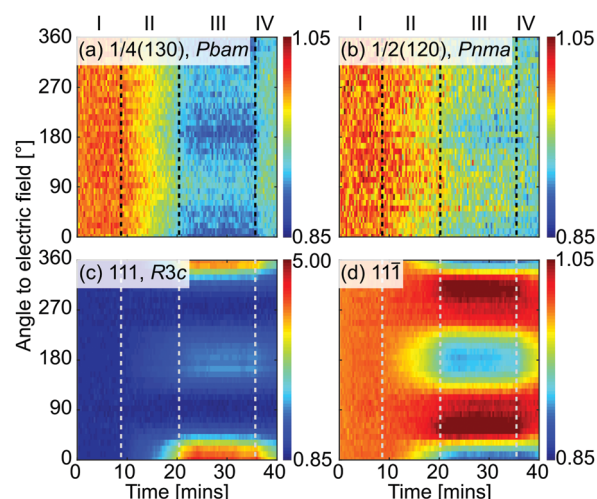


Fig. 3 Integrated peak intensity change during the electric field-time profile (see Fig. 2a) as a function of the lattice tilt angle to the electric field (and azimuthal angle on the 2D detector). 0°, 180° and 360° are parallel to the applied electric field, while 90° and 270° are perpendicular. Peak intensity is represented by the color scale with red indicating high intensity and blue low intensity. Shown are: (a) the 1/4(130) peak intensity from the antiferroelectric *Pbam* phase, (b) the 1/2(120) peak intensity from the nonpolar *Pnma* phase, (c) the (111) peak from the *R3c* phase, and (d) the main (11 $\bar{1}$ ) peak from all phases.

(2) a domain texture, where the ferroelectric domains of the *R3c* phase are preferentially oriented with their polarization direction parallel to the electric field. The 1/4(130) and 1/2(120) peaks both decreased in intensity during Stages II and III of the poling profile (*cf.* Fig. 2) while simultaneously developing an azimuthal orientation dependence. During Stage III, this texture developed such that the volume fraction of the *Pbam* and *Pnma* phases were significantly lower in grains whose {111} directions are oriented parallel to the electric field (0° or 360° in Fig. 3a and b), and only marginally lower in grains whose {111} directions are oriented perpendicular to the electric field (90° or 270° in Fig. 3a and b). At the same time, the (111) peak associated with the *R3c* phase increased intensity during Stages II and III, and developed a strong texture in favor of the electric field direction (Fig. 3c and d, see high intensity at 0°, 180° or 360°).

Following recent developments,<sup>8</sup> the time constants and coercive fields for electric-field-induced phase transformations can be quantitatively extracted from time-dependent diffraction intensities by fitting an exponential response function. Notably, this assumes that the phase transformation is occurring on the same time scale as the ramping period (confirmed by the steady intensity in Stage III in Fig. 2). Using the same methods as in ref. 8, we extended this approach to model reversible transformations from arbitrary perturbations by using a first-order response function in which the volumetric rate of change is proportional to the difference in the instantaneous and coercive electric fields (Fig. 4). The differential equation has the form:

$$\tau \frac{dv(t)}{dt} = av(t) - [E_C - E(t)] \quad (1)$$

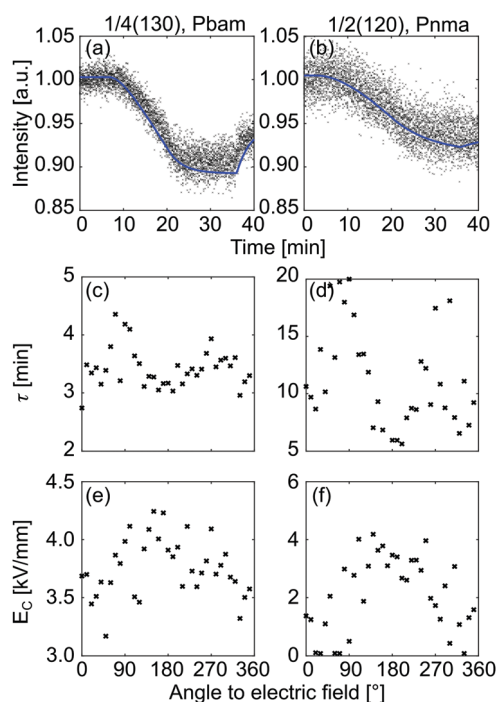


Fig. 4 Phase transformation dynamics and orientation dependence. The time-dependent integrated intensity points plotted for the 1/4(130) (a) and 1/2(120) (b) peaks were determined by fitting to the orientation bin at 0°, see panels (a) and (b) where dots and solid line correspond to experimental data and the fit, respectively. These data were then fit at each azimuthal angle using a first-order response function (eqn (1)) to extract the orientation-dependence of the time constants (c and d) and coercive field (e and f) for each transformation pathway.

where  $\tau$  is the time constant,  $v(t)$  and  $E(t)$  are the time-dependent volume of a given phase and electric fields, respectively,  $\frac{dv(t)}{dt}$  is the volume rate of change,  $E_C$  is the coercive field of the transformation, and  $a$  is a proportionality constant. Numerically solving this equation to fit the measured intensities of the *Pbam* 1/4(130) and *Pnma* 1/2(120) peaks thus should provide a quantitative estimate of the transformation rate constants and coercive fields for both the *Pbam*-to-*R3c* and *Pnma*-to-*R3c* pathways, and their dependence on lattice orientation with respect to the electric field.

The calculated mean time constants, over the 0-to-360° azimuthal angle, were 3.4 and 11.1 minutes for the *Pbam*-to-*R3c* and *Pnma*-to-*R3c* transformations, respectively. These rate constants are orders of magnitude larger than for many other ferroelectrics exhibiting electric-field induced phase transformations. For example, transformation rate constants in  $\text{BaTiO}_3\text{-BiZn}_{1/2}\text{Ti}_{1/2}\text{O}_3$ <sup>8</sup> are of the order of 1 ms, while for strongly disordered materials such as  $\text{Bi}_{1/2}\text{Na}_{1/2}\text{TiO}_3\text{-BaTiO}_3$  it is typically on the order of 100 ms.<sup>17</sup> In BSFO, the slower transformation rate of the *Pnma* phase could explain why its volume fraction changes so little compared to *Pbam*. Both phases exhibit a significant orientation dependence to this transformation rate. The variation in these rates was much greater in the *Pnma* phase than the *Pbam*, but this may also

relate to poorer statistics due to the low volume fraction of the *Pnma* phase in the ceramics. The coercive field for the transformation was typically lower in the *Pnma* phase (mean values of  $2.1 \text{ kV mm}^{-1}$  vs.  $3.8 \text{ kV mm}^{-1}$  for *Pbam*) and follows a similar trend in terms of orientation dependence, with increased coercive field values in grains whose {111} directions are perpendicular to the applied electric field. We note that the coercive field calculated for the phase transformations are ~33% of the values observed for domain reorientation in the *R3c* phase ( $13 \text{ kV mm}^{-1}$ , ref. 6).

The macroscopic polarization and strain responses of 15.5 mol% Sm-BFO ceramics, shown in Fig. 5, are consistent with an electric field induced phase transformation with slow dynamics. Previous descriptions of the electromechanical response of these materials<sup>6</sup> reported a slow “wake up” behavior, characterized by a progressive development of the ferroelectric response over multiple electric field cycles. In the samples investigated here, this wake-up behavior is clearly seen in the subcoercive (Fig. 5a) and supercoercive (Fig. 5b) polarization (*P-E*), current (*I-E*) and strain-electric field (*S-E*) hysteresis loops from the virgin sample. It is difficult to identify the effects of an emerging ferroelectric phase from the *P-E* loops

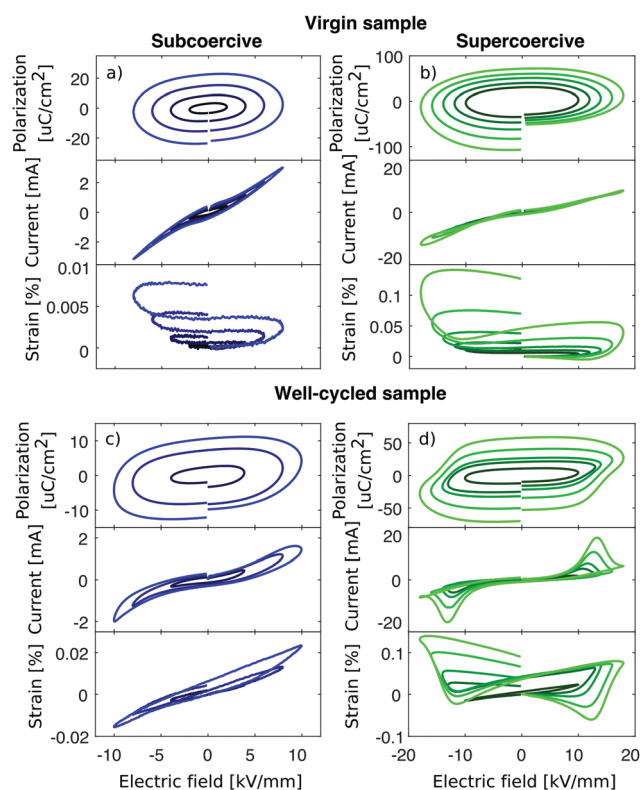


Fig. 5 Hysteresis loops of virgin (a and b), well-cycled (c and d) 15.5 mol% Sm-BFO. Panels show polarization-, current- and strain-electric field hysteresis behavior as the electric field was increased by  $1 \text{ kV mm}^{-1}$  increments up to a maximum electric field of  $18 \text{ kV mm}^{-1}$ , with a cycle frequency of 100 Hz. Panels on the left shows the subcoercive hysteresis loops at electric fields from  $2 \text{ kV mm}^{-1}$  to  $8 \text{ kV mm}^{-1}$ . Panels to the right shows the supercoercive hysteresis loops at electric fields from  $10 \text{ kV mm}^{-1}$  to  $18 \text{ kV mm}^{-1}$ .

due to the large leakage currents (typical of BSFO ceramics) and the increasing gap between starting and finishing points of the loops (likely due to charge injection during cycling).<sup>18</sup> However, the  $I$ - $E$  and  $S$ - $E$  loops both show characteristics consistent with weak ferroelectricity: the supercoercive  $I$ - $E$  loops show the emergence of small inflections under supercoercive cycling that indicate developing peaks associated with ferroelectric domain switching (also seen in ref. 6), while the subcoercive  $S$ - $E$  loops (Fig. 5a) – though low in magnitude ( $< 0.02\%$ ) – show the beginnings of the butterfly-like shape classically associated with ferroelectric/ferroelastic domain switching. This is even clearer in the supercoercive  $S$ - $E$  loops, and is also accompanied by a significant increase in the strain response ( $> 0.1\%$ ). Furthermore, both the subcoercive and supercoercive  $S$ - $E$  loops possess an asymmetric s-like shape, which is highly unusual for a classical ferroelectric (e.g. unmodified BFO<sup>19</sup>), and indicates a gradual transformation throughout the measurement cycles.

Confirming this hypothesis of an irreversible electric field induced transformations to the ferroelectric  $R3c$  phase, the macroscopic response of the material after 50 to 100 cycles at supercoercive electric field amplitudes of  $> 16 \text{ kV mm}^{-1}$  (described as the well-cycled material) is clearly ferroelectric in character (Fig. 5c and d). In particular, the supercoercive  $P$ - $E$  and  $I$ - $E$  loops have a square-shaped hysteresis and clear switching peaks, respectively. That these features are not present in the subcoercive regime implies they are a consequence of reversible ferroelectric domain switching. The  $P$ - $E$  and  $I$ - $E$  loops also exhibit substantially lower leakage in comparison to those from the virgin sample. While the precise mechanism behind this is not investigated here, the mobility of charged defects and creation of defect complexes during the application of electric fields is likely to result in the changing resistivity. At the same time, the  $S$ - $E$  loops exhibit classical linear piezoelectric and nonlinear ferroelectric behavior in the subcoercive and supercoercive regimes, respectively. This transition to a more typical ferroelectric strain behavior is an expected consequence as the ceramic becomes irreversibly transformed from  $Pbam$  to a majority  $R3c$  phase. The relaxation behavior observed with *in situ* XRD suggests that the characteristic progressive change in the shape of the  $S$ - $E$  loops during cycling at 100 Hz is likely related to the slow relaxation dynamics of the field induced phase transformation. Similarly, the gradual increase of strain with increasing field is likely related to both the slow dynamics and the crystallographic orientation dependence of the transformations observed during the *in situ* XRD experiments.

In conclusion, we carried out an *in situ* X-ray diffraction study of the electric field induced phase transformation in BSFO ceramics. We provide direct evidence of two distinct pathways for the field induced transformation, (1)  $Pbam$ -to- $R3c$  and (2)  $Pnma$ -to- $R3c$ . Under the tested poling fields (up to  $10 \text{ kV mm}^{-1}$ ), the transformations take place in grains of all orientations, albeit with a clear preference for grains whose  $\{111\}$  directions are aligned parallel to the electric field, which we ascribe to the faster transformation rates in these grains. Importantly, we note that the transformation dynamics are in

the order of 2–10 minutes; orders of magnitude slower than other ferroelectrics which exhibit electric field induced phase transformations. These slow dynamics may explain the wake-up and remnant strain behavior observed in the macroscopic hysteresis measurements.

## Conflicts of interest

There are no conflicts of interest to declare.

## Acknowledgements

The authors acknowledge the European Synchrotron Research Facility for providing beamtime through their user access program and Danscatt for providing travel assistance. J. O. acknowledges a Technical University of Denmark and Norwegian University of Science and Technology stipend under the tandem project framework. T. R. and M. M. acknowledge funding provided by the Slovenian Research Agency (program P2-0105 and project PR-08350). J. W. acknowledges the Slovenian research agency program J2-5483 and the Walker Science For Life Foundation.

## References

- 1 J. M. Moreau, C. Michel, R. Gerson and W. J. James, Ferroelectric BiFeO<sub>3</sub> X-ray and neutron diffraction study, *J. Phys. Chem. Solids*, 1971, **32**, 1315–1320.
- 2 G. L. Yuan and S. W. Or, Multiferroicity in polarized single-phase Bi<sub>0.875</sub>Sm<sub>0.125</sub>FeO<sub>3</sub> ceramics, *J. Appl. Phys.*, 2006, **100**, 024109.
- 3 D. Kan, L. Palova, V. Anbusathaiah, C. J. Cheng, S. Fujino, V. Nagarajan, K. M. Rabe and I. Keuchi, Universal Behavior and Electric-Field-Induced Structural Transition in Rare Earth Substituted BiFeO<sub>3</sub>, *Adv. Funct. Mater.*, 2010, **20**, 1108–1115.
- 4 S. Karimi, I. Reaney, Y. Han, J. Pokorny and I. Sterianou, Crystal chemistry and domain structure of rare-earth doped BiFeO<sub>3</sub> ceramics, *J. Mater. Sci.*, 2009, **44**, 5102.
- 5 J. Walker, H. Ursic, A. Bencan, B. Malic, H. Simons, I. Reaney, G. Viola, V. Nagarajan and T. Rojac, Temperature dependent piezoelectric response and strain–electric-field hysteresis of rare-earth modified bismuth ferrite ceramics, *J. Mater. Chem. C*, 2016, **4**, 7859–7868.
- 6 J. Walker, H. Simons, D. O. Alikin, A. P. Turygin, V. Y. Shur, A. L. Kholkin, H. Ursic, A. Bencan, B. Malic, V. Nagarajan and T. Rojac, Dual strain mechanisms in a lead-free morphotropic phase boundary ferroelectric, *Sci. Rep.*, 2016, **6**, 19630.
- 7 Z. Liao, F. Xue, W. Sun, D. Song, Q. Zhang, J. Li, L. Chen and J. Zhu, Reversible phase transition induced large piezoelectric response in Sm-doped BiFeO<sub>3</sub> with a composition near the morphotropic phase boundary, *Phys. Rev. B*, 2017, **95**, 214101.
- 8 T. Iamsasri, G. Esteves, H. Choe, M. Vogt, S. Prasertpalichat, D. P. Cann, S. Gorfman and J. L. Jones, Time and frequency-dependence of the electric field-induced phase transition in

- BaTiO<sub>3</sub>-BiZn<sub>1/2</sub>Ti<sub>1/2</sub>O<sub>3</sub>, *J. Appl. Phys.*, 2017, **122**, 064104, DOI: 10.1063/1.4998163.
- 9 J. Walker, P. Bryant, V. Kurusingal, C. Sorrell, D. Kuscer, G. Drazic, A. Bencan, V. Nagarajan and T. Rojac, Synthesis-phase-composition relationship and high electric-field-induced electromechanical behavior of samarium-modified BiFeO<sub>3</sub> ceramics, *Acta Mater.*, 2015, **83**, 149–159.
- 10 T. Rojac, M. Kosec, B. Budic, N. Setter and D. Damjanovic, Strong ferroelectric domain-wall pinning in BiFeO<sub>3</sub> ceramics, *J. Appl. Phys.*, 2010, **108**, 074107.
- 11 N. H. Khansur, T. Rojac, D. Damjanovic, C. Reinhard, K. G. Webber, J. A. Kilmington and J. E. Daniels, Electric-field-induced domain switching and domain texture relaxations in bulk bismuth ferrite, *J. Am. Ceram. Soc.*, 2015, **98**, 3884–3890.
- 12 C.-J. Cheng, D. Kan, S.-H. Lim, W. R. McKenzie, P. R. Monroe, L. G. Salamanca-Riba, R. L. Withers, I. Takeuchi and V. Nagarajan, Structural transitions and complex domain structures across a ferroelectric-to-antiferroelectric phase boundary in epitaxial Sm-doped BiFeO<sub>3</sub> thin films, *Phys. Rev. B: Condens. Matter Mater. Phys.*, 2009, **80**, 014109.
- 13 H. Simons, J. Daniels, W. Jo, R. Dittmer, A. Studer, M. Avdeev, J. Rodel and M. Hoffman, Electric-field-induced strain mechanisms in lead free 94%(Bi<sub>1/2</sub>Na<sub>1/2</sub>)TiO<sub>3</sub>-6%BaTiO<sub>3</sub>, *Appl. Phys. Lett.*, 2011, **98**, 082901.
- 14 Z. Zhou, W. Sun, Z. Liao, S. Ning, J. Zhu and J. Li, Ferroelectric domains and phase transition of sol-gel processed epitaxial Sm-doped BiFeO<sub>3</sub>(001) thin films, *J. Mater. Chem.*, 2018, **4**, 27–34.
- 15 A. Pramanick, D. Damjanovic, J. E. Daniels, J. C. Nino and J. L. Jones, Origins of Electro-Mechanical Coupling in Polycrystalline Ferroelectrics During Subcoercive Electrical Loading, *J. Am. Ceram. Soc.*, 2011, **94**, 293–309.
- 16 D. M. Hatch, H. T. Stokes and W. Cao, Allowed mesoscopic point group symmetries in domain averaged engineering of perovskite ferroelectric crystals, *J. Appl. Phys.*, 2003, **94**, 5220–5227.
- 17 A. J. Royles, A. J. Bell, J. E. Daniels, S. J. Milne and T. P. Comyn, Observation of a time-dependent structural phase transition in potassium sodium bismuth titanate, *Appl. Phys. Lett.*, 2011, **98**, 182904, DOI: 10.1063/1.3582616.
- 18 T. Schenk, E. Yurchuk, S. Mueller, U. Schroeder, S. Starschich, U. Bottger and T. Mikolajick, About the deformation of ferroelectric hysteresis, *Appl. Phys. Rev.*, 2014, **1**, 041103.
- 19 T. Rojac, H. Ursic, A. Bencan, B. Malic and D. Damjanovic, Mobile domain walls as a bridge between nanoscale conductivity and macroscopic electromechanical responses, *Adv. Funct. Mater.*, 2015, **25**, 2099–2108.

## 2.4 Limitations of our current approach

Our work with *in situ* powder diffraction above provided useful quantitative and qualitative information on the nature of the electric-field-induced phase transformation. Such methods provide insight into the structural dynamics, since we can relate the phase distribution to the electrical measurements and obtain time constants for the different phases. They also shows how polarization in grains align to the electric field with the texture on the peak intensity. However, relating the defects movements and effects to these measurements is not possible using powder diffraction. In  $\text{BiFeO}_3$  point defects in the form of vacancies or substitution atoms, can form conducting domain walls [36].

These very local effects are extremely important to the properties of the average material, and to exclude such information from fundamental studies will obscure the conclusions. Facilitating this paradigm shift towards including and understanding the local structural dynamics is a key motivation for this thesis. In the following, I present our methodology for such an endeavour.

### 3 Hypothesis

Electric field induced phase transformations are an important phenomena dictating the local and macroscopic behaviour and properties of many ferroelectric and related electro-active (e.g. multiferroic) materials. However, we know that both locally- and globally-applied electric fields can induce ionic currents that displace and reconfigure local defects and heterogeneities, such as domain walls and oxygen vacancies. Moreover, this reconfiguration, as well as the electric-field-induced phase transition itself, depends strongly on the local and global energy landscape and boundary conditions of the sample. This leads to the core question of the thesis: How *exactly* do defects and heterogeneities interact with an electric field induced phase transformation in the bulk?

Admittedly, this sounds like a question that could already have an answer - I am certainly not the first to address the role of defects in phase transformations. However, one major issue has limited our ability to address this question in the past: so far, we haven't been able to determine conclusively - at a qualitative and quantitative fundamental level - how phase transformations and heterogeneities interact, because macroscopic measurements and powder diffraction of the bulk behavior haven't been able to observe these interactions at a local scale.

In the following chapters of the thesis, I will start by introducing the technique that I believe removes many of these past limitations: Dark Field X-ray Microscopy (DFXM). By utilizing the unique capabilities of the DXFM, we image spatial variations in the lattice structure of large (i.e. bulk) single crystals of BaTiO<sub>3</sub>. By developing and implementing an *in situ* system capable of maintaining an elevated temperature with a very high degree of stability while applying an electric field, local information about the structural dynamics can be recorded. This is carried out by obtaining time resolved reciprocal space maps (i.e. single crystal diffraction), microscopic images of the structural features, and strain maps of the bulk. These data are then related to the changes and structure to their external parameters of temperature and electric field. Essentially, I create a framework and pipeline for which to measure and understand various phenomena in bulk materials that were previously impossible to do so.

## 4 Methodologies

This chapter introduces Hard X-Ray Microscopy and one of its key modalities - Dark Field X-ray Microscopy (DFXM) - the main experimental technique used in this thesis work. The chapter will give the reader an overview of its capabilities and how it overcomes some of the important limitations of the other characterization techniques discussed in section 1.3. Furthermore, I describe the importance of DFXM's 3D and multi-scale capabilities for this work, and for material science in general, as well as its consequence for future research. The second part of this chapter will introduce the "STEF" holder; the sample environment I designed for *in-situ* DFXM (and other) measurements capable of utilizing all modes of the Hard X-ray Microscope while applying an extremely stable elevated temperature and an external electric field. This system is used in further studies in this thesis, and allows for the unique investigation of fundamental structural phenomena in ferroelectric and related materials.

### 4.1 Hard- and Dark-Field X-Ray Microscopy (HXRM and DFXM)

Recent years have seen an increase in the precision and capability of x-ray instrumentation and the brightness of x-ray sources. Combined with the development of x-ray lenses, we now have the ability to carry out full-field x-ray microscopy at hard x-ray energies ( $E > 15$  keV). The recently-constructed hard x-ray microscope (HXRM) at ID06 of the ESRF is intended as a multi-scale microscope capable of capturing images, videos and maps of strain and lattice distortions from structural elements in bulk materials, and in 3D. This capability is a crucial next step for understanding complex materials interaction as pointed out in the introduction [41][42][43].

One of the essential modalities of the HXRM is dark field x-ray microscopy (DFXM), which enables the characterization of morphological features in bulk materials by exploiting the contrast created by Bragg diffraction. The instrument is cable of producing 3D grain maps with various techniques like 3DXRD and DCT, which can be combined with DFXM imaging of more local phenomena to give it multi-scale capability [43][44]. It is possible to change between these modalities with out dismounting the sample, thus keeping the samples reference system intact, which insures easier comparison of data between the different modalities. Furthermore, DFXM data can be directly related to 3D models of material dynamics via pipelines currently under development[45]. Collectively, the functionalities associated with such a quantitative microscopy method will be vital to future approaches for material simulation and computational material design, since it can provide local structural information about the bulk structural dynamics across many relevant length scales.

Recent research demonstrates the 3D and multi-scale capability of DFXM on BaTiO<sub>3</sub> ferroelectrics, in particular as a tool for the research and characterization of ferroelectric materials. Simulations of ferroelectric phenomena in bulk materials tend to be highly dependent on the boundary conditions and the assumptions concerning the mechanistic behavior of local morphologies. For example, while DFT simulations have predicted that strain field from defects and hetoergenities in ferroic materials to extend in the order of Angstroms [38], experiments indicates they instead extend over several microns

[32]. Clearly, there is a striking need for experimental guidance and validations with the 3D multi scale data, such as that afforded by the characterization functionalities of DFXM.

Since this work mostly focuses on the use of DFXM, an overview of its components and geometry is given in figure 4.1. While in principle it is an analog to dark field transmission electron microscopy in that it uses an objective lens to create a real-space image from the x-rays diffracted by the sample at an oblique angle, the high x-ray energies used by DFXM mean it can image features embedded within the bulk of the material. Since the method uses synchrotron radiation, the high flux allows for time-resolved imaging at a rate of 1-10 images/second. With the current lens setup, a spatial resolution of 100 nm is achievable. The objective lens used for the experimental work in this thesis was a compound refractive lenses (CRL) consisting of 40-60 Be or SU8 lenslets [46], which additionally provides the option to change magnification by reconfiguring the lens stack. With the newly upgraded source at the ESRF and the development of Multi-layer Laue Lenses (MLLs), it is suggested that this could lead to a spatial resolution of 20 nm [43][47]. As with most microscopy techniques, such increases in resolution are a trade-off that results in a smaller field of view. Changing the configuration of the lenslets, however, allows the system to effectively zoom in and out with out changing the setting of the sample.

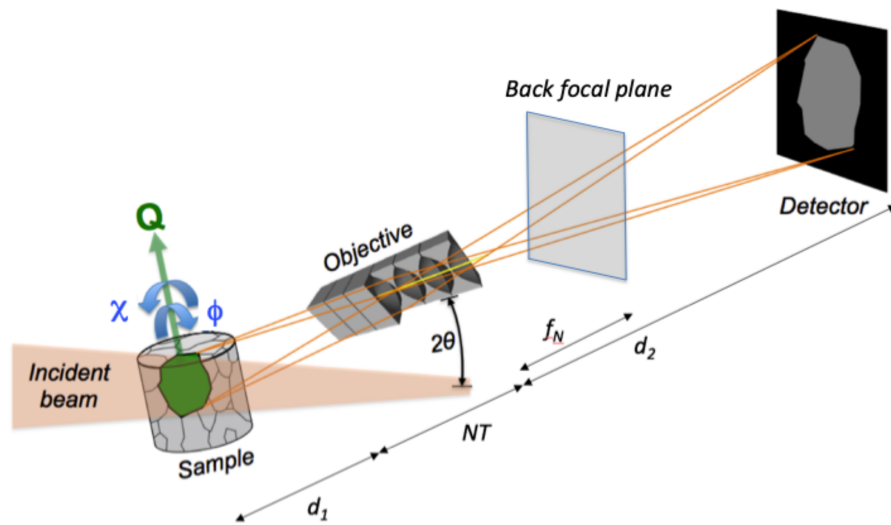


Figure 4.1: Geometry and operation of DFXM. Incident x-ray beam of monochromatic photons illuminated the sample and the diffracted beam is focused on to a detector via an objective lens stack. The lens stack consists of  $N$  lenses with the thickness of  $T$ .  $\chi$  and  $\phi$  are the sample tilt axis and  $2\theta$  is the scattering angle. while  $f_N$  is the focus length of the lens stack, while  $d_2/d_1$  give an approximation of the magnification [43][42]

The majority of studies with the instrument so far have used a line-shaped incident x-ray beam, where the x-ray beam is focused via 1D lenses to illuminate a thin “slice” of the sample, typically of  $200\mu m \times 200\mu m \times 200nm$  in dimension. Obtaining a 3D volume from the sample is then possible by recording multiple images while moving the sample in the thickness direction in adequate steps (relative to the beam thickness). For each layer in the 3D volume, several modalities can be used to obtain further types of data in 3D, such

as:

**Lattice tilt maps:** By scanning the sample through the tilt angles  $\chi$  and  $\phi$ , spatially resolved maps of the local crystallographic orientation can be acquired, in relation to a position on a pole figure. With this technique, a distribution of angular tilt (in reciprocal space) can be ascribed to each voxel in the sample [42].

**Reciprocal space maps (RSM):** For each illuminated layer, the lenses can be moved out of the beam path so that the detector (as illustrated in figure 4.1) is now in the far-field regime. By scanning the sample through the Bragg conditions, it is then possible to obtain single crystal diffraction patterns with an angular resolution of  $0.001 - 0.03^\circ$  [43][42], from which RSMs can be derived. We also note that, if lenses are not to be removed, it is possible to collect the RSM in the back focal plane of the imaging configuration, which is illustrated in figure 4.1.

**Axial strain map:** By scanning the objective and detector together through the  $2\theta$  angle, maps of a single axial strain component (i.e. parallel to the scattering vector) can be generated. While each point in such a map is given by the average strain, in combination with tilt mapping (described above) it can also be used to obtain local RSMs for each point in the image [48]. While this is the most used method of obtaining strain with DFXM so far, we also note that strain maps can similarly be collected by scanning a slit or other absorbing feature through the back focal plane [49].

As described in chapter 1 and 2, most ferroelectric materials used in industrial settings are bulk and ceramic materials. Their macroscopic responses are ultimately a consequence of microscopic changes in morphological features, such as domains and domain walls. DFXM is unique in its ability to map domains in embedded grains and bulk single crystals, while simultaneously following their evolution over time as the sample is subjected to an externally applied electric field [32]. The potential for sub-second resolution makes this kind of measurement particularly useful for comparing to multi scale computational simulations, e.g. via phase-field or Monte-Carlo models [43].

Defects and dislocations have long been known to have an effect on the local structure, with their density and distribution influencing the macroscopic response [12][21][13]. DFXM has also shown it can be used as a non-destructive method for mapping such structural distortions. Specifically, recent studies show how strain fields from dislocations can induce additional polarization due to the flexoelectric effect [48]. Due to this effect, the magnitude of polarization is enhanced close to edge dislocations, in a head-to-head or tail-to-tail configuration, depending on the specific dislocation. Combined with the demonstration that these distortions affected the sample on a mesoscopic scale [48], this enabled research to quantify the structural response of electro-active materials over several length scales.

In the following section, I present my development of the apparatus and methodology to control the external parameters relevant to studying electric-field-induced phase transformations in ferroelectrics, and their dependence on local heterogeneities. My approach allows high precision of temperature control, which is needed when studying electric field induced phase transformations in  $\text{BaTiO}_3$  and other ferroelectrics close to their Curie temperature.

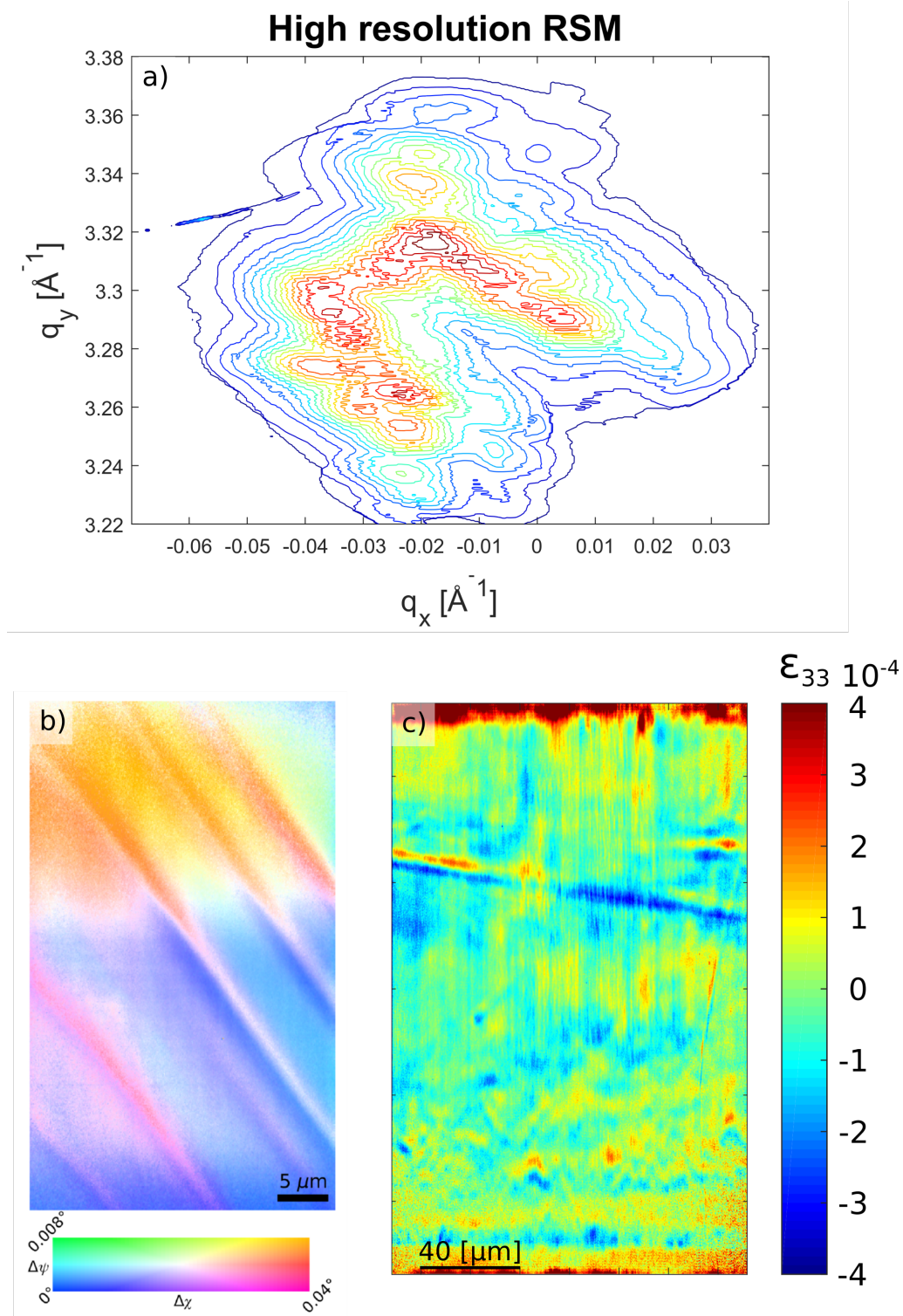


Figure 4.2: DFXM mapping capabilities: a) high resolution RSM of a single Crystal  $\text{BaTiO}_3$  at  $150^\circ\text{C}$ , b) orientation map of single crystal  $\text{BaTiO}_3$  taken with MLL, with parts of a pole figure inserted below to relate orientation. c) an axial strain map of  $\text{BaTiO}_3$  above  $T_C$  is shown with an external electric field applied at  $0.8 \text{ kV/mm}$ .

## 4.2 Paper 2: Imaging microstructural dynamics and strain fields in electro-active materials *in situ* with dark field x-ray microscopy

*Throughout this work, we have focused our effort on BaTiO<sub>3</sub>, which is a prototypical ferroelectric with a first order phase transformation. This type of transformation is very abrupt and is extremely sensitive to thermal fluctuations. Initial experiments with less rigorous control of temperature proved to be insufficient to deliver the experimental design of parameter required. This spawned the need for a holder system that could keep a temperature stable within tens of a degrees Celsius for extended periods of time, while applying an electric field.*

*The STEF (Stable Temperature and Electric Field) holder presented in the following article, is capable of temperature control with a stability below  $\pm 0.01^\circ\text{K}$  at a ramp rate of  $0.5^\circ\text{K}/\text{min}$  up to  $200^\circ\text{C}$ . Simultaneously, it can safely apply an electric field with a magnitude up to  $2\text{ kV}/\text{mm}$  and a precision of  $\partial E = 0.3\text{mV}/\text{mm}$ . The article describes the design that allows for these functionalities, while utilizing the data acquisition methods mentioned in previous section.*

*RSM's are acquired of above and below the Curie temperature to show the nominal patterns from the cubic and tetragonal phase of BaTiO<sub>3</sub>. Followed up by RSM's of above the Curie temperature with an applied electrical field of  $0.8\text{ kV}/\text{mm}$  and the subsequent pattern after the field is removed. The latter shows that the phase transformation induced by the electric field is not fully reversible in the specific circumstances.*

*In this study the ability to capture temporal resolved intensity images is used to image the electric field induced phase transformation, showing the us of the holder system for further characterization. The last results presented here is strain maps at elevated temperatures just above the Curie point. One map show the spatially-distributed strain configuration of the initial sample, while the other shows it after the electric field has been applied. This demonstrates that the holder system can be used to obtain reliable strain maps, which can be used in the quantitative characterization of defects, dislocation and domains. In short, the holder system has proven effective in controlling relevant external parameters simultaneously, while utilizing the full range of data acquisition modalities of the DFXM. The article has been accepted for publication in Review of Scientific Instruments.*

# Imaging microstructural dynamics and strain fields in electro-active materials *in situ* with dark field x-ray microscopy

Cite as: Rev. Sci. Instrum. **91**, 065103 (2020); <https://doi.org/10.1063/1.5142319>

Submitted: 17 December 2019 . Accepted: 14 May 2020 . Published Online: 03 June 2020

Jeppe Ormstrup , Emil V. Østergaard , Carsten Detlefs , Ragnvald H. Mathiesen , Can Yildirim , Mustafacan Kutsal , Philip K. Cook , Yves Watier, Carlos Cosculluela, and Hugh Simons 



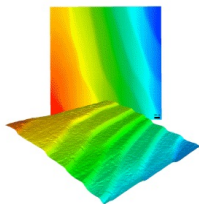
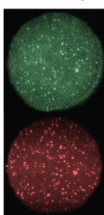
View Online



Export Citation



CrossMark

	<p>Nanopositioning Systems</p> 	<p>Modular Motion Control</p> 	<p>AFM and NSOM Instruments</p> 	<p>Single Molecule Microscopes</p> 
---	--	--	---	--

# Imaging microstructural dynamics and strain fields in electro-active materials *in situ* with dark field x-ray microscopy

Cite as: Rev. Sci. Instrum. 91, 065103 (2020); doi: 10.1063/1.5142319

Submitted: 17 December 2019 • Accepted: 14 May 2020 •

Published Online: 3 June 2020



Jeppe Ormstrup,<sup>1,a)</sup>  Emil V. Østergaard,<sup>1</sup>  Carsten Detlefs,<sup>2</sup>  Ragnvald H. Mathiesen,<sup>3</sup>  Can Yildirim,<sup>2,4</sup>  Mustafacan Kutsal,<sup>1,2</sup>  Philip K. Cook,<sup>2</sup>  Yves Watier,<sup>2</sup>  Carlos Cosculluela,<sup>2</sup> and Hugh Simons<sup>1</sup> 

## AFFILIATIONS

<sup>1</sup>Department of Physics, Technical University of Denmark, 2800 Kgs. Lyngby, Denmark

<sup>2</sup>ESRF – The European Synchrotron, Avenue des Martyrs, 38000 Grenoble, France

<sup>3</sup>Department of Physics, Norwegian University of Science and Technology, 7491 Trondheim, Norway

<sup>4</sup>OCAS, Pres. J.F. Kennedylaan 3, BE-9060 Zelzate, Belgium

<sup>a)</sup> Author to whom correspondence should be addressed: [jepor@dtu.dk](mailto:jepor@dtu.dk)

## ABSTRACT

The electric-field-induced and temperature induced dynamics of domains, defects, and phases play an important role in determining the macroscopic functional response of ferroelectric and piezoelectric materials. However, distinguishing and quantifying these phenomena remains a persistent challenge that inhibits our understanding of the fundamental structure–property relationships. *In situ* dark field x-ray microscopy is a new experimental technique for the real space mapping of lattice strain and orientation in bulk materials. In this paper, we describe an apparatus and methodology for conducting *in situ* studies of thermally and electrically induced structural dynamics and demonstrate their use on ferroelectric BaTiO<sub>3</sub> single crystals. The stable temperature and electric field apparatus enables simultaneous control of electric fields up to  $\approx 2$  kV/mm at temperatures up to 200 °C with a stability of  $\Delta T = \pm 0.01$  K and a ramp rate of up to 0.5 K/min. This capability facilitates studies of critical phenomena, such as phase transitions, which we observe via the microstructural change occurring during the electric-field-induced cubic to tetragonal phase transition in BaTiO<sub>3</sub> at its Curie temperature. With such systematic control, we show how the growth of the polar phase front and its associated ferroelastic domains fall along unexpected directions and, after several cycles of electric field application, result in a non-reversible lattice strain at the electrode–crystal interface. These capabilities pave the way for new insights into the temperature and electric field dependent electromechanical transitions and the critical influence of subtle defects and interfaces.

Published under license by AIP Publishing. <https://doi.org/10.1063/1.5142319>

## INTRODUCTION

Characterizing the dynamics of microstructural features under external stimuli is critical to understanding structure–property relationships in a wide range of materials. It is particularly critical for electro-active materials, such as piezoelectric, ferroelectrics, and multiferroics, where macroscopic properties depend strongly on the motion and interactions of domain walls, phase boundaries, and other defects.<sup>1</sup> For example, the density and mobility of domain walls in the archetypal ferroelectric lead zirconate titanate (PZT) are strongly affected by the presence of defects,<sup>2</sup> such as grain boundaries<sup>3</sup> and dislocations.<sup>4</sup> Spatially resolved models (e.g., phase field)

can predict the dynamics and interactions of domain walls and heterogeneous defects; however, such models lack quantitative experimental validation.<sup>5</sup> Thus, there is a strong need for experimental techniques capable of imaging the local environment around microstructural features at the relevant length scales.

The hard x-ray microscope (HXRM) on beam line ID06 at the European Synchrotron Radiation Facility (ESRF) is a newly developed instrument for multiscale *in situ* 3D imaging of bulk materials.<sup>6,7</sup> It can be operated in both transmission and reflection geometries and can change between multiple imaging and diffraction modalities to suit a given sample at the temporal, spatial, and angular resolutions required. In particular, HXRM is capable of

both bright field and dark field imaging modes. In bright field, the contrast mechanisms are attenuation or scattering in the forward direction. In dark field, the contrast is produced from the scattering intensity at high angles, allowing for very high selectivity between various Bragg peaks. Uniquely, dark-field x-ray microscopy (DFXM) directly maps structural features in the sample by forming a real-space image from the scattered beam (e.g., Bragg peak) via an x-ray objective lens.<sup>8–11</sup> In comparison, techniques such as transmission electron microscopy (TEM) and piezoresponse force microscopy (PFM) directly measure atomic displacement and polarization of domains, but are limited to thin samples or surface measurements, respectively. While nanoprobe x-ray diffraction and polarized light microscopy overcome these limitations to some degree, DFXM offers improved temporal or spatial resolution when tracking the morphological kinetics.<sup>7–9</sup> Additionally, the apparatus required for DFXM is capable of collecting time-resolved reciprocal space maps (RSMs) with high angular resolution ( $\sim 10^{-5} \Delta q/q$ ), allowing us to observe subtle perturbations to crystallographic phases. Collectively, this allows us to track and analyze morphological kinetics such as phase fronts and domain wall motion, making the HXRM well suited for studies of structure dynamics in bulk electro-active materials.

In this paper, we describe a system for imaging deeply embedded structures in bulk materials *in situ*, with precise temperature and electrical field control. We demonstrate how the system can be used to image the dynamics of topological features and relate these to strain maps, exemplified by studying the electric-field-induced phase transformation in single crystal  $\text{BaTiO}_3$  using full-field HXRM in the DFXM mode. Crucially, the critical nature of the first order phase transition in  $\text{BaTiO}_3$  at the Curie temperature requires extremely precise control of the sample temperature and electric field.<sup>12</sup>

## METHODOLOGY

HXRM operates as a conventional Galilean microscope, in which an x-ray objective lens forms a full-field magnified image of the sample on the 2D detector (Fig. 1). In the bright field mode, the detector and objective are placed in the forward direction, and absorption contrast dominates the image. In DFXM, the objective and detector are aligned to a Bragg peak related to the feature of interest (e.g., a domain wall). Spatial maps of lattice tilts can be measured by rotating the sample away from the scattering vector,

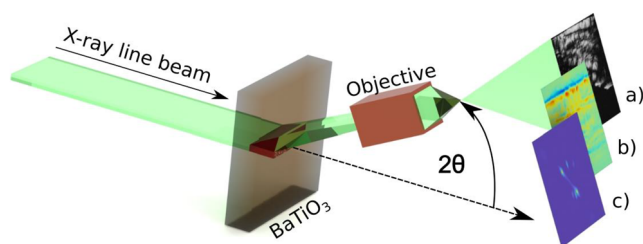


**FIG. 1.** Schematic of the HXRM in the DFXM mode in transmission geometry. A line-beam illuminates a section of the  $\text{BaTiO}_3$  sample (marked in red). At the  $2\theta$  angle for a given Bragg reflection, the objective is inserted to acquire real-space images shown in (a). Local strain maps can then be acquired by scanning the objective lens through  $2\theta$ , seen in (b). By removing the objective, x-rays scattered from the interaction volume will form a 2D diffraction intensity map.

while maps of lattice strain can be measured by collectively moving the objective lens and detector through the diffracted beam.<sup>7</sup> By operating at hard x-ray energies (10–30 keV), the microscope can probe embedded volumes in mm-size samples with typical spatial resolutions of 100 nm, imaging frame rates of 0.01–3 s/image and, in the dark-field mode, a strain resolution of  $10^{-5} (\Delta\epsilon/\epsilon)$ .<sup>6,8,11</sup> The magnification is given by the focal power of the objective lens and the sample-to-detector distance. The aberrations of the x-ray objective lens, along with the numerical aperture and Darwin width of the crystal, ultimately limit the spatial resolution.

## Requirements for the holder system

To characterize the morphological kinetics of a material, a system is required to precisely perturb the sample without compromising the imaging capabilities of the HXRM. Figure 2 shows the Stable Temperature and Applied Field (STEF) holder and gives an overview of the overall holder design and the placement of its individual components. The design is optimized to maintain a stable temperature from 22 °C (ambient) to 200 °C, simultaneously with a controlled electric field on commercially grown single crystal samples of  $5 \times 5 \times (0.15\text{--}0.5) \text{ mm}^3$ . The microscope's photon energy range (10–30 keV) places limits on the useful sample thickness due to attenuation. Selecting an optimum photon energy for a given experiment involves many considerations in terms of the microscope

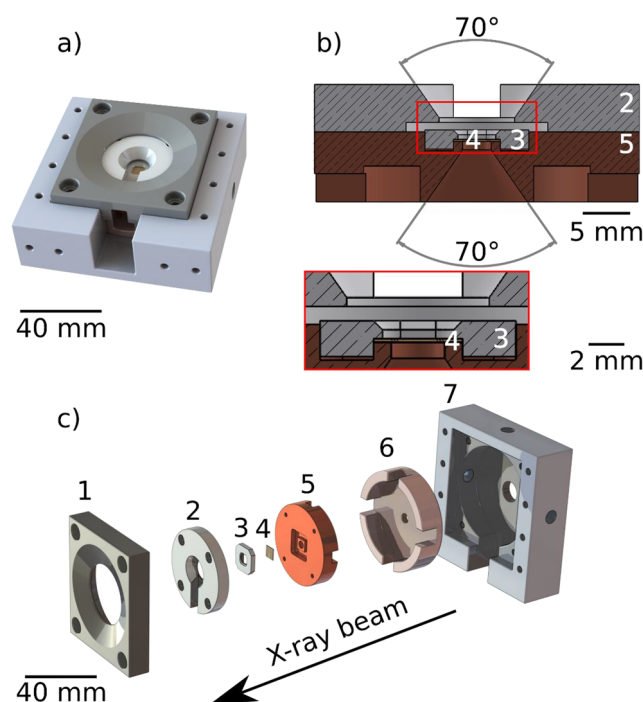


**FIG. 2.** (a) The assembled holder system and (b) the cross section of assembled parts 2–5 showing the  $70^\circ$  opening angle of the window through the (annotated) parts. The red square shows the close-up of the center of the holder. (c) Exploded view of the STEF holder with all parts numbered as follows: (1) the PEEK clamp, (2) MACOR ceramic cover, (3) MACOR ceramic spacer, (4)  $5 \times 5 \times 0.5 \text{ mm}^3$  sample, (5) copper disk, (6) ceramic cup, and (7) aluminum main holder.

parameters and sample conditions. These considerations are beyond the scope of this article and can be found in the literature.<sup>6–10</sup>

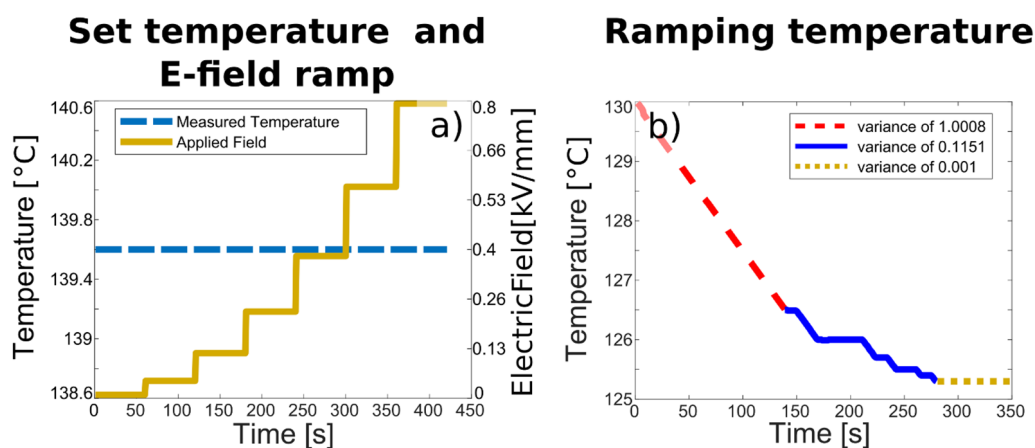
Parts 3 and 5 [as shown in Fig. 2(c)] are the two most critical components because they are responsible for the fixed placement of the sample (part 4) and the control of the temperature. Part 5 is copper, with a recess on the back side that holds a coiled resistance Kanthal-wire heating element and pt-100 four-point thermal measurement probe. Parts 2, 3, and 6 are fabricated out of MACOR (2, 3) and stumalit (6) ceramic due to their good thermal-insulation and electrical-insulation properties. Parts 1 and 7 are PEEK and aluminum, respectively. The relatively large amount of material surrounding the sample provides thermal mass to improve stability, while part 5 also serves as the electrical ground for the system.

Collectively, the different parts create a large thermal mass relative to the sample. The ceramic parts insulate the sample from environmental fluctuations, and the copper enables good thermal conduction from the heating element.<sup>15</sup> However, the temperature feedback loop, e.g., the measured temperature and subsequent regulation of the heating element, is the most critical component for controlling and maintaining the temperature. This is achieved by installing a small pt-100 element (platinum wire) in the recess of part 5, between the heating element and the sample. Using a four-point resistance measurement of the pt-100 element in conjunction with a Lakeshore 332/331 temperature controller and Delta Elektronika SM 120-13 power supply, we have been able to regulate the measured temperature with a precision of 0.01 K at a ramp rate of 0.5 K/min up to 250 °C (Fig. 3). The open-air nature of the holder inevitably results in convection and, thus, temperature fluctuations across the sample.<sup>14</sup> However, our tests indicate that this does not adversely affect the precision or stability of the system. Nonetheless, due to the design with the four-point measurement close to the heating element, the STEF-holder shows a  $\approx 9^\circ\text{C}$  higher temperature than at the sample, when measured against a calibrated thermocouple. This offset remained stable above 80 °C and decreased as the temperature was lowered toward ambient.

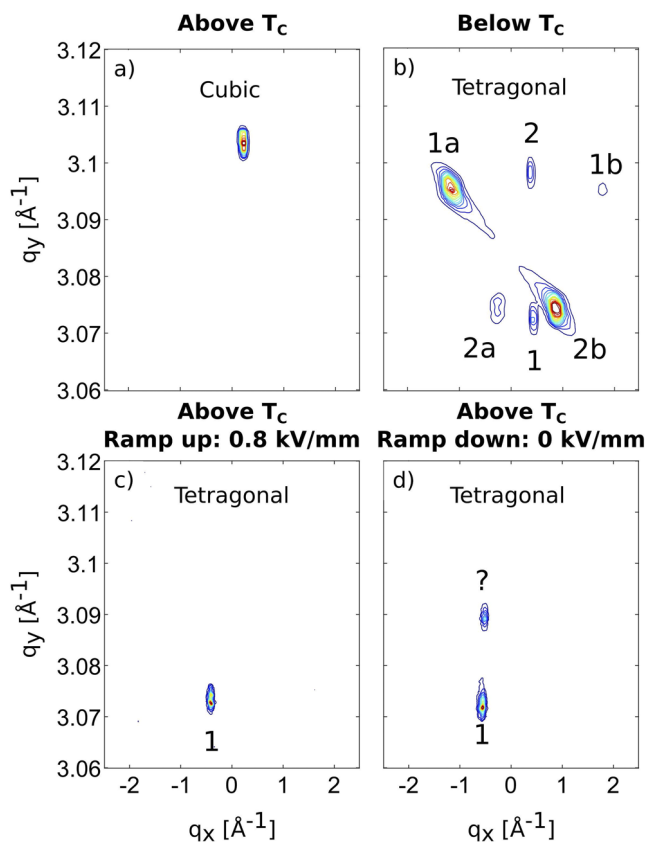
Many previous systems for applying electric fields *in situ* during x-ray measurements use a dielectric fluid (e.g., silicon oil) to prevent arcing around the sample.<sup>12</sup> However, this method was not used here in order to reduce complexity and avoid small-angle scattering and attenuation from the liquid, which will aberrate the image and reduce contrast.<sup>14</sup> Applying electric fields in air reduces the maximum applicable field; however, we note that the electrical breakdown field of air is 3 kV/mm, beyond the coercive fields of many common ferroelectric materials (e.g.,  $E_c$  for BaTiO<sub>3</sub> is 300 V/mm).<sup>16</sup> The electric field was applied via two hand painted silver electrodes ( $\sim 4 \times 4 \text{ mm}^2$  in size) on the opposing  $5 \times 5 \text{ mm}^2$  sides of the sample. A programmable DC power supply (Delta Electronica SM 120-13) was then used to create the electric field across the electrodes according to the user-defined voltage. For the samples used, the system had a nominal electric field precision of  $\delta E = 0.3 \text{ mV/mm}$ . Prior to use, an ohmmeter was used to ensure there were no short circuits and that electrical resistance was minimized wherever possible (e.g., across electrodes). We also note the importance of a closed circuit across the sample to prevent the accumulation of electrical charge at the sample surfaces during x-ray measurements, which may potentially affect the local depolarization field.<sup>17</sup>

Figure 4(a) illustrates that the STEF apparatus allows maintaining elevated temperatures while simultaneously ramping a field across the sample. It should be noted that we did not experience any electrical breakdown at the given fields. Furthermore, the temperature could be ramped to a set temperature with an undershoot of less than 0.01 K, as shown by the variance at the given set temperature (dotted line) in Fig. 4(b).

The aforementioned capabilities of the STEF apparatus are essential for the case study of phase transformations in BaTiO<sub>3</sub> discussed next. In comparison to a similar *in situ* system implemented on ceramic BaTiO<sub>3</sub>,<sup>12</sup> this system offers the ability to directly image the local perturbation and dynamics of the material system. The scope of this article is to demonstrate these claims and introduce the prospective analyses our system offers.



**FIG. 3.** (a) Voltage ramp at constant temperature; the temperature is a straight line since the variation is lower than the measuring accuracy of 0.005 K. (b) Ramping temperature to a stable set point at a low ramping rate. The PID controller gradually manages the temperature change so that no undershoot of the set temperature occurs when cooling or heating (not shown).



**FIG. 4.** Reciprocal space maps of the sample in the high temperature cubic phase at 150 °C and the tetragonal phase at room temperature, in (a) and (b), respectively. The different twin planes in the RSM below  $T_C$  at 80 °C are annotated with the number of the parent  $d$ -spacing<sup>1,2</sup> and the letter for the twin configuration [(a) and (b)], related to the domain interface it is a part of. [(c) and (d)] The RSM above  $T_C$  with the ramping field at maximum field and after the field removed, respectively. Note that the symmetry does not completely revert to cubic upon removal of the electric field. Instead, we observe the intermediate reflection marked by a question mark (?).

### Case study: Electric-field-induced phase transformations in BaTiO<sub>3</sub>

To demonstrate and explore the capabilities of the STEF apparatus, we used it to investigate electric-field-induced phase transformations in BaTiO<sub>3</sub>, a canonical ferroelectric. Electric field-induced phase transformations may yield large dielectric and piezoelectric response.<sup>18</sup> Notably, when heated just above the Curie temperature ( $T_C$ ), BaTiO<sub>3</sub> exhibits an electric-field-induced phase transition from cubic ( $Pm\bar{3}m$ ) to tetragonal ( $P4mm$ ) lattice symmetry. This makes it a model system for high strain lead-free piezoelectrics<sup>19</sup> and electrocalorics.<sup>20</sup> Several previous studies in BaTiO<sub>3</sub> and related systems have been carried out using *in situ* x-ray diffraction to extract the average structure and transformations pathways.<sup>21</sup> Our system provides the opportunity to image the dynamics of the *local* domain structure, phase distribution, and strain during these transformations.

Our experiment utilized the {200} Bragg reflection, as it shows clear splitting upon transition from the cubic and tetragonal lattice symmetries.<sup>7,12</sup> DFXM was used together with classical x-ray reciprocal space mapping. This provides both an overview of the average crystallographic changes occurring during the transformations (both thermally and electric-field-induced) and the local information of the strain and phase distribution within the crystal.

The BaTiO<sub>3</sub> single crystal was obtained commercially (Crystal GmbH, Germany) with initial dimensions of  $5 \times 5 \times 0.5 \text{ mm}^3$ . The sample was then attached to metal stub using a low-temperature adhesive wax. The mounted sample was surrounded by four pieces of 0.14 mm-thick glass to help ensure that the sample surfaces remained flat and parallel during grinding. The sample thickness was reduced by grinding using silicon carbide paper of grit No. 800, No. 1200, No. 2400, and No. 4000, with each step inspected by optical microscopy before progressing to the next. When the sample thickness measured  $0.15 \pm 0.01 \text{ mm}$ , the  $5 \times 5 \text{ mm}^2$  surfaces were polished with suspended silica particles of size  $0.04 \mu\text{m}$  (OPS, Struers A/S, Denmark). To relax the residual stresses induced during the grinding and polishing, the sample was thermally annealed in a box furnace. Specifically, the sample was heated at a rate of 1 K/min from 26 °C to 400 °C and held at 400 °C for 2 h before being cooled to room temperature at a rate of 1 K/min.

The DFXM experiment used an x-ray energy of 17 keV (energy bandwidth  $\Delta E/E$  of  $10^{-4}$ ). A Be-based 1D compound refractive lens created a line-beam on the sample  $\sim 400 \mu\text{m}$  wide and  $1 \mu\text{m}$  high, thus illuminating only a cross section of the BaTiO<sub>3</sub> sample. The objective comprised a 2D Be CRL with a focal length of  $\sim 250 \text{ mm}$ , resulting in a total geometrical magnification of  $19\times$ . Magnified 2D images of the illuminated cross section were collected with a FReLoN CCD camera, resulting in a final effective pixel size of 70 nm. The reciprocal space maps were measured with both the condenser and objective lens removed and using a large field-of-view detector comprising a CMOS camera (Basler Ace), a scintillator, and a wide-angle lens, yielding an effective pixel size of  $55 \mu\text{m}$ .<sup>6,9</sup>

The experiments were conducted as follows: sub- $T_C$  measurements were taken at 120 °C to confirm that the structure stayed tetragonal even at elevated temperatures. Initially, the temperature was elevated significantly above  $T_C$  to 150 °C to ensure complete transformation from tetragonal to cubic. Reciprocal space maps (RSMs) were also collected at these two temperatures. The sample then went through four heating and cooling cycles crossing  $T_C$  with each cycle to ensure that the thermal hysteresis normalized and that  $T_C$  occurs at a repeatable temperature. The sample was then cooled to a recorded 139.6 °C,  $\sim 1 \text{ K}$  above the measured  $T_C$  (which have slight fluctuations after normalization), and kept stable for several minutes to ensure that latent heat would not affect the measurements. At this point, a strain map was measured by rotating the sample  $\pm 0.05^\circ$  and  $2\theta$  range of  $\pm 0.06^\circ$ . Subsequently, a stepwise ramping of the electric field was applied across the sample. With the electric field still applied, another strain map was measured. The field ramped to 0.8 kV/mm in steps of  $j \times 0.038 \text{ kV/mm}$ , where  $j = (1, 2, 3, 4, 5, 6)$ .

### RESULTS

The RSMs in Figs. 4(a) and 4(b) show that we have a cubic phase above  $T_C$  and a tetragonal phase below  $T_C$ . The cubic phase

possesses a fourfold rotation symmetry around all three axes with equal lattice spacing. When aligning the single crystal to the (200) reflection, a single peak is observed, as seen in Fig. 4(a). The tetragonal phase only possesses a fourfold symmetry along the elongated axis, producing two unique lattice spacings. The domain formation, and hence the polarization orientation, produces the two main peaks, annotated as 1 and 2 in Fig. 4(b). Twinning along the domain walls gives rise to four new peaks (1a, 1b, 2a, and 2b), arising from the lattice distortion associated with the requirement for mechanical compatibility.<sup>1,22</sup> The tetragonal phase is characterized by its six different peaks, representing three crystallographic twins about 110-type lattice planes, seen in Fig. 4(b). The tails of the 1a and 2b peaks in Fig. 4(b) are due to strain associated with the domain wall. When applying the electrical field above  $T_C$ , the (200) peak associated with the cubic phase becomes extinct, and a single peak appears in the lower angle position (i.e., the same as position 1 in the zero-field tetragonal RSM). This indicates the absence of  $90^\circ$  domain walls, implying either the formation of either a monodomain or that only  $180^\circ$  domain walls exist in the diffracting volume of the sample.<sup>23</sup> In Fig. 4(d), it can be seen that removing the electric field

from the sample did not return the sample back to the original cubic phase, as two diffraction spots appear in the RSM. This indicates that the electric-field-induced cubic-to-tetragonal phase transition is irreversible at this temperature.<sup>15</sup> The peak indicated with “?” does not correspond to any of the reflections seen in Fig. 4(b). However, it has a higher  $q_y$  value, indicating lower  $d$ -spacing. We speculate that the polarization and, thus, the spontaneous strain might have diminished in some part of the crystal after the field was removed. The RSM method probes the average structure of the illuminated region and does not provide information about the local environment in real space. This establishes a clear need for carrying out microscopic investigations of the dynamic behavior of these phenomena.

To this end, Fig. 5(a) shows a DFXM image of the microstructure of the BaTiO<sub>3</sub> sample in the cubic phase prior to the application of the electric field. The indicated temperature is 139.6 °C, with the  $T_C$  at 138.5 °C. Although the RSM did not show any indication of tetragonal phase above  $T_C$ , heterogeneous structures are clearly evident in the DFXM images. Furthermore, the wavy, fringe-like features in the images are uncharacteristic of the domain structures

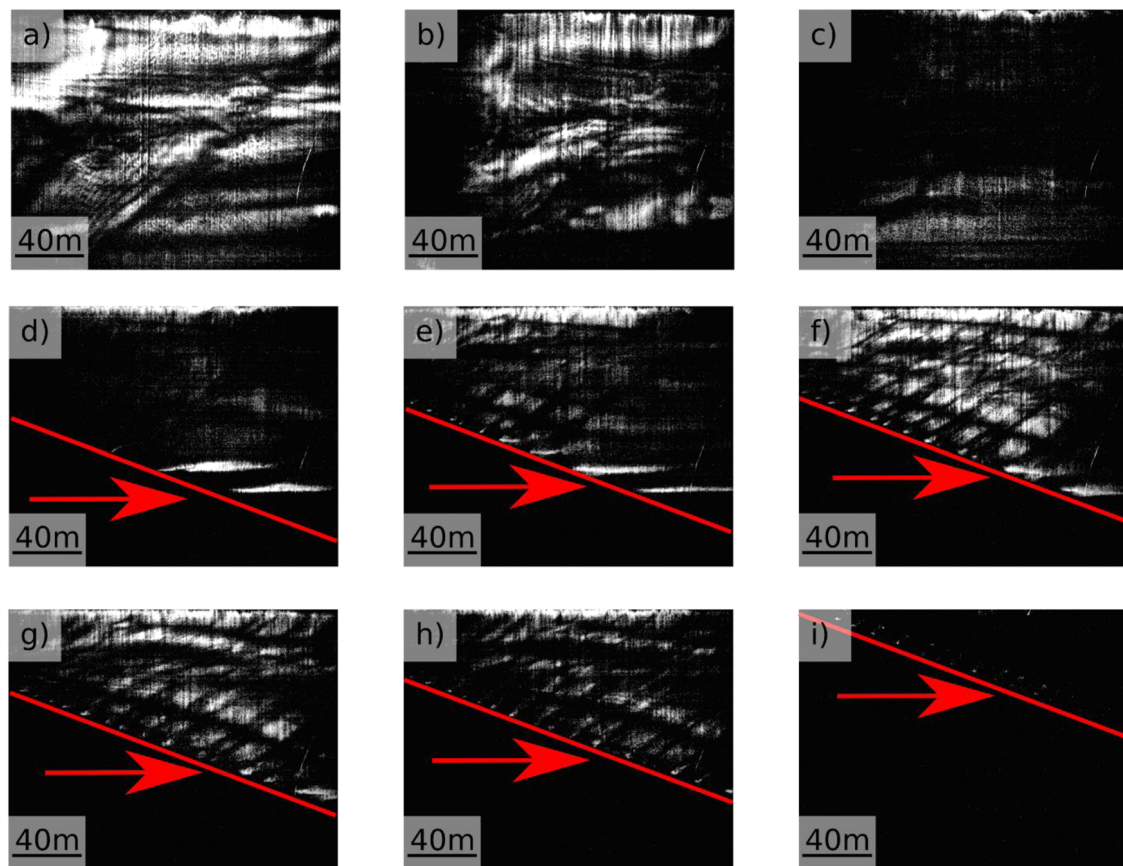


**FIG. 5.** Contrast in figure is scattered intensity: (a) the initial state of the sample before any field is applied above  $T_C$ . The illuminated slice of the sample shows several wavy bands, which are not related to domains structures. [(b)–(h)] The partial illuminated slice shows the phase front propagating through the sample and (i) showing the almost finished transformation, with only a small fraction of the cubic phase remaining in the upper right corner.

normally seen in the tetragonal phase of  $\text{BaTiO}_3$ .<sup>24</sup> These structures could be related to local lattice strains and misorientations due to dislocations, crystal growth defects, or accumulations of atomic defects.<sup>25</sup> We note that these features were observed to remain very stable over time, even close to  $T_C$ . The image stability is taken to indicate very high thermal stability of the system, as even subtle changes (e.g., strains less than  $10^{-4}$ ) in lattice strain/orientation would be readily detectable in the DFXM image.

The images shown in Fig. 5 are taken from a dataset of 422 images, acquired while ramping the field to 0.8 kV/mm. Slow ramping of the electrical field changed these heterogeneous wavy structures considerably, even at very low electric fields of 0.02 kV/mm. The cubic-to-tetragonal phase transition occurred when the field reached a critical value of 0.4 kV/mm, identified by a sudden drop in intensity accompanied by changing wavy patterns in Fig. 5(b). Since we were imaging the cubic peak, the intensity reduces further in Fig. 5(c) as the transition continues. In the sequence of images from Figs. 5(d)–5(i), a phase front propagates through the sample from the left-hand side, diagonally toward the upper right corner of the image. The phase front propagates through the field of view, until no more intensity from the cubic phase can be observed (not showing the final, completely dark image). During this propagation, the structure inside the illuminated area changes its internal structure, with  $45^\circ$  domain-like structures appearing at the cubic side of the phase front. The periodic pattern could potentially be a lattice distortion or intermediate phase or structure, as suggested in previous studies.<sup>24</sup> We note that the wavy, fringe-like features present in the cubic phase remain clearly visible throughout the phase transformation.

It is not readily possible to quantitatively characterize the distortions created by defects or interfaces with single-exposure images such as those in Fig. 5. However, such dynamically acquired image sequences can be an excellent means to characterize the dynamics of topological features, such as domain wall motion, domain growth, domain density, and phase front speed.<sup>7</sup>

Quantitative characterization of these defects requires maps of strain and misorientation, which can be achieved by acquiring several images at different  $2\theta$  angles of the objective-detector arm. At present, such scans are time-consuming and, therefore, not suitable for dynamic studies of processes occurring within seconds or less.<sup>6,7</sup> Nonetheless, strain maps acquired before and after the transformation provide unique insight into the underlying defect structure inside the reached state. By observing the strain map in Fig. 6(a), taken above  $T_C$  with zero applied field, wavy patterns similar to those seen in Fig. 5(a) are clearly visible. Since they are measured under the same conditions, it seems reasonable to attribute both patterns to local lattice distortions. Figure 6(b) shows a similar strain map, acquired with the same experimental parameters but now under a field of 0.8 kV/mm. The difference in strain is clear, with some of the wavy features weakly present in the map. The large change in strain is a strong indication of the phase transformation that has been observed with RSMs and in DFXM image series. The changes in strain along the wavy patterns and sample interphase at the surface are clear and can potentially be attributed to the alignment of misorientations with the electric field and compressive strains at the surface induced by the electric field.<sup>26</sup>

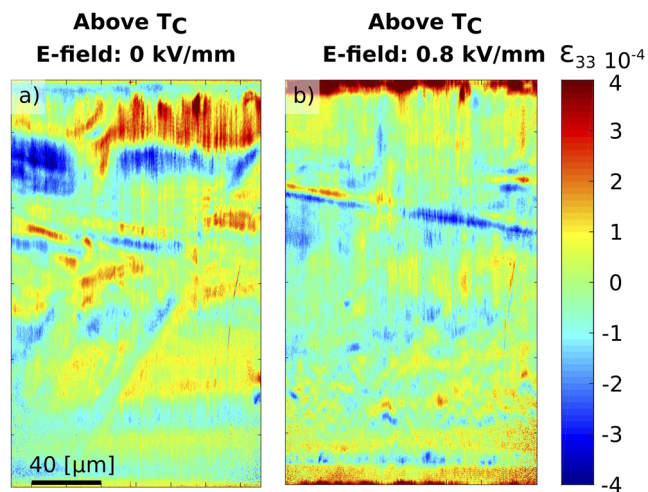


FIG. 6. (a) The strain map above  $T_C$  at zero field and (b) the strain map above  $T_C$  with an applied field of 0.8 kV/mm.

## SUMMARY AND CONCLUSIONS

The sample environment system we describe has demonstrated the ability to acquire diffraction, time-dependent, and strain-dependent datasets in a single experimental setting. Moreover, experiments can be carried out in bulk samples under highly controlled thermal and electrical boundary conditions. Ultimately, this makes it possible to detect bulk dynamics in real time. Phase fronts, domain walls, and other features can be detected and tracked with the DFXM mode, and the associated strain from the transformations can be characterized. The thermal stability of the system has proven to be of high importance, and STEF has been shown to possess the capability of temperature control of  $\Delta T = \pm 0.01$  K in the 20–250 °C range. At the same time, we have applied fields at least up to 0.8 kV/mm without short-circuiting. This makes it a very versatile holder system, which can be used for many thermal and electroactive materials.

The possibility to probe different elements of thermodynamic parameter space could make it a tool for improving and validating phase-field and other thermodynamic models. While Landau–Ginsburg–Devonshire (LGD) theory<sup>27</sup> predicts phase transformations similar to what we have shown here, it is strongly dependent on the accuracy of the material data it uses and the assumptions it makes regarding symmetry and the presence of local heterogeneity. Thus, providing LGD models with quantitative data under specific thermal and/or electrical boundary conditions could provide a more precise prediction of material properties and behavior using LGD-type approaches. Furthermore, such theories may provide further insight into how domain and phase fronts might be propagated in directions non-parallel to the electric field.<sup>28</sup>

The natural evolution for the STEF system presented here would be to implement computer vision methods of tracking topological features and classifying datasets.<sup>29</sup> We foresee that this will lead to the development of either machine or deep-learning based methods that can be integrated with this or similar *in situ* systems.

This could lead to a much more profound method of studying materials and create a new type of synergy between theoretical models and experiments.

## ACKNOWLEDGMENTS

The authors are grateful for beam times and the use of the facilities at the ESRF. The authors are particularly grateful for the help from the machine workshops at DTU Physics, NTNU Gløshaugen, and sample environment team at ESRF. They thank Julia Glaum for providing them with excellent samples for their beam time. They specially thank Julian Walker for motivational discussions. They also thank DANSCATT for support of travels. H.S. acknowledges support from ERC Starting Grant No. 804665 “3D-PXM.”

## REFERENCES

- <sup>1</sup>A. K. Tagantsev, L. E. Cross, and J. Fousek, *Domains in Ferroic Crystals and Thin Films* (Springer Science, 2010).
- <sup>2</sup>S. V. Kalinin, S. Jesse, B. J. Rodriguez, Y. H. Chu, R. Ramesh, E. A. Eliseev, and A. N. Morozovska, *Phys. Rev. Lett.* **100**, 155703 (2008).
- <sup>3</sup>D. M. Marincel, H. Zhang, A. Kumar, S. Jesse, S. V. Kalinin, W. M. Rainforth, I. M. Reaney, C. A. Randall, and S. Trolrier-McKinstry, *Adv. Funct. Mater.* **24**, 1409–1417 (2014).
- <sup>4</sup>M.-W. Chu, I. Szafraniak, D. Hesse, M. Alexe, and U. Gösele, *Phys. Rev. B* **72**, 174112 (2005).
- <sup>5</sup>Y. A. Genenko, S. Zhukov, S. V. Yampolskii, J. Schütrumpf, R. Dittmer, W. Jo, H. Kungl, M. J. Hoffmann, and H. von Seggern, *Adv. Funct. Mater.* **22**, 2058 (2012).
- <sup>6</sup>H. Simons, A. C. Jakobsen, S. R. Ahl, C. Detlefs, and H. F. Poulsen, *MRS Bull.* **41**, 454 (2016).
- <sup>7</sup>H. Simons, A. B. Haugen, A. C. Jakobsen, S. Schmidt, F. Stöhr, M. Majkut, C. Detlefs, J. E. Daniels, D. Damjanovic, and H. F. Poulsen, *Nat. Mater.* **17**, 814 (2018).
- <sup>8</sup>H. F. Poulsen, P. K. Cook, H. Leemreize, A. F. Pedersen, C. Yildirim, M. Kutsal, A. C. Jakobsen, J. X. Trujillo, J. Ormstrup, and C. Detlefs, *J. Appl. Crystallogr.* **51**, 1428 (2018).
- <sup>9</sup>H. F. Poulsen, A. C. Jakobsen, H. Simons, S. R. Ahl, P. K. Cook, and C. Detlefs, *J. Appl. Crystallogr.* **50**, 1441 (2017).
- <sup>10</sup>A. F. Pedersen, V. Chamard, C. Detlefs, T. Zhou, D. Carbone, and H. F. Poulsen, *Phys. Rev. Lett.* (submitted).
- <sup>11</sup>N. Mavrikakis, C. Detlefs, P. K. Cook, M. Kutsal, A. P. C. Campos, M. Gauvin, P. R. Calvillo, W. Saikaly, R. Hubert, H. F. Poulsen, A. Vaugeois, H. Zapolsky, D. Mangelinck, M. Dumont, and C. Yildirim, *Acta Mater.* **174**, 92 (2019).
- <sup>12</sup>Z. Wang, K. G. Webber, J. M. Hudspeth, M. Hinterstein, and J. E. Daniels, *Appl. Phys. Lett.* **105**, 161903 (2014).
- <sup>13</sup>P. Nath and K. L. Chopra, *Thin Solid Films* **20**, 53 (1974).
- <sup>14</sup>J. Walker, H. Simons, D. O. Alikin, A. P. Turygin, V. Y. Shur, A. L. Kholkin, H. Ursic, A. Bencan, B. Malic, V. Nagarajan, and T. Rojac, *Sci. Rep.* **6**, 19630 (2016).
- <sup>15</sup>L.-M. Zhang, C. Jahns, B. S. Hsiao, and B. Chu, *J. Colloid Interface Sci.* **266**, 339–345 (2003).
- <sup>16</sup>P. Glogar and V. Janovec, *Czech. J. Phys.* **13**, 261 (1963).
- <sup>17</sup>S. Kumar, M. Sharma, S. Powar, E. N. Kabachkov, and R. Vaish, *J. Eur. Ceram. Soc.* **39**, 2915 (2019).
- <sup>18</sup>J. Rödel, K. G. Webber, R. Dittmer, W. Jo, M. Kimura, and D. Damjanovic, *J. Eur. Ceram. Soc.* **35**, 1659 (2015).
- <sup>19</sup>R. Dittmer, K. G. Webber, E. Aulbach, W. Jo, X. Tan, and J. Rödel, *Acta Mater.* **61**, 1350 (2013).
- <sup>20</sup>H. Zhang, W. Jo, K. Wang, and K. G. Webber, *Ceram. Int.* **40**, 4759 (2014).
- <sup>21</sup>J. E. Daniels, G. Picht, S. Kimber, and K. G. Webber, *Appl. Phys. Lett.* **103**, 122902 (2013).
- <sup>22</sup>E. V. Østergaard, “The thermal and electric field stability of square-net domain patterns in barium titanate” (unpublished).
- <sup>23</sup>A. S. Everhardt, S. Matzen, N. Domingo, G. Catalan, and B. Noheda, *Adv. Electron. Mater.* **2**, 214 (2016).
- <sup>24</sup>T. T. A. Lummen, Y. Gu, J. Wang, S. Lei, F. Xue, A. Kumar, A. T. Barnes, E. Barnes, S. Denev, A. Belianinov, M. Holt, A. N. Morozovska, S. V. Kalinin, L. Chen, and V. Gopalan, *Nat. Commun.* **5**, 3172 (2014).
- <sup>25</sup>B. M. Park, S. J. Chung, H. S. Kim, W. Si, and M. Dudley, *Philos. Mag. A* **75**(3), 611 (1997).
- <sup>26</sup>B. Matthias and A. von Hippel, *Phys. Rev.* **73**, 1378 (1948).
- <sup>27</sup>A. F. Devonshire, *Adv. Phys.* **3**, 85 (1954).
- <sup>28</sup>D. Damjanovic, *Rep. Prog. Phys.* **61**, 1267 (1998).
- <sup>29</sup>J. Madsen, P. Liu, J. Kling, J. B. Wagner, T. W. Hansen, O. Winther, and J. Schiøtz, *Adv. Theory Simul.* **1**, 1800037 (2018).

### 4.3 Discussion and implications of the STEF-holder

The holder system presented in chapter 4 is the fourth generation of that system. It has shown excellent temperature control and multi-instrument integration options as demonstrated with both DXFM and polarized light microscopy (PLM), seen in section 4.2 and A.1, respectively. Here I will discuss some of the detailed points for potential improvements of the holder system, with respect to achieving more accurate control of the sample environment and, ultimately, higher quality data.

Arguably the most important feature of the STEF holder is the stable temperature it can produce and maintain with a high degree of precision. Furthermore, it can simultaneously apply an electric field to the sample, allowing the investigation of multiple parameters and their combined effect on the material system. It is worth mentioning, however, that the current generation of the holder system is not capable to applying controlled temperature gradients. This is mainly due to the single heating source configuration and control. Regulating and controlling a temperature gradient across the sample is not possible in the present design, which is limited to stable measurements at a constant temperature. I believe that this limitation can be overcome by implementing multiple heat sources and temperature measuring elements into the design. Such changes would open up more temperature modes and interaction settings that could be measured, allowing for further investigations of structural dynamics in solid materials.

Further development of the method for applying electrical contacts to the sample could help improve the difficult task of ensuring good contact without short circuiting the system. Building in conductive electrodes to the surface of the sample (e.g. by sputtering) would avoid the error-prone step of hand-painting silver paint onto the electrodes. For X-ray experiments, applying the silver layer for contacting doesn't significantly complicate matters if evenly distributed across the sample. However, it has been understandably problematic for integration with optical imaging systems, since the silver paint is optically opaque, and creates a temperature gradient in the sample. This gradient then creates different phase transformation point across the sample, which have been demonstrated in the related work by E. V. Østergaard, see appendix A.1. Here, the sample was sputtered with a layer of ITO to act as transparent surface electrodes. However, even with transparent electrodes we needed silver paint to create a proper contact to the electric circuit. If the STEF holder had a *built-in* contacting mechanism, this strong temperature gradient could be avoided.

For now, the fourth generation of the STEF holder can reliably generate stable ramping and static temperature while applying electric fields. Originally designed for DXFM studies, the holder has the capability to be utilized for optical microscopy as well. This has allowed several studies of bulk morphological features and dynamics in BaTiO<sub>3</sub> not previously possible.

With the STEF holder, we have successfully collected data that clearly visualizes the electrical field induced phase transformation at elevated temperatures, and the strain maps before and after this process. With the results described in the STEF holder paper, section 4.2, we can claim to have seen changes to the local bulk morphology during an electrical field induced phase transformation.

The intensity images of the phase transformation and strain maps together prove that we have developed a method for gaining information about local structural changes in bulk materials. Structural features observed in the initial intensity image are also qualitatively present in the strain map of the initial state of the sample. By proving these capabilities, we address the second point in the hypothesis, in which I state that no technique capable of this has existed so far.

## 5 The interaction between defects and domain walls

In this chapter, the interactions between defects and domains configurations are studied at elevated temperatures to ascertain the persistence of defects and their impact on structure in the absence of polarization and other driving forces for domain formation. Previous studies have found that surface layers can exhibit imprints by dipole defects of the ferroelectric state well above  $T_C$  [50], or tetragonal distortions stabilized by ionic species relaxing the surface [31]. Even though these defect mechanisms could predict bulk imprints and LGD based models have shown defect agglomerations along  $90^\circ$  domain walls [21], it remains to be experimentally verified. Here I present the relevant theory and our observations on the bulk behavior above  $T_C$ . Our observation with DFXM indicates ferroelastic domains with a high degree of curvature and local strain sufficient to raise  $T_C$  tens of  $^\circ\text{K}$  in bulk  $\text{BaTiO}_3$ . I believe this is the first direct observation of domain imprint in the bulk.

### 5.1 Domain wall imprinting

Difference between the surface and bulk structures of ferroelectrics is not a new phenomenon, and has been known since Merz's first experiments [24] (and potentially before). Various mechanisms play a role in determining structure and functional behaviour at the surfaces [27]. Strain-related mechanisms seem to be the primary driving force behind imprinting polar phases and keeping them stable across a larger-than-normal temperature range [50][31][17][51].

One of the suggested mechanisms for stabilizing structural distortions at the surface is the upwards movement of anions, which would stabilize the out-of-plane polarization observed above  $T_C$  [31]. It is worth noting, however, that oxygen vacancies at the surface can have a similar effect and produce surface polarization above  $T_C$ , induced by the strain field and subsequent tetragonal distortion [50]. Recent studies have suggested that dagger domains, pinned to the surface and extending tens of nm into the materials, persist above  $T_C$ , which would stabilize the ferroelectric phase at the surface [50]. This effect is claimed to preserve the bulk ferroelectric state up to  $150^\circ\text{K}$  above  $T_C$ .

Regarding the influence of the surface structure on the bulk state, things might not be as simple as presented by Mathieu [50]. Evidence of this is shown in figure 5.1. The figure shows DFXM intensity images taken in transmission mode of the tetragonal ferroelectric phase (crystallographic reflection (200)) from a single crystal of  $\text{BaTiO}_3$  at room temperature. Figure 5.1a shows a cross-section through the material, with clear evidence of the tetragonal structure in both surface and bulk. However it can also be seen that the surface exhibits distortions to this structure that are not seen in the bulk. This fact is even more clear in figure 5.1b, where the sample is rotated off the optimum Bragg angle for the bulk. Here only the surface features satisfy the Bragg condition, indicating they have a different structural state (strain or orientation) to the bulk.

The surface distortions could be created by the mechanisms presented by Höfer and Mathieu [31][50], though our measurements suggest they might be longer-ranging than they predict. Figure 5.1c shows a different sample in a heating experiment, where the sample was heated through  $T_C$  and the domain structure in this is more visible as a likely

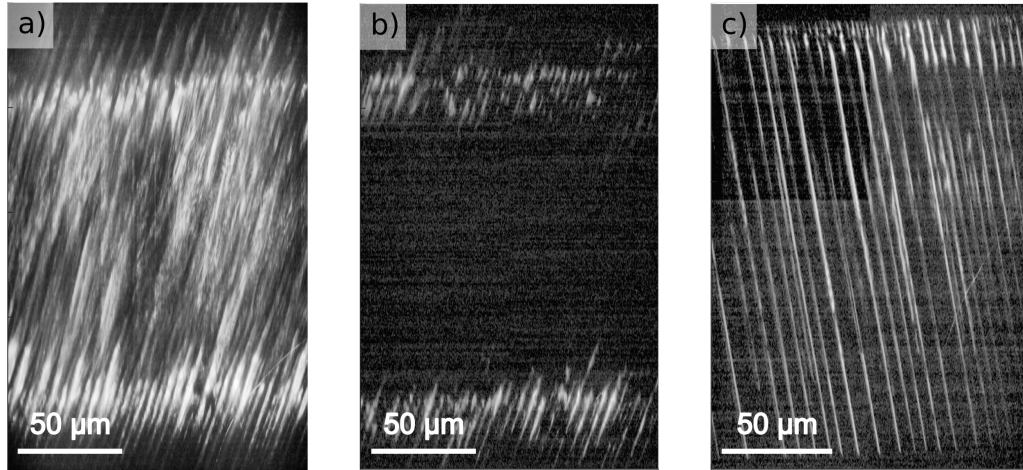


Figure 5.1: The figure shows DFXM intensity images of single crystal BaTiO<sub>3</sub>. The cross section depicts the front and back of the sample, on the bottom and top of each images, respectively. a) is taken from the optimal Bragg angle, while b) is taken with a light sample tilt of the optimal Bragg angle. c) shows a different sample at optimal Bragg angle, approximately 1 °K from T<sub>C</sub>.

result of additional steps taken in the sample preparation stage. The surface layer, however, is still distorted and is clearly observed when crossing T<sub>C</sub>. This underlines that structure in the surface layers can't convey the structural state in the bulk, as otherwise claimed [31][50]. Moreover, the thin dead-layer or inversion layer discussed in the two earlier papers, shouldn't extend several microns into the material, which is observed in figure 5.1a, b and c. Considering these observation of deeply penetrating surface features, it can be said that the physical understanding needs to be expanded. Specifically, the causality for domain formation and strain above T<sub>C</sub>, which can be experimentally studied in bulk single crystals using DFXM.

The influence of defects on lattice structures is obviously not limited to the surface, since majority of defects usually exist in the bulk. Simulations of the local environment in bulk BaTiO<sub>3</sub> and the interplay between domain walls and oxygen vacancy defects, have been achieved via LDG-based phase field models [21]. The 90° domain walls in BaTiO<sub>3</sub> exhibits an asymmetric charge distribution arising from the difference in  $\mathbf{P}_s$ , which results in a potential drop across the domain wall. The simulation shows agglomerations of electrons and oxygen vacancies on apposing side of a 90° domain wall, as a consequence. An important note about this research, however, is that the diffusion coefficients for oxygen vacancies were modified to allow for faster convergence. This implies the final output of the model was after the diffusion process was completed. This is arguably fine, and may also explain why we don't see strong experimental evidence of this in virgin samples with great regularity. Nonetheless, it clearly points out the fact that oxygen vacancies and charge carriers will be drifting towards distortions with an associated change in potential, thus, forming regions with higher density of opposite charge.

As discussed in chapter 2, the injection of charged defects along domain walls can pin them, retarding the switching of polarization, or augmenting polarization [12][23]. Large strain and recoverable strain from an electric field induced switching process have also been attributed to defects stabilizing the domain structure [14]. This occurs upon cooling a single crystal through T<sub>C</sub> and subsequent aging at 80°C, where after the defects will distribute such that they have an effective polarization aligned with the  $\mathbf{P}_s$ , as suggested by X.

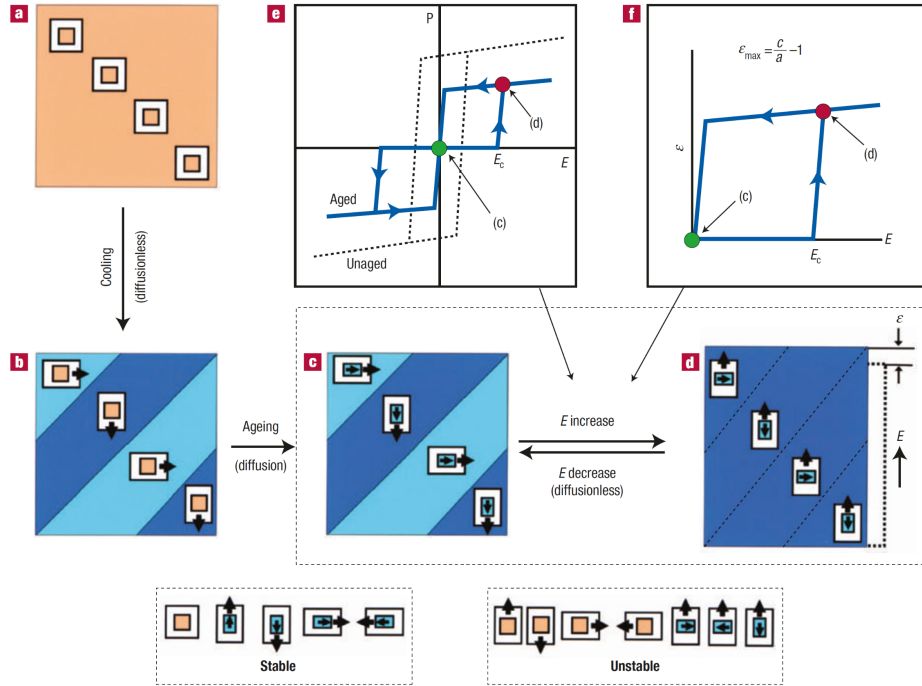


Figure 5.2: Mechanism of large electro-strain effect by reversible domain switching in aged ferroelectrics due to the symmetry-conforming property of point defects. a), Equilibrium cubic paraelectric crystal. b), Multi-domain tetragonal ferroelectric crystal immediately after the cubic-to-tetragonal transition, in which defects are unstable. c), Stable state after ageing (diffusion) in the ferroelectric state, in which defect symmetry follows crystal symmetry in every domain. d), Unstable state after domain switching from c by electric field  $E$ . e), Double hysteresis loop ( $P$ – $E$  curve) during reversible domain switching between c and d, which contrasts the normal hysteresis loop (dotted loop). f), Huge recoverable strain ( $\epsilon$ – $E$  curve) during reversible domain switching between c and d. See Fig. 1 for definitions of the squares, rectangles and arrows. Stable states are those where the defect symmetry matches the crystal symmetry; unstable states are those where they do not match. [14]

Ren [14] This is due to the diffusion of defects which, driven by the polar direction, bias the distribution of defects. Since the diffusion direction of charge defects can be influenced by a field [52], this seems like a reasonable claim. The macroscopic consequence of this process is a double hysteresis loop with a large recoverable strain in both polarization directions. When defect dipole stabilised domains experiences a electric-field-induced switching of  $\mathbf{P}_s$ , it occurs abruptly and without diffusion. Hence, no migration of defects happens and the defect dipole orientation and domain recovering driving force stays intact. This initial structure is also shown to be recoverable over multiple cycles, allowing it to retain a large recoverable strain throughout [14][15]. This essentially shows that ageing, a diffusion effect, can lock morphological features into materials via an interaction between vacancies and domain walls.

In ferroelectrics such a  $\text{BaTiO}_3$ , it has been shown that heterogeneities can exist well above  $T_C$  and might be the precursor for the domain formation while cooling it through  $T_C$  [31][35]. In particular, dislocations with long-ranging distortions and strain fields may ef-

fectively shift the Curie temperature [51]. It can be said that all defects and heterogeneities might have similar effects, though the difference in magnitude of the strains they generate must be taken into account. Predicting domain nucleation from long-range defects and heterogeneities, has yet to be demonstrated with a large degree confidence. To show we have moved past previous inabilities to study structural distortion locally above the Curie temperature, I here present our paper in which we measure vacancy-induced distortions above  $T_C$  and their potential role in imprinting domain-like features.

## 5.2 Paper 3: Bulk heterogeneity in barium titanate above the Curie temperature

*The following paper discusses the potential for the thermally-activated arrangement of heterogeneities and its implication for imprinting domain-like features in the microstructure above  $T_C$ . It utilizes data in the form of DFXM images, high resolution RSMs, lattice tilt maps and local RSMs extracted from the strain/mosaicity map. The sample is a single crystal of  $\text{BaTiO}_3$  heated to the  $150^\circ\text{C}$  and, while heated for an extended period, it showed the domain like features at the core of this study. Such features or imprints of domains above  $T_C$  have been observed before, however the features we observe possess a large curvature at their boundaries, which can't be explained by the previous work. The high resolution RSMs in this work also reveal a much more complex structure of lattice spacing, and shows a clear separation of d-spacing from the average bulk. This is further confirmed by analysing local RSM's on either side of one of the curved barriers separating the domain like features. This shows a clear shift in crystal structure across the barrier, along with a lattice tilt of  $0.01\text{-}0.02^\circ$ . We suspect that agglomeration of oxygen vacancies due to an aging process, which causes the vacancies to diffuse towards regions with higher affinity. The curvature of long-range strain fields are believed to be the reasoning behind the curved boundaries of the features we observed. The strain from these would be sufficient to increase  $T_C$  by a few  $^\circ\text{K}$ , suggesting the impurities pinning and imprinting domains patterns have an effect that is not limited to the surface, but permeates into the bulk.*

## Bulk heterogeneity in barium titanate above the Curie temperature

Jeppe Ormstrup<sup>1</sup>, Emil V. Østergaard<sup>1</sup>, Magnus S. Christensen<sup>3</sup>, Can Yildirim<sup>2, 4</sup>, Philip K. Cook<sup>2</sup>, Mustafacan Kutsal<sup>1, 2</sup>, Thomas Olsen<sup>1</sup>, Hugh Simons<sup>1</sup>

<sup>1</sup>. Department of Physics, Technical University of Denmark, 2800 Kgs. Lyngby, Denmark

<sup>2</sup>. ESRF – The European Synchrotron, Avenue des Martyrs, 38000 Grenoble, France

<sup>3</sup>. Department of Physics, Norwegian University of Science and Technology, 7491 Trondheim, Norway

<sup>4</sup>. OCAS, Pres. J.F. Kennedylaan 3, BE-9060 Zelzate, Belgium

**Using dark-field x-ray microscopy, we reveal subtle structural heterogeneity in BaTiO<sub>3</sub> single crystals at temperatures of 150°C – well above the Curie temperature of 125°C. Remarkably, the heterogeneity exhibits domain-like ordering on the scale of several micrometers and a preference for 110-type lattice directions. Complementary high-resolution x-ray reciprocal space measurements suggest that the features originate from point defects (most likely oxygen vacancies) that coalesce along pre-existing domain walls during the aging process. A simple thermodynamic model suggests that the weak elastic strains associated with the heterogeneity are likely to locally raise the Curie temperature in their vicinity, creating nucleation sites for the ferroelectric phase upon cooling through the ferroelectric phase transition.**

Structural heterogeneity is crucial to many of the macroscopic functional properties of ferroelectric materials. Local variations to the lattice can have marked effects on local polarization [1, 2] and electronic structure [3], as well as serving as pinning centers for mobile interfaces [3,4] or nucleation sites for new phases [3]. In complex oxide ferroelectrics, the typical sources of structural heterogeneity range from oxygen vacancies, dislocations, domain walls, interphase and grain boundaries, and inclusions and pores. These defects and their associated electric and elastic fields create lattice distortions at nearly every relevant length scale, from the atomic to the scale of entire grains (and potentially beyond) [5,6]. Correspondingly, defects have the potential to influence – and even define – the macroscopic functionality of ferroelectric materials and devices. For example, the dynamic formation and distribution of vacancy dipoles can enhance the recoverable energy density and strain via domain wall pinning [7,8] and, at larger scales, homo-interfaces such as domain walls are rapidly demonstrating the potential for digital memory storage in nanoelectronics [9-11]. On the other hand, defects such as vacancies and domain walls may also give rise to electrical conductivity [12], while the stability and mobility of domain patterns can be unpredictably and catastrophically affected by long-range clamping strains from grain boundaries and dislocations. Whether such heterogeneities improve or diminish the final macroscopic properties of a ferroelectric material depends entirely on the complex interplay between the type of defects present, their interactions, and their distribution.

Heterogeneity is also believed to be critical to the phase transition between the paraelectric and ferroelectric states, where the electric and elastic fields created by defects influence the nucleation and growth of domains, and can significantly affect the resulting domain morphology [13]. Even in relatively “pure” ferroelectrics, such as BaTiO<sub>3</sub>, polar heterogeneity can be inferred from dielectric spectroscopy and x-ray scattering measurements well above the Curie temperature ( $T_C$ ) [14]. While it is speculated, this may seed the formation of polar domains at the transition, it has not been directly observed. It is also likely domains nucleate from defects with long-ranging strain fields, such as dislocations [15]. Reliably predicting nucleation from such long-ranging heterogeneities, however, is a significant challenge, requiring a coherent simulation framework that spans multiple length scales. Such models require either an exceptionally large grid size (which is computationally intensive) [16], or an amalgamation of different models (which is complex and seldom robust) [17]. Furthermore, multi-scale data does not exist for guiding and validating such multi-scale models. As such,

the role of structural heterogeneity is not typically accounted for in many theoretical and simulated treatments of phase transitions in ferroelectrics.

To date, experimental investigations into the role of defects in the ferroelectric phase transition have been limited to either individual length scales or the surfaces of samples. For example, surface imaging techniques, such as second harmonic generation (SHG) microscopy [13], piezoresponse force microscope (PFM) [13,18], scanning x-ray diffraction microscopy [13] and x-ray photoelectron emission microscopy (X-PEEM) [18] are prevalent for studying the morphology and structure of the emerging ferroelectric phase. However, the biaxial strain state at the surfaces of samples means the measurements of both the defects and the phase transition itself may not be representative of the bulk material. Macroscopic properties and average structural measurements, such as of the large-signal polarization and strain hysteresis [19] and the dielectric response [19], provide direct insight into the functional and property changes associated with the phase transition, while high-energy powder x-ray diffraction provides a direct correlation with structural change [5,6,13]. Though sensitive to the bulk material, such macroscopic and average measurements cannot correlate the transition and morphology to specific defects and their local vicinity. Ultimately, we require the ability to visualize the structure and morphology *in situ* around individual embedded defects during the ferroelectric phase transition.

Dark field x-ray microscopy (DFXM) can probe a defined volume in a bulk material, where both the elastic distortions around individual defects and the nucleating domains can be imaged directly and in real-time during heating, cooling or the application of electric fields [5,6, 20]. In this paper, we report the presence of extremely subtle, ordered microscale structures in BaTiO<sub>3</sub> single crystals at temperatures well above T<sub>c</sub>. Based on both DFXM images and high-resolution x-ray reciprocal space maps (RSMs), we show that the structures likely originate from the agglomeration of point defects around pre-existing domain walls. Using a thermodynamic approach, we speculate that the lattice distortions associated with these structures act as nucleation centers for domains and domain walls, presumably resulting in the repeatability of the domain structure upon successive heating and cooling cycles.

Single crystals of BaTiO<sub>3</sub> were purchased commercially (Crystal GmbH, Germany) with dimensions of 5 × 5 × 0.5 mm, and ground and polished to a final thickness of 0.15 mm. To remove any residual strains imparted during polishing, the crystals were subsequently annealed at 400°C for two hours with a heating and a cooling rate of 1 °K/min. Silver electrodes were hand-painted onto the opposing 5 × 5 mm faces, with approximate dimensions of 4 × 4 mm. In addition to allowing the application of electric fields to the sample, the silver electrodes also act as a charge sink to avoid charge build-up during the synchrotron x-ray experiments.

The experiments were carried out at the hard x-ray microscope located on beamline ID06 at the European Synchrotron Radiation Facility (ESRF). The sample was mounted using a prototype sample environment [21], and heated using a hot gas blower (Cyberstar, France). A photon energy of 17 keV (dE/E = 10 eV) was used such that the crystal could be imaged in transmission geometry through the 0.15 mm direction with an attenuation of approximately 75%. The 200 Bragg reflection was used for both the DFXM and RSM measurements, at a scattering angle of  $2\theta \approx 20.92^\circ$ . The measurements sampled a 400 × 0.5 μm section through the sample, generated using line-profile illumination from a one-dimensionally-focusing compound refractive lens (CRL) positioned 500 mm upstream of the sample. In DFXM mode, an objective CRL with a 250 mm focal length was placed between the sample and CCD-based x-ray imaging deflector, along the path of the 200 Bragg reflection. This resulted in a geometrical magnification of 19× and a nominal spatial resolution of 70 and 183 nm/pixel in the horizontal and vertical directions, respectively. Acquiring images while scanning the tilt

of the sample around the two axes orthogonal to the scattering vector then permitted the reconstruction of quantitative maps of the local lattice misorientation within the selected scattering volume.

Figure 1 shows DFXM intensity images obtained at room temperature (a) and at 150°C (b) – approximately 25°C above the  $T_C$  for BaTiO<sub>3</sub>. The room temperature image shows the clear stripe-like contrast one would expect from a ferroelastic single crystal with domains along 110 lattice planes. This corresponds well with both previous DFXM images of BaTiO<sub>3</sub> using the 200/002 reflection [5,6], as well as images obtained using comparable techniques, such as electron microscopy [22].

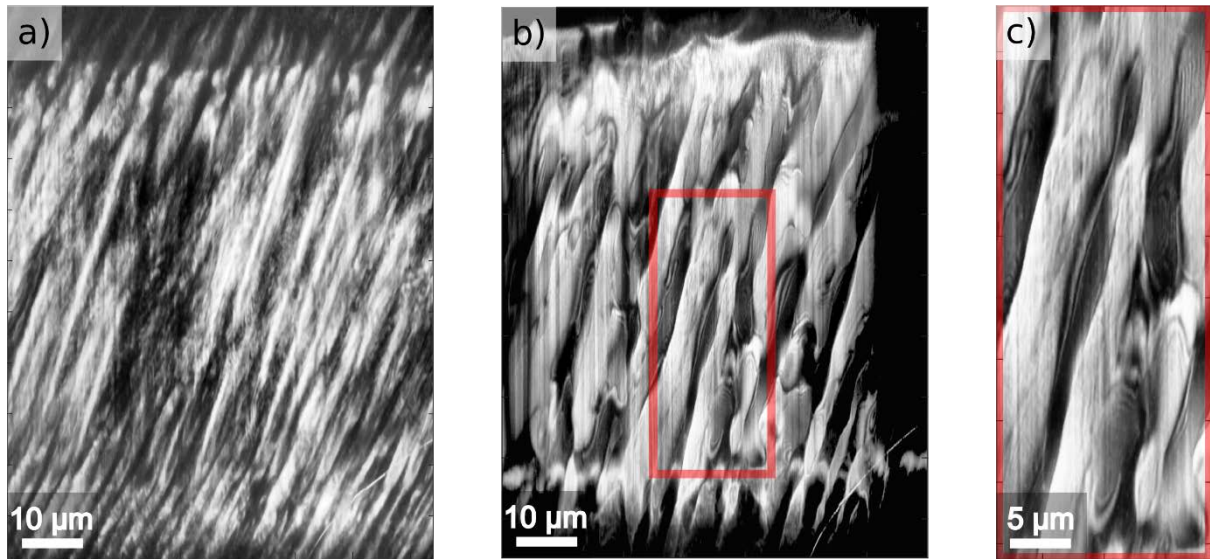


**Figure 1:** DFXM intensity images of the BaTiO<sub>3</sub> single crystal, acquired using the (200) Bragg reflection. a) Room-temperature image characterized by straight domain walls through the entirety of the bulk. b) high-temperature (150°C) image above  $T_C$  ( $T_C = 125^\circ\text{C}$ ) exhibiting wavy features across the entire field of view. c) Close-up region of interest of the high-temperature image showing visible fringe patterns between the different areas with low and high intensity. We note that for all images the sample surfaces are located at the top and bottom extremes of the image, and are parallel to the incident x-ray wave-front.

We initially hypothesized that, upon heating the crystal above  $T_C$ , the stripe-like contrast from the domains should completely disappear as the sample transformed from the ferroelastic tetragonal phase to the paraelectric cubic phase, which cannot contain crystallographic twins. The DFXM intensity image of the paraelectric crystal should therefore be a flat representation of the sample with no discernable contrast. Instead, the DFXM images we acquired revealed clear, ordered stripes, with a periodicity of approximately 3-10  $\mu\text{m}$ . The stripes alternate in light and dark intensity, are approximately oriented at the same angle as the room temperature domains, but have a 4-5-fold increase in width. Most strikingly, the boundaries between the stripes exhibit significant curvature reminiscent of those seen in improper ferroelectrics [10]. To our knowledge, no structural features resembling those in Figure 1b have been reported in the literature. However, we note that the DFXM intensity images correspond to an extremely small region of reciprocal space [23] and, as such, it is possible these features are blurred and obscured when imaged by diffraction-based techniques with larger angular bandwidth.

Before speculating on the origin of these features, we first consider whether they could arise as an artifact of the DFXM technique. Similar to other diffraction imaging methods like dark-field TEM or x-ray section topography, DFXM is susceptible to artifacts from dynamical scattering, which appear as alternating bright and dark sinusoidal fringes parallel to the incident wave-front [24]. In the present case, however, the regions are clearly oblique to the

incident wave-front (which is parallel to the bottom of the image frame), and the intensity variations have relatively sharp boundaries that do not resemble sinusoids (see Supplementary Information A). Though it is conceivable that the fringe-like features we do observe may be a consequence of dynamical effects, these fringes must follow the contours of sharp structural boundaries in the diffracting volume. Thus, we conclude that the wavy domain-like features depict true structural heterogeneities within the crystal.

Another possible explanation for the wavy, stripe-like features is that the crystal was not sufficiently beyond the  $T_C$  to be completely paraelectric, and that the features are simply ferroelastic domains of the room-temperature tetragonal symmetry. However, the mechanical compatibility requirements for ferroelastic domains dictate that the walls lie on well-defined lattice planes (e.g. 110), meaning this cannot explain the pronounced curvature of the boundaries we observe. We note that, while local strains may cause domain wall curvature, such strains would be clearly visible in the DFXM images and, due to their required magnitude, would certainly obscure the stripe-like features altogether. Purely ferroelectric domain walls (i.e.  $180^\circ$ ) do not have the same elastic compatibility requirements, and as such, may be curved. However, the contrast in DFXM images of  $180^\circ$  domain walls is entirely phase contrast [25], and as such, cannot account for the large difference in the average intensity of the alternating stripes we observe.

Excluding the possibility of instrument artifacts or domains, we employed high-resolution x-ray reciprocal space mapping to provide more detailed insight into the crystallographic irregularities within the sampling volume of the crystal. As the RSMs were measured using the same experimental setting and geometry as the DFXM images (i.e. by simply removing the objective lens) [5,6,20], the maps correspond to the same volume of material probed in Figure 1. Figure 2 shows integrated projections through each of the three orthogonal reciprocal space dimensions, detailing the extent of the structural heterogeneity. The reciprocal space intensity distribution can be summarized as two rod-like features, each with slightly different positions and orientations. Given the intensity distribution from an ideal (i.e. un-strained) cubic crystal should be a single ellipsoidal feature, we conclude that our diffracting volume contains two discrete 200 lattice vectors (see Supplementary Materials B), and thus the crystalline distortions necessary to rotate the relatively large volumes of the material defined by the wavy stripe-like features.

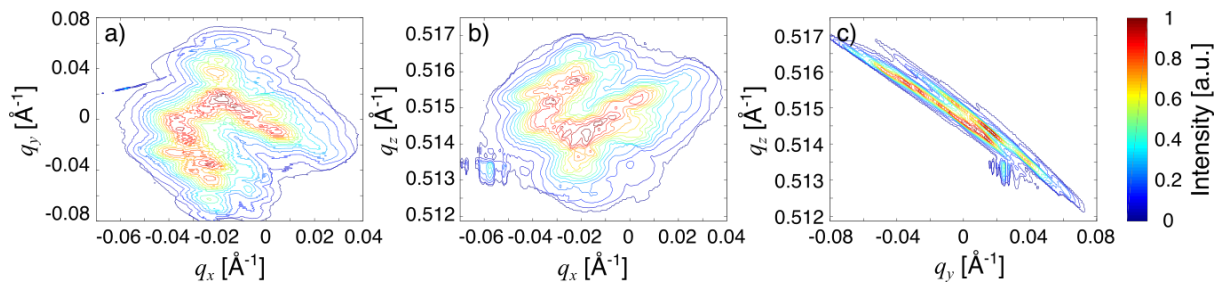


**Figure 2:** High resolution RSMs of the 200 Bragg peak measured at  $150^\circ\text{C}$  (i.e. above  $T_C$ ). Each panel show an integration over different dimensions in  $q$ -space; a)  $q_z$ , b)  $q_y$  and c)  $q_x$ . The scale bar denotes average (measured) photon count.

The small rotations in the lattice vector seen in the RSMs can be directly correlated to the stripe-like features in the DFXM images by studying the map of lattice mosaicity maps reconstructed from DFXM images acquired under different sample tilt angles (Figure 3). Here, the map represents the average local lattice tilt (misorientation) around the rotational axis concentric with the azimuthal axis of the x-ray scattering. Assuming a coherent lattice (i.e. no dislocations), this misorientation must arise from local lattice strain.

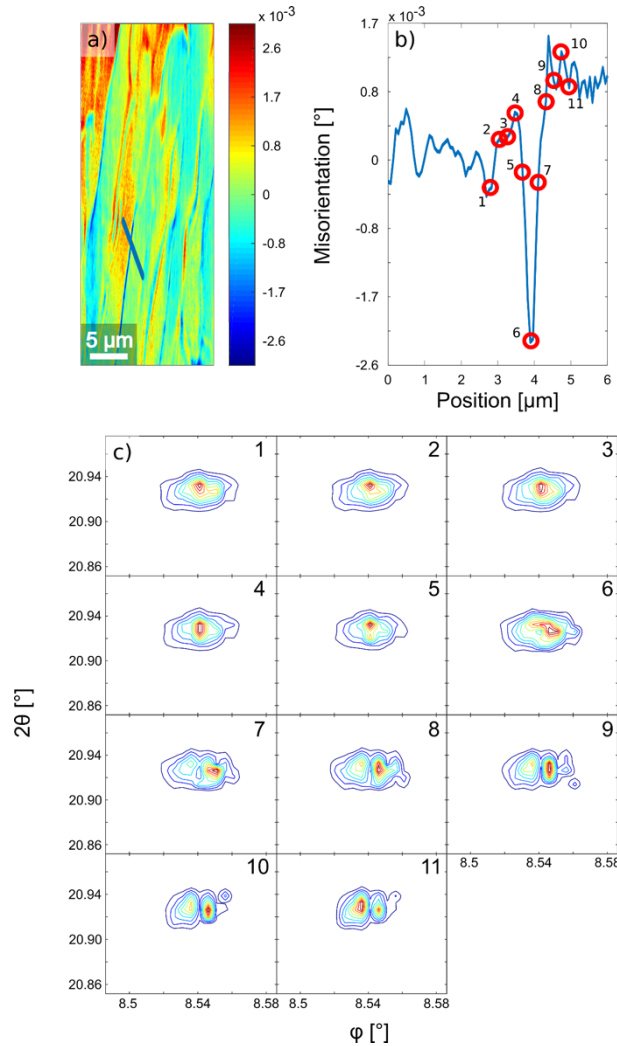


**Figure 3:** a) Lattice tilt map with drawn line. b) the intensity of the drawn line with points of interest parked as red circles. c) 2D RSM for every point of interest.

In general, the stripe-like features have a relatively constant lattice orientation that are separated by much larger changes in orientation at their boundaries. This is exemplified by the line plot in Figure 3b, where an angular deviation of  $-0.0023^{\circ}$  is observed at the boundary between two adjacent stripes. Furthermore, the local intensity-angle reciprocal space maps (extracted from the raw DFXM datasets) for each (interpolated) pixel along this line indicate the boundary region is correlated with the local emergence of a second peak, seen in figure 3c. This second peak is well defined in reciprocal space, and is located approximately  $0.01$ - $0.02^{\circ}$  from the main peaks associated with the stripes.

At this point, it is pertinent to exclude the possibility that the additional peaks in the reciprocal space volumes are due to dislocations. In oxide perovskites, such as  $\text{BaTiO}_3$ , the Burger's vector is of the order of  $2.8 \text{ \AA}$  [26], resulting in lattice tilts of  $0.13^{\circ}$  - orders of magnitude larger than we observe here. As such, we instead posit that the distortions at the stripe boundaries are caused by local chemical heterogeneity.

such a small and localized lattice distortions are most likely explained by the presence of oxygen vacancies, which are well known to agglomerate in complex oxide materials [4]. The strain fields from individual vacancies generally have a fast, inverse-cube decay with distance from a point defect over the surrounding unit cells. However, it is conceivable that the agglomeration of many such vacancies would combine to produce an appreciable strain field whose average magnitude would be correlated to the average density of vacancies.

This agglomeration is likely driven by ageing, i.e., the accumulation of oxygen vacancies at local regions where the affinity is highest. It is well known that such regions may occur at domain walls (particularly when charged), and that these regions may be distorted by residual strains [2,4,6]. It is therefore conceivable that the distortion of these high-affinity lines by long-range residual strains results in the curved boundaries we observe.

Our interpretation of our observations would, therefore, be closely related to domain imprint. Using a photoemission electron microscopy-based methods, stripe-like features resembling domains have been observed at the surfaces of ferroelectric single crystals (including BaTiO<sub>3</sub>) well above T<sub>C</sub> [18]. Similarly, the explanations of this imprint tend to be based on the accumulation of point defects (namely oxygen vacancies) at domain walls. However, while prior work concluded that domain imprint is predominantly a surface phenomenon [18,27], our results indicate that it may instead be a bulk phenomenon that occurs deep within macroscopically-sized single crystals.

It is difficult to ascertain exactly what role domain imprinting might have in the bulk of a macroscopic single crystal. One explanation is that the imprint acts as nucleation sites for the ferroelectric phase upon cooling through T<sub>C</sub>. More specifically, the elastic strains around the boundaries between our domain-like features may be sufficient to locally raise the T<sub>C</sub> in the vicinity [28]. These regions would then be the first to transform into the ferroelectric state and act as seeds for the further growth of the domain throughout the bulk.

To estimate the extent to which T<sub>C</sub> may be augmented by the residual strains imparted by oxygen vacancies, we first used density functional theory (DFT) to calculate the average volume change around a single oxygen vacancy in BaTiO<sub>3</sub>. Simulating single vacancies in 2 × 2 × 2 and 3 × 3 × 3 supercells revealed a tetragonal distortion with a volume increase of 0.8%. Using the tabulated value for the elastic modulus of BaTiO<sub>3</sub> of 65 GPa [28], this results in approximate stress on the order of 400 MPa in the immediate vicinity of the defects. Following the work of Rosetti [29] and others, compressive stress will augment the Curie temperature according to:  $\Delta T_C = 2\varepsilon_0 C(Q_{11}\sigma_3 + Q_{12}\sigma_1)$ , which, again using tabulated values for the electrostrictive coefficients, suggests a local increase in T<sub>C</sub> on the order of 40K [28] (see supplementary material C and D for further details). Such significant local variation to T<sub>C</sub> at stable locations within a bulk crystal would, of course, have played a major role in determining the final domain structure upon cooling through the ferroelectric phase transition, and potentially explain the “memory effect” often observed in ferroelectric domain structures.

In summary, we used dark-field x-ray microscopy to reveal an unusual pattern of structural heterogeneity embedded within the bulk of a BaTiO<sub>3</sub> single crystal heated well above the Curie temperature. The patterns, which repeat on the scale of several μm, resemble classical ferroelastic domains, but with boundaries that exhibit an unusually high degree of curvature. Although the lattice distortions associated with these features are small (on the order of 0.01°), the stresses associated with them are sufficient to locally increase the Curie temperature by tens of K. As these features exist above the T<sub>C</sub>, we speculate they may act as nucleation sites for ferroelastic domains upon cooling. While similar examples of domain imprinting have been observed at the surfaces of ferroelectrics, to our knowledge this is the first observation of such phenomena within the bulk. As such, it demonstrates that defect-mediated domain imprinting is not purely a surface effect, but one that should be considered in ferroelectric materials of all geometries.

#### **Acknowledgments:**

This work is supported by a DTU-NTNU tandem PhD agreement. This authors are grateful to the ESRF for providing beamtime on ID06, as well as Danscatt for financial support

associated with travel to and from beamtime. The authors are particularly grateful to the help provided by the beamline scientist at ESRF Carstern Detlefs and visiting Post. Doc. Ashley Bucsek. Special thanks to Julia Glaum and Theodor Secanell Holstad from NTNU, for helping out with samples and stimulating discussion. H.S. acknowledges financial support from an ERC Starting Grant 3D-PXM.

## **References:**

- [1] Acosta, M., Novak, N., Rojas, V., Patel, S., Vaish, R., Koruza, J., Rossetti, G. A., Rödel, J. (2017). BaTiO<sub>3</sub>-based piezoelectrics: Fundamentals, current status, and perspectives. *Applied Physics Reviews*, 4(4). <https://doi.org/10.1063/1.4990046>
- [2] Qiao, Q., Zhang, Y., Contreras-Guerrero, R., Droopad, R., Pantelides, S. T., Pennycook, S. J., Ogut, S., Klie, R. F. (2015). Direct observation of oxygen-vacancy-enhanced polarization in a SrTiO<sub>3</sub>-buffered ferroelectric BaTiO<sub>3</sub> film on GaAs. *Applied Physics Letters*, 107(20). <https://doi.org/10.1063/1.4990046>
- [3] Jesse, S., Rodriguez, B. J., Choudhury, S., Baddorf, A. P., Vrejoiu, I., Hesse, D., Alexe, M., Eliseev, E. A., Morozovska, A. N., Zhang, J., Chen, L. Q., Kalinin, S. V. (2008). Direct imaging of the spatial and energy distribution of nucleation centres in ferroelectric materials. *Nature Materials*, 7(3), 209–215. <https://doi.org/10.1038/nmat2114>
- [4] Hong, L., Soh, A. K., Du, Q. G., & Li, J. Y. (2008). Interaction of O vacancies and domain structures in single crystal BaTiO<sub>3</sub>: Two-dimensional ferroelectric model. *Physical Review B - Condensed Matter and Materials Physics*, 77(9), 094104. <https://doi.org/10.1103/physrevb.77.094104>
- [5] Simons, H., Haugen, A. B., Jakobsen, A. C., Schmidt, S., Stöhr, F., Majkut, M., ... Poulsen, H. F. (2018). Long-range symmetry breaking in embedded ferroelectrics. *Nature Materials*, 17(9), 814–819. <https://doi.org/10.1038/s41563-018-0116-3>
- [6] Simons, H., Jakobsen, A. C., Ahl, S. R., Poulsen, H. F., Pantleon, W., Chu, Y. H., ... Valanoor, N. (2019). Nondestructive Mapping of Long-Range Dislocation Strain Fields in an Epitaxial Complex Metal Oxide. *Nano Letters*, 19(3), 1445–1450. rapid-communication. <https://doi.org/10.1021/acs.nanolett.8b03839>
- [7] Ren, X. (2004). Large electric-field-induced strain in ferroelectric crystals by point-defect-mediated reversible domain switching. *Nature Materials*, 3(2), 91–94. <https://doi.org/10.1038/nmat1051>
- [8] Li, W. B., Zhou, D., & Pang, L. X. (2017). Enhanced energy storage density by inducing defect dipoles in lead free relaxor ferroelectric BaTiO<sub>3</sub>-based ceramics. *Applied Physics Letters*, 110(13), 3–8. <https://doi.org/10.1063/1.4979467>
- [9] Mundy, J. A., Schaab, J., Kumagai, Y., Cano, A., Stengel, M., Krug, I. P., ... Meier, D. (2017). Functional electronic inversion layers at ferroelectric domain walls. *Nature Materials*, 16(6), 622–627. <https://doi.org/10.1038/nmat4878>
- [10] Meier, D., Leo, N., Maringer, M., Lottermoser, T., Fiebig, M., Becker, P., & Bohatý, L. (2009). Topology and manipulation of multiferroic hybrid domains in MnWO<sub>4</sub>. *Physical Review B - Condensed Matter and Materials Physics*, 80(22), 1–6. <https://doi.org/10.1103/PhysRevB.80.224420>
- [11] Merz, W. J. (1953). Double hysteresis loop of BaTiO<sub>3</sub> at the curie point. *Physical Review*, 91(3), 513–517. <https://doi.org/10.1103/PhysRev.91.513>

- [12] Seidel, J., Martin, L. W., He, Q., Zhan, Q., Chu, Y. H., Rother, A., ... Ramesh, R. (2009). Conduction at domain walls in oxide multiferroics. *Nature Materials*, 8(3), 229–234. <https://doi.org/10.1038/nmat2373>
- [13] Tagantsev, A. K., & Cross, L. E. (n.d.). *Ferroic Crystals*.
- [14] Lummen, T. T. A., Gu, Y., Wang, J., Lei, S., Xue, F., Kumar, A., ... Gopalan, V. (2014). Thermotropic phase boundaries in classic ferroelectrics. *Nature Communications*, 5, 1–9. <https://doi.org/10.1038/ncomms4172>
- [15] Chu, M. W., Szafraniak, I., Hesse, D., Alexe, M., & Gösele, U. (2005). Elastic coupling between 90° twin walls and interfacial dislocations in epitaxial ferroelectric perovskites: A quantitative high-resolution transmission electron microscopy study. *Physical Review B - Condensed Matter and Materials Physics*, 72(17), 1–5. <https://doi.org/10.1103/PhysRevB.72.174112>
- [16] Chen, L. Q. (2008). Phase-field method of phase transitions/domain structures in ferroelectric thin films: A review. *Journal of the American Ceramic Society*, 91(6), 1835–1844. <https://doi.org/10.1111/j.1551-2916.2008.02413.x>
- [17] Daniel, L., Hall, D. A., & Withers, P. J. (2014). A multi-scale model for reversible ferroelectric behaviour of polycrystalline ceramics. *Mechanics of Materials*, 71, 85–100. <https://doi.org/10.1016/j.mechmat.2014.01.006>
- [18] Höfer, A., Fechner, M., Duncker, K., Hölzer, M., Mertig, I., & Widdra, W. (2012). Persistence of surface domain structures for a bulk ferroelectric above T C. *Physical Review Letters*, 108(8), 1–4. <https://doi.org/10.1103/PhysRevLett.108.087602>
- [19] Zhang, L. X., & Ren, X. (2005). In situ observation of reversible domain switching in aged Mn-doped BaTiO<sub>3</sub> single crystals. *Physical Review B - Condensed Matter and Materials Physics*, 71(17), 1–8. <https://doi.org/10.1103/PhysRevB.71.174108>
- [20] Poulsen, H. F., Jakobsen, A. C., Simons, H., Ahl, S. R., Cook, P. K., & Detlefs, C. (2017). X-ray diffraction microscopy based on refractive optics. *Journal of Applied Crystallography*, 50(5), 1441–1456. <https://doi.org/10.1107/S1600576717011037>
- [21] Ormstrup, J., Østergaard, E. V., Detlefs, C., Mathiesen, R., Yilidrim, C., Kutsal, M., Cook, P., Watier, Y., Cosculluela, C., Simons, H. (n.d.). Imaging microstructural dynamics and strain fields in electro-active materials in-situ with dark field x-ray microscopy. *Review of Scientific Instruments*, accepted.
- [22] Damjanovic, D. (1998). Ferroelectric, dielectric and piezoelectric properties of ferroelectric thin films and ceramics. *Reports on Progress in Physics*, 61, 1267. Retrieved from <http://iopscience.iop.org/0034-4885/61/9/002/>
- [23] Simons, H., Jakobsen, A. C., Ahl, S. R., Detlefs, C., & Poulsen, H. F. (2016). Multi-scale 3D characterization with dark-field x-ray microscopy. *MRS Bulletin*, 41(6), 454–459. <https://doi.org/10.1557/mrs.2016.114>

- [24] Amalinckx, S (1964). The Direct Observation of Dislocations. In *Solid State Physics*, Academic Press (6).
- [25] Enari, M., Sakahira, H., Yokoyama, H., Okawa, K., Iwamatsu, A., & Nagata, S. (1998). A caspase-activated DNase that degrades dna during apoptosis, and its inhibitor ICAD (Mature (1998) 391 (43-50)). *Nature*, 393(6683), 396. <https://doi.org/10.1038/30782>
- [26] Zhu, X., Zhu, J., Zhou, S., Liu, Z., & Ming, N. (2008). Hydrothermal synthesis of nanocrystalline BaTiO<sub>3</sub> particles and structural characterization by high-resolution transmission electron microscopy. *Journal of Crystal Growth*, 310(2), 434–441. <https://doi.org/10.1016/j.jcrysgro.2007.10.076>
- [27] Mathieu, C., Lubin, C., Le Doueff, G., Cattelan, M., Gemeiner, P., Dkhil, B., ... Barrett, N. (2018). Surface Proximity Effect, Imprint Memory of Ferroelectric Twins, and Tweed in the Paraelectric Phase of BaTiO<sub>3</sub>. *Scientific Reports*, 8(1), 2–8. <https://doi.org/10.1038/s41598-018-31930-4>
- [28] Geiger, P. T., Clemens, O., Khansur, N. H., Hinterstein, M., Sahini, M. G., Grande, T., Webber, K. G. (2017). Nonlinear mechanical behaviour of Ba<sub>0.5</sub>Sr<sub>0.5</sub>Co<sub>0.8</sub>Fe<sub>0.2</sub>O<sub>3-δ</sub> and in situ stress dependent synchrotron X-ray diffraction study. *Solid State Ionics*, 300, 106–113. <https://doi.org/10.1016/j.ssi.2016.11.027>
- [29] Rossetti, G. A., Cross, L. E., & Kushida, K. (1991). Stress induced shift of the Curie point in epitaxial PbTiO<sub>3</sub> thin films. *Applied Physics Letters*, 59(20), 2524–2526. <https://doi.org/10.1063/1.105940>

### Supplementary A: Intensity variation of curved boundaries in DFXM images

The line profiles of intensity taken from figure 1b and 1c are shown in figure A1 and the placement of the profiles in figure A2. This shows that the barriers between the different illuminated regions has a sharp transition, with respect to intensity change. T

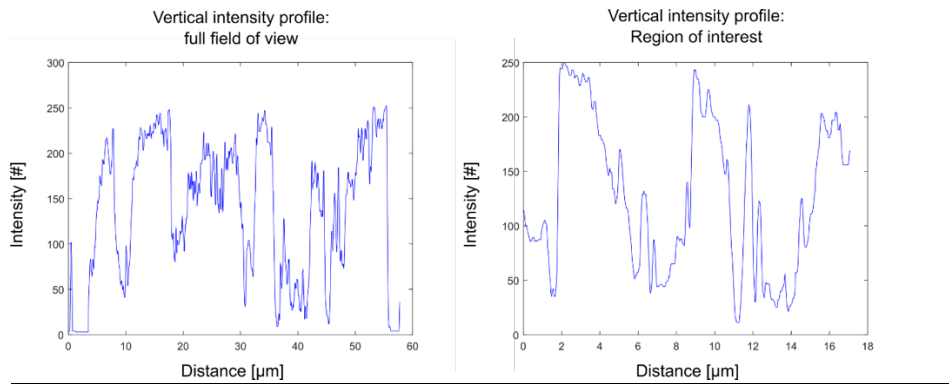


Figure A1: show the two different intensity lines taken from figure 1b and 1c.

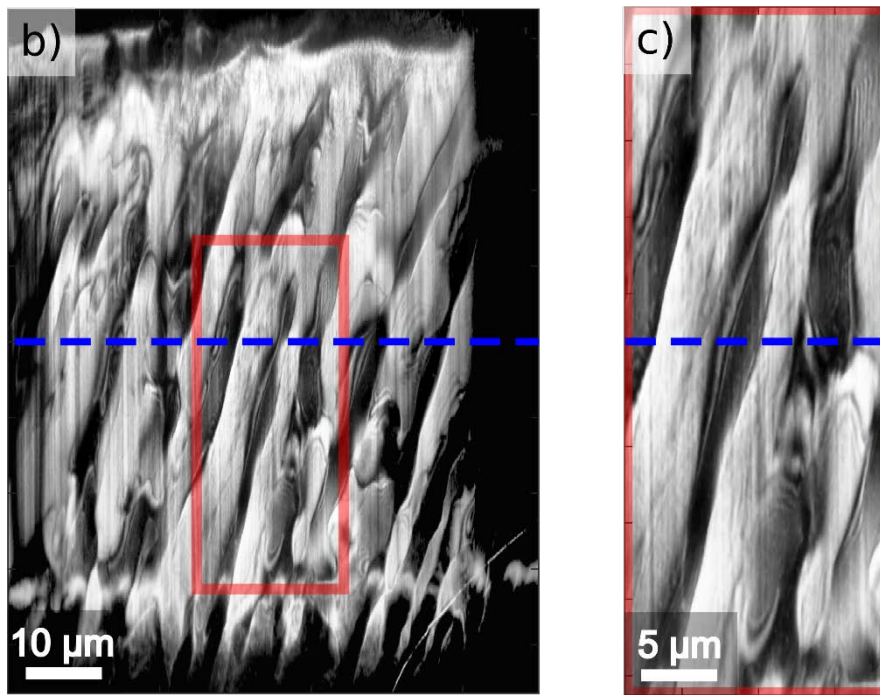
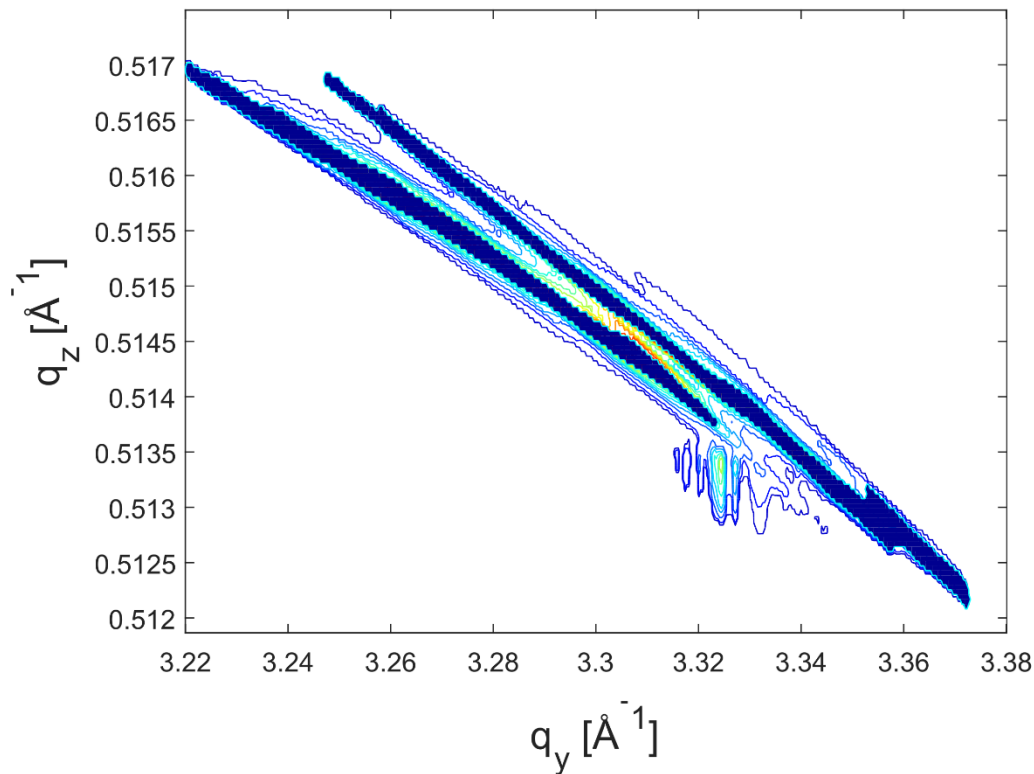


Figure A2: Location of the intensity line.

### **Supplementary B: Region detection in high-resolution RSMs**

The high resolution RSM along the  $q_x$  axis was analyzed by using the MATLAB edge-zero-crossing algorithm. The algorithm detected regions along the two prominent features in the RSM as argued in the main manuscript. Between the two regions, the intensity crosses the zero point values, which is hard to immediately discern from the RSM. This identifies them as separate regions in reciprocal space, thus separate crystallographic planes.



**Figure B1:** The figure shows the region detected in the RSM from figure 2c, using a zero crossing algorithm.

### **Supplementary C: DFT calculation details**

The DFT calculations were performed with the electronic structure software package GPAW [10.1088/0953-8984/22/25/253202] relying on the Atomic Simulation environment (ASE) [10.1088/1361-648X/aa680e]. All calculations were performed using the projector augmented wave method (PAW) using a plane-wave basis set with an energy cutoff of 600 eV and the Perdew-Burke-Ernzerhof exchange-correlation functional [10.1103/PhysRevLett.77.3865]. For the 2x2x2 supercell we used a Brillouin zone sampling of 3x3x3 k-points and relaxed the structure until forces were below 1 meV/Å. For the 3x3x3 supercell, we used a 2x2x2 k-point grid and relaxed the structure until all forces were below 5 meV/Å.

### **Supplementary D: Thermodynamic calculations**

While a single perfect crystal in a completely relaxed state should not exhibit any change in Curie temperature, changes to the state might give a different outcome. Most theoretical work on the state and structure of ferroelectric materials has been done by using thermodynamic or mean-field theories. Similarly, here we explore known concepts based on previous work by G. Rossetti, to give a possible explanation for the morphological features

that seems to persist well above  $T_c$ .

Phenomenological description of the temperature dependent free-energy in  $\text{BaTiO}_3$ , can be used to model the change in Curie Temperature. G. Rossetti describes in his work[x,y], how 2D compressive stress and 3D hydrostatic stress can change the Curie temperature. We start with the different energy functions for the cubic and tetragonal state, where  $P_1=P_2=P_3=0$  for cubic and  $P_1=P_2=0, P_3 \neq 0$  for tetragonal. By setting the two energy functions to be equal to each other's the following equilibrium is found:

$$0 = \alpha_1(T_c)P_3^2 + \alpha_{11}(T_c)P_3^4 + \alpha_{111}(T_c)P_3^6 - Q_{11}\sigma_3P_3^2 + Q_{12}(\sigma_1P_3^2 + \sigma_2P_3^2)$$

This energy equilibrium have the following solution for  $P_3$ :

$$P_{3,S}^2 = -\frac{\alpha_{11}}{3\alpha_{111}} \pm \sqrt{\frac{\alpha_{11}^2}{9\alpha_{111}^2} - \frac{1}{3\alpha_{111}}(Q_{11}\sigma_3 + Q_{12}\sigma_1 - \alpha_1)}$$

Given these excretions for the polarization, we ask at what temperature would the spontaneous polarizations of the stressed and the unstressed material be the same,  $P_{3,S}^2(\sigma=0) = P_{3,S}^2(\sigma \neq 0)$ . The stress will change the thermodynamic coefficients, were it is here assumed that only be the  $a_1$  that has a temperature dependency. Which is given in the form of,

$$\alpha_{11} = \frac{T - T_c}{2\varepsilon_0 C}$$

The different stress states will give rise to different Curie temperatures which we note,  $T_{C,0}$  and  $T_{C,\sigma}$ , and of course  $a_{1,0}$  and  $a_{1,\sigma}$ . By expanding the polarization equilibrium with the stress modified thermodynamic coefficients, we find the following:

$$\alpha_{1,0} = Q_{11}\sigma_3 + Q_{12}\sigma_1 - \alpha_{1,\sigma}$$

Which is equal to,

$$T_{C,0} - T_{C,\sigma} = 2\varepsilon_0 C(Q_{11}\sigma_3 + Q_{12}\sigma_1)$$

Giving the difference in Curie temperature between the stressed and unstressed state.

$$\Delta T_C = 2\varepsilon_0 C(Q_{11}\sigma_3 + Q_{12}\sigma_1) \cup \Delta T = 4\varepsilon_0 C Q_{12} H$$

Here we write the equations for the 3D hydrostatic and 2D compressive stress and plot them in figure 8.

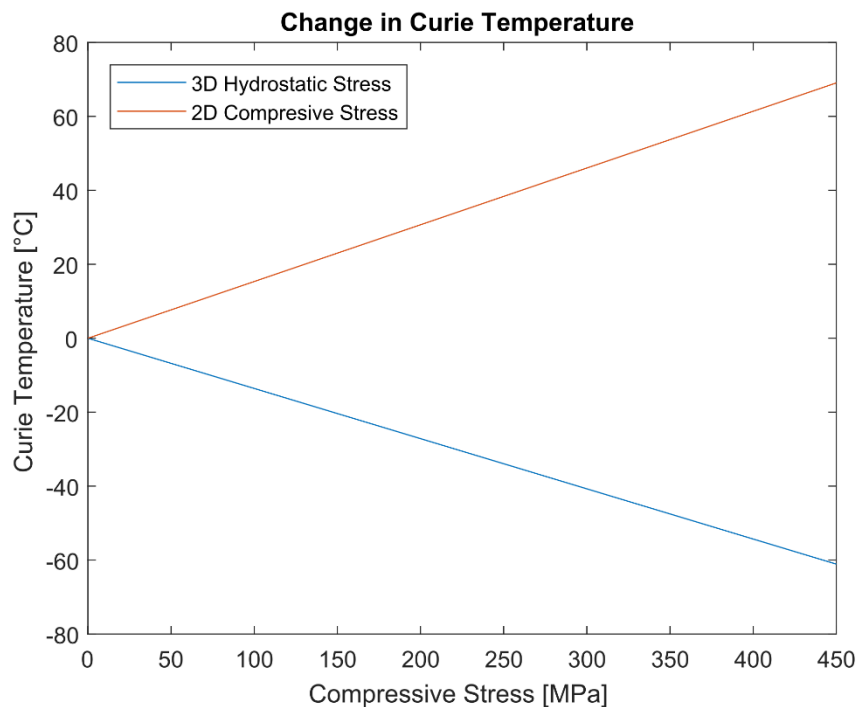


**Figure A1:** The 2D compressive stress orange line shows an increase in Curie temperature, while the 3D hydrostatic stress blue line shows a decrease in Curie temperature.

This simple model has been shown to be in good approximation with experimental data [Rossetti]. Important to note is the only if the compressive stress is orthogonal to the  $c$  axis, will it lead to a high Curie temperature. This modelling of  $T_C$  present with a possible theoretically explanation of the existence of the morphological features above  $T_C$ .

### **Supplementary E: DFXM and RSM measurement details**

The high resolution done by doing 400 steps over the sample rotation  $\phi$ , in total an angular range of  $0.0002^\circ$ . At each step of the rotation, the CCD was illuminated for 3 seconds. The CCD is an ESRF FreLoN camera with 2048 x 2048 pixels, with an effective pixel size of  $1.56 \mu\text{m}^2$ . The camera is places at a distance of 5 meters to the sample at approximately  $20.92^\circ$ , giving each pixel an angular resolution of  $15.6 \times 10^{-6}^\circ$  [10.1088/1757-899X/580/1/012007]. The images collected were interpolated over a grid of 500-by-500, giving each point a final angular resolution of  $63.49 \times 10^{-6}^\circ$ . The setup geometry and the sweeping through  $q$ -space give the final range giving in figure 2.

### 5.3 Further discussion

Domain patterns in BaTiO<sub>3</sub> are a consequence of twinning of the non-centrosymmetric structure. We see these domains clearly in figure 5.1; these patterns are well known and the morphological features observed with DFXM and PLM are predictable and repeatable. Normally, when a ferroelectric or ferroelastic structure transforms into a cubic phase, it is expected to become more or less free from all structural heterogeneities. However, wavy features not following any nominal crystallographic orientation appears in our intensity images of the cubic phase. Our images not only shows the wavy features, but also a high degree of uniformity of illumination along the surface of the sample. The surface region has been shown to exhibit slightly different structures than the bulk in figure 5.1. Qualitative comparison with the strain maps would suggest these wavy features are local elastic distortions of the lattice, and thus must perturb the ferroelectric order parameter  $\mathbf{P}_S$ . This underlines that the bulk situation can't be ascertained by knowing just the sample conditions and analyzing them with surface-sensitive techniques.

The electric field induced phase transformation from cubic to tetragonal above  $T_C$  was clearly shown by the RSMs in section 4.2. Furthermore, it indicated that the samples goes into a mono-domain state while the electric field is applied. However, removing the electric did not cause it to reverse back to a cubic state, i.e. the tetragonal structure was metastable. The metastable phase shows the reflection peak at a higher  $q_y$  than when filled applied. The metastable phase has a slightly less elongated unit cell structure, as one would expect in the absence of an externally-applied electric field. The presence of the metastable phase suggest the system does not have enough thermal energy to revert back to the cubic phase.

The strain map acquired at the largest applied electric field does not show any strong features that suggest the sample had any significant residual strain. Potentially, it is still in a mono-domain configuration and will not show any heterogeneous features with in the form of strain or intensity variations. It is known that BaTiO<sub>3</sub> has hysteresis with respect to the thermally-induced tetragonal-to-cubic phase transition, where the Curie temperature differs slightly for the phase transition upon heating versus cooling. Electric field induced phase transformations in polycrystalline BaTiO<sub>3</sub> has been shown to only occur a few degrees above  $T_C$  [53]. Typically, single crystal BaTiO<sub>3</sub> exhibit a sharper transition, giving credibility to the suggestion that the system lacks thermal energy to transform back.

## 6 Electric field induced defect migration

This chapter focuses on measuring and understanding how defects are distributed and migrate in bulk barium titanate. The core part of this work comprises the paper presented later in this chapter, which was conducted with the STEF holder described in section 4.2. This investigation specifically addressed the migration of oxygen vacancies during an electric field induced phase transformation from the cubic to tetragonal phases. The motivation behind this investigation of point defects and their dynamics was prompted by the growing attention to such defects and their functional use in modern materials and application [11].

With DFXM, we can acquire internal strain maps of a bulk sample that give us access to information about the local magnitude and distribution of strain within the crystal. Given the present resolution limit of DFXM at approximately 100 nm, it is extremely unlikely we would be able to detect the strain from a single vacancy, whose spatial decay is on the order of Angstroms [38]. However, it is conceivable that we might detect the strain generated by clusters of vacancies. If we assume that the vacancies within this cluster are distributed uniformly, then the cluster can be thought of as an inclusion defined by its chemical strain relative to the surrounding lattice. The classic work by J. D. Eshelby formulated a solution for the strain decay from such a strained inclusion (e.g. thermal residual stress). Importantly, Eshelby's formalism is such that, with knowledge of the strain decay induced by the inclusion, the average strain inside the inclusion can be found. Motivated by this idea, I here present a novel method for detecting the density (and hence absolute number) of point defects from the strain decay around every pixel in the strain map. Thus, by recording strain maps both before and after an electric field is applied, we can ascertain the relative movement of the detected defects. This has broad applications, for example helping validate models of the agglomerations of defects along domains walls [21], or the distribution of defects and subsequent effect on macroscopic properties after an aging process [14]. In general, our results from this new method confirm the concentration and mobilities of vacancies that, previously, could only be measured indirectly [54].

## **6.1 Paper 4: Non-destructive imaging of mesoscopic oxygen vacancy diffusion in barium titanate**

*The paper in this section introduces our new method of detecting oxygen vacancies in bulk materials. This is done from the strain maps acquired with the DFXM under stable elevated temperatures. While at elevated temperature two strain map was acquired, these maps was also report in earlier section 4.2. One map of the initial condition and another after an electrical field was applied and kept stable at 0.8 kV/mm. Using our method of detecting the oxygen vacancies in both condition, we can model the ionic current from the detected movement. The result we have compared to a model of the ionic current [52] and measure current from a sample under similar condition in a TF analyser. The results show a relative good match with discrepancies in conduction which can potentially be explained by the photo induces current during x-ray experiment at a high brilliance source like the ESRF.*

# Non-destructive imaging of mesoscopic oxygen vacancy diffusion in barium titanate

Jeppé Ormstrup, Thomas Olsen, and Hugh Simons\*

*Department of Physics, Technical University of Denmark, 2800 Kgs. Lyngby, Denmark*

(Dated: June 13, 2020)

Dark field x-ray microscopy (DFXM) enables imaging of structural distortions in bulk crystalline materials. By applying a statistical analysis of local strain distributions, we demonstrate the ability to detect the size and position of clusters of oxygen vacancies in an embedded slice within a macroscopic single crystal of BaTiO<sub>3</sub>. Our approach is based on an adaptation of Eshelby's theory describing the strain fields around an embedded inclusion, combined with *ab initio* calculations of the chemical strain generated by individual oxygen vacancies. Together, they facilitate the precise determination of the number of oxygen vacancies within each pixel of the DFXM image, and hence the full distribution of vacancies within the diffracting volume of the bulk material. This opens a new door to revealing fundamental mechanisms involving the distribution and dynamics of oxygen vacancies and other point defects roles in bulk material.

Oxygen vacancies have a multitude of effects on the properties and behaviour of oxide ferroelectrics [1],[2]. In particular, oxygen vacancies can substantially increasing the recoverable macroscopic strain and polarization by pinning domain walls [3], [4]. On the other hand, the continued diffusion and accumulation of oxygen vacancies at structural interfaces via the aging process can also *decrease* certain aspects of the performance of ferroelectric materials [5], and can be critical to mean time to failure for devices such as capacitors [6]. As a consequence, there is a strong and persistent need to both qualitatively and quantitatively analyse the distribution and diffusion of oxygen vacancies in ferroelectrics materials under realistic (e.g. driven) conditions.

The pathway for the movement of oxygen vacancies in an oxide perovskite occurs via the opening formed by A- and B-site atoms [7]. The critical radius for ionic hopping of vacancies from a given site is thus affected by lattice strains and the defects that create them, such as dislocations and domains walls. Such defects promote the migration of oxygen vacancies, albeit only in a very localized region, occurring either around individual points in the structure, or through networks of high charge carrier density, such as along domain walls [8]. To date, several models have helped provide a physical interpretation of the oxygen vacancy migration process. The electric-field-assisted migration of oxygen vacancies and their agglomeration near electrodes was described in terms of the current density in Randall et al. [6], based on thermally stimulated depolarization current (TSDC) analysis [9]. However, this interpretation lacked a model for the effects of domains on the distribution of defects and carriers. Hong et al. [8], however, developed a 2D phase field model to predict the distribution of oxygen vacancies along 90° domain walls, resulting from the local changes in charge density induced by the domain walls themselves. Experimental validation with scanning probe microscopy have similarly create frameworks for

understanding the role of vacancies and other point defects in nucleation and structure-property relations in ferroelectric thin films [10]. Likewise, high-resolution TEM has convincingly documented the role of oxygen vacancies in a variety of important phenomena, such as domain wall pinning and electronic conduction. However, in both cases such measurements are limited to surfaces and thin foils, and cannot reveal the behaviour of oxygen vacancies in embedded volumes, such as within bulk materials.

In this paper, we present a method for identifying and mapping accumulations of oxygen vacancies at a mesoscopic length scales in embedded volumes of bulk materials. Such data is ideally suited to further validating previous models as well as guiding the development of new models of complex oxides systems and the dynamics of the defects within them. Using the dark-field x-ray microscopy (DFXM), maps of the strain in bulk materials were acquired [11] from a single crystal of BaTiO<sub>3</sub>, at elevated temperatures above  $T_C$ , and both with and without an applied electric field. By analysing the local strain distribution in localized populations of pixels, we were able to detect the regions containing above-average densities of vacancies, and then quantitatively estimate the number of vacancies contained within them. By comparing the distribution of oxygen vacancies from images measure with and without the applied electric field, this allowed for a local measurement of oxygen vacancy diffusion across mesoscopic length scales with within a fully embedded volume in a macroscopic single crystal. We then discuss this result in the context of bulk diffusion models as a metric to verify this new approach.

Our method detects and quantifies clusters of oxygen vacancies from axial strain maps obtained using DFXM by considering the local strain decay from the elastic lattice distortions around said clusters. Specifically, it is assumed that the clusters of oxygen vacancies are approximately spherical and possess a homogeneous lattice distortion within them, implying that the concentration of vacancies is also homogeneously distributed within the cluster. Although such assumptions may not strictly account for the complex and random nature of vacancy distributions, they allow for a relatively simple approach

---

\* husimo@fysik.dtu.dk

to determining the size and concentration of the vacancy clusters, and thus the total number of vacancies within them. This approach is based on Eshelby's theory of strain from an inclusion in an isotropic matrix [12].

The stochastic nature of x-ray diffraction imaging means that DFXM strain maps contain noise that makes direct fitting of strain fields in 2D extremely challenging. Such fits tend to be time-consuming and prone to significant errors. As such, we determine the size and concentration of the vacancy clusters by fitting the histogram of their strain fields within a spatial window. This results in a much faster and more robust solution which, as we will show, corresponds well with the expected physical values for the defect distribution and diffusion. Furthermore, we note that this approach of fitting the strain histogram lends itself to fitting strain profiles from other types of defects as well, expanding the potential applications of this method considerably.

Assuming such a spherical inclusion of constant chemical strain, the lattice displacements in the material surrounding the inclusion will have a radial inverse-cubic decay. Accounting for the finite thickness of the x-ray beam illuminating the sample, a histogram of the strain obtained from a circular window will be described by Equation 1, below (see Appendix for full derivation and explanation):

$$\Omega_{\epsilon_0} = \left( \frac{\epsilon - \frac{\delta\epsilon}{2}}{\epsilon_0 r_{incl}^3} \right)^{-2/n} - \left( \frac{\epsilon + \frac{\delta\epsilon}{2}}{\epsilon_0 r_{incl}^3} \right)^{-2/n} \quad (1)$$

where  $\epsilon$  is the strain at a specific bin in the histogram,  $\epsilon_0$  is the initial strain for each point,  $r_{incl}$  is the radius of inclusion and  $n$  is the exponent that governs the rate of the strain decay.

With an analytical function describing the histogram in terms of the inclusion radius and its chemical strain, we fit the quasi-statistical distribution to the experimentally-obtained strain data in a predefined circular region around every pixel in the strain map. If the relationship between the chemical strain and the vacancy density is known (e.g. from measurements or ab-initio simulations), one can readily derive the number of expected vacancies for a given pixel as follows:

$$N_v = \frac{4}{3} \pi r_{incl}^3 \left[ \frac{(\epsilon_0 + 1)^3 - 1}{\Delta\alpha_v} \right] \quad (2)$$

where  $\Delta\alpha_v$  is the volume expansion from a single vacancy.

To demonstrate our analysis approach, we here consider the electric-field-driven migration of oxygen vacancies in a single crystal of barium titanate. The sample was heated above the Curie temperature to remove all domains, leaving only oxygen vacancies remaining sources of strain in the crystal. The crystal was purchased commercially (Crystal GmbH, Germany), with nominal dimensions of  $5 \times 5 \times 0.5$  mm, and then ground to a thickness of  $\approx 0.2$  mm to ensure adequate transmission of the x-ray

beam. To reduce residual stresses, which may interfere with the DFXM strain maps, the crystal surfaces were polished with a suspended silica particles solution with  $0.04 \mu\text{m}$  particle size (OPS, Struers A/S, Denmark), and the sample annealed at  $400^\circ\text{C}$  for two hours. Heating and cooling ramp rates of  $^\circ\text{C}/\text{min}$  were used to avoid thermal shock. Finally, silver electrodes were hand-painted on the  $5 \times 5$  mm faces to facilitate the application of electric fields.

The DFXM experiment was carried out using the hard x-ray microscope on beamline ID06 of the European Synchrotron (ESRF). A photon energy of 17 keV (bandwidth  $\Delta E/E$  of 10-4) was selected, and a focused "line" beam of approximately  $400 \mu\text{m}$  in width and  $0.5 \mu\text{m}$  height was created using a 1D Be-based compound refractive lens. The line-beam illuminates a cross-section of the sample, resulting in a DFXM image corresponding to a well-defined volume within the crystal. The crystal was oriented such that the [002] lattice planes were in the Bragg condition, and this diffracted beam was then focused onto a CCD-based detector via an x-ray objective lens. This objective lens was a 2D Be-based CRL with a magnification ratio of 19, resulting in an effective pixel size of 70 nm and 140 nm in the horizontal and vertical directions, respectively. A custom-built sample environment was used to apply the electric fields to the sample while maintaining an extremely constant temperature of  $150^\circ\text{C} \pm 0.01^\circ\text{C}$ . Details on the microscope can be found in [13],[14], while a detailed description of the sample environment can be found in [15].

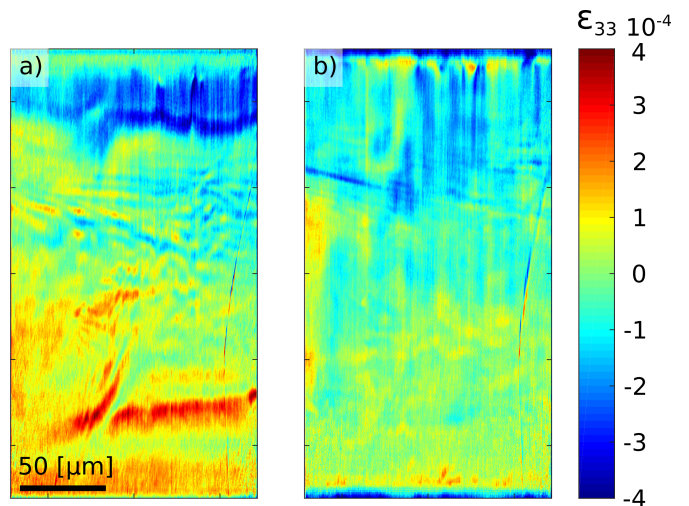


FIG. 1. Temperature for both images is measured to be 0.5 K above  $T_C$ . a) shows the strain at zero electric field and b) at an electrical field of 0.8 kV/mm.

Figure 1 shows the two strain maps obtained using DFXM both in the initial (as annealed) state, and after 11 hours under a constant electric field of 0.8 kv/mm at  $150^\circ\text{C}$ . Both images show no evidence of ferroelectric domains or other defects, such as dislocation. Therefore, we assume the remaining heterogeneity evident in

the maps is predominantly a consequence of the ordering and accumulation of oxygen vacancies across mesoscopic scales. As such, it serves as a suitable basis for a proof-of-principle of the vacancy mapping approach outlined above.

The vacancy mapping algorithm used a circular sliding window with a radius of 21 pixels, seen in Figure 2a and b, which traverses the entire  $1000 \times 1000$  pixel strain map. For each position of the window, we extract the strain magnitude and plot the frequency of their values as a histogram with a bin width of a tenth of the strain range within that specific region (figure 2c). The piecewise function (Eq. 1) is then fit to the distribution, allowing us to extract  $\epsilon_0$  and  $r_{incl}$  for each pixel.

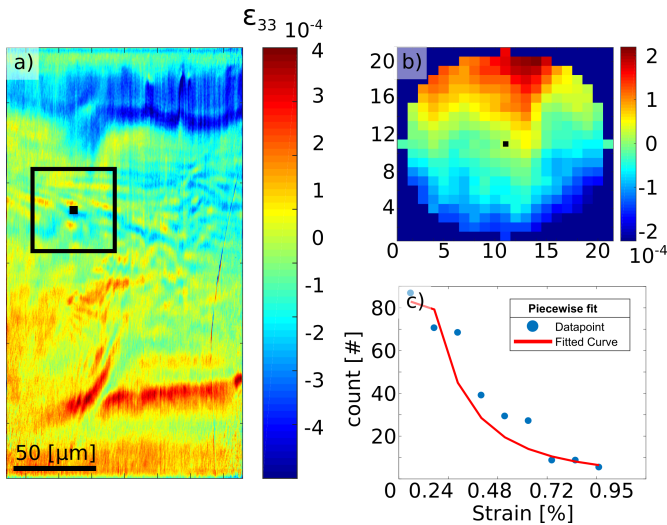


FIG. 2. The different stages of the detection process. a) the strain map from fig 1b annotated to show the fitting window (not to scale). b) the marked area of  $21 \times 21$  pixels. c) the results of fitting Eq. 1 for the histogram for the strain data from the window in b). The color scale denotes the strain magnitude for the maps in both a) and b).

Limiting the absolute strain distribution to a localized area implies that the fit pertains to the decay in strain from only a few inclusion-like features. Furthermore, considering the mesoscopic 100 nm spatial resolution of DFXM, every pixel will most likely contain multiple vacancies (or other point defects). Determining the number of vacancies within a strained inclusion when the radius and the magnitude of its strain is known requires a quantitative correlation between the density of vacancies and the chemical strain they induce.

To this end, we used density functional theory (DFT) to calculate the average volume change around a single oxygen vacancy in  $\text{BaTiO}_3$  (see appendix for details). Simulating single oxygen vacancies in  $2 \times 2 \times 2$  and  $3 \times 3 \times 3$  supercells revealed a tetragonal distortion with a volume increase of 0.8% upon relaxation. This calculated volume expansion was then used as a calibration point for the linear relationship between the oxygen vacancy con-

centration and the volumetric chemical strain. Taking into account the spherical geometry of the inclusion, this permits a quantitative estimation of the number of vacancies within each pixel, illustrated in Figure 3.

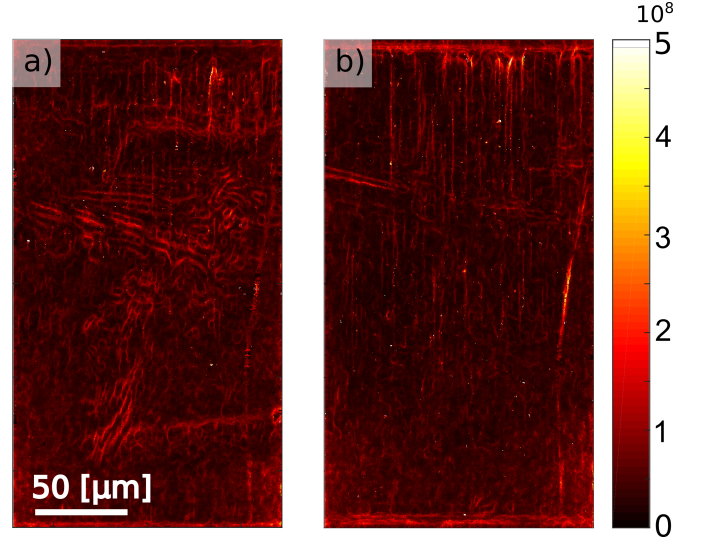


FIG. 3. a) and b) Show the maps with number of vacancies per pixel, modelled from the strain map with zero and 0.8 kV/mm applied electric field, respectively.

In its cubic state, the  $\text{BaTiO}_3$  crystal is (in principle, at least) free of domain walls and other heterogeneities, meaning that the remaining defects are overwhelmingly expected to be oxygen vacancies. As such, the relative movement of these vacancy clusters under an applied electric field is expected to be representative of the ionic current within the diffraction volume.

The relative displacement of the oxygen vacancy clusters is calculated for each column in the image (i.e. parallel to the electric field direction) by finding the difference between the weighted average of the number of vacancies (i.e. the zeroth distribution moment) for the initial and final states. By normalizing this distance by the sample thickness and multiplying by the average numbers of vacancies in the two columns and the nominal charge of the oxygen vacancies, we estimate the total charge transferred within the sampling volume. We then invoke  $I_{data} = \Delta Q / \Delta t$  to calculate the associated ionic current, and normalize by the cross-sectional area of the diffraction volume to find the current density from the two maps.

We now validate the ionic current density obtained from our method by comparing it to both calculations and measurements of macroscopic ionic conduction in  $\text{BaTiO}_3$ . In 2013, Randall *et al.* proposed the following model for ion conduction based on the transport of oxygen vacancies:

$$J_{Randall} = 2q_0 N_{av} \exp\left(-\frac{U}{K_B T}\right) \sinh\left(\frac{q_0 E a}{K_B T}\right) [6]. \quad (3)$$

Here,  $q_0$  is the elementary charge,  $N$  is the number of ionic species involved,  $a$  is the characteristic jump distance,  $\nu$  is the ion jump frequency,  $U$  is activation energy,  $K_B$  is the Boltzmann constant,  $T$  is the temperature and  $E$  is the applied electric field. Using published values for the activation energy ( $0.70 \pm 0.04$  eV for BTO above  $T_C$  [16]) and the jump frequency (tens of PHz [17]), results in a predicted value for the current density of  $J_{Randall} = 1.36 \times 10^{-5} A/cm^2$  - approximately six times smaller than the value derived from our method:  $J_{Ormstrup} = 2.11 \times 10^{-6} A/cm^2$ .

Further validation with macroscopic current measurements reveal a measured current density of  $J_{macroscopic} = 4.04 \times 10^{-5} A/cm^2$ . The current density was measured during a classical P-E large signal measurement, after the field reached its peak magnitude. Under such conditions, and in the paraelectric state, the measured current should predominantly represent the ionic current. The explanation for the deviation between our method and the model are likely a consequence of the parameters used for the jump frequency and activation energy. At the same time, our method is expected to under-predict the current density, since it is sensitive only to the movement of relatively large clusters of defects, which presumably do not comprise many of the vacancies in the material.

We envision that one of the most valuable applications of this technique will be to guide and validate 3D materials models involving vacancy-related phenomena. In particular, we note that the mesoscopic length scales accessible with DFXM are well matched with the current state-of-the-art in phase field modelling. For example, Hong *et al.* [8] developed such a model to predict the agglomeration of oxygen vacancies along  $90^\circ$  domain walls and electrode interface in  $BaTiO_3$  - not unlike our observations here (Figure 3b). A natural development of our approach would therefore be to account for the presence of a second type of defect, such as ferroelectric domain walls. Then, it could be directly observed and measured how the strained areas around such features change the local diffusion characteristics for the oxygen vacancies (e.g. via locally augmenting the characteristic jump distance, Eqn. ).

In conclusion, we demonstrate a statistical approach for quantifying defect distributions and dynamics based on DFXM axial strain maps. Our measurements of the vacancy clusters and their associated ionic current are comparable to both macroscopic measurements as well as theoretical models. We posit that the general framework of this approach is straightforward to adapt to different types of defects, for example dislocations and twin walls, allowing for quantitative studies of population dynamics in a fast and efficient manner. Such studies are particularly relevant to mesoscopic and multi-scale modelling approaches, where quantitative data obtained under realistic conditions and *in-situ* drivers is essential for guidance and validation. In the context of oxygen vacancies, however, the presented method could reveal the mechanisms behind such pervasive and important phenomena

as aging and nucleation [18].

## ACKNOWLEDGMENTS

The authors are grateful to the ESRF for providing beamtime for this work and Danscatt for providing financial assistance for travel to and from beamtime. This work is financed through a NTNU-DTU tandem PhD agreement. In addition, H.S. acknowledges support from an ERC Starting Grant.

## Appendix A: Derivation of strain histogram

We here derive our model for the strain and displacement fields around an embedded inclusion. We assume the fields are measured using dark-field x-ray microscopy, which implies the following:

- The strain and displacement fields comprise the “axial” components only, i.e. the strains and displacement parallel to the scattering vector  $\vec{Q}_{hkl}$ .
- The measurements are made in the “section” geometry in which the sample is illuminated with a line-profiled x-ray beam of finite thickness. The images therefore resemble a cross-section through the sample, albeit integrated through the thickness of the line profile.

To simplify matters, we assume the inclusion is spherical and that its matrix is isotropic. The strain and displacement fields are therefore radially symmetric, meaning they can be defined in terms of the radial position vector  $\vec{r}$  and its magnitude  $r$ . These, in turn, are defined in terms of Cartesian coordinates:

$$\vec{r} = \begin{pmatrix} x \\ y \\ z \end{pmatrix}, \quad r = \sqrt{x^2 + y^2 + z^2} \quad (\text{A1})$$

The model assumes that, in this coordinate system,  $z$  is parallel to  $\vec{Q}_{hkl}$ , with  $x$  and  $y$  mutually perpendicular and normal to  $z$ .

The displacement originates from two sources: the *eigenstrain* of the inclusion itself, and the *residual strain* the inclusion imparts to the matrix. Based on Eshelby’s arguments, we assume the residual strain affects only the matrix, i.e. where  $\vec{r}$  is beyond the position of the inclusion-matrix interface,  $r_i$ :

$$\vec{u} = \begin{cases} \epsilon_{eig} \vec{r} & r \leq r_i \\ \epsilon_{res} \vec{r} & r \geq r_i \end{cases} \quad (\text{A2})$$

In Eshelby’s formalism, the eigenstrain and the residual strain have the following form:

$$\epsilon_{eig} = A, \quad \epsilon_{res} = \frac{B}{r^3} \quad (\text{A3})$$

where  $A$  and  $B$  are constants, found by considering the compatibility conditions at the inclusion-matrix interface.

As Eshelby assumes the eigenstrain is constant throughout the inclusion,  $A$  is simply the strain of the inclusion relative to the matrix, i.e.  $A = \epsilon_i$ . We then find  $B$  by assuming the lattice is continuous at inclusion-matrix interface (i.e. at  $r = r_i$ ):  $A = \frac{B}{r_i^3}$ . Thus,  $B = Ar_i^3 = \epsilon_i r_i^3$ . We can then write the complete displacement field for the Eshelby case:

$$\vec{u} = \begin{cases} \epsilon_i \vec{r} & r \leq r_i \\ \epsilon_i \frac{r_i^3}{r^3} \vec{r} & r \geq r_i \end{cases} \quad (\text{A4})$$

Taking the derivative of the displacement field with respect to  $z$  then gives us a piecewise expression for the axial strain:

$$\epsilon_{zz} = \begin{cases} \epsilon_i & r \leq r_i \\ \epsilon_i (x^2 + y^2 - 2z^2) \frac{r_i^3}{r^5} & r \geq r_i \end{cases} \quad (\text{A5})$$

The average strain averaged over a symmetrical line beam of thickness  $\delta_z$  is then given by:

$$\langle \epsilon_{zz} \rangle_{\delta_z} = \frac{1}{\delta_z} \int_{-\delta_z/2}^{+\delta_z/2} \epsilon_{zz} dz \quad (\text{A6})$$

Which gives us the final strain field, as measuring using DFXM:

$$\langle \epsilon_{zz} \rangle_{\delta_z} = \begin{cases} \epsilon_i \leq r_i \\ \epsilon_i \frac{r_i^3}{(r_{xy}^2 + \delta_z^2/4)^{3/2}} & r \geq r_i \end{cases} \quad (\text{A7})$$

where  $r_{xy}^2 = x^2 + y^2$ , i.e. the radial position in the  $(x, y)$  plane.

The strain *histogram* is essentially then a plot of how much area in the sampling window has values of the strain magnitude within some given range:  $\epsilon - \delta_\epsilon/2 \leq \langle \epsilon_{zz} \rangle_{\delta_z} \leq \epsilon + \delta_\epsilon/2$ , where  $\epsilon$  is the target strain (i.e. the center of the strain bin) and  $\delta_\epsilon$  is the width of the strain bin. Because the strain magnitude is constantly decreasing with  $r_{xy}$ , this area is simply:

$$\Omega_\epsilon = \pi (r_{-\delta_\epsilon}^2 - r_{+\delta_\epsilon}^2) \quad (\text{A8})$$

where  $r_{\pm\delta_\epsilon}$  are the values of  $r_{xy}$  where  $\langle \epsilon_{zz} \rangle_{\delta_z} = \epsilon \pm \delta_\epsilon/2$ , respectively. These are written explicitly as:

$$r_{-\delta_\epsilon}^2 = \frac{1}{r_i^2} \left( \frac{\epsilon_i}{\epsilon - \delta_\epsilon} \right)^{2/3} - \frac{\delta_z^2}{4}, \quad (\text{A9})$$

$$r_{+\delta_\epsilon}^2 = \frac{1}{r_i^2} \left( \frac{\epsilon_i}{\epsilon + \delta_\epsilon} \right)^{2/3} - \frac{\delta_z^2}{4} \quad (\text{A10})$$

The strain histogram can then be found by finding  $r_{\pm\delta_\epsilon}^2$  for each relevant value of  $\epsilon$ . Note that the distribution is bounded since  $r_{xy}$  cannot be smaller than  $r_i$ , nor larger than the radius of the sampling window. Furthermore, the histogram should include the contribution from the inclusion itself,  $\pi r_i^2$ , located at  $\epsilon = \epsilon_i$ .

## Appendix B: Derivation of number of oxygen vacancies

The number of oxygen vacancies within a given pixel is given by:

$$N = \rho V \quad (\text{B1})$$

where  $\rho$  is the volumetric density of oxygen vacancies for that pixel and  $V = 4/3 r_i^3$  is the inclusion volume. To calculate  $\rho$ , we consider the volumetric chemical strain:

$$\epsilon_V = \alpha \rho \quad (\text{B2})$$

where  $\alpha$  is the volume change associated with one vacancy (determined from DFT calculations, detailed below). The volumetric strain  $\epsilon_V$  is related to the measured axial strain through:

$$\langle \epsilon_{zz} \rangle_{\delta_z} = \sqrt[3]{1 + \epsilon_V} - 1. \quad (\text{B3})$$

Substituting Eq. X into Eq. Y and solving for  $\rho$  then gives us:

$$\rho = \frac{1}{\alpha} [(\langle \epsilon_{zz} \rangle_{\delta_z}^3 - 1)^3 - 1] \quad (\text{B4})$$

And thus the total number of vacancies per pixel is:

$$N = \frac{r_i^3}{\alpha} [(\langle \epsilon_{zz} \rangle_{\delta_z}^3 - 1)^3 - 1] \quad (\text{B5})$$

## Appendix C: Details of density functional theory calculations

The DFT calculations were performed with the electronic structure software package GPAW [10.1088/0953-8984/22/25/253202] relying on the Atomic Simulation environment (ASE) [19]. All calculations were performed using the projector augmented wave method (PAW) using a plane-wave basis set with an energy cutoff of 600 eV and the Perdew-Burke-Ernzerhof exchange-correlation functional [20]. For the 2x2x2 supercell we used a Brillouin zone sampling of 3x3x3 k-points and relaxed the structure until forces were below 1 meV/Å. For the 3x3x3 supercell, we used a 2x2x2 k-point grid and relaxed the structure until all forces were below 5 meV/Å.

- 
- [1] Y. Zhou, H. K. Chan, C. H. Lam, and F. G. Shin, Mechanisms of imprint effect on ferroelectric thin films, *Journal of Applied Physics* **98**, 024111 (2005).
- [2] D. Damjanovic, Ferroelectric, dielectric and piezoelectric properties of ferroelectric thin films and ceramics, *Reports on Progress in Physics* **61**, 1267 (1998).
- [3] L. X. Zhang and X. Ren, In situ observation of reversible domain switching in aged mn-doped batio<sub>3</sub> single crystals, *Physical Review B - Condensed Matter and Materials Physics* **71**, 174108 (2005).
- [4] X. Ren, Large electric-field-induced strain in ferroelectric crystals by point-defect-mediated reversible domain switching, *Nature Materials* **3**, 91 (2004).
- [5] Y. A. Genenko, N. Balke, and D. C. Lupascu, Migration of charged defects in local depolarization fields as a mechanism of aging in ferroelectrics, *Ferroelectrics* **370**, 196 (2008).
- [6] C. A. Randall, R. Maier, W. Qu, K. Kobayashi, K. Morita, Y. Mizuno, N. Inoue, and T. Oguni, Improved reliability predictions in high permittivity dielectric oxide capacitors under high dc electric fields with oxygen vacancy induced electromigration, *Journal of Applied Physics* **113**, 014101 (2013).
- [7] M. Li, M. J. Pietrowski, R. A. De Souza, H. Zhang, I. M. Reaney, S. N. Cook, J. A. Kilner, and D. C. Sinclair, A family of oxide ion conductors based on the ferroelectric perovskite na<sub>0.5</sub>bi<sub>0.5</sub>ti<sub>0.3</sub>, *Nature Materials* **13**, 31 (2014).
- [8] L. Hong, A. K. Soh, Q. G. Du, and J. Y. Li, Interaction of o vacancies and domain structures in single crystal bati o<sub>3</sub>: Two-dimensional ferroelectric model, *Physical Review B - Condensed Matter and Materials Physics* **77**, 094104 (2008).
- [9] W. Liu and C. A. Randall, Thermally stimulated relaxation in fe-doped sr<sub>1-x</sub>ti<sub>3</sub> systems: I. single crystals, *Journal of the American Ceramic Society* **91**, 3245 (2008).
- [10] S. Jesse, B. J. Rodriguez, S. Choudhury, A. P. Baddorf, I. Vrejoiu, D. Hesse, M. Alexe, E. A. Eliseev, A. N. Morozovska, J. Zhang, L. Q. Chen, and S. V. Kalinin, Direct imaging of the spatial and energy distribution of nucleation centres in ferroelectric materials, *Nature Materials* **7**, 209 (2008).
- [11] H. Simons, A. B. Haugen, A. C. Jakobsen, S. Schmidt, F. Stoumlhr, M. Majkut, C. Detlefs, J. E. Daniels, D. Damjanovic, and H. F. Poulsen, Long-range symmetry breaking in embedded ferroelectrics, *Nature Materials* **17**, 814 (2018).
- [12] J. ESHELBY, The determination of the elastic field of an ellipsoidal inclusion, and related problems, *Proceedings of the Royal Society of London Series A-mathematical and Physical Sciences* **241**, 376 (1957).
- [13] H. Simons, A. C. Jakobsen, S. R. Ahl, C. Detlefs, and H. F. Poulsen, Multiscale 3d characterization with dark-field x-ray microscopy, *Mrs Bulletin* **41**, 454 (2016).
- [14] H. F. Poulsen, A. C. Jakobsen, H. Simons, S. R. Ahl, P. K. Cook, and C. Detlefs, X-ray diffraction microscopy based on refractive optics, *Journal of Applied Crystallography* **50**, 1441 (2017).
- [15] O. Jeppe, O. Emil, D. Carsten, M. Ragnvald, Y. Can, K. Mustafacan, C. Philip, W. Yves, C. Carlos, and S. Hugh, Imaging microstructural dynamics and strain fields in electro-active materials in-situ with dark field x-ray microscopy, *Review of Scientific Instruments* (2019).
- [16] M. Kessel, R. A. De Souza, and M. Martin, Oxygen diffusion in single crystal barium titanate, *Physical Chemistry Chemical Physics* **17**, 12587 (2015).
- [17] S. SHARMA, M. MACHT, and V. NAUNDORF, Impurity-diffusion investigations in amorphous ti<sub>60</sub>ni<sub>40</sub>, *Physical Review B* **49**, 6655 (1994).
- [18] R. Pandey, G. Vats, J. Yun, C. R. Bowen, A. W. Hobbaillie, J. Seidel, K. T. Butler, and S. I. Seok, Mutual insight on ferroelectrics and hybrid halide perovskites: A platform for future multifunctional energy conversion, *Advanced Materials* **31**, 1807376 (2019).
- [19] A. Hjorth Larsen, J. J. Mortensen, J. Blomqvist, I. E. Castelli, R. Christensen, M. Dulak, J. Friis, M. N. Groves, B. Hammer, C. Hargus, E. D. Hermes, P. C. Jennings, P. B. Jensen, J. Kermode, J. R. Kitchin, E. L. Kolsbjerg, J. Kubal, K. Kaasbjerg, S. Lysgaard, J. B. Maronsson, T. Maxson, T. Olsen, L. Pastewka, A. Peterson, C. Rostgaard, J. Schiøtz, O. Schutt, M. Strange, K. S. Thygesen, T. Vegge, L. Vilhelmsen, M. Walter, Z. Zeng, and K. W. Jacobsen, The atomic simulation environment—a python library for working with atoms, *Journal of Physics-condensed Matter* **29**, 273002 (30 pp.), 273002 (30 pp.) (2017).
- [20] J. P. Perdew, K. Burke, and M. Ernzerhof, Generalized gradient approximation made simple, *Physical Review Letters* **77**, 3865 (1996).

## 6.2 Discussion of the fitting of strains from vacancy clusters

Recall the form of the expression for the strain histogram from a spherical Eshelby inclusion:

$$\Omega_{\epsilon_0} = \left[ \left( \frac{\epsilon - \frac{\delta\epsilon}{2}}{\epsilon_0 r_{incl}^3} \right)^{-2/n} - \frac{\delta z^2}{4} \right] - \left[ \left( \frac{\epsilon + \frac{\delta\epsilon}{2}}{\epsilon_0 r_{incl}^3} \right)^{-2/n} - \frac{\delta z^2}{4} \right] \quad (6.1)$$

Here  $\epsilon$  is the strain at a specific bin in the histogram,  $\epsilon_0$  is the initial strain for each point,  $\delta z$  is the thickness of the line beam illuminating the sample,  $r_{incl}$  is the radius of inclusion, and  $n$  is model exponent factor. Furthermore, please note that this is not the full piecewise function, derivations and boundaries for each piece can be found in the supplementary material of the following paper, section 6.1. From this formalism it is possible to extract several parameters across used in the model, allowing for local mapping of these fitted parameters as seen in figure 6.1.

The data presented in the paper assumed a fixed value of 3 for the exponent  $n$ . This value is derived from the inverse cubic decay of strain in 3D solids, and is evident in Eshelby's original formalism. However, based on our observations that an exponent of 3 often results in an unexpectedly sharp profile in the strain histogram, we here consider a variation to that approach used in the paper, where the exponent  $n$  is also fitted to the decay.

Figure 6.1 shows the fitted parameters from strain maps above  $T_C$ , with and without an applied electric field. This also shows us that the fitted parameters are being gathered from all over the map, in a pattern related to the strain map. The map containing the initial strain conditions  $\epsilon_0$  and inclusion radius  $r_{incl}$ , have an inherent physical meaning. The exponent factor  $n$ , however, is a little more tricky to interpret. When  $n$  has a value lower than three the decay from an inclusion is slower, ergo having longer reaching strain fields. Since Eshelby's theory assumes a sharp transition from the inclusion with homogeneous strain to surrounding matrix, pixels with a value close to three, will be more closely represented by this assumption. We can say that if the area is saturated, e.g. a homogeneous distribution of vacancies, or at least have a higher density near saturation, it would form a close to ideal decay. Vice versa, for pixels with an  $n$  value lower than three, assumptions of the sharp inclusion edge is not strictly true. This could be interpreted as a more diffuse boundary between the inclusion and matrix. This would make sense, since in this case the inclusion represents a cluster of vacancies. Hence, it can be stated that the strain distribution of pixel, which possess a value of  $n$  close to 3 should have a more ideal decay, while they should also contain in average a higher number of vacancies than average.

Shown in figure 6.2, is the comparison of the distributions of the initial strain and the number of vacancies for both the normal data set and the data subjected to a threshold by values of  $n$  close to three. In pixels with  $n$  values close to three, it can indeed be seen, that a sharper strain distribution is present and the average number of vacancies are much higher. However, charged defects and their movement have not usually been analysed in the bulk via microscopy. Hence we explore other models of a more traditional fashion for which to make a comparison against our new method.

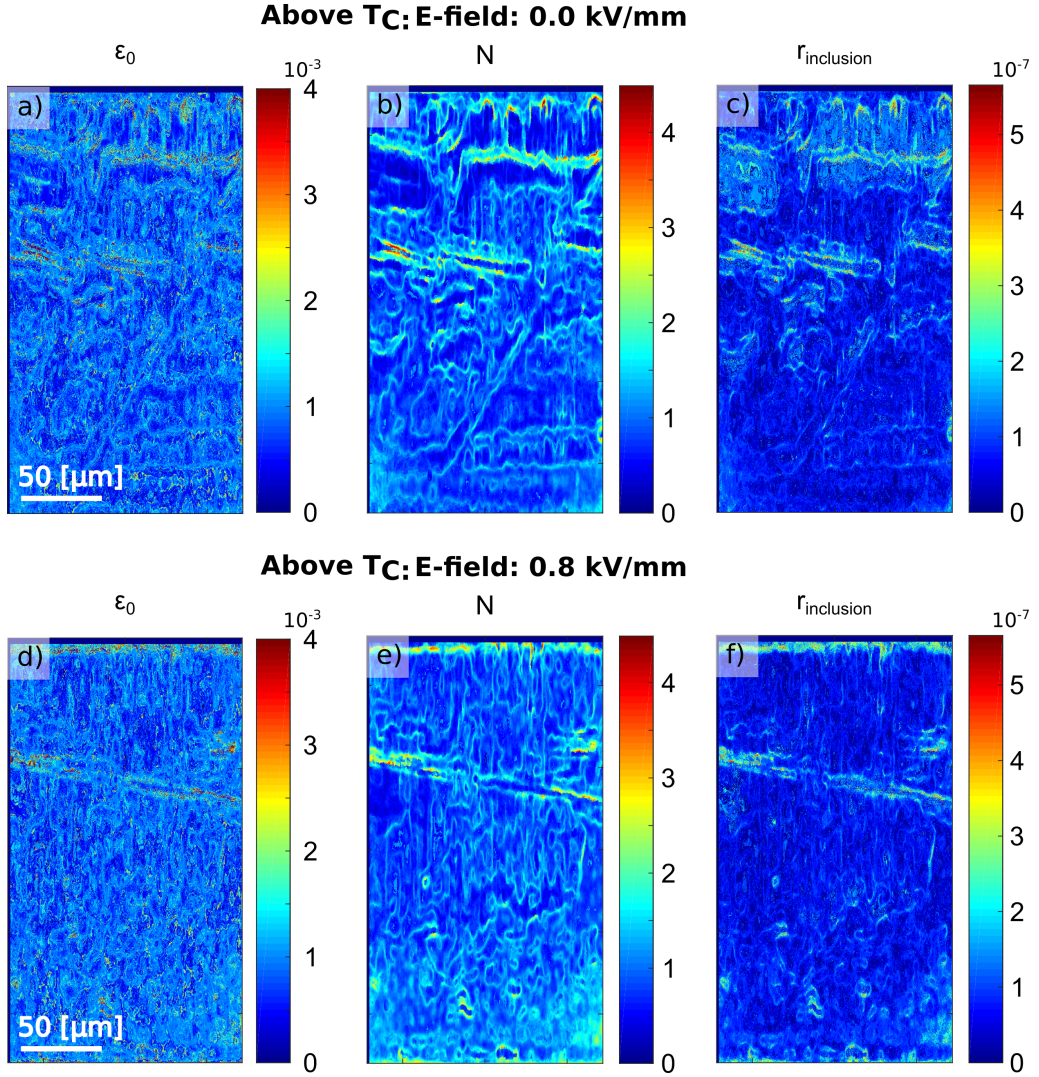


Figure 6.1: The figure shows a map of the fitted parameters from the defect detection method. a) and d) show the fitted initial strain, b) and e) shows the fitted exponent  $N$  and c) and f) shows the fitted radius of the inclusion. a), b) and c) is from the case with no applied field, while d), e) and f) is from the case with an applied field of 0.8 kV/mm.

### 6.3 Discussion of the diffusion/migration of charged defects in oxide perovskites

Defects in most ferroic materials will with time diffuse/migrate within the material, i.e. it will age the material. This usually follows with a system-specific change of properties, mostly linked to the stabilization of domain walls. Several process such as ionic drift [55], orientation of defects dipoles [14] and the formation of space charge regions [31][20] contribute. The aforementioned mechanisms are all related to defects ordering in the material. The diffusion of defects can be described in many ways under different conditions, normally all linked to some way of formulating a coefficient for the mobility of the defects, the most usual case is a vacancy. The general case in solids can be formulated with an Arrhenius equation, though here it expand the diffusion coefficient to the following:

$$D_v = \frac{1}{6} a^2 \nu z \exp\left(-\frac{U}{RT}\right) [56]. \quad (6.2)$$

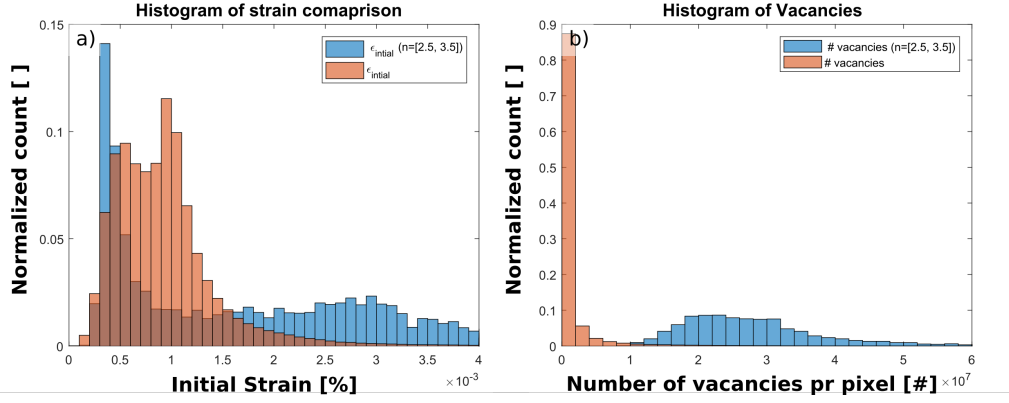


Figure 6.2: a) comparison of the normalized distribution of initial strain for the threshold data  $n = [2.5 - 3.5]$ , and the full data set. b) comparison of the normalized distribution of the vacancies per pixel for the threshold data  $n = [2.5 - 3.5]$ , and the full data set.

Here  $1/6$  is the coordination number,  $a$  the lattice constant,  $z$  is number of possible site it can jump to,  $\nu$  is the jump frequency,  $R$  is the gas constant,  $T$  the temperature and  $U_m$  is the activation energy barrier for migration. This description of mass diffusivity is used in many models to ascertain the physical mechanisms of migration. One such model has been proposed C. Randall [52], where ionic species migration under an electrical field can be formulated as a current:

$$I_{model} = 2q_0 N a \nu \exp\left(-\frac{U}{K_B T}\right) \sinh\left(\frac{q_0 E_a}{K_B T}\right) [52]. \quad (6.3)$$

Here  $q_0$  is the elementary charge,  $N$  is the number of charges carriers,  $K_B$  is the Boltzmann constant and  $E_a$  is the applied electrical field.

From this model it is clear that if the temperature is static, the driving force for migration should only be the applied electrical field. The applied field has the added effect of promoting the migration parallel to the field direction. Seen from the STEF holder paper 4.2, we applied a field to the two flats of the sample and illuminated the cross section of the sample. With the stable temperature of the system and strain maps under different field applications we meet the requirement to use the model for ionic current. Hence, if our method can detect charged defects and their movement, it can then be related to the ionic current from the model. It is important to note that the strain map from the sample are only taken after the field has hit the maximum value for some time, to ensure the capacity current is not influencing the measurement.

# 7 Discussion and Conclusion

Following the work presented in the previous chapters, this chapter serves to discuss their relevance to the main aims and hypotheses for the thesis, and to state the major conclusions that can be made as a result. An outlook describing potential directions for future work will then be given as the final component of this thesis.

## 7.1 General Discussion

In the previous chapters, the capabilities of DXFM and related methods have been presented with a focus on phenomena relating to materials. The results they detail demonstrate that we have clearly moved beyond the surface, and into the bulk when it comes to the analysis of local effects in crystalline materials. As stated in the hypothesis chapter 3, this is a significant limitation for our continued understanding of ferroelectric (and perhaps all) materials. The methodologies presented in this thesis are the first step towards imaging defects and heterogeneities in bulk ferroelectrics, and form a significant part of a larger effort to achieve insight and understanding of the fundamental mechanisms governing multi-scale structural dynamics in ferroelectric materials. But how did these new capabilities help answer the question stated in the hypothesis; how do defects and heterogeneities interact with an electric field induced phase transformation in the bulk?

The answer is not a straightforward “detective story” to find a single explanation for the wide variety of phenomena we have seen unfold in the DXFM data. While the material system  $\text{BaTiO}_3$  is an archetypal ferroelectric, many fundamental aspects of the phase transformation, its dynamics, and the role of vacancies and heterogeneities, are still not particularly well-understood [18][53][32][21]. Many phenomena relating to these interactions have multiple explanations and interpretations, as well as considerable doubt regarding the length scales the mechanisms are believed to act over [31][48][22]. As a consequence of this ambiguity, I am therefore motivated to argue that no single effect can govern the event that give rise to our observations, specifically the seemingly intermediate phase after field has been removed, the wavy domain-like features above  $T_c$  and distribution of defect clusters in the bulk. Moreover, the multitude of fundamental effects we have investigated throughout this study - electric field induced phase transformations, domain formation and defect migration - might all play a simultaneous role. In this section I attempt to relate their role in the multitude of complex interaction and effects they might have on the complex response of the material system. Thus, for the reader’s consideration, I present a detailed discussion addressing the core questions posed in the introduction and hypothesis.

The evidence of domain imprint above  $T_c$  in bulk crystals show clear structural heterogeneities in the average and local RSM’s. Furthermore, the strain related to the imprint features indicated that it was capable of raising  $T_c$  by several K, potentially resulting in a “memory” of the previous domain structure. It is worth noting that the agglomeration of vacancies along the domain walls may not be evenly distributed along the wall. The fluctuation of this density was presumably preceded by a fluctuation in affinity for vacancy density. This initial variation in the affinity for vacancy agglomeration is most likely a consequence of underlying heterogeneity in the strain fields in the bulk. Although these strain fields probably originated from  $90^\circ$  domain walls along 110-type directions, they are not required to follow strict crystallographic directions as well. This could help to explain the curved nature of the imprint features. This also explains why we predominantly see

features along a 45° angle, approximately parallel to the 90° domain walls in the room-temperature ferroelectric state. Importantly, the chemical strain from the vacancies would cause a rise in local entropy and an increase in lattice parameter due to the volume expansion. The diffusion coefficient for vacancies can be formulated in a way where we can see the effect of the increase in entropy, as follows:

$$D_v = \frac{1}{6} a^2 z \nu \exp\left(\frac{\Delta S}{R}\right) \exp\left(\frac{-\Delta H}{RT}\right) [56] \quad (7.1)$$

Here,  $a$  is the characteristic jump distance,  $\nu$  is the ion jump frequency,  $z$  is number of possible site it can jump to,  $R$  is the gas constant and  $T$  is the temperature. The effect of the vacancies on the local environment is clearly not spatially symmetrical around its position and, since the entropy and lattice parameter both are larger in close proximity to the vacancy, this will increase the diffusion coefficient as a consequence. Thus, regions are created with a higher affinity for vacancies to agglomerate in.

The accumulation and ordering of vacancies along elastic fields in the bulk would not only arise in the ferroelectric phase but also in a cubic phase, as shown in our paper presented in section 6.1. Here we show the vacancy distribution following the strain field to some extent, without them needing to be strongly discontinuous heterogeneities, such as domain walls [21].

In our example where the electrical field was applied while the sample is heated to just above  $T_C$ , we see that the distribution of vacancies change such that they create a bias towards the electrode surface. During this process, we could clear see that a phase transformation occurred, and that the sample exhibited a monodomain configuration. The current generated by the polarization change would aid in the migration of the charged vacancies, but is altogether believed insignificant compared to the sustained application of the electric field during the measurement. Hence, we have demonstrated a method for detecting clusters of defects and their movement in the bulk, free of larger heterogeneities, such as grain boundaries, domain walls and dislocations. However, we note that the method might potentially also work in regions possessing multiple domains, provided their structural signals could be detected and deconvolved from the signal corresponding to the vacancies.

In general, it can be argued that elastic and electric fields can alter the density of vacancies according to the distribution of these fields within the sample. These fields can either be generated by domain walls, clusters of vacancies, or any other sources of local strain variation. The agglomerations of defects can lead to the imprint of domain-like features above  $T_C$ , which then act as seeds for domain nucleation when cooled through  $T_C$ . The distribution of charged defects can be altered by biasing their migration with an applied field. In turn, this also affect the domains configuration, for example by leading to a monodomain state.

## 7.2 Conclusions

Based on the work described in this thesis, the following conclusions and statement can be made:

- Combined with 50 years of literature on the topic, our investigations mean we can say the local morphological features have an defining impact on the ferroelectric properties, and thus need to be quantified at all relevant length and time scales in order to predict their specific influences.
- Mapping critical phenomena, such as phase transformations, requires an extremely high degree of stability in terms of the temperature and electric field the sample is subject to. To this end, the STEF holder was developed and used with great success. The fourth generation of the holder is capable of sufficient precision of  $\pm 0.01^\circ\text{K}$  and control of the temperature, which is demonstrated through a variety of studies of the first order phase transformation in the prototypical ferroelectric material  $\text{BaTiO}_3$ .
- Furthermore, the STEF holder is able to be integrated into multiple other characterization techniques that utilize the same transmission geometry, with the allowable space for the holder and the working distance of the probe being the only key limitation. We demonstrate that the system works well with polarization light optical microscopy (see Appendix), however the system could also be used with e.g. powder diffraction, SEM and related electron microscopy techniques.
- For the first time, we observe domain imprint above the Curie temperature in the bulk ferroelectric single crystals. On a related note, we can state that the surface has clear distortions that differentiate it from the bulk. Furthermore, from these observations we can also claim that defects influences the local domain structure and formation, on both sides of the para-to-ferroelectric phase transformation.
- We have proven that, with our method, it is possible to detect oxygen vacancies clusters and follow their migration in bulk ferroelectrics during the application of a constant electric field. This can lead to the potential of quantifying of oxygen vacancy distributions and their effect on morphological features, such as the wavy domain imprint above  $T_C$  and along grain boundaries.
- Finally, I present a framework in the form of a holder system and methods, which have been produced to guide further investigation into the fundamental nature of structural dynamics in ferroelectric materials, with the focus of revealing the governing mechanism of heterogeneous nucleation in solid-state phase transformation.

### 7.3 Outlook

In many fields of science and engineering, tracking morphological features in image data has become routine and a very valuable tool. Closely related to our type of data, is images obtained with high resolution TEM, where recent development have demonstrated good results with tracking atomic positions using deep learning techniques [57]. Based on convolutional neural networks, such algorithms can recognize different local structures in each dataset by first finding the atomic structures from high resolution TEM data. This is achieved by generating a training dataset with well established simulation tools for TEM images. These tool can generate the various permutation of images with respect to variations in machine instrumentation, aberrations and data collections, as detailed in [57].

For this method to work with our DFXM data sets, the framework for the generation of phantom data with perturbations to the images from instrument parameters (i.e. aberrations) would have to be built from the ground up. This has been proposed to be carried out with wave propagation approaches (e.g. multi-slice), which would then enable influence from the different aberration-inducing components of the microscope, such as lenses and slits. However, the input for such a model is a 3D representation for the atomic displacement field at the nm -  $\mu\text{m}$  scale. Such a model is currently under development, but so far unsuccessful in the case of  $\text{BaTiO}_3$ .

If this last problem is are solved, however, it could lead to a strong new tool for tracking morphological features in DFXM data. If it proves possible to produce a displacement field for various material system in the DFXM setting, it would likewise be a very versatile method.

The section about detecting defects is a presentation of our first methods of detecting vacancies in bulk strain data and using the information to reveal certain aspects of the fundamental behavior of features in the bulk material. Essentially, we attempt to separate the strain signal generated by the local cluster of defects from the overall background strain in the sample. At the current stage, it is an "ad hoc" deconvolution of the different strain signals in the data set. Better deconvolution algorithms and methods could surely be implemented to optimize the detection of vacancies and otter defects, both in terms of speed and accuracy.

The aforementioned perspective to future work could be the first steps in gathering *real* statistical data on bulk features. The obvious benefits of this is their use in the quantitative validation or evaluation of models and simulations. Tracking specific features in the DFXM intensity map would reveal individual characteristics of their behaviour and interaction and from larger data sets, their characteristics at a statistical level. This could be, for example, size, speed, roughness, inclination, distribution and variation of domains, domain walls, dislocations and other defects. These are relevant parameters for various models predicting the specific macroscopic properties of a given material. More importantly, given the origin of this project, it could be used to track various domains during heterogeneous nucleation.

Prevailing theories suggest that nucleation is seeded by some sort of defect or local lattice distortion, e.g. an inhomogeneity in the local strain. Even though tracking strain temporally is not yet realistic, initial and final strain condition of an *in situ* experiment are obtainable, allowing for the detecting of features in a strain map of the initial conditions.

The related features in the intensity map can the be tracked temporally and related to the final data. This, to some extent, resembles our method for detecting defects in that it compares initial and final strain maps and how features have moved within them. Track-

ing defects via a convolutional neural network will give a precise measure of the feature dynamics, as well as the ability to extract various parameters depending on the training data and input parameters. Such parameters could be a velocity of a domain wall or defect, while also revealing when it started moving during the experiment, if its speed was constant, and if it moved in a straight line. Combining this information about the microscopic movements and structures in time, combined with macroscopic measurements and boundary conditions, would be a powerful tool. It is my hope that such framework will spawn a string of models leading to better understand the fundamental mechanisms that governs heterogeneous nucleation in ferroelectric materials.

# Bibliography

- [1] Kirstin Alberi, Marco Buongiorno Nardelli, Andriy Zakutayev, Lubos Mitas, Stefano Curtarolo, Anubhav Jain, Marco Fornari, Nicola Marzari, Ichiro Takeuchi, Martin L. Green, Mercouri Kanatzidis, Mike F. Toney, Sergiy Butenko, Bryce Meredig, Stephan Lany, Ursula Kattner, Albert Davydov, Eric S. Toberer, Vladan Stevanovic, Aron Walsh, Nam Gyu Park, Alán Aspuru-Guzik, Daniel P. Tabor, Jenny Nelson, James Murphy, Anant Setlur, John Gregoire, Hong Li, Ruijuan Xiao, Alfred Ludwig, Lane W. Martin, Andrew M. Rappe, Su Huai Wei, and John Perkins. The 2019 materials by design roadmap. *Journal of Physics D: Applied Physics*, 52(1):013001, 2019.
- [2] Aditya Chauhan, Satyanarayan Patel, Rahul Vaish, and Chris R. Bowen. Antiferroelectric ceramics for high energy density capacitors. *Materials*, 8(12):8009–8031, 2015.
- [3] Denis O. Alikin, Anton P. Turygin, Julian Walker, Andreja Bencan, Barbara Malic, Tadej Rojac, Vladimir Ya Shur, and Andrei L. Kholkin. The effect of phase assemblages, grain boundaries and domain structure on the local switching behavior of rare-earth modified bismuth ferrite ceramics. *Acta Materialia*, 125:265–273, 2017.
- [4] Dennis M. Zogbi. Ceramic capacitors: World markets, technologies and opportunities: 2019-2024. 2019.
- [5] Susan Trolier-McKinstry and Clive A. Randall. Movers, shakers, and storers of charge: The legacy of ferroelectricians I. eric cross and robert e. newnham. *Journal of the American Ceramic Society*, 100(8):3346–3359, 2017.
- [6] Alexander K Tagantsev, L Eric Cross, and Jan Fousek. Domains in ferroic crystals and thin films. 2010.
- [7] Manfred Fiebig, Thomas Lottermoser, Dennis Meier, and Morgan Trassin. The evolution of multiferroics. *Nature Reviews Materials*, 1(8), 2016.
- [8] J. Mannhart. The interface is still the device. *Nature Materials*, 11(2):91–91, 2012.
- [9] Cheng Ma, Hanzheng Guo, Scott P Beckman, and Xiaoli Tan. Creation and destruction of morphotropic phase boundaries through electrical poling: a case study of lead-free  $(\text{Bi}_{(1/2)}\text{Na}_{(1/2)})\text{TiO}_3\text{-BaTiO}_3$  piezoelectrics. *Physical Review Letters*, 109(10):107602, 107602, 2012.
- [10] Margareth Gagliardi. Materials with market value: Global ceramic and glass industry poised to reach 1 trillion usd. *American Ceramic Society Bulletin*, 96(3):27–37, 2017.
- [11] S. Saremi, R. Gao, A. Dasgupta, and L. W. Martin. New facets for the role of defects in ceramics. *American Ceramic Society Bulletin*, 97(1):16–23, 2018.
- [12] Qiao Qiao, Yuyang Zhang, Rocio Contreras-Guerrero, Ravi Droopad, Sokrates T. Pantelides, Stephen J. Pennycook, Serdar Ogut, and Robert F. Klie. Direct observation of oxygen-vacancy-enhanced polarization in a  $\text{SrTiO}_3$ -buffered ferroelectric  $\text{BaTiO}_3$  film on GaAs. *Applied Physics Letters*, 107(20):201604, 2015.
- [13] Ming Wen Chu, Izabela Szafraniak, Dietrich Hesse, Marin Alexe, and Ulrich Gösele. Elastic coupling between  $90^\circ$  twin walls and interfacial dislocations in epitaxial ferroelectric perovskites: A quantitative high-resolution transmission electron microscopy

- study. *Physical Review B - Condensed Matter and Materials Physics*, 72(17):174112, 2005.
- [14] XB Ren. Large electric-field-induced strain in ferroelectric crystals by point-defect-mediated reversible domain switching. *Nature Materials*, 3(2):91–94, 2004.
- [15] L. X. Zhang and X. Ren. In situ observation of reversible domain switching in aged Mn-doped BaTiO<sub>3</sub> single crystals. *Physical Review B - Condensed Matter and Materials Physics*, 71(17):1–8, 2005.
- [16] J. Seidel, L. W. Martin, Q. He, Q. Zhan, Y. H. Chu, A. Rother, M. E. Hawkrige, P. Maksymovych, P. Yu, M. Gajek, N. Balke, S. V. Kalinin, S. Gemming, F. Wang, G. Catalan, J. F. Scott, N. A. Spaldin, J. Orenstein, and R. Ramesh. Conduction at domain walls in oxide multiferroics. *Nature Materials*, 8(3):229–234, 2009.
- [17] Dragan Damjanovic. Ferroelectric, dielectric and piezoelectric properties of ferroelectric thin films and ceramics. *Reports on Progress in Physics*, 61:1267, 1998.
- [18] M. Acosta, N. Novak, V. Rojas, S. Patel, R. Vaish, J. Koruza, G. A. Rossetti, and J. Rödel. BaTiO<sub>3</sub>-based piezoelectrics: Fundamentals, current status, and perspectives. *Applied Physics Reviews*, 4(4):041305, 2017.
- [19] Julian Walker, Hugh Simons, Denis O. Alikin, Anton P. Turygin, Vladimir Y. Shur, Andrei L. Kholkin, Hana Ursic, Andreja Bencan, Barbara Malic, Valanoor Nagarajan, and Tadej Rojac. Dual strain mechanisms in a lead-free morphotropic phase boundary ferroelectric. *Scientific Reports*, 6(November 2015):1–8, 2016.
- [20] Yuri A. Genenko and Doru C. Lupascu. Drift of charged defects in local fields as aging mechanism in ferroelectrics. *Physical Review B - Condensed Matter and Materials Physics*, 75(18):1–10, 2007.
- [21] L. Hong, A. K. Soh, Q. G. Du, and J. Y. Li. Interaction of O vacancies and domain structures in single crystal BaTiO<sub>3</sub>: Two-dimensional ferroelectric model. *Physical Review B - Condensed Matter and Materials Physics*, 77(9):094104, 2008.
- [22] Stephen Jesse, Brian J. Rodriguez, Samrat Choudhury, Arthur P. Baddorf, Ionela Vrejoiu, Dietrich Hesse, Marin Alexe, Eugene A. Eliseev, Anna N. Morozovska, Jingxian Zhang, Long Qing Chen, and Sergei V. Kalinin. Direct imaging of the spatial and energy distribution of nucleation centres in ferroelectric materials. *Nature Materials*, 7(3):209–215, 2008.
- [23] Linxing Zhang, Jun Chen, Longlong Fan, Oswaldo Diéguez, Jiangli Cao, Zhao Pan, Yilin Wang, Jinguo Wang, Moon Kim, Shiqing Deng, Jiaou Wang, Huanhua Wang, Jinxia Deng, Ranbo Yu, James F. Scott, and Xianran Xing. Giant polarization in super-tetragonal thin films through interphase strain. *Science*, 361(6401):494–497, 2018.
- [24] Walter J. Merz. Domain Formation and Domain Wall Motions in Ferroelectric BaTiO<sub>3</sub> Single Crystals. *Physical Review*, 95(3):690–698, 1954.
- [25] WJ MERZ. Double hysteresis loop of batio3 at the curie point. *Physical Review*, 91(3):513–517, 1953.
- [26] D. Walker, A. M. Glazer, S. Gorfman, J. Baruchel, P. Pernot, R. T. Kluender, F. Masiello, C. Devreugd, and P. A. Thomas. X-ray white beam topography of self-organized domains in flux-grown BaTiO<sub>3</sub> single crystals. *Physical Review B*, 94(2):1–7, 2016.

- [27] P. W. Forsbergh. Domain structures and phase transitions in barium titanate. *Physical Review*, 76(8):1187–1201, 1949.
- [28] Yi Jiang, Zhen Chen, Yimo Han, Pratiti Deb, Hui Gao, Saien Xie, Prafull Purohit, Mark W. Tate, Jiwoong Park, Sol M. Gruner, Veit Elser, and David A. Muller. Electron ptychography of 2d materials to deep sub-ångström resolution. *Nature*, 559(7714):343–349, 2018.
- [29] Sergei Lopatin, Bin Cheng, Wei Ting Liu, Meng Lin Tsai, Jr Hau He, and Andrey Chuvilin. Optimization of monochromated TEM for ultimate resolution imaging and ultrahigh resolution electron energy loss spectroscopy. *Ultramicroscopy*, 184:109–115, 2018.
- [30] Sergei Lopatin, Vladimir Roddatis, Tobias Meyer, Areej Aljarb, Lain-Jong Li, and Vincent Tung. 2D Materials Characterization: Should We Rely on HR STEM Imaging? *Microscopy and Microanalysis*, 25(S2):1638–1639, 2019.
- [31] A. Höfer, M. Fechner, K. Duncker, M. Hölzer, I. Mertig, and W. Widdra. Persistence of surface domain structures for a bulk ferroelectric above  $T_C$ . *Physical Review Letters*, 108(8):087602, 2012.
- [32] Hugh Simons, Astri Bjørnetun Haugen, Anders Clemen Jakobsen, Søren Schmidt, Frederik Stöhr, Marta Majkut, Carsten Detlefs, John E. Daniels, Dragan Damjanovic, and Henning Friis Poulsen. Long-range symmetry breaking in embedded ferroelectrics. *Nature Materials*, 17(9):814–819, 2018.
- [33] Yingxin Chen, Lei Zhang, Jiahao Liu, Xinli Lin, Weizhong Xu, Yifeng Yue, and Qun Dong Shen. Ferroelectric domain dynamics and stability in graphene oxide-P(VDF-TrFE) multilayer films for ultra-high-density memory application. *Carbon*, 144:15–23, 2019.
- [34] WF Egelhoff, PJ Chen, CJ Powell, RD McMichael, and MD Stiles. Surface and interface effects in the growth of giant magnetoresistance spin valves for ultrahigh-density data-storage applications. *Progress in Surface Science*, 67(1-8):355–364, 2001.
- [35] Tom T.A. Lummen, Yijia Gu, Jianjun Wang, Shiming Lei, Fei Xue, Amit Kumar, Andrew T. Barnes, Eftihia Barnes, Sava Denev, Alex Belianinov, Martin Holt, Anna N. Morozovska, Sergei V. Kalinin, Long Qing Chen, and Venkatraman Gopalan. Thermotropic phase boundaries in classic ferroelectrics. *Nature Communications*, 5:1–9, 2014.
- [36] Tadej Rojac, Andreja Bencan, Goran Drazic, Naonori Sakamoto, Hana Ursic, Bostjan Jancar, Gasper Tavcar, Maja Makarovic, Julian Walker, Barbara Malic, and Dragan Damjanovic. Domain-wall conduction in ferroelectric  $\text{BiFeO}_3$  controlled by accumulation of charged defects. *Nature Materials*, 16(3):322–7, 322–327, 2017.
- [37] Dennis Meier. Functional domain walls in multiferroics. *Journal of Physics Condensed Matter*, 27(46):463003, 2015.
- [38] Lin Zhu, Jeong Ho You, and Jinghong Chen. Effects of Defect on Ferroelectric Stability in  $\text{PbTiO}_3$  Thin Films. *Mrs Advances*, 1(5):363–368, 2016.
- [39] Biao Wang. Derivation of the landau-ginzburg expansion coefficients. *Advanced Topics in Science and Technology in China*, pages 321–375, 2013.

- [40] Jeppe Ormstrup, Maja Makarovic, Marta Majkut, Tadej Rojac, Julian Walker, and Hugh Simons. Dynamics and grain orientation dependence of the electric field induced phase transformation in Sm modified BiFeO<sub>3</sub> ceramics. *Journal of Materials Chemistry C*, 6(28):7635–7641, 2018.
- [41] M. Kutsal, P. Bernard, G. Berruyer, P. K. Cook, R. Hino, A. C. Jakobsen, W. Ludwig, J. Ormstrup, T. Roth, H. Simons, K. Smets, J. X. Sierra, J. Wade, P. Wattecamps, C. Yildirim, H. F. Poulsen, and C. Detlefs. The ESRF dark-field x-ray microscope at ID06. *IOP Conference Series: Materials Science and Engineering*, 580(1), 2019.
- [42] Hugh Simons, Anders Clemen Jakobsen, Sonja Rosenlund Ahl, Carsten Detlefs, and Henning Friis Poulsen. Multiscale 3D characterization with dark-field x-ray microscopy. *MRS Bulletin*, 41(6):454–459, 2016.
- [43] H. F. Poulsen. Multi scale hard x-ray microscopy. *Current Opinion in Solid State and Materials Science*, (March):100820, 2020.
- [44] Hugh Simons, A. King, W. Ludwig, C. Detlefs, Wolfgang Pantleon, Søren Schmidt, I. Snigireva, Frederik Stöhr, A. Snigirev, and Henning Friis Poulsen. Dark-field x-ray microscopy for multiscale structural characterization. *Nature Communications*, 6, 2015.
- [45] Jin Zhang, Stefan O. Poulsen, John W. Gibbs, Peter W. Voorhees, and Henning Friis Poulsen. Determining material parameters using phase-field simulations and experiments. *Acta Materialia*, 129:229–238, 2017.
- [46] A Snigirev, V Kohn, I Snigireva, and B Lengeler. A compound refractive lens for focusing high-energy x-rays. *Nature*, 384(6604):49–51, 1996.
- [47] Saša Bajt, Mauro Prasciolu, Holger Fleckenstein, Martin Domaracký, Henry N. Chapman, Andrew J. Morgan, Oleksandr Yefanov, Marc Messerschmidt, Yang Du, Kevin T. Murray, Valerio Mariani, Manuela Kuhn, Steven Aplin, Kanupriya Pande, Pablo Villanueva-Perez, Karolina Stachnik, Joe P.J. Chen, Andrzej Andrejczuk, Alke Meents, Anja Burkhardt, David Pennicard, Xiaojing Huang, Hanfei Yan, Evgeny Nazaretski, Yong S. Chu, and Christian E. Hamm. X-ray focusing with efficient high-na multilayer laue lenses. *Light: Science and Applications*, 7(3):17162, 2018.
- [48] Hugh Simons, Anders Clemen Jakobsen, Sonja Rosenlund Ahl, Henning Friis Poulsen, Wolfgang Pantleon, Ying Hao Chu, Carsten Detlefs, and Nagarajan Valanoor. Nondestructive Mapping of Long-Range Dislocation Strain Fields in an Epitaxial Complex Metal Oxide. *Nano Letters*, 19(3):1445–1450, 2019.
- [49] H. F. Poulsen, P. K. Cook, H. Leemreize, A. F. Pedersen, C. Yildirim, M. Kutsal, A. C. Jakobsen, J. X. Trujillo, J. Ormstrup, and C. Detlefs. Reciprocal space mapping and strain scanning using X-ray diffraction microscopy. *Journal of Applied Crystallography*, 51(5):1428–1436, 2018.
- [50] C. Mathieu, C. Lubin, G. Le Doueff, M. Cattelan, P. Gemeiner, B. Dkhil, E. K.H. Salje, and N. Barrett. Surface Proximity Effect, Imprint Memory of Ferroelectric Twins, and Tweed in the Paraelectric Phase of BaTiO<sub>3</sub>. *Scientific Reports*, 8(1):2–8, 2018.
- [51] George A. Rossetti, L. Eric Cross, and Keiko Kushida. Stress induced shift of the Curie point in epitaxial PbTiO<sub>3</sub> thin films. *Applied Physics Letters*, 59(20):2524–2526, 1991.
- [52] C. A. Randall, R. Maier, W. Qu, K. Kobayashi, K. Morita, Y. Mizuno, N. Inoue, and

- T. Oguni. Improved reliability predictions in high permittivity dielectric oxide capacitors under high dc electric fields with oxygen vacancy induced electromigration. *Journal of Applied Physics*, 113(1):014101, 2013.
- [53] Zhiyang Wang, Kyle G. Webber, Jessica M. Hudspeth, Manuel Hinterstein, and John E. Daniels. Electric-field-induced paraelectric to ferroelectric phase transformation in prototypical polycrystalline BaTiO<sub>3</sub>. *Applied Physics Letters*, 105(16):3–8, 2014.
- [54] Philipp T. Geiger, Oliver Clemens, Neamul H. Khansur, Manuel Hinterstein, Mtabazi G. Sahini, Tor Grande, Patrick Tung, John E. Daniels, and Kyle G. Webber. Nonlinear mechanical behaviour of Ba<sub>0.5</sub>Sr<sub>0.5</sub>Co<sub>0.8</sub>Fe<sub>0.2</sub>O<sub>3</sub> -  $\delta$  and in situ stress dependent synchrotron X-ray diffraction study. *Solid State Ionics*, 300:106–113, 2017.
- [55] Ming Li, Martha J. Pietrowski, Roger A. De Souza, Huairuo Zhang, Ian M. Reaney, Stuart N. Cook, John A. Kilner, and Derek C. Sinclair. A family of oxide ion conductors based on the ferroelectric perovskite Na<sub>0.5</sub>Bi<sub>0.5</sub>TiO<sub>3</sub>. *Nature Materials*, 13(1):31–35, 2014.
- [56] David A. Porter, Kenneth E. Easterling, and Mohamed Y. Sherif. *Phase transformations in metals and alloys, third edition*. CRC Press, 2009.
- [57] Jacob Madsen, Pei Liu, Jens Kling, Jakob Birkedal Wagner, Thomas Willum Hansen, Ole Winther, and Jakob Schiøtz. A Deep Learning Approach to Identify Local Structures in Atomic-Resolution Transmission Electron Microscopy Images. *Advanced Theory and Simulations*, 1(8):1800037, 2018.
- [58] E.A. Neppiras. Piezoelectric ceramics 1971. *Journal of Sound and Vibration*, 20(20):562–563, 1972.
- [59] Linxing Zhang, Jun Chen, Longlong Fan, Oswaldo Diéguez, Jiangli Cao, Zhao Pan, Yilin Wang, Jinguo Wang, Moon Kim, Shiqing Deng, Jiaou Wang, Huanhua Wang, Jinxia Deng, Ranbo Yu, James F. Scott, and Xianran Xing. Giant polarization in super-tetragonal thin films through interphase strain. *Science*, 361(6401):494–497, 2018.
- [60] S. V. Kalinin, S. Jesse, B. J. Rodriguez, Y. H. Chu, R. Ramesh, E. A. Eliseev, and A. N. Morozovska. Probing the role of single defects on the thermodynamics of electric-field induced phase transitions. *Physical Review Letters*, 100(15):2–5, 2008.
- [61] M. H. Braga, J. E. Oliveira, A. J. Murchison, and J. B. Goodenough. Performance of a ferroelectric glass electrolyte in a self-charging electrochemical cell with negative capacitance and resistance. *Applied Physics Reviews*, 7(1):011406, 2020.
- [62] Tobias Leonhard, Alexander D. Schulz, Holger Röhm, Susanne Wagner, Fabian J. Altermann, Wolfgang Rheinheimer, Michael J. Hoffmann, and Alexander Colsmann. Probing the microstructure of methylammonium lead iodide perovskite solar cells. *Energy Technology*, 7(3):1800989, 2019.
- [63] Julia Glaum, Hugh Simons, Jessica Hudspeth, Matias Acosta, and John E. Daniels. Temperature dependent polarization reversal mechanism in 0.94(Bi<sub>1/2</sub>Na<sub>1/2</sub>)TiO<sub>3</sub>-0.06Ba(Zr<sub>0.02</sub>Ti<sub>0.98</sub>)O<sub>3</sub> relaxor ceramics. *Applied Physics Letters*, 107(23):232906, 2015.
- [64] F. Marschall, A. Last, M. Simon, M. Kluge, V. Nazmov, H. Vogt, M. Ogurreck,

- I. Greving, and J. Mohr. X-ray full field microscopy at 30 keV. *Journal of Physics: Conference Series*, 499(1):012007, 2014.
- [65] Jane A Howell, Mark D Vaudin, Lawrence H Friedman, and Robert F Cook. Stress in Barium Titanate. 125(125013):1–22, 2020.
- [66] Hugh Simons, Sonja Rosenlund Ahl, Henning Friis Poulsen, and Carsten Detlefs. Simulating and optimizing compound refractive lens-based x-ray microscopes. *Journal of Synchrotron Radiation*, 24(2):392–401, 2017.
- [67] Long Qing Chen. Phase-field method of phase transitions/domain structures in ferroelectric thin films: A review. *Journal of the American Ceramic Society*, 91(6):1835–1844, 2008.
- [68] L. Daniel, D. A. Hall, and P. J. Withers. A multiscale model for reversible ferroelectric behaviour of polycrystalline ceramics. *Mechanics of Materials*, 71:85–100, 2014.
- [69] JD ESHELBY. The determination of the elastic field of an ellipsoidal inclusion, and related problems. *Proceedings of the Royal Society of London Series A-mathematical and Physical Sciences*, 241(1226):376–396, 1957.
- [70] Yueming Wang, Brian Van Devener, Xiaolong Li, and Jost O.L. Wendt. High resolution STEM/EDX spectral imaging to resolve metal distributions within  $\approx 100$  nm combustion generated ash particles. *Aerosol Science and Technology*, 53(7):783–792, 2019.
- [71] W. Cao and L. E. Cross. Theory of tetragonal twin structures in ferroelectric perovskites with a first-order phase transition. *Physical Review B (condensed Matter)*, 44(1):5–12, 5–12, 1991.
- [72] H. F. Poulsen, P. K. Cook, H. Leemreize, A. F. Pedersen, C. Yildirim, M. Kutsal, A. C. Jakobsen, J. X. Trujillo, J. Ormstrup, and C. Detlefs. Reciprocal space mapping and strain scanning using x-ray diffraction microscopy. *Journal of Applied Crystallography*, 51(5):1428–1436, 2018.



# **A Appendix**

## **A.1 Co-authorship 1: The thermal and electric field stability of square-net domain patterns in barium titanate**

# The thermal and electric field stability of square-net domain patterns in barium titanate

Emil V. Østergaard,\* Jeppe Ormstrup, and Hugh Simons  
Technical University of Denmark, Department of Physics  
(Dated: June 13, 2020)

We use *in-situ* polarized light microscopy in combination with an externally applied electric field to induce square-net domain patterns in top-seeded single crystals of barium titanate above the Curie temperature ( $T_C$ ). The patterns occur under a wide range of electric field magnitudes larger than  $\sim 200$  V/mm and at temperatures up to  $6^\circ\text{C}$  above  $T_C$ . We mapped this behavior on a pseudo phase diagram showing the region in electric field and temperature space where this domain configuration is stable. We observed the electric field induced transformation into the periodically ordered structure from both the cubic structure above  $T_C$  and the tetragonal structure below  $T_C$ . We conclude that the square-net domain pattern we observe is a result of domain structures perpendicular to the applied electric field, which appear in the vicinity of the transition point. Synchrotron X-ray reciprocal space maps indicate the presence of ferroelastic domains perpendicular to the electric field direction at a range of electric field magnitudes similar to those required to induce the periodic domain ordering we observe using polarized light microscopy.

Barium titanate may well be the most archetypal ferroelectric. But despite this, many of its phenomena, such as domain ordering close to the phase transition temperatures, remain an active area of research. One particularly long-standing mystery is the formation of square-net domain patterns under certain conditions close to the Curie temperature ( $T_C$ ) [1], [2], [3]. For 70 years, square-net patterns have been observed in  $\text{BaTiO}_3$  single crystals using polarized light microscopy. The origin of these patterns are debated, but so far have only been observed in flux-grown single crystals during the para-ferroelectric phase transition just below  $T_C$ . These square-net patterns are well-recognized due to the spectacular images they create when viewed with polarized light microscopy. However, the striking nature of their birefringence and the seemingly narrow conditions under which they appear mean these square-net patterns pose the scientifically interesting question of how such a complex structure occur.

Square-net domain patterns were first observed in 1949 by Forsbergh [1], who studied the thermal stability of the patterns and proposed a possible explanation for the birefringence contrast in terms of a structure of intersecting wedged domains. After many years of dormancy on the topic, Schilling et al. [3] proposed an alternative domain structure that explained the birefringence, along with a corresponding phenomenological theory for the self ordering of this domain structure below the  $T_C$ . Finally, Walker et al. [2] used white beam X-ray topography to measure the surface strain due to the formation of these self-organized domains, mapping the distribution of elastic and spontaneous strain as a function of temperature. Crucially, these studies solely investigated the occurrence of the square-net pattern in the absence of an external electrical field. As such, the proposed domain structures

that give rise to the square net patterns require electric neutrality [3]. Furthermore, it was also concluded that the square-net pattern is restricted to flux-grown crystals and was not possible in crystals grown via top-seeded approaches [2]. With the understanding that top-seeded crystals tend to be purer than the flux-grown equivalents, these observations point to the conclusion that the phenomena is likely defect-driven.

By heating a top-seeded-grown single crystals of  $\text{BaTiO}_3$  to near  $T_C$  and applying an electric field, we observed a square net pattern similar to those reported for flux-grown crystals. The pattern appears to be stable in a large temperature range around  $T_C$  and at electric field magnitudes above a critical value. By taking *in-situ* polarized light microscopy videos of the transition from cubic or tetragonal phases and digitally identifying the square-net pattern at varying fields and temperatures, we track the onset of the square-net pattern and construct a pseudo phase diagram to describe its region of stability. A representative image of the patterns we observe can be seen in Figure 1. In this paper, we show that this ordered phase is stable in a well defined electric field - temperature regime close to the para- to ferroelectric phase transition.

The experiments were carried out on a commercially-grown (Crystal GmbH, Germany)  $\text{BaTiO}_3$  single crystal, grown via the top-seeded method and polished to  $5 \times 5 \times 0.15$  mm<sup>3</sup>. A custom-designed apparatus [4] was used to precisely control the temperature of the crystal and its applied electric field during the experiments. Optically transparent electrodes were applied to the  $5 \times 5$  mm<sup>2</sup> faces by coating them with a thin layer ( $\sim 100$  nm) of indium tin oxide (ITO) using magnetron sputtering at  $100^\circ\text{C}$  for 30 min. The two ITO electrodes reduced the optical transmission of the sample to 80-90% for visible light, while giving an electrical resistivity on the order  $\sim 10^{-4}$   $\Omega/\text{cm}$  [5]. While the bottom face of the sample was in electrical and thermal contact with the electrically-grounded sample holder, an electrode was

---

\* s163995@student.dtu.dk

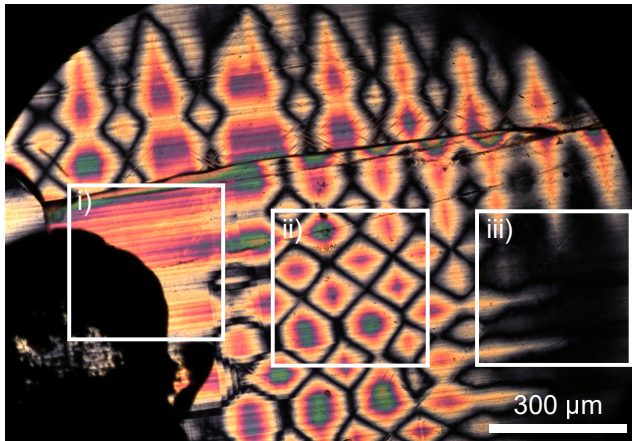


Figure 1: a) BaTiO<sub>3</sub> observed at 400 V/mm and at sample holder temperature 142.7°C. i) Close to the electrode the sample is cooled and domains are parallel to the surface. ii) Square net pattern is observed in an area between the cold electrode and how sample. iii) Close to the holder the sample is at high temperature and in a tetragonal state parallel to the field.

connected to the top side using a thin copper wire and silver paste. This silver paste at the electrode-wire junction facilitated heat loss through the wire and resulted in a temperature gradient over the sample in the vicinity of this junction. This temperature gradient is responsible for the (potentially) erroneous observation of different phase transition temperatures across the sample. Assuming the true  $T_C$  is invariant across the sample, videos of the phase front moving across the sample were used to create a calibration map of the temperature gradients over the sample, as seen in Figure 2, Step 3. Using this calibration map enables reliable and precise determination of the temperature and electric field strength in each pixel of the polarized light microscopy images.

Figure 1 shows an example of the electric-field induced square-net domain pattern. When the field is first increased, a regular tetragonal domain perpendicular to the field grows out from the electrode (from cold to hot). Remnants of this domain type can be seen close to the electrode on the left side of Figure (1), marked i), where the sample is at the lowest temperatures. At a critical field strength depending on the sample temperature, the growing tetragonal domains start to display the square net ordering, as seen centrally in Figure 1, marked ii). Due to the temperature gradient in the sample, this critical field magnitude varies across the sample. At measured temperatures above 145 °C, the ordered phase is not seen and increasing the field will result in a transformation into the tetragonal phase whose domains are parallel to the field. This state can be seen in the right part of Figure 1, marked iii). The sample temperature is highest in this region due to being close to the copper edge of the sample holder. At this temperature, the

transformation from cubic to tetragonal is only visible for a short period where the phase front appears as perpendicular surface domains before quickly flipping parallel to the field direction and disappearing from view.

In order to map the transition between the paraelectric phase, the ferroelectric phase and the square-net pattern, we conducted *in-situ* polarized light microscopy experiments at varying temperatures and electric field strengths. Our procedure involved first heating the sample above the  $T_C$  (150 °C at the holder), where the transition into cubic state could be seen as a complete darkness in the microscope due to the loss of birefringence. Then, after allowing the system to stabilize at a constant temperature for few minutes, the sample was cooled to the desired temperature, after which the electric field was continuously increase from 0-800 V/mm at 6.67 V/(mm s). This procedure was repeated for indicated temperatures ranging from 142 to 149 °C in steps of 1 °C.

An Olympus CX31-P microscope with a 4x objective lens and a Olympus SC50 digital camera was used as microscopy setup. All experiments were carried out under crossed polarizers with the primary axis of the sample at 45 ° angle to the polarization. As such, the intensity transmitted through the sample can be written as:

$$I = I_0 \sin^2 \frac{\pi d \Delta n}{\lambda} \quad (1)$$

where  $I_0$  is the incident intensity,  $d$  is the sample thickness,  $\Delta n$  is the birefringence and  $\lambda$  is the light wavelength in the sample. From this, we can expect both cubic domains and tetragonal domains whose spontaneous polarization is oriented parallel to the incident light to be completely dark, since  $\Delta n = 0$ . Conversely, tetragonal domains whose spontaneous polarization is perpendicular to the incident light should be visible in the microscopy images as an increased intensity. However, we note that, in our observations, field-aligned tetragonal domains induced by weak electric fields do not result in complete darkness as expected.

The videos resulting from the series of *in-situ* polarized light microscopy experiments at varying temperatures and electric-field magnitudes were then used to track the onset of the square net pattern, and thus the critical temperature and electric field magnitudes (see Figure 2). After capturing the videos of the transformation, the analysis process involved first grayscaleing and thresholding the color images into binary representations according to their total intensity. The regions in the binary images were then sorted by their area and eccentricity such that only regions associated with the square net patterns are considered. By correlating the geometrical properties of the binarized intensity regions to the temperature and applied electric field, a pseudo phase diagram detailing the stability of these phases could be constructed (Figure 3). We further note that, by assuming that the zero electric field phase transition occurs at the same  $T_C$  at all points of the sample, we can assign an offset temperature

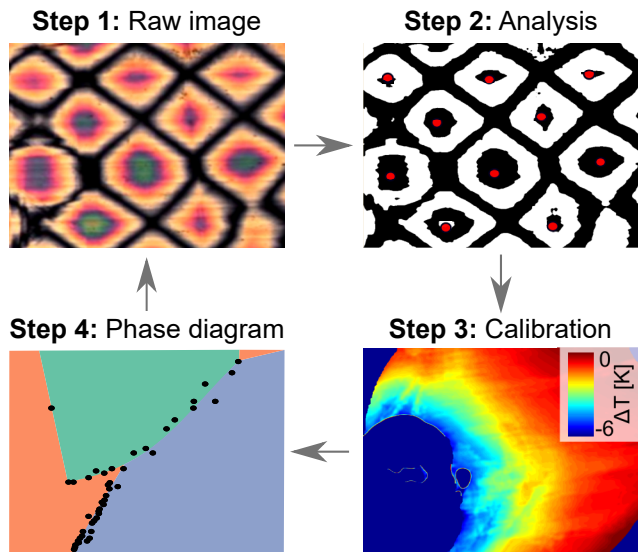


Figure 2: Method for tracking square net patterns. 1) An image from the video is loaded. For each image the sample holder temperature and applied electric field has been recorded. 2) Squares on the loaded image are detected. 3) Using the temperature map constructed from the phase transition temperature a temperature is assigned to each detected square. 4) Temperature and electric field values for the square net pattern are recorded on the phase diagram.

to every pixel of every image in the videos, and correct the reported temperatures and electric fields accordingly.

The resulting temperature-electric field pseudo phase diagram is shown in Figure 3, and describes the transformation into and out of the square net pattern in relation to the more conventionally expected cubic and tetragonal phases, in the temperature and electric field ranges of 138-145 °C and 200 V/mm and above. Though we observe the pattern become less pronounced at high field strengths, we were not been able to identify an upper electric field limit due to the high-field capabilities of the sample holding apparatus. We note that some degree of hysteresis is observed when lowering the field as the square net pattern persists in a range of electric fields but disappear just before the field is completely removed.

We also mention that crack growth was observed at multiple positions in the sample during the electric field induced phase transition. We assume the cracking occurs due to a combination of the thermal stresses induced by the thermal gradient and the heterogeneous stresses from the spontaneously strained domains that form upon the phase transition. If we assume the domains comprising the square-net pattern are surface structures (as concluded by ref. [2]), they result in a spherical bending of the sample. However, due to the sample being clamped down at the edges, this bending will give rise to tensile stresses on the opposite side to the square net

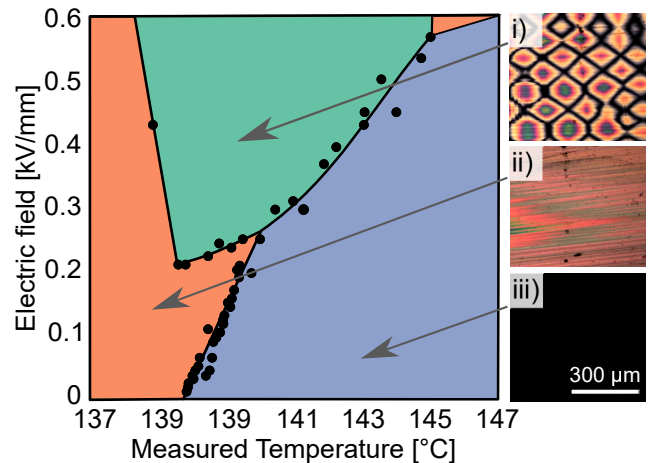


Figure 3: Phase diagram for the field induced phase transition. The region of periodic domain ordering is observed between the cubic to tetragonal phase transition at sample holder temperatures from 138 to 145 °C. Below this temperature region the sample remains in the tetragonal phase which at high fields align with the field direction. Above 145°C the cubic state transits into a tetragonal state align with the field direction at high field magnitudes.

pattern, which in turn promotes crack growth. Electrical resistance measurements of the sample surface after crack growth indicates that the conducting ITO film was not completely broken, and that the field distribution on the sample should be approximately uniform across the cracks.

To provide further insight into the structural changes occurring during the transformation to and from the square-net pattern, we repeated the experiment while carrying out *in-situ* synchrotron X-ray single crystal diffraction. The experiment was carried out at beamline ID06 at the European Synchrotron (ESRF) at an X-ray energy of 17 keV ( $\Delta E/E = 10^{-4}$ ). Diffraction intensity maps were measured on a high-resolution CCD detector located approximately 5 m from the sample, resulting in a reciprocal space resolution of approximately  $10^{-5} \text{ \AA}^{-1}$ . The sample environment was heated to 139.6°C; approximately  $1^\circ$  above the measured transition temperature, and rocking scans through the  $[2\ 0\ 0]$  Bragg reflection were then carried out at increasing electric field magnitudes 0 to 800 V/mm to investigate the changes to the average crystal structure. By tracking the intensity distribution in reciprocal space as a function of electric field strength, we clearly identify the electric field induced transformation from the cubic to the tetragonal phase, as well as the lattice strains they manifest (4 a)). Close to the phase transition at 300 V/mm, a tetragonal domain variants whose spontaneous strain is perpendicular to the electric field direction appears in a narrow range of electric fields between 300 and 500 V/mm. Upon removal of the electric field, the sample relaxes into a combination

of the two types of tetragonal domain variants. Shown in Figure 4 b), fraction of measured intensity associated with the perpendicular domains with respect to the total intensity (i.e. the volume fraction) indicates that, during the transformation, most of the diffracting volume in the sample is in either the cubic state, or the tetragonal with domains parallel to the electric field during. The volume of material possessing the perpendicular domain configuration comprises only a small fraction of the total sample.

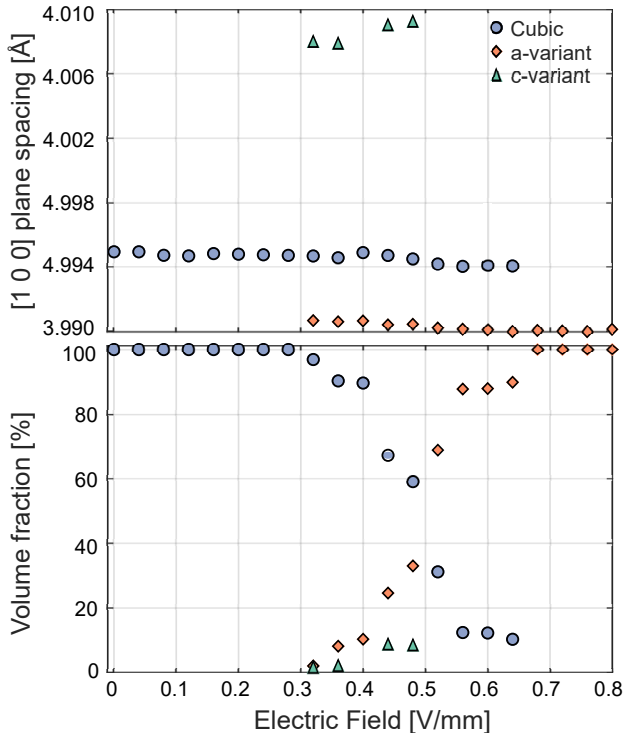


Figure 4: Results from RSM's taken at varying electric fields just above  $T_C$  **a)** d spacing of the present  $[1\ 0\ 0]$  planes for field strengths between 0 and 800 V/mm. **b)** Amount of the sample in the respective phases.

We postulate that the tetragonal domains oriented perpendicular to the electric field we observe in the X-ray diffraction measurements could be the same as those responsible for the square-net domain ordering seen in the polarized light microscopy. However, as they are only observed in a narrow range of field magnitudes (300-500 V/mm) compared to our microscopy measurements (200->1000 V/mm), however, these two measurements conflict to some degree. This difference could possibly be a consequence of the fact that X-ray measurements corresponded to a local spatial region of the sample deter-

mined by the beam size ( $200 \times 150 \times 1\ \mu\text{m}$ ), and was not representative of the entire square-net pattern observed by the microscope. An alternative explanation for this narrow region of stability is that the square net pattern observed in the microscope might in fact *require* the temperature gradient induced by the silver electrode, which we were not able to observe in the X-ray measurement. We also note that, while the X-ray intensity measurements should accurately correlate the diffraction intensity to the volume fraction of material, the same cannot be said of the birefringence signal measured during the polarized light microscopy measurements, which only originates from the (potentially very small) birefringent regions of the material that are interacting. Previous observations of these patterns have been conducted under zero external electric field which means that all possible domain configurations must have a net zero polarization. However as we observe the same pattern under an external field the domain structure is allowed to have a net polarization proportional to the external field.

In conclusion, we observed square net domain ordering in  $\text{BaTiO}_3$  single crystals grown by the top-seeded solution method. Uniquely, the square-net patterns were observed above  $T_C$  and under the application of electric fields with magnitudes of the order of 200 V/mm. These observations contradict earlier assumptions that the pattern was restricted to flux-grown crystals below  $T_C$ . The square-net pattern appears to be stable over a wide range of temperatures and electric-field magnitudes, and in multiple samples. Furthermore, structural measurements obtained using high-energy synchrotron *in-situ* X-ray diffraction support these findings. Collectively, these insights suggest that the formation of these spectacular square-net patterns may be more broadly occurring in  $\text{BaTiO}_3$  - and perhaps other ferroelectrics - than typically thought. To this end, we believe the investigation of the morphology of the domains within these square-net patterns using a non-destructive 3D mapping technique would shed considerable light on this long-standing conundrum.

## ACKNOWLEDGMENTS

The authors gratefully acknowledge beamtime provided by the ESRF, as well as travel support provided by Danscatt. In addition, the authors are grateful to Ole Trinhammer and X for the loan of equipment necessary for the microscopy measurements along with Andrea Crovetto for assistance with ITO sputtering. J.O. acknowledges support from an NTNU-DTU tandem PhD project agreement, and H.S. acknowledges support from an ERC Starting Grant.

[1] P. W. Forsbergh, Domain structures and phase transitions in barium titanate, *Physical Review* **76**, 1187

(1949).

- [2] D. Walker, A. M. Glazer, S. Gorfman, J. Baruchel, P. Pernot, R. T. Kluender, F. Masiello, C. Devreugd, and P. A. Thomas, X-ray white beam topography of self-organized domains in flux-grown BaTiO<sub>3</sub> single crystals, *Physical Review B* **94**, 1 (2016).
- [3] A. Schilling, A. Kumar, R. G. McQuaid, A. M. Glazer, P. A. Thomas, and J. M. Gregg, Reconsidering the origins of Forsberg birefringence patterns, *Physical Review B* **94**, 1 (2016).
- [4] J. Ormstrup, E. V. Østergaard, C. Detlefs, R. H. Mathiesen, C. Yildirim, M. Kutsal, P. K. Cook, Y. Watier, C. Cosculluela, and H. Simons, Imaging microstructural dynamics and strain fields in electro-active materials in situ with dark field x-ray microscopy, *Review of Scientific Instruments* **91**, 065103 (2020).
- [5] M. Strandgaard, A. Crovetto, and B. Seger, Development of contact materials for conversion of solar energy, (2018).
- [6] N. Novak, R. Pirc, and Z. Kutnjak, Effect of electric field on ferroelectric phase transition in BaTiO<sub>3</sub> ferroelectric, *Ferroelectrics* **469**, 61 (2014).
- [7] A. Grünebohm, M. Marathe, and C. Ederer, Ab initio phase diagram of BaTiO<sub>3</sub> under epitaxial strain revisited, *Applied Physics Letters* **107**, 10.1063/1.4930306 (2015), arXiv:1507.05512.
- [8] C. Ma, H. Guo, and X. Tan, A new phase boundary in (Bi<sub>1/2</sub>Na<sub>1/2</sub>)TiO<sub>3</sub>-BaTiO<sub>3</sub> revealed via a novel method of electron diffraction analysis, *Advanced Functional Materials* **23**, 5261 (2013).
- [9] C. Ma and X. Tan, In situ transmission electron microscopy study on the phase transitions in lead-free (1-x)(Bi<sub>1/2</sub>Na<sub>1/2</sub>)TiO<sub>3</sub>-xBaTiO<sub>3</sub> Ceramics, *Journal of the American Ceramic Society* **94**, 4040 (2011).
- [10] J. Hotovy, J. Hüpkes, W. Böttler, E. Marins, L. Spiess, T. Kups, V. Smirnov, I. Hotovy, and J. Kováč, Sputtered ITO for application in thin-film silicon solar cells: Relationship between structural and electrical properties, *Applied Surface Science* **269**, 81 (2013).
- [11] W. J. Merz, Domain formation and domain wall motions in ferroelectric BaTiO<sub>3</sub> single crystals, *Physical Review* **95**, 690 (1954).
- [12] V. M. Fridkin, A. A. Grekov, N. A. Kosonogov, and T. R. Volk, Photodomain effect in BaTiO<sub>3</sub>, *Ferroelectrics* **4**, 169 (1972).
- [13] W. J. Merz, Double hysteresis loop of BaTiO<sub>3</sub> at the curie point, *Physical Review* **91**, 513 (1953).
- [14] M. Acosta, N. Novak, V. Rojas, S. Patel, R. Vaish, J. Koruza, G. A. Rossetti, and J. Rödel, BaTiO<sub>3</sub>-based piezoelectrics: Fundamentals, current status, and perspectives, *Applied Physics Reviews* **4**, 10.1063/1.4990046 (2017).

## **A.2 Co-authorship 2: The ESRF dark-field x-ray microscope at ID06**

PAPER • OPEN ACCESS

## The ESRF dark-field x-ray microscope at ID06

To cite this article: M Kutsal *et al* 2019 *IOP Conf. Ser.: Mater. Sci. Eng.* **580** 012007

View the [article online](#) for updates and enhancements.

### Recent citations

- [Impact of 3D/4D methods on the understanding of recrystallization](#)  
D. Juul Jensen and Y.B. Zhang
- [Microscale Mapping of Structure and Stress in Barium Titanate](#)  
Jane A. Howell *et al*
- [Probing nanoscale structure and strain by dark-field x-ray microscopy](#)  
Can Yildirim *et al*

# The ESRF dark-field x-ray microscope at ID06

M Kutsal<sup>1,2</sup>, P Bernard<sup>1</sup>, G Berruyer<sup>1</sup>, P K Cook<sup>1</sup>, R Hino<sup>1</sup>, A C Jakobsen<sup>1</sup>, W Ludwig<sup>1,3</sup>, J Ormstrup<sup>2</sup>, T Roth<sup>1</sup>, H Simons<sup>2</sup>, K Smets<sup>4</sup>, J X Sierra<sup>5</sup>, J Wade<sup>1,2</sup>, P Wattecamps<sup>1</sup>, C Yildirim<sup>1,6</sup>, H F Poulsen<sup>2</sup> and C Detlefs<sup>1</sup>

<sup>1</sup> European Synchrotron Radiation Facility, 38043 Grenoble, France

<sup>2</sup> Department of Physics, Technical University of Denmark, 2800 Kgs. Lyngby, Denmark

<sup>3</sup> MATEIS, INSA-Lyon, 69621 Villeurbanne Cedex, France

<sup>4</sup> LAB Motion Systems, 3001 Leuven, Belgium

<sup>5</sup> Department of Energy, Technical University of Denmark, 4000 Roskilde, Denmark

<sup>6</sup> OCAS, Pres. J.F. Kennedylaan 3, BE-9060, Zelzate, Belgium

E-mail: [detlefs@esrf.fr](mailto:detlefs@esrf.fr)

**Abstract.** We present an instrument for dark-field x-ray microscopy installed on beamline ID06 of the ESRF — the first of its kind. Dark-field x-ray microscopy uses full field illumination of the sample and provides three-dimensional (3D) mapping of micro-structure and lattice strain in crystalline matter. It is analogous to dark-field electron microscopy in that an objective lens magnifies diffracting features of the sample. The use of high-energy synchrotron x-rays, however, means that these features can be large and deeply embedded. 3D movies can be acquired with a time resolution of seconds to minutes. The field of view and spatial resolution can be adapted by simple reconfiguration of the x-ray objective lens, reaching spatial and angular resolution of 30-100 nm and 0.001°, respectively. The instrument furthermore allows pre-characterization of samples at larger length scales using 3DXRD or DCT, such that a region of interest (e.g. a single grain) can be selected for high-resolution studies without the need to dismount the sample. As examples of applications we show work on mapping the subgrains in plastically deformed iron and aluminum alloys, mapping domains and strain fields in ferroelectric crystals, and studies of biominerals. This ability to directly characterize complex, multi-scale phenomena *in-situ* is a key step towards formulating and validating multi-scale models that account for the entire heterogeneity of materials. As an outlook, we discuss future prospects for such multi-scale characterization by combining DFXM with 3DXRD/DCT, and coherent x-ray methods for coarser and finer length-scales, respectively.

## 1. Introduction

Many, if not most, technological materials are composed of crystalline elements that are hierarchically organized over length scales ranging from millimeters to nanometers, spanning up to 6 orders of magnitude. The same is true for biominerals, ice, sand and geological materials in general. Crystalline elements and substructures such as grains, domains and atomic-scale defect networks determine many of the macroscopic physical and mechanical properties of these materials. Understanding the interplay of physical phenomena and structural dynamics at, and between, these different lengths scales is therefore a critical and persistent issue across materials and geological sciences. Our understanding, however, is still limited by the lack of a non-destructive three-dimensional (3D) probe of the local crystal lattice (structure, strain,



and orientation) that can be rapidly switched between different length scales and that enables acquisition of movies during processing.

The need to probe the local crystallography favours a diffraction-based approach. Existing 3D techniques, however, have shortcomings with respect to multi-scale characterization. Electron-based methods can provide very high spatial resolution, but are either limited to thin foils [1, 2] or involve serial sectioning [3, 4]. Scanning [5, 6, 7, 8, 9, 10] and coherent [11, 12, 13, 14, 15, 16, 17, 18] x-ray methods are rapidly progressing towards 20 nm resolution, but are limited to small sampling volumes. Furthermore, all methods face the challenge that the illuminated part of a bulk sample may comprise millions or even billions of structural elements whose diffracted signals overlap, rendering data analysis and interpretation complicated and in many cases impossible.

Aiming to overcome these limitations, dark-field x-ray microscopy (DFXM) is a full-field imaging technique for non-destructive mapping of the structure, orientation, and strain of deeply embedded crystalline elements in 3D [19, 20, 21, 22, 23, 24]. By placing an x-ray objective lens in the diffracted beam, direct space resolutions of 30–100 nm can be reached while maintaining a comfortable working distance of 10 cm or more between the sample and x-ray lens. The spatial resolution and field of view can be adapted by changing the focal length of the lens and thus “zooming” in or out. Furthermore, through its narrow angular and real space field of view, the objective also filters stray diffraction signals, suppressing unwanted overlap and isolating the individual structural element of interest.

As a first implementation of the method a dedicated dark-field x-ray microscope was recently installed on beamline ID06 of the European Synchrotron Radiation Facility (ESRF, Grenoble, France). The instrument is designed to combine DFXM with coarse scale 3D grain mapping techniques such as 3D X-Ray Diffraction (3DXRD) [25, 26, 27, 28, 29] and diffraction contrast tomography (DCT) [30, 31], as well as classical tomography and diffraction topography. This combination enables the user to rapidly progress from fast overviews of the entire specimen to detailed studies of local phenomena in a single experimental setting, without the need to dismount the sample.

Following an introduction to DFXM, in this article we present the **instrumentation** of the microscope at ID06, providing details on all relevant hardware components. In particular we present the refractive optics used for condensing and imaging. Compound refractive lenses (CRLs) were until recently the only choice, providing a reasonably large field of view but being limited in terms of spatial resolution by lens aberrations. As a newly developed alternative, multilayer Laue lenses (MLLs) offer larger numerical apertures (NAs) and improved spatial resolution, at the expense of a smaller field of view and reduced working distance. Next, we demonstrate the performance of the instrument on three selected examples in materials science: the processing of plastically deformed metals, the distribution of strain and orientation gradients in ferroelectrics, and hierarchical organization in bio-minerals.

### *1.1. The geometry and principle of DFXM*

The geometry and operational principle of dark-field x-ray microscopy (see figure 1) is conceptually similar to dark-field transmission electron microscopy (TEM): the diffracted beam passes through an x-ray objective lens, creating a magnified image of a specific region of interest with contrast from local variations in lattice symmetry, orientation and strain [21]. The sample-to-detector distance  $d_1 + NT + d_2$  is 2–6 m, enabling magnification ratios of up to 50 while still maintaining sufficient space around the sample for complex sample environments.

A defining feature of the dark-field x-ray microscope is the x-ray objective. Like a visible light microscope, the x-ray objective can be reconfigured to adjust the magnification, field-of-view, and numerical aperture, hence allowing adjustment of the spatial resolution according to specific experimental requirements. So far primarily compound refractive x-ray lenses made of

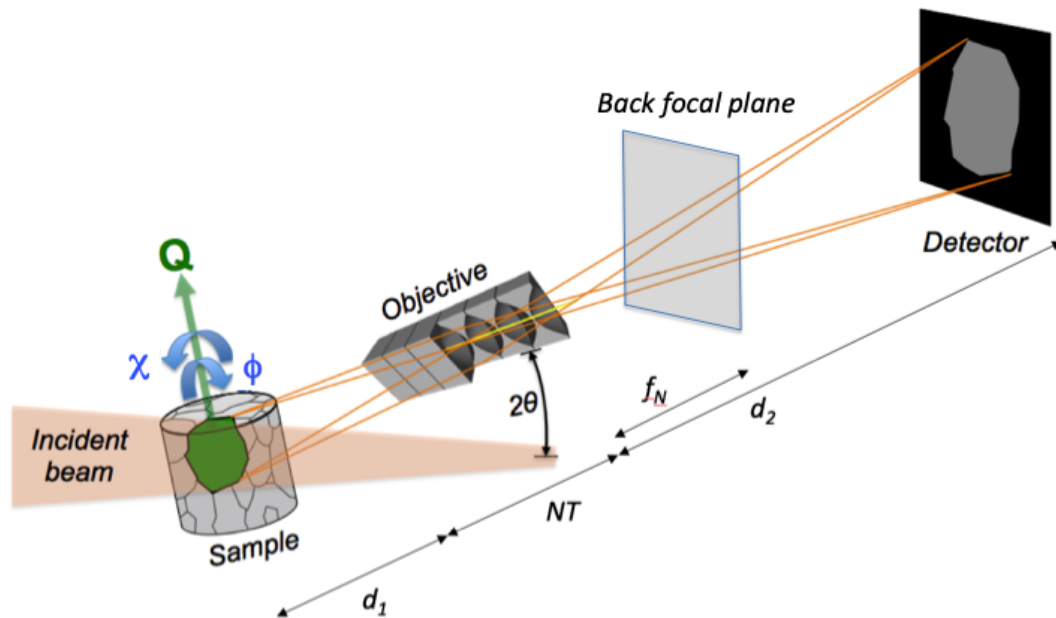


**Figure 1.** Principle of dark-field x-ray microscopy. Monochromatic x-rays illuminate a crystalline element of interest, and the diffracted radiation is imaged by means of an x-ray objective and a 2D detector. The objective is here a compound refractive lens, comprising  $N$  lenslets each with a thickness of  $T$ .  $d_1, d_2, f_N$  are the sample plane-entry of CRL distance, exit of CRL – image plane distance and the focal distance, respectively. Scanning the sample tilt ( $\chi, \phi$ ), and scattering ( $2\theta$ ) angles facilitate mapping of orientation and axial strain respectively, while different projections can be obtained by rotating the sample about its scattering vector,  $\vec{Q}$ .

Beryllium [32] or SU-8 polymer [33] have been used. Their performance is discussed below along with a presentation of the first results using multilayer Laue lenses as objectives — with the aim to improve the spatial resolution. Irrespective of the choice, the imaging system is associated with a Fourier plane, the back focal plane downstream of the objective, see figure 1. Similar to dark field microscopy operation in a TEM, the direct space (imaging) information in the image plane and the Fourier space (diffraction) information in the back focal plane may be combined in a variety of ways [22].

Like the TEM, the dark-field x-ray microscope can be operated in a variety of modes. Most experiments so far have used a one-dimensionally-focusing condenser to create a narrow line-beam [34] that illuminates a ‘layer of the material (typically  $200 \mu\text{m} \times 200 \mu\text{m} \times 200 \text{nm}$ ), which is then imaged at an oblique angle. Experiments typically involve the use of a succession of modalities including

- *Rocking curve imaging in section topography:* The dependence of the intensity on the Bragg angle (rocking scan) is analyzed pixel by pixel. It is possible to combine rocking curve imaging in magnified and non-magnified (using a near-field camera, see below) modes

without unmounting the sample.

- *Mosaicity scans*: By systematically varying the sample tilts,  $\chi$  and  $\phi$ , a spatially resolved local pole figure can be acquired [21].
- *Strain scans*: By scanning longitudinally ( $\theta$ - $2\theta$ -scan) the strain component along the scattering vector is imaged [21]. Typically, this is combined with a rocking scan or with integration over the rocking profile at each  $2\theta$  setting. As an alternative, strain mapping may be performed in the back focal plane [22].
- *Reciprocal space maps*: A high resolution reciprocal space map of the illuminated volume is available either in the back focal plane [22] or in the far-field regime (see below).

3D mapping can be performed in two ways. Firstly, by stacking layers of the kind described above. This is performed by translating the sample through the planar beam in small increments. A second, faster method is *magnified topo-tomography*. Here, projections of the sample are acquired while the sample is rotated about the scattering vector [35, 21], and a 3D representation is reconstructed using tomographic principles. Again, data can be taken in magnified and non-magnified mode. Experimental protocols and reconstruction codes for magnified topo-tomography are currently under development.

By setting  $2\theta$  to zero, magnified bright field imaging is obtainable [36, 37]. Translating the sample along the optical axis makes it possible to acquire pure absorption contrast images or phase contrast images at any Fresnel number. Moreover, by placing a phase plate in the back focal plane, Zernike type phase contrast images are created [38].

When based on the use of CRLs, the entire imaging system is accurately described by geometrical optics. However, the length of the CRL,  $NT$ , tends to be of the same order as the focal length  $f_N$ , implying that the thin lens approximation is not valid. Analytical expressions for the NA, field of view, depth of field, and spatial resolution in bright field mode are provided in [39]. For dark field microscopy, operating in the image plane, expressions for the resolution in both direct space and reciprocal space spatial resolution are provided in [21]. Correspondingly, in [22] equations are provided for the reciprocal space resolution in the back focal plane and the corresponding strain resolution.

### 1.2. Complementary imaging on longer length scales

It is necessary to combine DFXM with more traditional imaging in order to identify local regions of interest and to provide overviews during processing studies. The microscope at ID06 enables this in several ways:

- A *near-field camera* with high resolution placed close to the sample can provide classical absorption or phase contrast tomography, non-magnified diffraction topographies, and DCT measurements.
- A *diffraction camera* with large pixels can provide 3DXRD type mapping as well as classical (sample averaged) diffraction information.
- *Far-field imaging* can provide high resolution reciprocal space maps [27]. Conveniently this modality can be obtained with the same detector as shown in figure 1 by simply translating the objective out of the diffracted beam.

More details about these cameras are provided below.

## 2. Description of beamline components

### 2.1. Overall beamline layout and optical scheme

The beamline is located at the high-beta straight section ID06 of the ESRF in Grenoble, France. It consists of one white beam optics hutch, OH, and two monochromatic beam experimental

**Table 1.** Undulator parameters obtained from fits of the observed gap with maximum flux as function of photon energy to the theoretical curve.

		U18 CPMU	U27
Min. gap	[mm]	6.05	11
Max. gap	[mm]	30	300
Period $\lambda_u$	[mm]	18.25(2)	27.19(2)
$B_0$	[T]	2.44(2)	1.93(2)
$\alpha$		1.10(1)	1.00(1)

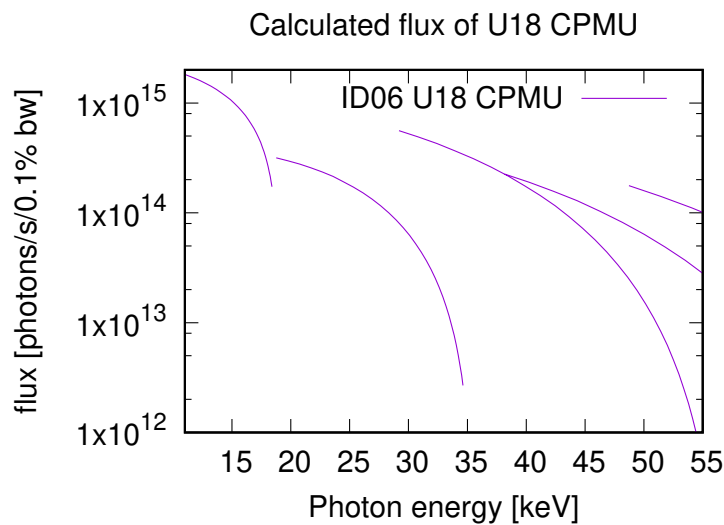


**Figure 2.** Calculated flux of the ID06 U18 CPMU undulator as function of photon energy, in photons per second into a  $1 \times 2 \text{ mm}^2$  aperture at 28 m from the source, and for a 0.1% band width. This calculation is for the pre-upgrade ESRF, without taking into account absorption in diamond and Beryllium windows.

hutches, EH1 and EH2. OH houses standard ESRF high power primary slits, a UHV section where temporary white beam experiments can be set up [40, 41, 37], the monochromator, secondary slits and intensity monitor, a Transfocator, and, finally, the safety shutter for EH1. The dark-field x-ray microscope is implemented in EH1, whereas EH2 houses the Large Volume Press (LVP) that is described elsewhere [42].

The coordinate system used at ID06 has  $x$  along the beam axis,  $y$  horizontal and away from the storage ring, and  $z$  upwards.

## 2.2. Source

Two source devices are installed in the straight section (see Table 1): A U18 cryogenic permanent magnet in-vacuum undulator (CPMU) with minimum gap 6 mm [43] covers the energy ranges from 11–20 keV and 33–100 keV, see figure 2. Additionally a U27 out-of-vacuum permanent magnet undulator with minimum gap 11 mm covers the energy ranges 7.5–11 keV below the fundamental, and 20–33 keV in between the fundamental and third harmonic of the U18.

### 2.3. Monochromator

The ID06 double crystal monochromator, located in OH at 35.8 m downstream of the nominal source point, is the first optical element of the beamline apart from a 300  $\mu\text{m}$  diamond window that separates the beamline and storage ring vacuum systems, and the white beam primary slits located 27.8 m downstream of the source. The monochromator was designed and built by Cinel Strumenti Scientifici (Vigona, Italy) to ESRF specifications. It has been in continuous operation on ID06 since 2008. It houses two pairs of flat crystals in Bragg-Bragg geometry mounted side by side. By horizontally translating the entire monochromator vessel, either symmetric Si(111) or Si(311) reflections can be selected. The Bragg angle  $\theta$  can be adjusted between  $2.05^\circ$  to  $53.5^\circ$ , covering 2.46–55 keV using the Si(111) pair of crystals, and 4.72–105 keV using the Si(311) pair. In practice, the vast majority of experiments uses the Si(111) pair. The monochromator is operated in fixed exit geometry with an offset of  $z = +15$  mm between the white and monochromatic beams.

The peak monochromatic flux at the sample position is  $\approx 10^{13}$  photons/s at 11 keV, with an unfocused spot size of  $\approx 1$  mm( $h$ )  $\times$  0.5 mm( $v$ ).

### 2.4. Transfocator

The UHV Transfocator [44] is located in OH at a distance of 38.7 m from the source point. The mechanical design is based on in-vacuum piezo-actuators for groups of lens elements. The vacuum chamber can be moved in  $y$ ,  $z$ , pitch and yaw to align the optical axis of the Transfocator to the beam (ESRF in-house design, which is based on a similar device at Petra III [45]). It contains sets of 1D (vertically focusing) and 2D (bi-dimensionally focusing) compound refractive lenses made of Be (RXOptics, Juelich, Germany) that can be moved into and out of the beam in groups. The Transfocator can be used as a collimator or pre-focusing device. Due to the ratio of the distances towards the source and the sample, however, the demagnification of 1:3.9–1:4.8 (depending on the position of the main block of the instrument) remains fairly moderate. For larger demagnification, i.e. smaller spot size or line height at the sample position, condenser optics can be employed close to the sample, see section 2.5.3. The installed lenses allow collimation from 7.5–30 keV and focusing from 7.5–30 keV.

### 2.5. Microscopy bench

The hard x-ray microscope was implemented in the existing experiments hutch EH1 of ID06. The design was therefore restricted by the existing infrastructure and beamline optics as described above.

A Be exit window at 52.4 m from the source ends the UHV section of the beam path. The remainder of EH1 is utilized by the microscopy bench and far-field detector frame, see figure 3. The beam travels in air, without flight paths.

The design goal of the hard x-ray microscope was to achieve a resolution better than 50 nm. For this, optimum mechanical stability is required on short (vibrations) and long (thermal drifts) time scales. Due to its high density, high damping factor and low thermal expansion coefficient, granite is very well suited as the construction material.

In particular, the relative position of the sample and objective lens is critical, as any differential movement of these elements will be amplified in the far-field detector by the geometrical magnification. Common-mode vibrations, however, are not magnified. We have therefore chosen to implement the critical elements on a common granite support (the “main block”), which can be moved on air pads on a support bench, also made from granite. In choosing the position of the main block a compromise has to be made between the maximum scattering angle (limited by the maximum height of the far-field detector, favoring position further downstream) and maximum geometrical magnification (limited by the focal length of the objective lens and the distance to the far-field detector, favoring a position further upstream).

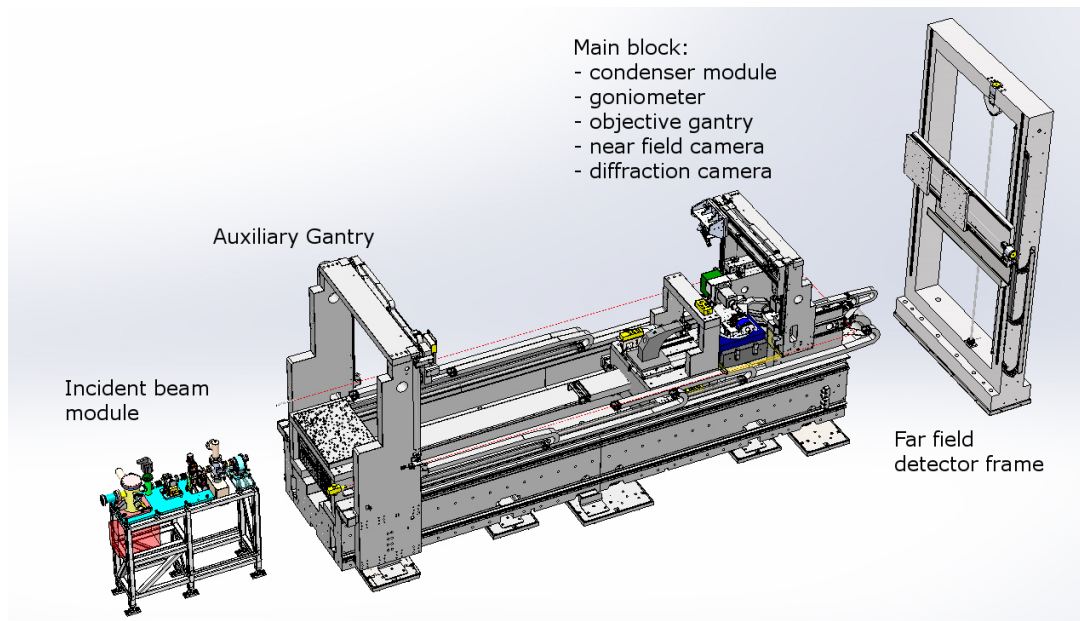


**Figure 3.** The microscopy bench. Along the beam (left to right), elements are: Incident beam module, main block with condenser module, goniometer, near-field camera, objective gantry and diffraction camera. The auxiliary gantry can be moved along the entire length of the bench. The far-field detector frame is located at the downstream end of the hutch.

The support bench, main block, and alignment mechanics were designed and built by LAB motion systems (Leuven, Belgium) to ESRF specifications. An overview is shown in figure 3, further details on the different components are given below.

The bench is assembled from several granite blocks, whose weight was limited by the capacity of the available overhead crane (6 t). Its total weight is about 22 t. It is mounted on 13 adjustable Wedgmount levelers (AirLoc Schrepfer, Oetwil am See, Switzerland) – this lucky number is the result of the blocks being individually supported to aid with their relative alignment before they are rigidly bolted together. Steel plates have been set in the concrete floor to spread the load, provide a flat and level mounting surface, and to anchor the tension bars of the levelers. The complete bench can be disassembled, e.g. to remount it on a different beamline. It is, however, also possible to inject epoxy resin under the bench to permanently bond it to the concrete floor. The bench is 6 m long and 1.4 m wide. The air bearing surface is 0.5 m above the floor.

*2.5.1. Incident beam module* The incident beam module consists of a 0.6 m long optical bread board mounted in fixed position at the upstream end of the bench, 53.7 m from the source. The optical elements on it are (upstream to downstream):

- Beam position monitor based on a quadrupole ionization chamber and ESRF Quadera error amplifier. The vertical beam position detected here is used for feedback on the monochromator's second crystal pitch.
- Secondary slits (AT-F7-AIR, JJ X-ray, Hoersholm, Denmark) at 53.9 m from the source.
- Decoherer (optional) a spinning disk of graphite (Goodfellow 613 136 00) to produce a fluctuating wave front that will average out any speckle from structure in the incident beam's wave front [46].

- Ionization chamber intensity monitor (ESRF design). The ionization chamber can be moved out of the beam by a motorized translation to insert a beam profile monitor (ESRF design using a Basler ace acA1300-30gm CCD camera and Infinity InfiniStix 2× objective) or visible light mirror reflecting a pre-aligned laser beam as an alignment aid.
- Fast shutter, synchronized with the exposure signal of the different cameras.

*2.5.2. Main block* The main block serves as common support for the sample goniometer and for optical elements in close vicinity of the sample, i.e. condenser, near-field camera, diffraction camera, and objective. It can be moved on air pads along the length of the bench. For experiments, its position is typically fixed and the air is turned off. The main block is 2.3 m long and can be translated by 2.8 m.

*2.5.3. Condenser* The condenser unit is the first element on the main block. A translation stage with 340 mm stroke along  $x$  can be equipped with a small hexapod (H-824, Physik Instrumente, Karlsruhe, Germany) and compact Transfocator (ESRF in-house development) with Be lenses for moderate focusing, or a granite arch with  $y$ ,  $z$ , pitch and yaw alignment mechanics for Si, polymer or multilayer Laue lenses for more aggressive focusing. Downstream of the lenses a set of 4-blade motorized slits (AT-F7-AIR, JJ X-ray, Hoersholm, Denmark) and a compact ionization chamber (ESRF design) for intensity monitoring can be mounted.

In recent practice, the most frequently used condenser is a set of 58 vertically focusing 1D Be lenses with apex radius of curvature 100  $\mu\text{m}$  (RXOptics, Juelich, Germany) mounted in a fixed enclosure on the hexapod. This is used in conjunction with 2D lenses in the OH Transfocator to optimize the flux on the entrance pupil of the condenser. A set of 1D SU-8 polymer lenses (KIT, Karlsruhe, Germany) for use at higher photon energies is under commission.

*2.5.4. Sample goniometer* The sample goniometer is mounted on the main block, downstream of the condenser. By moving the main block, the sample can be positioned between 53.6 and 56.4 m from the source and, correspondingly, between 2.2 and 5.0 m from the plane of the far-field detector frame (see section 2.6).

The sample goniometer is assembled from several components. The goniometer base consists of two orthogonal air-bearing rotation stages rotating about the  $z$  (outside) and  $y$  (inside) axes, and an air-bearing  $y$ -stage. It was designed and manufactured by LAB motion systems (Leuven, Belgium) to INSA (Lyon, France) and ESRF specifications. The goniometer provides high quality rotational movement about the horizontal and vertical axes of each respective air bearing rotation stage – the large rotation stage about the  $z$  axis has a maximum rotational error of 36 nm and axial error of 23 nm, and the smaller rotation stage about the  $y$  axis has a maximum rotation error of 80 nm and axial error of 56 nm. The center of rotation can be aligned to the beam axis by the goniometers  $y$ -stage and a stepper motor driven  $z$ -stage (AXMO, Brétigny/Orge, France) underneath the goniometer.

Shown in figure 4 is the part of the goniometer that is closest to the sample. Mounted on the horizontal  $\omega$  rotation stage are a motorized crossed swivel stage (SA04B-RS, Kohzu, Japan) for the “sample tilts”  $\phi$  and  $\chi$ , and a piezo-based  $xyz$  micropositioner for sample centering (SmarAct, Oldenburg, Germany).

The goniometer pre-dates the dark field microscopy project. Its configuration allows for rotations about a horizontal scattering vector (“topo-tomo” or azimuthal scan) [30, 31] when the Bragg angle is set by the outside  $z$  rotation stage. As, due to the asymmetry of the source, the preferred scattering geometry is in the vertical plane, the goniometer should be replaced by a new instrument optimized for topo-tomo in the vertical scattering plane, i.e. with a  $y$ -rotation stage outside and  $z$ -rotation stage inside [21].

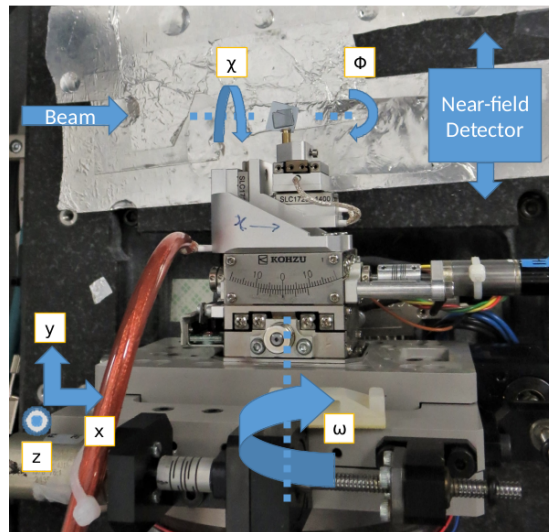


**Figure 4.** View of goniometer: LAB goniometer, Kohzu tilts and SmarAct  $xyz$  stage. Showing beam direction in blue,  $xyz$  coordinate system, and goniometer axes of rotation.

*2.5.5. Near-field camera* The near-field camera is an indirect detector, consisting of a thin scintillator, x-ray transparent mirror, and an optical microscope coupled to a CCD camera. The optics were designed and built by Optique Peter (Lentilly, France) to ESRF specifications. The semi-transparent scintillator can be positioned within millimeters of the sample, e.g. for classical tomography or for DCT-type experiments [30, 31]. Free-standing gadolinium gallium garnet (GGG) single crystals of  $25\ \mu\text{m}$  and  $50\ \mu\text{m}$  thickness are available, as well as thinner scintillator films on a substrate. The objective lens (Mitutoyo M-Plan Apo 10x/0.28 or 5x/0.14) is protected from radiation damage by a lead glass window. Optical parameters of the near-field camera are listed in table 2. The CCD camera is a ESRF FreLoN 2K camera [47].

In addition to  $xyz$  linear alignment axes, the near-field camera is mounted on a rotation table to swing it out of the way when other optical elements, such as the objective lens, need to be positioned in close proximity to the sample, or when a full  $360^\circ$  rotation about the goniometers  $z$  axis is required for alignment purposes.

**Table 2.** Optical parameters of the different cameras of the dark field microscope.

CCD	pixel size [ $\mu\text{m}^2$ ]	Magnification			Effective pixel size [ $\mu\text{m}^2$ ]	Field of view [ $\text{mm}^2$ ]
<b>Near-field camera</b>		Objective	Tube lens	Eye piece		
Atmel TH7899M	14×14	5x 10x	0.9x	2.5x	1.24×1.24 0.62×0.62	2.49×2.49 1.24×1.24
<b>Diffraction camera</b>		Fiber taper				
Atmel TH7899M	14×14	(0.296x)			47.3×47.3	94.6×94.6
<b>Wide-field far field camera</b>		Objective (12 mm f/1.8)				
Sony ICX445	3.75×3.75	≈0.08x			48×48	62×45
<b>High resolution far field camera</b>		Objective	Tube lens			
Atmel TH7899M	14×14	10x	0.9x		1.56×1.56	3.1×3.1

*2.5.6. Diffraction camera* The diffraction camera is a fiber-taper coupled FreLoN camera [48, 47] with effective pixel size (after distortion correction) of  $47.3 \mu\text{m} \times 47.3 \mu\text{m}$ , and field of view  $94.6 \text{ mm} \times 94.6 \text{ mm}$  (see table 2). The camera can be inserted at a distance of 180 to 560 mm downstream of the sample, or be removed completely from the beam path to make room for the objective lens or auxiliary optics and detectors.

It is equipped with a movable beam stop which in turn can be equipped with a photodiode to monitor the intensity of the direct beam. The purpose of the diffraction camera is to record complete diffraction rings at elevated photon energies in order to reconstruct 3D grain maps of the sample using 3DXRD techniques [25, 26, 27, 28]. Grains thus determined can then be studied with ultimate resolution using dark field microscopy or, eventually, coherent techniques.

*2.5.7. Objective* The objective stage allows for  $xyz$ , pitch and yaw adjustment of an objective lens. The pitch (model 5202.60) and yaw (model 410) stages were supplied by Huber Diffraktionstechnik (Rimsting, Germany). The linear and angular travel ranges are large enough to keep the lens aligned with the axis of a diffracted beam up to scattering angles ( $2\theta$ ) of  $30^\circ$ .

The centers of rotation of the pitch and yaw stages intersect in the center of the lens assembly. For rotations about the sample position, e.g. for varying the scattering angle  $2\theta$  during strain scans, the rotations therefore have to be combined with the appropriate translations. The objective stages center of rotation can be positioned between 0 and 380 mm downstream of the sample. The finite length of the lens assemblies imposes further practical limits. In the  $y$ - $z$  plane the objective stage can be moved up to 500 mm away from the beam axis.

Mechanically, the objective stage is implemented as a gantry with two lead screw drives for the  $x$ - and  $z$ - motions, and one lead screw drive for the  $y$ -motion. The  $x$  and  $z$  motions need to be driven simultaneously to avoid skew motions and eventual mechanical damage to the system. This is handled through the ESRF Icepap's "linked axis" firmware option. The  $x$ ,  $y$  and  $z$ -stages are equipped with pneumatic clamps to further improve the mechanical stability when at fixed position.

During the conception of the objective gantry particular attention was paid to minimizing thermal and vibration effects, as the relation of these movements relative to the sample are significantly magnified on the far-field camera based upon the ratios shown in figure 1. Thermal

**Table 3.** Parameters of the different objective lenses.  $E$  is the working energy, NA the numerical aperture,  $N$  and  $T$  the number and distance between lens elements, and  $f$  is the focal length.

	$E$ [keV]	NA [mrad]	Resolution [nm]	$N \times T$ [mm]	$f$ [mm]
Be	17	0.55	$\approx 100$	$68 \times 1.6 + 20 \times 2.0$	277
SU-8	33	0.18	$\approx 140$	$(65(h) + 65(v)) \times 0.77$	330
MLL	17.3	2(h), 1.6(v)	$\approx 30$	–	9.5(h), 13.7(v)
MLL	34.5	0.4(h), 0.7(v)	$\approx 30$	–	37(h), 40(v)

stability was ensured by the choice of granite as the base material linked with the stabilization of the climate in EH1, and reducing wherever possible the thickness of materials with higher coefficients of expansion. To create a rigid structure to reduce the vibration effects, this led to several developments in the placement of rails and sliding carriages to ensure the maximum possible rigidity based on space and translation constraints. This can be seen particularly in the gantry legs whereby two rails have been mounted each side at 90 degrees to each other, which provides a better average stiffness in the  $z$  and  $y$  axes. The rails are also spaced apart and the lower rail provides a strong lever arm against the vibrations in the tops of the structure.

After measuring the frequency response of the objective gantry was found to have its first harmonic at 40 Hz. Given the size of the gantry, this is encouraging and correlates with the original computer simulations completed by both the ESRF and LAB Motion Systems.

At present, three different types of objective lens are used for microscopy experiments:

*Beryllium CRL* Low absorption and high ratio of refractive index decrement over absorption ( $\delta/\beta$ ) make Beryllium in theory the best CRL material at all photon energies [49]. For working energies of  $\approx 15$ – $20$  keV we therefore use a CRL of 88 2D Be lenses with apex radius of curvature of  $50 \mu\text{m}$  (RXOptics, Juelich, Germany). In practice the CRLs are limited by aberration to a resolution around 100 nm.

Optical parameters of the Be CRL are summarized in table 3.

*SU-8 polymer CRL* The chromaticity of the CRL (focal length is approximately proportional to the square of the working energy) limits the practical use of Be in objective lenses to working energies below  $\approx 20$  keV.

While Si-based lenses can potentially achieve very high resolution [50, 51, 39], strong absorption limits their apertures to very small values, which in turn dictates very short working distances – thus the resolution obtained under the practical working conditions of a materials science x-ray microscope (working distance  $\approx 100$ – $300$  mm) is much worse than the ultimate limit of  $\approx 50$  nm that has been demonstrated in optics tests.

SU-8 polymer lenses as developed by the IMT group at KIT present an interesting solution for working energies above 20 keV, combining manufacturing precision, homogeneous material and cost-effectiveness [33].

Optical parameters of the SU-8 CRL are summarized in table 3.

*Multilayer Laue lenses* Recently we successfully tested Multilayer Laue Lenses (MLLs) as objectives for both phase and diffraction contrast imaging [52]. MLLs can have a NA 10 times better than compound refractive lenses, and virtually no manufacturing errors [53]. MLLs are therefore a candidate for achieving a spatial resolution as good as 10 nm or alternatively 10–100

times faster data acquisition. Similar to Si refractive lenses, however, the MLLs available today have small physical apertures and thus require very short working distances [54].

Optical parameters of the two MLL objective lenses that have been tested on the instrument are summarized in table 3. Further optimization in terms of both manufacturing (a larger physical aperture) and alignment is required, but the work is seen as encouraging.

*2.5.8. Auxiliary gantry* The auxiliary gantry is a  $xyz$  alignment stage that can travel along the entire length of the bench. It allows the mounting of additional optical elements for future experiments beyond simple microscopy. Possible uses include the insertion of slits, phase shifters or cameras upstream of the condenser or between the objective lens and far-field detector, e.g. in the back focal plane.

### *2.6. Far-field detectors*

The far-field detector frame is located at the downstream end of EH1, separate from the support bench. It allows  $yz$  positioning of two detectors, a wide-field detector and a high resolution detector. It consists of a granite frame with  $y$  and  $z$  translation stages (AXMO, Brétigny/Orge, France), a cradle that can be inclined to orient the cameras perpendicular to the diffracted beam (Design et Mécanique, Montaud, France), and the detectors.

The far-field detector frame is located 60.64 m downstream of the source, i.e. between 2.2 and 5.0 m downstream of the sample, depending on the position of the main block. Its travel range (using the high resolution detector and direct beam axis as reference points) is  $-0.8$  to  $+0.6$  m in the horizontal ( $y$ ) and  $-0.5$  to  $+2.3$  m in the vertical ( $z$ ) direction.

*2.6.1. Wide-field far camera* This is a simple indirect detector based on a plastic scintillator screen, Linos MeVis-C 12mm f/1.8 machine vision lens, and a C-mount CCD camera (Basler acA1300-30gm). Details are given in table 2.

*2.6.2. High resolution detector* The high resolution detector is an indirect detector composed of a scintillator screen (typically  $10\ \mu\text{m}$  LuAG:Eu on a  $170\ \mu\text{m}$  YAG substrate) [55], optical microscope with Olympus UIS2 UPlanSApo 10x/0.40 objective and Olympus U-TLU-1-2 tube lens. The optical microscope is operated without an eye piece, projecting the intermediate image directly onto an ESRF FreLoN camera [47] with  $2048 \times 2048$  pixels. This combination yields an effective pixel size of  $1.56 \times 1.56\ \mu\text{m}^2$  and a field of view of  $3.1 \times 3.1\ \text{mm}^2$ . The thickness of the scintillator screen is a compromise between quantum efficiency (x-ray absorption) and resolution (due to the limited depth of field of the objective) [56].

The narrow field of view of the high-resolution camera can make finding the diffracted beam somewhat challenging. To facilitate this, both cameras are rigidly mounted on the same support. It is thus possible to first locate and center the diffracted beam in the wide-field camera, and to then switch to the high resolution camera by simply translating the camera support by the predetermined spacing between the cameras.

For dark field microscopy in the horizontal scattering plane (e.g. topo-tomo experiments with the present goniometer), an additional far-field detector can be mounted on a table equipped with  $y$  and  $z$  translations and a rotation about the  $z$  axis. The detector configuration is identical to the high-resolution far-field detector described above.

## **3. Examples**

Below we provide three examples of DFXM applications. Other lines of work performed so far include imaging of dislocations within semiconductors and oxides [23], and processing studies of fuel cells [57].

### 3.1. Deformed metals and alloys

When a pure metal or a metallic alloy is plastically deformed, dislocations self organize into walls surrounding defect-free regions known as cells or subgrains with a size of  $\approx 1 \mu\text{m}$ . Moreover, these cells organize into intricate patterns inside existing grains. During subsequent annealing the stored energy is released by the processes of recovery and recrystallisation. In the former the cells refine and strain is released. In the latter new strain-free grains are nucleated and grow at the expense of the deformed matrix. Recovery and recrystallisation co-exist within the sample. Electron microscopy has been extensively used for post mortem studies of both the plastic deformation and the annealing phenomena. DFXM provides a unique opportunity to study these multi-scale phenomena *in situ* from deeply embedded grains within  $\approx \text{mm}$ -sized specimens [19, 58, 59, 24].

In a first example, DFXM was used to study a deeply embedded alpha iron grain within a  $330 \mu\text{m}$  thick sample of Fe with 850 ppm Nitrogen [24]. Prior to the experiment, the sample was solutionized at 580 C for 15 hours. Using a 33 keV full field beam and the SU-8 polymer lens as objective, projections were acquired. The exposure time was 1 s. The high angular resolution of DFXM enables us to resolve the mosaic spread in the rocking ( $\theta$ ) and rolling ( $\chi$ ) directions, within the grain. Despite the annealing the mosaicity map of the (110) reflection shows a substantial angular spread (figure 5(a)). The orientation gradient in this figure can be resolved with EBSD. The local misorientation, however, falls below the angular resolution of conventional EBSD.

In a second example, DFXM was used to study a deeply embedded recrystallized grain in a 50% recrystallized Al 1050 alloy [19]. A cross-sectional layer was illuminated with a condensed line beam and imaged with the Be CRL as objective at 17 keV with exposure time of 1 s. The mosaicity map presented in figure 5(b) clearly shows the subgrain structures separated by low-angle boundaries within the recrystallized grain.

In a recent experiment, we have generalised DFXM to allow observation of the microstructure in highly deformed materials of key industrial interest. Specifically the microstructural changes during *in-situ* annealing of a steel sample deformed to a true strain of  $\epsilon \approx 2$  were studied (to be presented elsewhere [60]).

### 3.2. Strain and domain mapping in ferroelectrics

Ferroelectric, ferroelastic and multiferroic materials are typified by the presence of domains: distinct regions of similar lattice orientation, separated by atomically-coherent domain walls (e.g. inversion about a zone axis) [61]. In response to stresses, electric fields, or other perturbations, these domain structures self-organize via the collective motion of domain walls. Given the strong anisotropy of many of these materials, the modulation of domain structures is often accompanied by significant macroscopic responses (e.g. changes in the dielectric and piezoelectric coefficients). These large responses are widely utilized in a range of applications including shape-memory alloys, digital memory and solid-state capacitors. Furthermore, the discovery of emergent phenomena at the domain walls (e.g. photoelectricity) has renewed interest in the local structure at and around such walls [62]. The ability to quantitatively probe the lattice strain and misorientation in the vicinity of the domain walls is expected to yield important insights into what drives these emergent phenomena.

Here, DFXM was used to reveal the domain structure embedded within a bulk single crystal of barium titanate ( $\text{BaTiO}_3$ ). Figure 6 shows the image intensity acquired in a single exposure, which shows clear contrast from the individual domains. Given the 001-orientation of the crystal, it is evident that the domain walls lie on  $\langle 110 \rangle$  lattice planes, and that the domain walls are not completely straight. The curvature of domain walls in this manner indicates the presence of underlying electric or elastic heterogeneities, such as vacancies or dislocations, that cause the walls to distort from their lowest-energy configuration. The key advantage of investigating such

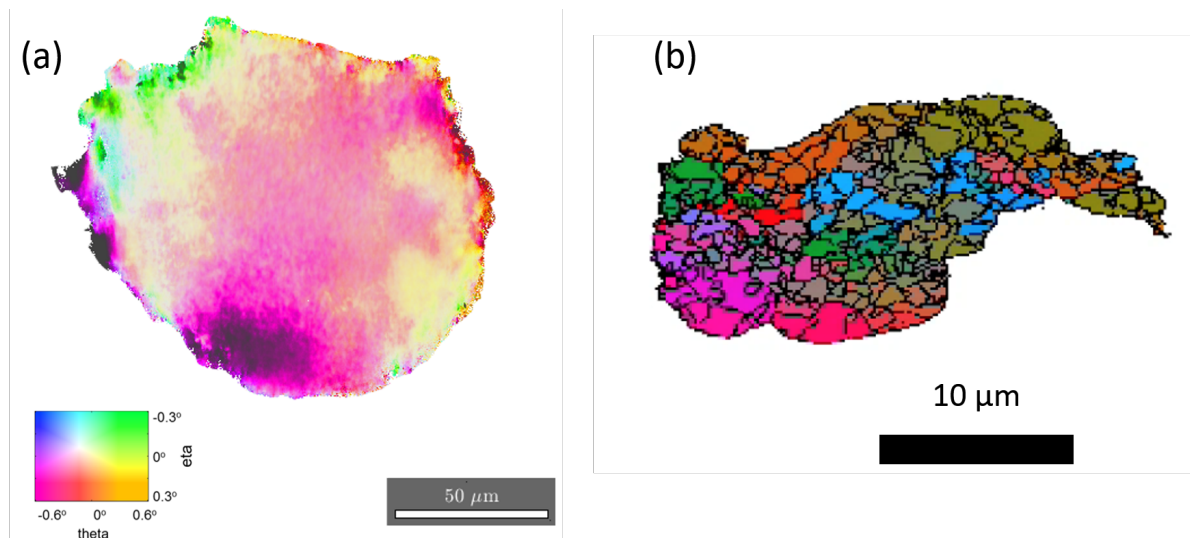


**Figure 5.** (a) Mosaicity map of a Fe-850 ppmN grain after annealing at 580 C for 15 h. This is a projection image with the color code indicating angular variation within parts of a (110) pole figure. (b) Mosaicity map of a layer within a recrystallized grain in 50% recrystallized Al 1050. The colors indicates angular variation within parts of a (200) pole figure.

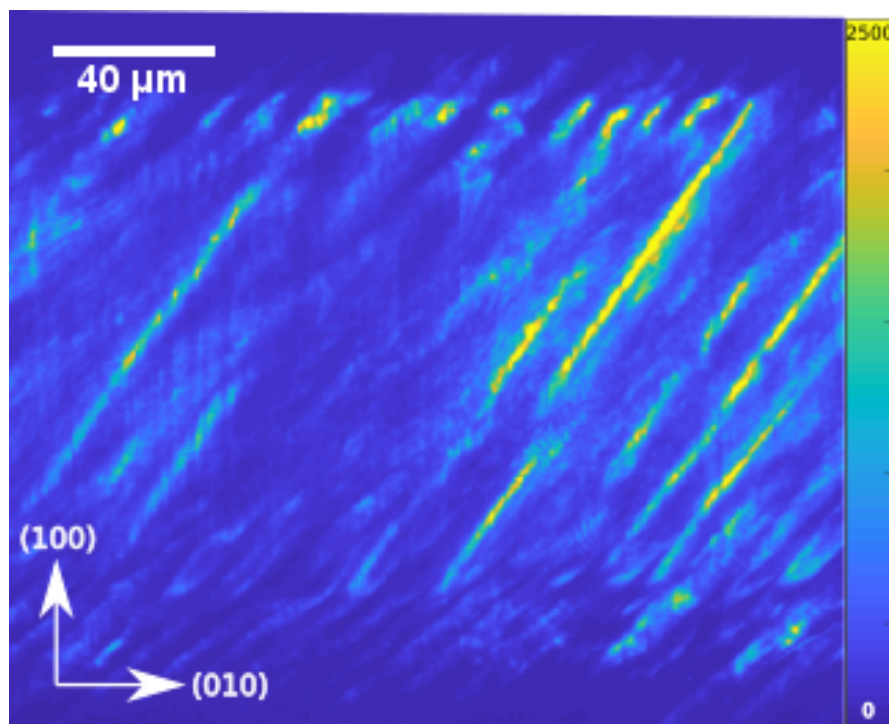


**Figure 6.** Dark field x-ray microscopy image of domains embedded in a single crystal of  $\text{BaTiO}_3$ . The domain walls are clearly curved, indicating the presence of underlying elastic or electric heterogeneities. The color code to the right indicates intensity in arbitrary units.

domain structures using DFXM is that it is a full-field imaging technique. As such, full images of embedded domain structures may be captured in a single exposure within a second or less. This allows for dynamic studies of multiscale structures under applied electric fields or at elevated temperatures [63]. These measurements are key to understanding and accurate modelling of ferroelectricity and ferroelasticity, and are directly comparable to multi-scale models, such as phase-field and Monte-Carlo simulations.

Shown in figure 7 are the first DFXM results using the MLL as the objective. The figure shows a map of the average lattice misorientation from a projection through the BaTiO<sub>3</sub> crystal. The ferroelastic domain walls are clearly visible as diagonal lines aligned with the 110 direction of the sample. In this map, the transition region between neighbouring domain orientations at the domain wall is in the order of 1  $\mu\text{m}$  thick. The map also shows a clear misorientation between the top and bottom parts of the image, which is likely to be attributable to an out-of-plane domain wall along 101-type planes. This allows the local lattice distortions at the intersection of the 101- and 110-oriented domain walls to be investigated directly and in detail.

### 3.3. Microstructure of biominerals

Biominerals are hierarchical materials found throughout nature [64]. Examples are widespread, including bone, tooth, corals, shells, and otoliths. Biominerals form as a combination of inorganic mineral and organic template under strict biological control by the organism, yielding an exceptional control of final structure in both crystallography and habit [64]. This control has evolved to yield materials whose properties are optimized for particular functions, such as wear resistance for teeth, or strength and crack resistance for protective shells [64]. Like nature, materials science aims to produce function-optimized materials. Bio-inspired structures are becoming increasingly common as scientists seek to understand and replicate natural growth processes *in vitro*. Nonetheless, there remain many aspects of biomineralization that remain to be fully understood.

As examples, we present two types of biominerals that have been examined with DFXM [65]. The first relates to the nacreous layer in a mussel shell. This grows in a brick-and-mortar-like assembly, composed of calcium carbonate platelets surrounded by proteinaceous organic matrix. A piece of shell from the edge was broken off and mounted on the sample support. Examination with the dark-field microscope permitted visualization of a multitude of platelets with a large range in orientation (figure 8) [65]. Reflections were observed across the full scan range of  $0.6^\circ$  on both  $\theta$  and in the azimuth. This unique view of the platelets *in-situ* illustrates their highly controlled assembly and inter-platelet relationships.

The second biomineral examined was fish otolith [65]. Otoliths are calcium carbonate accretions that grow in the inner ear of vertebrate fish. They are composed of aragonite fibres which extend from the nucleus to the outer surface [66]. A hierarchical structure is present, comprising the fibre, bundles of prismatic crystalline units, and nanogranules. DFXM reveals evidence of all of these levels of organization (figure 9). The visible otolith fibre is  $\approx 100 \mu\text{m}$  long and individual bundles of prismatic crystalline units are visible along its length. The interruptions between bundles along the growth axis likely correspond to daily growth layers governed by the individuals circadian rhythm. Single crystalline units can be seen stacked side by side across the fibre. Individual nanogranules cannot be resolved, but small clusters can be seen. The prismatic crystalline units are closely oriented with respect to the growth axis, with the crystal  $c$  axes coherent to within  $\pm 2^\circ$ . The orientation of the  $a$  and  $b$  axes, however, appears to be isotropic, with prisms occupying a wide range of orientations around the  $c$  axis.

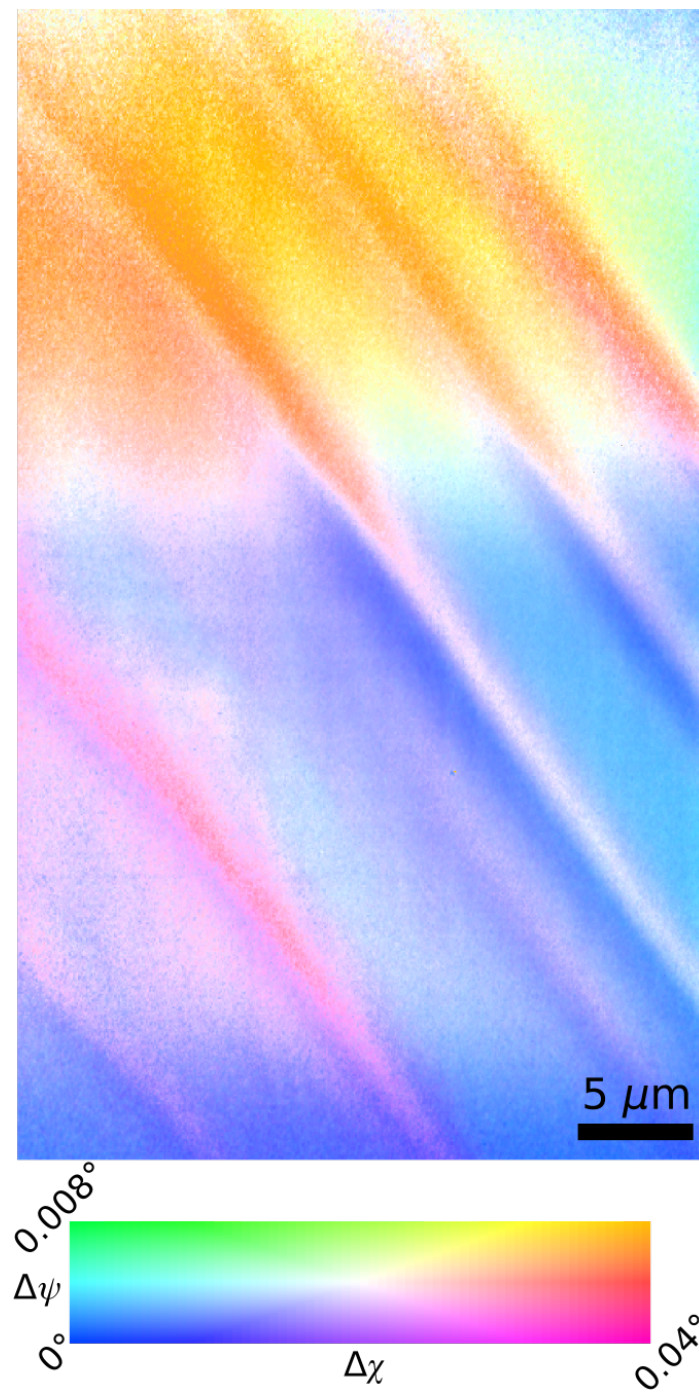


**Figure 7.** Dark-field x-ray microscopy images using the MLL as objective. Projection image of lattice misorientations around ferroelastic/ferroelectric domains in a BaTiO<sub>3</sub> single crystal. The misorientation is represented by colour according to the part of a pole figure below

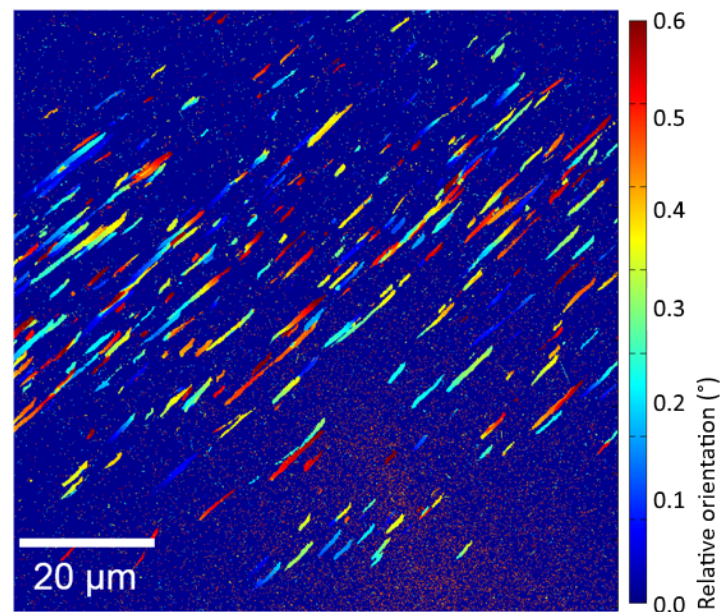


**Figure 8.** Orientations of nacre platelets in a mussel shell imaged by dark-field X-ray microscopy. The colours indicate orientation differences according to the scale to the right. Figure adapted from [65].

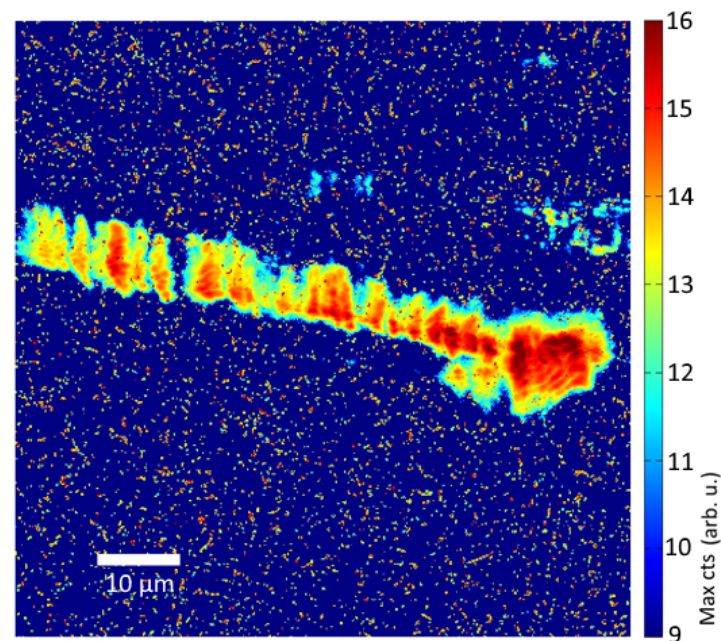


**Figure 9.** A dark-field image of an aragonite fibre from a fish otolith shows its growth from left to right in sequential layers, each composed of multiple crystalline units. The colour scale indicates intensity. Figure taken from [65].

**Table 4.** Present and future source parameters of ID06 [71]

		Present source	EBS Upgrade
Horizontal rms source size	[ $\mu\text{m}$ ]	387.8	27.2
Horizontal rms source divergence	[ $\mu\text{rad}$ ]	10.3	5.2
Vertical rms source size	[ $\mu\text{m}$ ]	3.5	3.4
Vertical rms source divergence	[ $\mu\text{rad}$ ]	1.2	1.4

## 4. Outlook

### 4.1. A multi-scale view of microstructure

Dark-field x-ray microscopy is a promising technique for multi-scale characterization of hierarchical microstructures in materials. Yet, the field of view and spatial resolution of DFXM cover only a portion of this range. Moreover, the field of view in reciprocal space is very restricted, such that only one Bragg reflection of one grain can be studied at any given time. In order to obtain a complete multi-scale view, DFXM has to be combined with complementary diffraction and imaging techniques that can provide the missing information. In particular, DCT or 3DXRD can be used to obtain three-dimensional maps of the position and orientation of all grains within a sample, with relatively lower real space and reciprocal space resolution. Acquisition of such maps would enable users to differentiate and select the relevant regions of interest (ROI) in the microstructure. Furthermore, we have ongoing work to develop a high-resolution variant of 3DXRD to bridge the gap between conventional far-field 3DXRD and DFXM.

The spatial resolution of DFXM is ultimately limited by the numerical aperture of the objective lens. In the need of higher resolution, coherent x-ray techniques such as (Bragg) coherent diffraction imaging [11, 15, 16, 13, 17, 18, 67] or Fourier ptychography [68, 69, 70] can be employed to extend DFXM towards higher spatial and reciprocal space resolution.

Common to all these techniques is that they employ hard x-rays. Therefore, it is possible, with some technical development, to perform all of the aforementioned techniques on the same instrument without the need to re-mount the sample.

The instrument at ID06 is designed with this need in mind. Efforts for on-line data analysis and integration of DCT and 3DXRD results into the DFXM data acquisition strategies are ongoing. The integration of all of the mentioned techniques is the main focus of the upcoming EBS upgrade beamline.

### 4.2. EBS upgrade beamline

The HXRM project has been selected for implementation as an Upgrade beamline for the ESRF EBS (Extremely Bright Source) upgrade. The microscope will be installed at a dedicated beamline with optics and infrastructure fully optimized for x-ray microscopy. We expect that the project will be implemented in 2022, and that the new beamline will be open to external users via the ESRF general user proposal system in 2023.

With the EBS upgrade [71], the source parameters will be improved significantly, as shown in table 4. In combination with a new, fully optimized undulator this will lead to a 10–30 fold increase in the maximum photon flux at the sample, but more importantly to a 200–600 fold increase in coherent flux.

The dedicated beamline will also allow pink beam operation. For bright field imaging the chromatic aberration associated with both refractive and diffractive optics can be overcome by focusing the incoming beam on the back focal plane [41], and pink beam operation can therefore lead to an increase in useful flux by two orders of magnitude. For dark field operation

a bandwidth of 1 % is not optimal, but numerical simulations indicate that it may be of relevance [72].

### Acknowledgments

The authors thank Élise Dufour (UMR 7209 CNRS/Muséum National d'Histoire Naturelle) for providing otolith samples for study. We acknowledge the Karlsruhe Nano Micro Facility (KNMF) at Karlsruhe Institute of Technology (KIT) for the provision of SU-8 polymer lenses and DTU Nanolab for provision of a Si based condenser. We acknowledge the S. Bajt at the CFEL for the provision of the multilayer Laue lenses. The authors thank Tao Zhou for assistance during Fe-N experiment and the loan of SU-8 polymer lenses.

### References

- [1] Liu H H, Schmidt S, Poulsen H F, Godfrey A, Liu Z Q, Sharon J A and Huang X 2011 *Science* **332** 833–834
- [2] Midgley P A and Dunin-Borkowski R E 2009 *Nature Materials* **8** 271–280
- [3] Zaaferani N, Raabe D, Singh R, Roters F and Zaeferrer S 2006 *Acta Mater.* **54** 1863–1876
- [4] Uchic M D, Groeber M A, Dimiduk D M and Simmons J 2006 *Scripta Mater.* **55** 23–28
- [5] Larson B C, Yang W, Ice G E, Budai J D and Tischler J Z 2002 *Nature* **415** 887–890
- [6] Hofmann F, Abbey B, Liu W, Xu R, Usher B F, Balaur E and Liu Y 2013 *Nat. Commun.* **4** 2774
- [7] Schroer C G, Kurapova O, Patommel J, Boye P, Feldkamp J, Lengeler B, Burghammer M, Riekel C, Vince L, van der Hart A and Kuchler M 2005 *Appl. Phys. Lett.* **87** 124103
- [8] Mimura H, Handa S, Kimura T, Yumoto H, Yamakawa D, Yokoyama H, Matsuyama S, Inagaki K, Yamamura K, Sano Y, Tamasaku K, Nishino Y, Yabashi M, Ishikawa T and Yamauchi K 2009 *Nat. Phys.* **6** 122–125
- [9] Ice G E, Budai J D and Pang J W L 2011 *Science* **334** 1234
- [10] Xu C, Zhang Y, Godfrey A, Wu G, Liu W, Tischler J Z, Liu Q and Juul Jensen D 2017 *Scientific Reports* **7**
- [11] Miao J, Charalambous P, Kirz J and Sayre D 1999 *Nature* **400** 342–344
- [12] Dierolf M, Menzel A, Thibault P, Schneider P, Kewish C M, Wepf R, Bunk O and Pfeiffer F 2010 *Nature* **467** 436–439
- [13] Pfeifer M A, Williams G J, Vartanyants I A, Harder R and Robinson I K 2006 *Nature* **442** 63–66
- [14] Shapiro D, Thibault P, Beetz T, Elser V, Howells M, Jacobsen C, Kirz J, Lima E, Miao H, Neiman A M and Sayre D 2005 *Proc. Nat. Acad. Sci. USA* **102** 15343–15346
- [15] Chapman H and Nugent K 2010 *Nature Phot.* **4** 833–839
- [16] Miao J, Ishikawa T, Robinson I K and Murnane M 2015 *Science* **348** 530–535
- [17] Chamard V, Stangl J, Carbone G, Diaz A, Chen G, Alfonso C, Mocuta C and Metzger T 2010 *Phys. Rev. Lett.* **104** 165501
- [18] Yau A, Cha W, Kanan M, Stephenson G and Ulvestad A 2017 *Science* **356** 739–742
- [19] Simons H, King A, Ludwig W, Detlefs C, Pantleon W, Schmidt S, Stöhr F, Snigireva I, Snigirev A and Poulsen H F 2015 *Nat. Commun.* **6** 6098
- [20] Simons H, Jakobsen A C, Ahl S R, Detlefs C and Poulsen H F 2016 *MRS Bulletin* **41** 454
- [21] Poulsen H F, Jakobsen A C, Simons H, Ahl S R, Cook P K and Detlefs C 2017 *J. Appl. Cryst.* **50** 1441
- [22] Poulsen H F, Cook P K, Leemreize H, Pedersen A F, Yildirim C, Kutsal M, Jakobsen A C, Trujillo J X, Ormstrup J and Detlefs C 2018 *J. Appl. Cryst.* **51** 1428–1436
- [23] Jakobsen A C, Simons H, Ludwig W, Yildirim C, Leemreize H, Porz L, Detlefs C and Poulsen H F 2019 *J. Appl. Cryst.* **52** 122
- [24] Mavrikakis N, Detlefs C, Cook P, Kutsal M, Campos A, Gauvin M, Calvillo P, Saikaly W, Hubert R, Poulsen H, Vaugeois A, Zapolsky H, Mangelinck D, Dumont M and Yildirim C 2019 *Acta Materialia* **174** 92–104
- [25] Poulsen H F, Nielsen S F, Lauridsen E M, Schmidt S, Suter R M, Lienert U, Margulies L, Lorentzen T and Juul Jensen D 2001 *J. Appl. Cryst.* **34** 751
- [26] Schmidt S, Nielsen S F, Gundlach C, Margulies L, Huang X and Juul Jensen D 2004 *Science* **305** 229–232
- [27] Jakobsen B 2006 *Science* **312** 889–892
- [28] Hefferan C M, Lind J, Li S F, Lienert U, Rollett A D and Suter R M 2012 *Acta Mater.* **60** 4311–4318
- [29] Pokharel R 2018 *Overview of High-Energy X-Ray Diffraction Microscopy (HEDM) for Mesoscale Material Characterization in Three-Dimensions* (OSTI, 2018)
- [30] King A, Johnson G, Engelberg D, Ludwig W and Marrow J 2008 *Science* **321** 382–385
- [31] Ludwig W, Reischig P, King A, Herbig M, Lauridsen E M, Johnson G, Marrow T J and Buffiere J Y 2009 *Rev. Sci. Instrum.* **80** 033905
- [32] Snigirev A, Kohn V G, Snigireva I I and Lengeler B 1996 *Nature* **384** 49

- [33] Marschall F, Last A, Simon M, Kluge M, Nazmov V, Vogt H, Ogurreck M, Greving I and Mohr J 2014 *Journal of Physics: Conference Series* **499** 012007
- [34] Stöhr F, Wright J, Simons H, Michael-Lindhard J, Hübner J, Jensen F, Hansen O and Poulsen H F 2015 *J. Micromech. Microeng.* **25** 125013
- [35] Ludwig W, Cloetens P, Härtwig J, Baruchel J, Hamelin B and Bastie P 2001 *J. Appl. Cryst.* **34** 602–607
- [36] Lengeler B, Schroer C, Tümmler J, Benner B, Richwin M, Snigirev A, Snigireva I and Drakopoulos M 1999 *J. Synchrotron Rad.* **6** 1153–1167
- [37] Falch K V, Casari D, Di Michiel M, Detlefs C, Snigirev A, Snigireva I, Honkimäki V and Mathiesen R H 2016 *J. Mater. Sci.* **52** 3497–3507
- [38] Falch K V, Lyubomirskij M, Casari D, Detlefs C, Snigirev A, Snigireva I, Detlefs C, Di Michiel M, Lyatun I and Mathiesen R H 2018 *Ultramicroscopy* **184** 267
- [39] Simons H, Ahl S R, Poulsen H F and Detlefs C 2017 *J. Synchrotron Rad.* **24** 392
- [40] Van Vaerenbergh P, Detlefs C, Härtwig J, Lafford T A, Masiello F, Roth T, Schmid W, Wattecamp P and Zhang L 2010 *AIP Conf. Proc.* **1234** 229
- [41] Falch K V, Detlefs C, Di Michiel M, Snigireva I, Snigirev A and Mathiesen R H 2016 *Appl. Phys. Lett.* **109** 054103
- [42] Guignard J and Crichton W A 2015 *Rev. Sci. Instrum.* **86** 085112
- [43] Chavanne J, Le Bec G and Penel C 2011 *Synchrotron Rad. News* **24** 10–13
- [44] Snigirev A, Snigireva I I, Vaughan G B M, Wright J P, Rossat M, Bytchkov A and Curfs C 2009 *J. Phys. Conf. Ser.* **186** 012073
- [45] Zozulya A V, Bondarenko S, Schavkan A, Westermeier F, Grübel G and Sprung M 2012 *Opt. Express* **20** 18967
- [46] Falch K V, Detlefs C, Paganin D, Christensen M S and Mathiesen R 2019 *Opt. Express* In press
- [47] Labiche J C, Mathon O, Pascarelli S, Newton M A, Guilera Ferre G, Curfs C, Vaughan G, Homs A and Fernandez Carreiras D 2007 *Rev. Sci. Instrum.* **78** 091301
- [48] Coan P, Peterzol A, Fiedler S, Ponchut C, Labiche J C and Bravin A 2006 *J. Synchrotron Rad.* **13** 260–270
- [49] Serebrennikov D, Clementyev E, Semenov A and Snigirev A 2016 *J. Synchrotron Rad.* **23** 1315–1322
- [50] Schroer C G and Lengeler B 2005 *Phys. Rev. Lett.* **94**(5) 054802
- [51] Simons H, Stöhr F, Michael-Lindhart J, Jensen F, Hansen O, Detlefs C and Poulsen H F 2015 *Opt. Commun.* **359** 460
- [52] Murray K T, Pedersen A F, Mohacsi I, Detlefs C, Morgan A J, Prasciolu M, Yildirim C, Simons H, Jakobsen A C, Chapman H N, Poulsen H F and Bajt S 2019 *Opt. Express* **27** 7120
- [53] Bajt S, Prasciolu M, Fleckenstein H, Domaracký M, Chapman H N, Morgan A J, Yefanov O, Messerschmidt M, Du Y, Murray K T, Mariani V, Kuhn M, Aplin S, Pande K, Villanueva-Perez P, Stachnik K, Chen J P, Andrejczuk A, Meents A, Burkhardt A, Pennicard D, Huang X, Yan H, Nazaretski E, Chu Y S and Hamm C E 2017 *Light: Science & Applications* **7** 17162–17162
- [54] Morgan A J, Prasciolu M, Andrejczuk A, Krzywinski J, Meents A, Pennicard D, Graafsma H, Barty A, Bean R J, Barthelmess M, Oberthuer D, Yefanov O, Aquila A, Chapman H N and Bajt S 2015 *Sci. Rep.* **5** 9892
- [55] Martin T and Koch A 2006 *Journal of Synchrotron Radiation* **13** 180–194
- [56] Koch A, Raven C, Spanne P and Snigirev A 1998 *J. Opt. Soc. Am. A* **15** 1940–1951
- [57] Sierra J, Poulsen H, Jørgensen P, Detlefs C, Cook P, Simons H, Jakobsen A and Bowen J 2019 *Journal of Power Sources* **413** 351–359
- [58] Ahl S, Simons H, Zhang Y, Detlefs C, Stöhr F, Jakobsen A, Juul Jensen D and Poulsen H 2017 *Scripta Materialia* **139** 87–91
- [59] Ahl S, Simons H, Detlefs C, Juul Jensen D and Poulsen H F 2019 Subgrain dynamics during recovery of partly recrystallized aluminium to be published
- [60] Yildirim C *et al.* 2019 Dark field x-ray microscopy study of in-situ annealing of a highly deformed steel sample in preparation
- [61] Tagantsev A K, Cross L E and Fousek J 2010 *Domains in ferroic crystals and thin films* vol 13 (Springer)
- [62] Catalan G, Seidel J, Ramesh R and Scott J F 2012 *Reviews of Modern Physics* **84** 119
- [63] Simons H, Haugen A B, Jakobsen A C, Schmidt S, Stöhr F, Majkut M, Detlefs C, Daniels J E, Damjanovic D and Poulsen H F 2018 *Nature Materials* **17** 814
- [64] Gilbert P U P A, Abrecht M and Frazer B H 2005 *Rev. Mineral. Geochem.* **59** 157–185
- [65] Cook P K, Simons H, Jakobsen A C, Yildirim C, Poulsen H F and Detlefs C 2018 *Microscopy and Microanalysis* **24** 8889
- [66] Dauphin Y and Dufour E 2008 *Micron* **39** 891 – 896 ISSN 0968-4328
- [67] Pedersen A F, Chamard V, Detlefs C, Zhou T, Carbone D and Poulsen H F 2018 X-ray coherent diffraction imaging with an objective lens: towards 3d mapping of thick polycrystals (*Preprint arxiv:1810.04268*)
- [68] Simons H, Poulsen H F, Guigay J P and Detlefs C 2016 X-ray fourier ptychographic microscopy (*Preprint*)

- arxiv:1609.037513)
- [69] Wakonig K, Diaz A, Bonnin A, Stampanoni M, Bergamaschi A, Ihli J, Guizar-Sicairos M and I A M 2019 *Sci. Adv.* **5** eaav0282
- [70] Detlefs C, Beltran M A, Guigay J P and Simons H 2019 Translative lens-based full field coherent x-ray imaging (*Preprint arxiv:1905.01916*)
- [71] Dimper R, Reichert H, Raimondi P, Sanchez Ortiz L, Sette F and Susini J 2014 *The Orange book: ESRF Upgrade Programme Phase II (2015-2022)* (ESRF, Grenoble (France))
- [72] Pedersen A F, Chamard V and Poulsen H F 2018 *Optics Express* **26** 23411

### **A.3 Co-authorship 3: Reciprocal space mapping and strain scanning using X-ray diffraction microscopy**

# Reciprocal space mapping and strain scanning using X-ray diffraction microscopy

H. F. Poulsen,<sup>a,\*</sup> P. K. Cook,<sup>b</sup> H. Leemreize,<sup>c,a</sup> A. F. Pedersen,<sup>a</sup> C. Yildirim,<sup>b,d</sup>  
M. Kutsal,<sup>b</sup> A. C. Jakobsen,<sup>a</sup> J. X. Trujillo,<sup>e</sup> J. Ormstrup<sup>a</sup> and C. Detlefs<sup>b</sup>

<sup>a</sup>Department of Physics, Technical University of Denmark, 2800 Kongens Lyngby, Denmark, <sup>b</sup>European Synchrotron Radiation Facility, 71 avenue des Martyrs, CS40220, 38043 Grenoble Cedex 9, France, <sup>c</sup>Danish Technological Institute, Denmark, <sup>d</sup>OCAS, J. F. Kennedylaan 3, 9060 Zelzate, Belgium, and <sup>e</sup>Department of Energy Storage and Conversion, Technical University of Denmark, 4000 Roskilde, Denmark. \*Correspondence e-mail: hfpo@fysik.dtu.dk

Received 18 June 2018  
Accepted 9 August 2018

Edited by A. Borbély, Ecole National Supérieure des Mines, Saint-Etienne, France

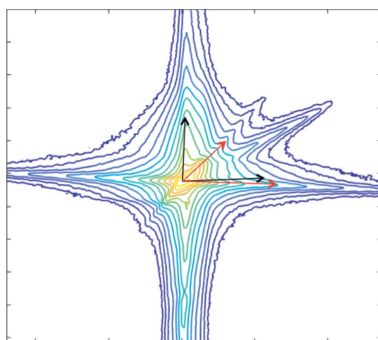
**Keywords:** X-ray diffraction microscopy; diffraction contrast tomography; structural characterization; synchrotron radiation; tomography; diffraction imaging.

Dark-field X-ray microscopy is a new full-field imaging technique for nondestructively mapping the structure of deeply embedded crystalline elements in three dimensions. Placing an objective in the diffracted beam generates a magnified projection image of a local volume. By placing a detector in the back focal plane, high-resolution reciprocal space maps are generated for the local volume. Geometrical optics is used to provide analytical expressions for the resolution and range of the reciprocal space maps and the associated field of view in the sample plane. To understand the effects of coherence a comparison is made with wavefront simulations using the fractional Fourier transform. Reciprocal space mapping is demonstrated experimentally at an X-ray energy of 15.6 keV. The resolution function exhibits suppressed streaks and an FWHM resolution in all directions of  $\Delta Q/Q = 4 \times 10^{-5}$  or better. It is demonstrated by simulations that scanning a square aperture in the back focal plane enables strain mapping with no loss in resolution to be combined with a spatial resolution of 100 nm.

## 1. Introduction

Dark-field X-ray microscopy (DFXRM) is a new full-field imaging technique for mapping crystallographic features in bulk specimens in three dimensions (Simons *et al.*, 2015). Similar to bright-field X-ray microscopy (Schroer *et al.*, 2001), an objective lens is inserted between the sample and a high-resolution two-dimensional detector, but in this case in the Bragg diffracted beam. This enables nondestructive mapping of structure, orientation and strain within deeply embedded crystalline elements (Simons *et al.*, 2015). A first implementation at beamline ID06 at the European Synchrotron (ESRF) is based on the use of a monochromatic beam in the 15–35 keV range and a compound refractive lens (CRL) (Snigirev *et al.*, 1996) as objective. The magnification and field of view can be modified by changing the focal length of this objective. Lens imperfections currently limit the spatial resolution to  $\sim 100$  nm.

In combination with coarse-scale grain mapping methods such as three-dimensional X-ray diffraction (Poulsen, 2004, 2012; Hefferan *et al.*, 2012) and diffraction contrast tomography (King *et al.*, 2008; Ludwig *et al.*, 2009), DFXRM has proven to be a powerful method for multi-scale studies of polycrystals and their dynamics (Simons *et al.*, 2016). First applications include work on the processing of plastically deformed metals (Ahl *et al.*, 2015), the distribution of strain and orientation gradients in ferroelectrics (Simons *et al.*, 2018),



© 2018 International Union of Crystallography

and the three-dimensional mapping of dislocations (Simons *et al.*, 2016), as well as studies of biominerals (Cook, 2018).

Poulsen *et al.* (2017) provided a detailed description of the optics of the image plane of this microscope, including parameters such as numerical aperture, vignetting, and the resolution in both direct and reciprocal space. It was shown that the resolution function in reciprocal space can be highly anisotropic and can vary as a function of position within the field of view. Procedures for sampling and conservation of integrated intensities were presented. We shall refer to this work as Paper 1 throughout.

Similar to classical light microscopy and transmission electron microscopy (Williams & Carter, 2009), the hard X-ray microscope is associated with a back focal plane (BFP). The intensity distribution in the BFP is equivalent to the distribution in the Fraunhofer far-field limit. This has been utilized for bright-field microscopy studies (Bosak *et al.*, 2010; Ershov *et al.*, 2013; Falch *et al.*, 2018).

Complementary to Paper 1, in this work we provide a detailed description of the optics of the BFP in the dark-field mode. Analytical expressions are derived from a thick-lens ray-transfer-matrix formalism following Simons *et al.* (2017). When relevant, this work is supplemented by full-scale wavefront simulations based on fractional Fourier transforms (Ozaktas & Mendlovic, 1995; Le Bolloch *et al.*, 2012; Pedersen *et al.*, 2018). Procedures for reciprocal space mapping based on placing a two-dimensional detector in the BFP are presented. Next, we consider placing an aperture in the BFP in combination with a detector in the imaging plane. It is shown that high strain resolution may be obtained without losing spatial resolution. In §4, the reciprocal space mapping is demonstrated by an experimental study at 15.6 keV.

## 2. Geometry and formalism

### 2.1. Dark-field microscopy geometry

The geometry of the dark-field X-ray microscope is illustrated in Fig. 1. The sample goniometer provides a base tilt,  $\mu$ , a rotation,  $\omega$ , and two orthogonal sample tilts,  $\chi$  and  $\phi$ . The incident beam is defined by a slit close to the source and/or by a condenser. It is characterized by angular divergences  $\Delta\zeta_v$  and  $\Delta\zeta_h$  in the vertical and horizontal directions, respectively, and by an energy bandwidth  $\Delta E/E$ . The motors  $\chi$ ,  $\phi$  and  $\mu$  are used to orient an embedded crystalline element of choice (*e.g.* a grain or domain) such that it is in the Laue condition with its diffraction vector,  $\mathbf{Q}$ , parallel to the rotation axis  $\omega$ , implying that  $\mathbf{Q}$  remains in the diffraction condition at all values of  $\omega$  (the so-called topo-tomography setting). The direction of the optical axis of the diffracted beam is described by the scattering angle,  $2\theta$ , and the azimuthal angle,  $\eta$  (Fig. 1).

The objective is in the following a CRL comprising  $N$  identical parabolic shaped lenslets with a radius of curvature  $R$  and a distance between the centers of adjacent lenslets  $T$ . Let the linear attenuation coefficient and the refractive index decrement of the lens material be  $\mu_{\text{att}}$  and  $\delta$ , respectively. The objective magnifies the diffracted beam by a factor  $\mathcal{M}_{\text{CRL}}$  and

generates an inverted two-dimensional image in the image plane. The distance from the sample plane to the front of the objective is  $d_1$ , and the distance between sample plane and image plane is  $d_1 + NT + d_2$  (see Fig. 1). With  $NT$  typically of the same order as  $d_1$ , a thick-lens description is required. Simons *et al.* (2017) provided a comprehensive thick-lens description for the bright-field case using a ray-transfer-matrix (RTM) approach. In Paper 1, the same RTM formalism is used to provide equations for the dark-field case in relation to direct and reciprocal space resolution functions and a discussion of sampling strategies.

Three equations from Paper 1 of key interest for this work are

$$f_N = f\varphi \cot(\varphi N), \quad (1)$$

$$\sigma_a \simeq \delta \frac{\mathcal{M}_{\text{CRL}}}{\mathcal{M}_{\text{CRL}} + 1} \left( \frac{2N}{\mu_{\text{att}} R} \right)^{1/2}, \quad (2)$$

$$\sigma_v = \frac{2\delta}{\mu_{\text{att}} \sigma_a} [N^2 \varphi^2 - \sin^2(N\varphi)]^{1/2}. \quad (3)$$

Here  $f = R/(2\delta)$  is the focal length of one lenslet,  $\varphi = (T/f)^{1/2}$ , and  $f_N$  is the focal length of the CRL and therefore the distance from the end of the objective to the back focal plane (*cf.* Fig. 1).  $\sigma_a$  is the r.m.s. width of the angular attenuation profile, describing the numerical aperture.  $\sigma_v$  is the r.m.s. width of the Gaussian distribution associated with vignetting.

Following Paper 1, for simplicity in the following we assume  $\omega = \eta = 0$ . Furthermore we introduce two direct space coordinate systems: the imaging system – defined by  $\hat{x}$  being parallel to the diffracted beam and  $\hat{y}$  perpendicular to the incoming beam in the horizontal plane – and a reference system offset from the imaging system by an angle  $\theta$  around the common  $y$  axis. In both cases we can define colinear reciprocal space coordinate systems. For the reference system the coordinates are  $(\hat{q}_{\text{rock}}, \hat{q}_{\text{roll}}, \hat{q}_{\parallel})$ . Here ‘rock’ refers to the

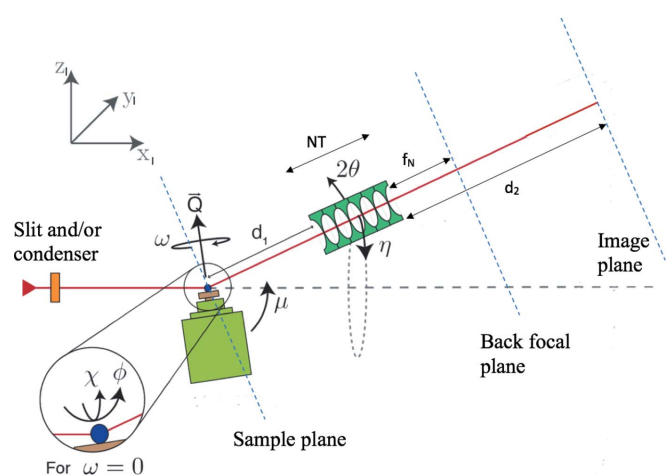


**Figure 1** Principle of dark-field X-ray microscopy. The red line between the pivotal point of the goniometer and the detector (image plane) is the optical axis of the diffracted beam. The laboratory coordinate system  $(x_1, y_1, z_1)$  is shown. See also main text.

transverse in-plane ‘rocking’ direction of classical two-axis diffractometers, ‘roll’ to the out-of-plane ‘rolling’ around the incoming beam and  $\parallel$  to the longitudinal (radial) direction in reciprocal space ( $\hat{q}_{\parallel}$  is parallel to  $\mathbf{Q}$ ). The corresponding coordinates for reciprocal space associated with the imaging system are defined as  $(\hat{q}_{\text{rock}'}, \hat{q}_{\text{roll}}, \hat{q}_{2\theta})$ . For more general settings and details of coordinate transforms see Paper 1.

### 2.2. Imaging in the back focal plane

In an ideal imaging system with a fully coherent beam, the (amplitude, phase) field in the BFP is a Fourier transform of the (amplitude, phase) field in the sample plane (Goodman, 2005). The BFP is in our case a plane perpendicular to the optical axis and is located at a distance of one focal length from the exit of the objective, as given by equation (1). Let  $(\hat{y}_B, \hat{z}_B)$  span the BFP and be colinear with the axes  $(\hat{y}_s, \hat{z}_s)$  in the sample plane. Then in geometrical optics there is a one-to-one correspondence between coordinates  $(y_B, z_B)$  and angles  $(\xi_{ys}, \xi_{zs})$  with respect to the optical axis – as measured in the sample plane. Using the RTM formalism, we have (*cf.* Simons *et al.*, 2017)

$$y_B = \frac{f_N}{\cos(N\varphi)} \xi_{ys}, \tag{4}$$

$$z_B = \frac{f_N}{\cos(N\varphi)} \xi_{zs}. \tag{5}$$

These expressions are independent of the position in the sample space.

### 3. Reciprocal space mapping

In a scattering geometry where the optical axis of the objective is aligned with the center of a Bragg diffracted beam, the angular deviations  $\xi_{ys}$  and  $\xi_{zs}$  are related to reciprocal space. Let  $(\Delta Q_{\text{rock}'}/|\mathbf{Q}_0|, \Delta Q_{\text{roll}}/|\mathbf{Q}_0|, \Delta Q_{2\theta}/|\mathbf{Q}_0|)$  be the deviation from the nominal Bragg lattice point,  $\mathbf{Q}_0$ . Then, following equations (52) and (71) in Paper 1, we have

$$y_B = \frac{2 \sin(\theta) f_N}{\cos(N\varphi)} \frac{\Delta Q_{\text{roll}}}{|\mathbf{Q}_0|}, \tag{6}$$

$$z_B = \frac{2 \sin(\theta) f_N}{\cos(N\varphi)} \frac{\Delta Q_{2\theta}}{|\mathbf{Q}_0|}. \tag{7}$$

The third direction in reciprocal space – when described by the imaging system coordinates – is  $\hat{q}_{\text{rock}'}$ . However, the parameter that can easily be varied experimentally is  $\hat{q}_{\text{rock}}$ , as this is defined by the ‘rocking angle’, the position of either  $\mu$  or  $\phi$  (*cf.* Fig. 1). Hence, the experimental data, as defined by detector coordinates and rocking angle, are not in an orthogonal system.

To generate data in an orthogonal system one therefore needs to interpolate. In the imaging coordinate system this implies the following relationship:

$$\frac{\Delta Q_{\text{rock}'}}{|\mathbf{Q}_0|} = (\phi - \phi_0) \cos(\theta), \tag{8}$$

$$\frac{\Delta Q_{\text{roll}}}{|\mathbf{Q}_0|} = \frac{\cos(N\varphi)}{2 \sin(\theta) f_N} y_B, \tag{9}$$

$$\frac{\Delta Q_{2\theta}}{|\mathbf{Q}_0|} = \frac{\cos(N\varphi)}{2 \sin(\theta) f_N} z_B - (\phi - \phi_0) \sin(\theta). \tag{10}$$

Here  $\phi_0$  corresponds to the maximum of the rocking curve, and to  $\mu$  being equal to the nominal Bragg angle.

### 3.1. The effect of attenuation

It is relevant to determine the range of the reciprocal space map and to know which area in the sample plane the reciprocal space map refers to. Both properties are defined by the attenuation of the CRL. Analytical expressions for the imaging plane are provided in Paper 1, which with simple modifications can be adapted to the BFP geometry.

For the point in the sample plane that is on the optical axis, the attenuation gives rise to an angular acceptance which is a Gaussian distribution defined by the numerical aperture. The r.m.s. width of the range in normalized reciprocal space  $\mathbf{q} = \mathbf{Q}/|\mathbf{Q}_0|$  becomes

$$\sigma_q = \frac{\sigma_a}{2 \sin(\theta)}. \tag{11}$$

For the point in reciprocal space which corresponds to the center of the region mapped, the intensity contributions from points in the sample plane are weighted with a Gaussian attenuation function, the vignetting. The width of this defines the field of view: the r.m.s. value is  $\sigma_v$ , as expressed by equation (3).

The attenuation for the general off-axis case is given by equation (24) of Simons *et al.* (2017). Consider a ray emerging from a point in the sample plane with position  $\mathbf{r}_s$  and at a distance  $\mathbf{q}_r$  to the nominal center in the (normalized)  $(q_{\text{roll}}, q_{2\theta})$  plane. The attenuation then becomes a product of three terms:

$$\text{Att}(r_s, \xi_s) = \exp(-\mu N T_w) \Omega(\mathbf{r}_s, \mathbf{q}_r) \text{Vign}(\mathbf{r}_s), \tag{12}$$

$$= \exp(-\mu N T_w) \exp\left(\frac{-\{q_r + [\gamma/2 \sin(\theta)] r_s\}^2}{2\sigma_q^2}\right) \times \exp\left(-\frac{r_s^2}{2\sigma_v^2}\right). \tag{13}$$

The first term reflects the attenuation caused by the web distances,  $T_w$ , between neighboring apices in the CRL. The second describes the angular acceptance, while the third is the vignetting term.

It appears that the vignetting in the sample plane remains the same as in the on-axis case. The middle term indicates that the range in reciprocal space is also unaltered, but the center position in reciprocal space shifts with varying  $r_s$  by  $\gamma r_s/2 \sin(\theta)$ . Expressions for  $\gamma$  are provided in the supplementary materials of Simons *et al.* (2017). For long to medium focal distances we have to a good approximation

$$1/\gamma = (d_1^2 + f^2 \varphi^2)^{1/2}. \tag{14}$$

Typical numerical values for  $1/\gamma$  are 10–30 cm.

### 3.2. Reciprocal space resolution

Initially we will be concerned with the widths – in three orthogonal directions – of the reciprocal space resolution function and shall neglect low-intensity tails. We anticipate that these widths are governed by the divergence and the energy bandwidth of the incoming beam. Furthermore we shall assume the incoming beam to be Gaussian. Such a model was derived for the reciprocal space resolution function in the image plane in §4.1 of Paper 1. Applying a similar approach here for the BFP, we treat the divergence as small perturbations ( $\zeta_{h,v}$ ) to the horizontal and vertical components of the incident beam vector,  $\mathbf{k}_{in}$ , and the energy bandwidth in the form of a longitudinal perturbation,  $\varepsilon = \Delta E/E = \Delta k/k$ , to both incident and diffracted beam vectors. In the imaging coordinate system the deviations from the nominal incident and diffracted wavevectors are thus

$$\Delta \mathbf{k}_{in} = k \begin{bmatrix} \cos(2\theta) & 0 & \sin(2\theta) \\ 0 & 1 & 0 \\ -\sin(2\theta) & 0 & \cos(2\theta) \end{bmatrix} \begin{pmatrix} \varepsilon \\ \zeta_h \\ \zeta_v \end{pmatrix}_{\text{Lab}}, \quad (15)$$

$$\Delta \mathbf{k}_{out} = k \begin{pmatrix} \varepsilon \\ 0 \\ 0 \end{pmatrix}_{\text{Imaging}}. \quad (16)$$

The deviation from the nominal scattering vector becomes

$$\frac{\Delta \mathbf{Q}}{|\mathbf{Q}_0|} = \frac{\Delta \mathbf{k}_{out} - \Delta \mathbf{k}_{in}}{2k \sin(\theta)} \quad (17)$$

$$= \frac{1}{2 \sin(\theta)} \left\{ \begin{array}{l} [1 - \cos(2\theta)]\varepsilon - \sin(2\theta)\zeta_v \\ -\zeta_h \\ \sin(2\theta)\varepsilon - \cos(2\theta)\zeta_v \end{array} \right\}_{\text{Imaging}}. \quad (18)$$

If we assume  $\zeta_h$ ,  $\zeta_v$  and  $\varepsilon$  to be independent variables, and each to occur randomly with a Gaussian distribution centered about zero, then the corresponding terms should be added in quadrature to estimate the r.m.s. widths in reciprocal space. Let  $\Delta \zeta_v$ ,  $\Delta \zeta_h$  and  $\sigma_\varepsilon$  be the r.m.s. widths of the corresponding distributions. Then the resulting r.m.s. widths are

$$\frac{\Delta Q_{\text{rock}'}}{|\mathbf{Q}_0|} = [\sin^2(\theta)\sigma_\varepsilon^2 + \cos^2(\theta)\Delta \zeta_v^2]^{1/2}, \quad (19)$$

$$\frac{\Delta Q_{\text{roll}}}{|\mathbf{Q}_0|} = \frac{\Delta \zeta_h}{2 \sin(\theta)}, \quad (20)$$

$$\frac{\Delta Q_{2\theta}}{|\mathbf{Q}_0|} = \left\{ \cos^2(\theta)\sigma_\varepsilon^2 + \left[ \frac{\cos(2\theta)}{2 \sin(\theta)} \right]^2 \Delta \zeta_v^2 \right\}^{1/2}. \quad (21)$$

Notably these equations are valid for all points in the sample plane, on-axis as well as off-axis.

In reality the resolution function is far from Gaussian. Similar to a classical triple-axis setup with a monochromator and an analyzer crystal (Rütt *et al.*, 1995), it is characterized by long tails caused by the surface truncation rods – in our case from the two crystals in the monochromator and the sample itself.

### 3.3. Reciprocal space mapping described as a convolution

Having introduced the various terms, we can now give a comprehensive description of the imaging properties of the BFP. We operate in the four-dimensional space spanned by position in sample plane  $\mathbf{r}_s$  and reciprocal space coordinates  $\mathbf{q} = (q_{\text{roll}}, q_{2\theta})$ . The geometrical optics formulation above provides a relation between the measured intensity distribution in the BFP,  $I(\mathbf{q})$ , the vignetting function in the sample plane,  $\text{Vign}(\mathbf{r}_s)$ , the angular attenuation,  $\Omega(\mathbf{r}_s, \mathbf{q})$ , the reciprocal space resolution function,  $\text{Res}(\mathbf{q})$ , and the field in the sample plane expressed as a distribution function,  $R(\mathbf{r}_s, \mathbf{q})$ . We have

$$I(\mathbf{q}) \propto \int_{-\infty}^{\infty} \text{Vign}(\mathbf{r}_s) \times \int_{-\infty}^{\infty} R(\mathbf{r}_s, \mathbf{q}') \Omega(\mathbf{r}_s, \mathbf{q}') \text{Res}(\mathbf{q} - \mathbf{q}') d\mathbf{q}' d\mathbf{r}_s. \quad (22)$$

For a suitable small and well centered object, we have  $\text{Vign} = 1$  and  $\Omega = \Omega(\mathbf{q}')$ . For some studies the reciprocal resolution function can be considered a delta function. Then equation (22) reduces to

$$I(\mathbf{q}) \propto \int_{-\infty}^{\infty} R(\mathbf{r}_s, \mathbf{q}) \exp\left(-\frac{q^2}{2\sigma_q^2}\right) d\mathbf{r}_s. \quad (23)$$

In that case, one image in the BFP simply represents one slice in the reciprocal space map of the entire grain, normalized by  $\exp(-q^2/2\sigma_q^2)$ . This slice is tilted by  $\theta$  with respect to  $\mathbf{G}$ . Other slices can be added by ‘rocking’ the sample [*cf.* equations (8)–(10)]. Experimentally, the ‘thickness’ of such a slice can be increased by integrating the signal over  $\theta$ , *e.g.* by a continuous rocking scan.

The range of the reciprocal space map can be enlarged by translating the objective. (A simultaneous translation of the detector in the BFP may be required by the field of view of the detector itself.) It is favorable at the same time to tilt the objective such that the optical axis always points to the same point in the sample plane. For changes of a few degrees in  $2\theta$  or  $\eta$  the relevant optical parameters are to a good approximation constant.

### 3.4. The effect of coherence

In order to study the effect of coherence we turn to a Fourier optics description. We shall approximate the incoming beam as a plane wave. The simulations will be based on the use of fractional Fourier transforms, FrFTs (Ozaktas & Mendlovic, 1995; Le Bolloch *et al.*, 2012). As presented by Pedersen *et al.* (2018), FrFT calculations can be orders of magnitude faster than traditional Fresnel propagation programs, in particular in connection with the use of a cascade of lenses (a CRL).

Shown in Fig. 2 are the results of an FrFT simulation of a 17 keV study of the pattern in the BFP from an  $8 \times 8 \mu\text{m}$  square pinhole placed on the optical axis in the sample plane. The incoming beam is assumed to be parallel with a Gaussian energy spread with  $\sigma_e = 10^{-4}$ , while the geometry of the Be

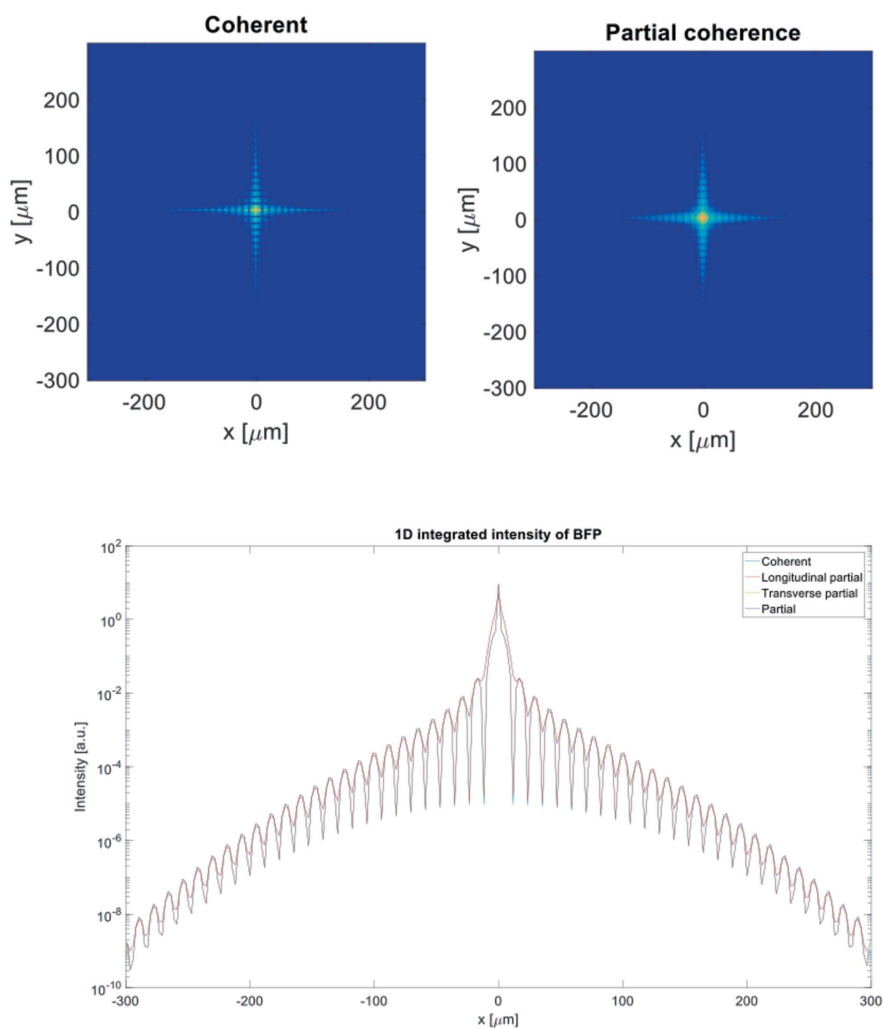


**Figure 2**  
 Above: simulated signal in the back focal plane from an  $8 \times 8 \mu\text{m}$  square pinhole in the sample plane for a fully coherent and a partially coherent case. Below: a projection onto the horizontal direction for a clearer view of the fringe pattern.

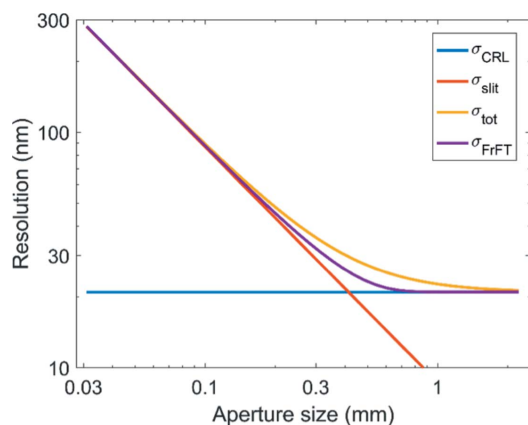


**Figure 3**  
 Spatial resolution of an imaging system with a CRL objective and a square aperture placed on the optical axis in the BFP. The figure shows the r.m.s. width in the image plane as a function of the aperture size. The blue, yellow and red lines represent geometrical optics calculations for the CRL alone, for the slit alone and for the combination (see text). Shown in purple is the corresponding wavefield simulation for the entire system based on the use of fractional Fourier transforms.

CRL objective is defined by  $N = 70$ ,  $R = 50 \mu\text{m}$ ,  $T = 1.6 \text{ mm}$ ,  $d_1 = 297 \text{ mm}$  and  $M = 10$ . Coherence was introduced according to Voelz (2011).

Comparing a fully coherent beam and a beam with a small coherence length (corresponding to placing a  $1 \times 1 \text{ mm}$  slit  $18 \text{ m}$  upstream from the sample) there is no difference in the image plane, but in the back focal plane a fringe pattern is observed for the coherent case. For partial coherence the fringes disappear and the pattern becomes the envelope of the fully coherent case. Similar to the case for bright-field microscopy (Lyubomirskiy *et al.*, 2016), it appears that one may use back focal plane images for characterizing the degree of vertical and horizontal coherence.

#### 4. Strain mapping by means of scanning an aperture in the back focal plane

In this section we shall consider the combination of an aperture in the BFP and imaging with a two-dimensional detector in the image plane. Similarly to operations with transmission electron microscopes, the major advantage of introducing an aperture is that it selects a small region in reciprocal space and that the maps acquired will represent the parts of real space that diffract into this region – without the aperture the region is fixed and given by the numerical aperture (NA) of the objective.

One challenge is that the diffraction limit of the spatial resolution in the imaging plane will deteriorate with decreasing size of the aperture,  $D$ . Fig. 3 shows results for  $17 \text{ keV}$  with a parallel incoming beam and with an objective having a focal length  $f_N = 27 \text{ cm}$  and a magnification of 10. The diffraction limit calculated from geometrical optics is shown for the CRL and the aperture in the BFP independently. The combined effect is not readily determined using geometrical optics, but as a heuristic, the combined effect is modeled as  $\sigma_{\text{tot}} = (\sigma_{\text{CRL}}^2 + \sigma_{\text{slit}}^2)^{1/2}$  (yellow curve). Also shown as a purple curve is the result of a corresponding wavefield simulation. In practice, imperfection in lens manufacture currently limits the resolution to around  $100 \text{ nm}$ . Hence, it appears from Fig. 3 that apertures larger than  $80 \mu\text{m}$  will not deteriorate the real space resolution.

We therefore propose to perform strain mapping in the sample plane by scanning a large aperture in the BFP. By a suitable sampling for each voxel in the sample one can derive a reciprocal space map with a strain resolution given by

equations (19)–(21). Moreover, it is possible to fit the position of a peak to a fraction of the width. As an example, in neutron strain scanning this ratio can be as high as 1:100. Hence a sensitivity to strain variations of  $10^{-5}$  or below is clearly within reach.

### 5. Experimental demonstration

The experiments took place at the dedicated dark-field microscopy instrument at ID06, with the goniometer placed 56.66 m from the source. An Si(111) Bragg–Bragg monochromator defined a 15.6 keV X-ray beam with an r.m.s. bandwidth of  $\sigma_e = 6 \times 10^{-5}$ . The divergence of the incoming beam was defined by two slits, positioned at distances of 27.8 and 53.9 m from the source, respectively. The openings of the two slits were both  $0.5 \times 0.5$  mm, implying divergences (FWHM) of  $\Delta\zeta_v = \Delta\zeta_h = 0.027$  mrad.

The experiment was performed in a vertical scattering geometry with  $\omega = \eta = 0$  (cf. Fig. 1). The objective comprised  $N = 45$  two-dimensional Be lenslets, each with a nominal radius of curvature of  $R = 50$   $\mu\text{m}$  and thickness of  $T = 1.6$  mm. Hence, the focal length was  $f_N = 0.406$  m. The magnification was determined to be  $\mathcal{M}_{\text{CRL}} = 12.32$ , from which follows  $\sigma_a = 0.24$  mrad. The two-dimensional detector placed in the BFP comprised a scintillator coupled by microscope optics to a pco2000  $2k \times 2k$  CCD with a physical pixel size of 7.4  $\mu\text{m}$ . The objective and eyepiece in the camera gave an inherent magnification by 10.

For this setup, 1 pixel (0.74  $\mu\text{m}$ ) in the back focal plane corresponds to a  $\Delta Q/Q$  of  $4.0 \times 10^{-6}$ . The range in reciprocal space (FWHM) is in the same units  $2.35\sigma_q = 1.35 \times 10^{-3}$ . The FWHM of the vignetting function is  $2.35\sigma_v = 5.1$  mm.

To test the model for the resolution function of the BFP, an Si wafer was studied in transmission, with diffraction from a

220 reflection at  $2\theta = 23.98^\circ$ . Scans were made of the ‘rocking angle’  $\phi$  within a range of  $\pm 0.015^\circ$  and with 150 equidistant steps. The monochromator was detuned to avoid saturation of the detector.

Three orthogonal projections of the resulting reciprocal space map are shown in Figs. 4, 5 and 6. In the  $(\hat{q}_{\text{rock}'}, \hat{q}_{2\theta})$  plane there are five streaks, of which two in the up/down direction of the figure are overlapping to some extent. We adopt a similar approach to that used with classical triple-axis diffractometers in a dispersive setup. We can associate one of these streaks – the one along  $\hat{q}_{\parallel}$  – with the ‘lambda streak’ and three of the others with surface streaks from the three Si single crystals in the beam. The one along  $\hat{q}_{\text{rock}}$  is from the Si test sample, while the two placed symmetrically around  $\hat{q}_{\parallel}$  are assigned to the two monochromator crystals. The strongest streak, however, is along the  $\hat{q}_{2\theta}$  axis. Figs. 5 and 6 reveal that the dominant contribution is an approximately circular disc in the  $(\hat{q}_{2\theta}, \hat{q}_{\text{roll}})$  plane in reciprocal space. This is exactly the signature expected of any contribution from the objective. Hence, we attribute this to ‘diffuse scattering’ from the CRL caused by aberration. Fig. 6 also exhibits additional low-intensity features, in particular in the lower left corner. We tentatively associate these with lens imperfections. Furthermore, we speculate that the lack of inversion symmetry in Fig. 4 is due to the detuning of the monochromator.

Considering only the central part of the resolution function, the experimental values for the FWHM are  $(\Delta Q_{\text{rock}'}/|Q_0|, \Delta Q_{\text{roll}}/|Q_0|, \Delta Q_{2\theta}/|Q_0|) = (13, 40, 40)10^{-6}$ . The simple Gaussian model provided by equations (19), (20) and 21 gives the corresponding values  $(34, 44, 143)10^{-6}$ . If as a test we insert  $\sigma_e = 1 \times 10^{-5}$  instead the results are  $(18, 44, 46)10^{-6}$ , which within experimental error is consistent with the experimental data. This finding as well as inspection of Fig. 4 points to a

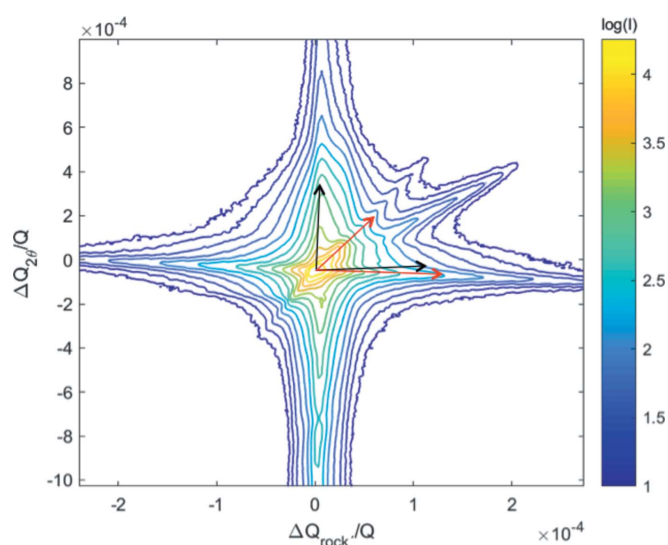


**Figure 4** Experimental reciprocal space resolution function. Projected intensity on the scattering plane. For ease of visualization the axes have different ranges. The  $(q_{\text{rock}'}, q_{2\theta})$  coordinate system is marked by black arrows and the  $(q_{\text{rock}}, q_{\parallel})$  coordinate system in red. The contour lines represent a  $\log_{10}$  scale as marked by the colorbar to the right.

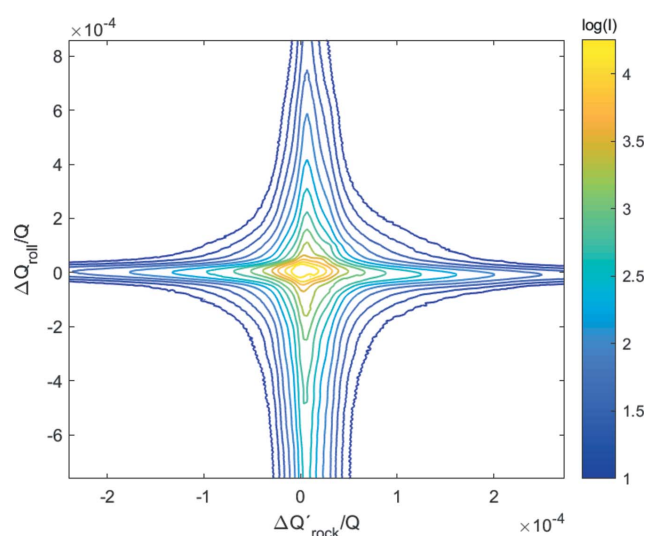


**Figure 5** Experimental reciprocal space resolution function. Projected intensity on the  $(q_{\text{rock}'}, q_{\text{roll}})$  plane. For ease of visualization the axes have different ranges. The contour lines represent a  $\log_{10}$  scale as marked by the colorbar to the right.

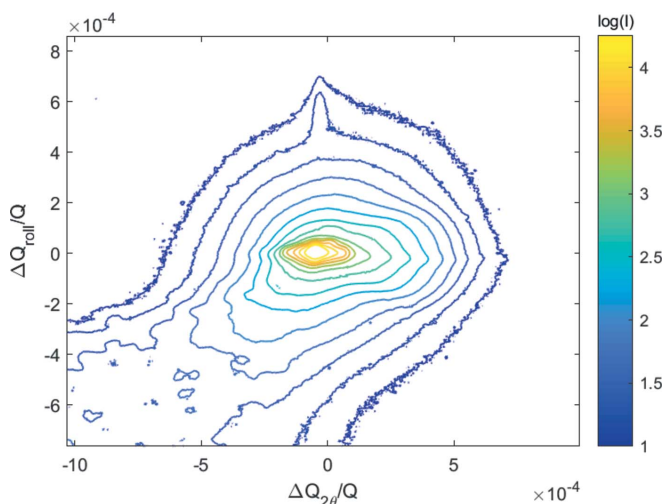


**Figure 6**  
Experimental reciprocal space resolution function. Projected intensity on the  $(q_{2\theta}, q_{roll})$  plane. The axes have identical ranges. The contour lines represent a  $\log_{10}$  scale as marked by the colorbar to the right.

much reduced ‘lambda streak’ in comparison to the simple Gaussian model.

The result is that the FWHM of the reciprocal space resolution function in all directions is small:  $40 \times 10^{-6}$  or below.

## 6. Discussion

### 6.1. Reciprocal space mapping

The classical approach to reciprocal space mapping is the use of a triple-axis diffractometer with identical monochromator and analyzer crystals (Pietsch *et al.*, 2004). For a nondispersive setup, where the  $d$  spacings of all crystals are nearly the same, the resolution function is as described, for example, by Neumann *et al.* (1994) and Liss *et al.* (1998). It is characterized by the presence of three streaks in the scattering plane: a ‘sample streak’ aligned with  $\hat{q}_{rock}$ , a ‘monochromator streak’ tilted by  $\theta$  with respect to  $\hat{q}_{\parallel}$  and an ‘analyzer streak’ tilted by  $-\theta$  with respect to  $\hat{q}_{\parallel}$ . The dispersive setup is described, for example, by Rütt *et al.* (1995). Here it is shown that the resolution function tends to be dominated by a streak in the longitudinal direction, the ‘lambda streak’, but also that all streaks are suppressed.

These features are manifest also in the BFP setting. In particular the ‘lambda streak’ is suppressed. Further work is required to establish a model that can predict the resolution function in detail. For now we propose to measure it in the manner adopted in this paper, using a semiconductor wafer as a reference sample with a reflection that has a scattering angle close to the one of interest for a given sample.

For reasons of sampling it may be of interest to have a resolution function with identical FWHM along the three principal axes. This can be enabled by varying the incoming divergences and matching the step size in the continuous scan of the rocking angle.

In comparison to the triple-axis configuration the BFP approach has a number of advantages and disadvantages

(1) Three-dimensional mapping. The triple-axis setup is confined to the scattering plane. As such it involves an integration over reciprocal space in the rolling direction. In contrast the resolution function in dark-field microscopy is three dimensional in nature, and may even be designed to be symmetric.

(2) Local information. Dark-field microscopy is favorable for combining reciprocal space mapping with direct space information.

(3) Range. A triple-axis setup can provide a map over a large fraction of reciprocal space. In contrast this is only possible in dark-field microscopy by a complicated combined movement involving both the objective and the BFP detector. Furthermore, owing to the Gaussian-type vignetting term in direct space, it is non-trivial to create a larger reciprocal space map by stitching together smaller parts (unless the sample is an ideal single crystal as is the case for an Si wafer). A similar challenge relates to mapping in the image plane, as discussed in Paper 1.

An alternative approach to reciprocal space mapping is to avoid using an analyzer and to place the detector in the true far-field (Fraunhofer) regime. This is central to Bragg coherent diffraction imaging type work, but is also used for incoherent beams (see *e.g.* Jakobsen *et al.*, 2006). The reciprocal space resolution for this case is identical to the BFP case – with the exception of spurious effects by the objective. One subtle difference though is the shift by  $\theta$  in which plane is viewed in reciprocal space.

### 6.2. Strain scanning

In Paper 1 it is described that ‘mosaicity maps’ visualizing the tilt of the diffraction vector (local pole figures) can be generated in two ways: first, by scanning the sample through  $(\phi, \chi)$  or linear combinations of these angles, and second, by scanning a combination of the base tilt  $\mu$  and a linear combination of  $(\phi, \chi)$  that is perpendicular to the beam for all values of  $\omega$ . With misorientations between neighboring grains or domains typically much larger than the numerical aperture of the objective, this procedure is well adapted to the task.

In Paper 1, a scanning procedure is also introduced for determining the axial strain. This involves scanning the  $2\theta$  arm, that is a combined translation and rotation of the objective and the detector. In this case the  $2\theta$  resolution – as defined by  $\sigma_a$  – is of the same order as the strain variation. Hence, one cannot derive a strain distribution for each point in the sample, but only the average strain as determined by the center-of-mass (CMS) of the strain scan.

Operating in the BFP is complementary to this approach as the intrinsic resolution in our case is  $5 \times 10^{-5}$ . Hence, for many specimens one may determine the entire strain distribution in each voxel. Furthermore, the CMS value of the distribution will be determined with a much higher precision. Also it is easier to ensure a mechanically stable operation by translating an aperture in the BFP than by a combined

translation of objective and detector. As already mentioned, a disadvantage of the BFP approach is the limitation in strain range. This can to a minor degree be helped by increasing the number of lenslets in the CRL [cf. equation (2)].

### 6.3. Limitations and outlook

It should be emphasized that the approach outlined above only probes reciprocal space in the vicinity of one diffraction vector. Hence, the full orientation of the domains is not determined, and only three out of the nine components of the displacement gradient tensor are monitored (Hofmann *et al.*, 2017). To provide a full description, the mapping has to be repeated for at least two other non-collinear reflections associated with the same domain. This is currently not possible without re-mounting the sample.

Dark-field X-ray microscopy is motivated by the need to generate three-dimensional volumetric data. There are two alternative strategies for obtaining three-dimensional maps. The first is using a one-dimensionally focusing condenser to illuminate a slice of the material, which is then imaged at the oblique angle of  $2\theta$ , *i.e.* a magnified version of classical section topography (Medrano *et al.*, 1997; Ohler *et al.*, 2000). In this case, a three-dimensional volume is obtained in a layer-wise manner by translating the sample through the planar beam in small increments. A second, faster but more involved method involves illuminating the entire grain and taking projections from different viewing angles while rotating the sample about  $\mathbf{Q}$  (*i.e.* rotation in  $\omega$ ) in the topo-tomography approach (Ludwig *et al.*, 2001). The three-dimensional maps are then reconstructed using adapted tomographic algorithms. The three-dimensional reconstruction algorithm itself, however, is outside the scope of this paper.

In outlook, recently multilayer Laue lenses (MLLs) have been manufactured with excellent optical performance (Morgan *et al.*, 2015). At ID06 we have successfully tested such devices as objectives for use in dark-field microscopy (to be reported elsewhere). In comparison to CRLs the MLLs have several advantages for operation in the BFP:

(1) Larger numerical aperture. The range in reciprocal space  $\sigma_q$  increases linearly with  $\sigma_a$ .

(2) Square aperture. The MLL is optically a thin lens characterized by a square aperture. This implies that for a small sample the detector image is directly proportional to the density in a square in  $(\hat{q}_{\text{roll}}, \hat{q}_{2\theta})$  space. This eases interpretation and stitching of partial maps.

(3) Reduced aberration. The dominant diffuse intensity in the  $(q_{2\theta}, q_{\text{roll}})$  plane, as shown by Fig. 6, can be avoided.

The main disadvantage is that two lenses with different focal lengths are needed: one horizontally and one vertically. Hence, their BFPs are not placed at the same distance. Moreover, the physical aperture of the MLLs manufactured is currently limited to 100  $\mu\text{m}$ . This implies that the MLL needs to be placed within a few centimetres of the sample to fully exploit the larger NA. This implies a loss in resolution.

We also remark that the concept of a dark-field neutron microscope and its implementation in a time-of-flight opera-

tion was proposed by Poulsen *et al.* (2014). Similar to the X-ray case, dark-field neutron microscopy may be seen as part of a multi-scale approach complementary to neutron absorption tomography and neutron diffraction tomography of grains (Peetermans *et al.*, 2014; Cereser *et al.*, 2017).

## 7. Conclusion

We have derived the relation between reciprocal space and the back focal plane of an X-ray dark-field microscope. Our results enable swapping between mapping in direct space and reciprocal space, which is a key part of many materials studies with transmission electron microscopes. In conjunction with Paper 1, the current article has presented optical tools that enable the transfer of this dual approach to the three-dimensional characterization of thick specimens. With analytical expressions for the main optical parameters we hope to ease alignment and to promote dark-field X-ray microscopy as a quantitative tool for materials science.

## Acknowledgements

The authors are grateful to Hugh Simons for stimulating discussions and D. M. Paganin for a critical reading of the manuscript. We thank the ESRF for beamtime.

## Funding information

We thank the instrument center DANSCATT for support of travel. HFP and ACJ acknowledge support by the ERC grant ‘Diffraction Based Transmission X-ray Microscopy’ (grant No. 291321).

## References

- Ahl, S. R., Simons, H., Jakobsen, A. C., Zhang, Y. B., Stöhr, F., Jensen, D. J. & Poulsen, H. F. (2015). *Mater. Sci. Eng.* **89**, 012016.
- Bosak, A., Snigireva, I., Napolskii, K. & Snigirev, A. (2010). *Adv. Mater.* **22**, 743–751.
- Cereser, A. *et al.* (2017). *Sci. Rep.* **7**, 9561.
- Cook, P., Simons, H., Jakobsen, A. C., Yildirim, C., Poulsen, H. F. & Detlefs, C. (2018). *Microsc. Microanal.* **24**, 88–89.
- Ershov, P., Kuznetsov, S., Snigireva, I., Yunkin, V., Goikhman, A. & Snigirev, A. (2013). *J. Appl. Cryst.* **46**, 1475–1480.
- Falch, K. V., Lyubomirsky, M., Casari, D., Snigirev, A., Snigireva, I., Detlefs, C., Michiel, M. D., Lyatun, I. & Mathiesen, R. H. (2018). *Ultramicroscopy*, **184**, 267–273.
- Goodman, J. (2005). *Introduction to Fourier Optics*. Englewood: Roberts and Company.
- Hefferan, C. M., Lind, J., Li, S. F., Lienert, U., Rollett, A. D. & Suter, R. M. (2012). *Acta Mater.* **60**, 4311–4318.
- Hofmann, F., Tarleton, E., Harder, R., Phillips, N., Ma, P.-W., Clark, J. N., Robinson, I., Abbey, B., Liu, W. & Beck, C. (2017). *Sci. Rep.* **7**, 45993.
- Jakobsen, B., Poulsen, H., Lienert, U., Almer, J., Shastri, S., Sørensen, H. O., Gundlach, C. & Pantleon, W. (2006). *Science*, **312**, 889–892.
- King, A., Johnson, G., Engelberg, D., Ludwig, W. & Marrow, J. (2008). *Science*, **321**, 382–385.
- Le Bolloch, D., Pinsolle, E. & Sadoc, J. F. (2012). *Phys. B Phys. Condens. Matter*, **407**, 3256–3259.
- Liss, K.-D., Royer, A., Tschentscher, T., Suortti, P. & Williams, A. P. (1998). *J. Synchrotron Rad.* **5**, 82–89.

- Ludwig, W., Cloetens, P., Härtwig, J., Baruchel, J., Hamelin, B. & Bastie, P. (2001). *J. Appl. Cryst.* **34**, 602–607.
- Ludwig, W., Reischig, P., King, A., Herbig, M., Lauridsen, E. M., Johnson, G., Marrow, T. J. & Buffière, J. Y. (2009). *Rev. Sci. Instrum.* **80**, 033905.
- Lyubomirskiy, M., Snigireva, I. & Snigirev, A. (2016). *Opt. Express*, **24**, 13679–13686.
- Medrano, C., Rejmánková, P., Ohler, M. & Matsouli, I. (1997). *Nouv. Cim. D*, **19**, 195–203.
- Morgan, A. J., Prasciolu, M., Andrejczuk, A., Krzywinski, J., Meents, A., Pennicard, D., Graafsma, H., Barty, A., Bean, R. J., Barthelmess, M., Oberthuer, D., Yefanov, O., Aquila, A., Chapman, H. N. & Bajt, S. (2015). *Sci. Rep.* **5**, 9892.
- Neumann, H.-B., Rütt, U., Bouchard, R., Schneider, J. R. & Nagasawa, H. (1994). *J. Appl. Cryst.* **27**, 1030–1038.
- Ohler, M., Sanchez del Rio, M., Tuffanelli, A., Gambaccini, M., Taibi, A., Fantini, A. & Pareschi, G. (2000). *J. Appl. Cryst.* **33**, 1023–1030.
- Ozaktas, H. M. & Mendlovic, D. (1995). *J. Opt. Soc. Am. A*, **12**, 743–751.
- Pedersen, A. F., Simons, H., Detlefs, C. & Poulsen, H. F. (2018). *J. Synchrotron Rad.* **25**, 717–728.
- Peetermans, S., King, A., Ludwig, W., Reischig, P. & Lehmann, E. H. (2014). *Analyst*, **139**, 5767–5771.
- Pietsch, U., Holy, V. & Baumbach, T. (2004). *High-Resolution X-ray Scattering*. New York: Springer.
- Poulsen, H. F. (2004). *Three-Dimensional X-ray Diffraction Microscopy*. Berlin: Springer.
- Poulsen, H. F. (2012). *J. Appl. Cryst.* **45**, 1084–1097.
- Poulsen, H. F., Jakobsen, A. C., Simons, H., Ahl, S. R., Cook, P. K. & Detlefs, C. (2017). *J. Appl. Cryst.* **50**, 1441–1456.
- Poulsen, S. O., Poulsen, H. F. & Bentley, P. M. (2014). *Nucl. Instrum. Methods Phys. Res. A*, **767**, 415–420.
- Rütt, U., Neumann, H.-B., Poulsen, H. F. & Schneider, J. R. (1995). *J. Appl. Cryst.* **28**, 729–737.
- Schroer, C., Günzler, T., Benner, B., Kuhlmann, M., Tümmeler, J., Lengeler, B. C., Rau, C., Weitkamp, T., Snigirev, A. & Snigireva, I. (2001). *Nucl. Instrum. Methods Phys. Res. A*, **467–468**, 966–969.
- Simons, H., Ahl, S. R., Poulsen, H. F. & Detlefs, C. (2017). *J. Synchrotron Rad.* **24**, 392–401.
- Simons, H., Haugen, A., Jakobsen, A., Schmidt, S., Stöhr, F., Majkut, M., Detlefs, C., Daniels, J., Damjanovic, D. & Poulsen, H. (2018). *Nat. Mater.* **17**, 814–819.
- Simons, H., Jakobsen, A. C., Ahl, S. R., Detlefs, C. & Poulsen, H. F. (2016). *MRS Bull.* **41**, 454–459.
- Simons, H., King, A., Ludwig, W., Detlefs, C., Pantleon, W., Schmidt, S., Stöhr, F., Snigireva, I., Snigirev, A. & Poulsen, H. F. (2015). *Nat. Commun.* **6**, 6098.
- Snigirev, A., Kohn, V. G., Snigireva, I. & Lengeler, B. (1996). *Nature*, **384**, 49–51.
- Voelz, D. (2011). *Computational Fourier Optics: A MATLAB Tutorial*. Bellingham: SPIE.
- Williams, D. B. & Carter, C. B. (2009). *Transmission Electron Microscopy*. Berlin: Springer.

Technical  
University of  
Denmark

Fysikvej, Building 307  
2800 Kgs. Lyngby  
Tlf. 4525 3344

[www.fysik.dtu.dk](http://www.fysik.dtu.dk)